COMPUTATIONAL STUDY OF COBALT OXIDE: NANOPARTICLES, SURFACES AND THIN FILMS SUPPORTED ON METAL OXIDE SURFACES

ALA’ OMAR HASAN ZAYED

FACULTY OF SCIENCE
UNIVERSITY OF MALAYA
KUALA LUMPUR

2018

COMPUTATIONAL STURY OF COBALT OXIDE: NANOPARTICLES, SURFACES AND THIN FILMS SUPPORTED ON METAL OXIDE SURFACES

ALA' OMAR HASAN ZAYED

THESIS SUBMITTED IN FULFILMENT OF THE REQUIREMENTS FOR THE DEGREE OF DOCTOR OF PHILOSOPHY

DEPARTMENT OF CHEMISTRY
FACULTY OF SCIENCE
UNIVERSITY OF MALAYA
KUALA LUMPUR

2018

UNIVERSITY OF MALAYA
ORIGINAL LITERARY WORK DECLARATION

Name of Candidate: Ala’ Omar Hasan Zayed

Matric No: SHC150006

Name of Degree: Doctor of Philosophy

Title of Project Paper/Research Report/Dissertation/Thesis (“this Work”):

COMPUTATIONAL STUDY OF COBALT OXIDE: NANOPARTICLES, SURFACES AND THIN FILMS SUPPORTED ON METAL OXIDE SURFACES.

Field of Study:

I do solemnly and sincerely declare that:

(1) I am the sole author/writer of this Work;
(2) This Work is original;
(3) Any use of any work in which copyright exists was done by way of fair dealing and for permitted purposes and any excerpt or extract from, or reference to or reproduction of any copyright work has been disclosed expressly and sufficiently and the title of the Work and its authorship have been acknowledged in this Work;
(4) I do not have any actual knowledge nor do I ought reasonably to know that the making of this work constitutes an infringement of any copyright work;
(5) I hereby assign all and every rights in the copyright to this Work to the University of Malaya (“UM”), who henceforth shall be owner of the copyright in this Work and that any reproduction or use in any form or by any means whatsoever is prohibited without the written consent of UM having been first had and obtained;
(6) I am fully aware that if in the course of making this Work I have infringed any copyright whether intentionally or otherwise, I may be subject to legal action or any other action as may be determined by UM.

Candidate’s Signature Date:

Subscribed and solemnly declared before,

Witness’s Signature Date:

Name: Prof. Dr. SHARIFUDDIN BIN MD ZAIN

Designation:

Witness’s Signature Date:

Name: Assoc. Prof. Dr. VANNAJAN SANGHIRAN LEE

Designation:

COMPUTATIONAL STUDY OF COBALT OXIDE: NANOPARTICLES, SURFACES AND THIN FILMS SUPPORTED ON METAL OXIDE SURFACES

ABSTRACT

In this study, investigation of the structural, energetic, electronic, and magnetic properties of several forms of cobalt oxides as clusters, films and surfaces had been carried out. Besides using our genetic algorithm code called Universal Genetic Algorithm (UGA) combined with DFT calculations to find the global and local energy minimum structures of $(CoO)_n$ ($n = 3 - 7$) clusters, we have also extended the search space to $(CoO)_n^q$ ($n = 3-10$, $q = 0, +1$) clusters by another code of ours, the Modified Basin-Hopping Monte Carlo Algorithm (MBHMC) program, accompanied by accurate DFT calculations. Analysis of the stability of these global minima structures are not just supported by the results of binding energies, second-order total energy difference, chemical hardness, chemical potential and HOMO-LUMO gaps, but also confirmed by the dissociation patterns of $(CoO)_n^q$ clusters that fit well with available experimental data. In addition, we also explored the electronic and magnetic behavior of the clusters to understand the reasons behind the remarkable stability of certain sizes of $(CoO)_n$ systems observed in previous experimental and computational studies. The growth mechanism of cobalt oxide (II) on the magnesia surface using the DFT+U calculations was also carried out. As the first steps in understanding the growth of the CoO film, we also addressed the diffusion and adsorption behavior of cobalt atom and cobalt oxide (II) molecule on the MgO(100) surface. Furthermore, the density of state and charge transfer calculations of CoO adsorption on the MgO(100) surface and the effect of the non-polar MgO(100) surface on the magnetic characteristic of the CoO layer had also been studied. Finally, results on the different properties of the Co_3O_4(100) surface are also presented.

Keywords: cobalt oxide, DFT, clusters, films, surfaces

KAJIAN PENGIRAAN KE ATAS KOBALT OKSIDA: JIRIM NANO, PERMUKAAN DAN FILEM NIPIS YANG DISOKONG DI ATAS PERMUKAAN TEROKSIDA

ABSTRAK

Dalam kajian ini, siasatan terhadap sifat-sifat struktur, tenaga, elektronik, dan sifat magnetik beberapa bentuk oksida kobalt dalam bentuk kelompok, filem dan jerapan permukaan. Selain menggunakan kod algoritma genetik kami, iaitu kod Universal Genetic Algorithm (UGA) yang digabungkan dengan pengiraan DFT untuk mencari struktur minimum global dan tempatan bagi kelompok $(CoO)_n$ $(n = 3 - 7)$, kami juga telah memperluaskan tahap ruang carian untuk kelompok $(CoO)_n^q$ $(n = 3{-}10, q = 0, +1)$ dengan kod Modified Basin Hopping Monte Carlo Algorithm (MBHMC) kami disertai dengan pengiraan DFT yang tepat. Analisis kestabilan struktur minima global tidak hanya disokong oleh keputusan tenaga ikatan, jumlah perbezaan tenaga orde kedua, kekerasan kimia, keupayaan kimia dan jurang HOMO-LUMO, namun juga melalui kajian ke atas corak penceraian $(CoO)_n^q$ yang sesuai dengan data eksperimen. Di samping itu, kami juga mengkaji tingkah laku elektronik dan magnetik untuk memahami sebab-sebab di sebalik kestabilan luar biasa saiz kelompok $(CoO)_n$ tertentu yang diperhatikan dari percubaan dan pengiraan sebelum ini Kami juga menganalisis mekanisme pertumbuhan oksida kobalt(II) di permukaan magnesia menggunakan pengiraan DFT+U. Sebagai langkah pertama dalam memahami pertumbuhan filem CoO kami juga mengkaji tingkah laku penyebaran dan penjerapan atom kobalt dan molekul oksida kobalt(II) di atas permukaan MgO(100). Tambahan pula, sifat distribusi ketumpatan dan pengiraan pemindahan cas bagi penjerapan di atas permukaan MgO(100) dan kesan permukaan (100) tidak berkutub MgO terhadap ciri magnet lapisan CoO telah juga dikaji. Akhir sekali, sifat-sifat yang berbeza untuk permukaan $Co_3O_4(100)$ telah dijalankan.

Kata kunci: oksida kobalt, DFT, jirim nano, filem, permukaan

ACKNOWLEDGEMENTS

Most students faced difficulties during their Ph.D. journeys. Some are fortunate enough to be surrounded by family and friends who know how to support them in their efforts to overcome these obstacles. By the grace of Allah, I was one of those.

First and foremost, I would like to thank the almighty Allah for giving me the power to achieve this work. I am deeply thankful to my mother for her sacrifices for me and our family. I will forever stay owe her more than what I am able to do for her. Mother, I always pray for Allah to give you the happiness and health consistently. My Sincere thanks go to my family. In particular, my brother, Hasan Zayed, who stood behind me in each step in my Ph.D. study.

I dedicate this thesis to my wife, in appreciation for her support, patience, and endless love, as well to my son, Amir Aldin, for giving me a reason to finish this project as soon as possible to be with him forever "insha'Allah" (God willing).

I would like to express my deepest thanks to my principal supervisor Prof. Dr. Sharifuddin Bin Md Zain for patiently guiding me along my studying and learning. I should say that I learned from him more than science, including the wisdom and humanity. My appreciation goes to Assoc. Prof. Dr. Vannajan Sanghiran Lee for her support and help with my Ph.D. project.

I would like to take the opportunity to express my honest appreciation to Dr. Arief C. Wibowo who always guiding me with his valuable advices that served as an inspiration in doing this work. I am grateful for all of my friends who have encouraged me throughout the dissertation process, in particular, my colleagues at the computational chemistry lab in the University of Malaya.

TABLE OF CONTENTS

LIST OF FIGURES

LIST OF TABLES

LIST OF SYMBOLS AND ABBREVIATIONS

$2S+1$	:	Spin multiplicities.
E_H	:	Electron-electron repulsion energy.
E_b	:	Binding energies.
E_C	:	Correlation energy.
E_{diff}	:	Diffusion barrier.
E_x	:	Exchange energy.
ΔE_{H-L}	:	HOMO-LUMO energy gaps.
ΔH	:	Adsorption enthalpy
$\Delta^2 E$	:	Second-order total energy differences.
H	:	Chemical hardness.
$\hat{H}$	:	Hamiltonian.
μ	:	Magnetic moment.
μ'_O	:	Oxygen chemical potential.
T	:	Residence time.
2D	:	Two-dimensional.
3D	:	Three-dimensional.
AFM	:	Antiferromagnetic.
ASE	:	Atomic Simulation Environment.
BCB	:	Bottom conduction band.
BCGA	:	Birmingham cluster genetic algorithm.
BH	:	Basin-hopping algorithm.
BHMC	:	Basin-Hopping Monte Carlo.
BOA	:	Born-Oppenheimer approximation.

BPGA	:	Birmingham parallel genetic algorithm.
BZ	:	Brillouin zone.
CDD	:	Charge density difference.
DFT	:	Density functional theory.
DOS	:	Density of states.
EF	:	Fermi energy.
EXX	:	Exact exchange energy.
FCC	:	Face centered cubic.
FFT	:	Fast Fourier Transforms.
FM	:	Ferromagnetic.
GA	:	Genetic algorithm.
GB	:	Grid-based.
GBM	:	Gaussian broadening method.
GGA	:	Generalized gradient approximation.
GKA	:	Goodenough–Kanamori-Anderson.
GPAW	:	Grid-based Projector Augmented Wave.
HEG	:	Homogeneous electron gas.
HF	:	Hartree-Fock.
Hkl	:	Crystalline plane.
HOMO	:	Highest occupied molecular orbital.
L-BFGS	:	Limited-memory Broyden-Fletcher-Goldfarb-Shanno.
LCAO	:	Linear Combination Atomic Orbital.
LDA	:	Local-density approximation.
LDOS	:	Local density of states.
LJ	:	Lennard-Jones.
LSDA	:	Local spin-density approximation.

LTM	:	Linear tetrahedron method.
LUMO	:	Lowest unoccupied molecular orbital.
MBHMC	:	Modified Basin-Hopping Monte Carlo.
MOPAC	:	Molecular Orbital PACkage.
MSBH	:	Monotonic sequence basin-hopping algorithm.
MTM	:	Modified tetrahedron method.
NCPP	:	Norm-conserving pseudopotentials.
PAW	:	Projector-augmented wave method.
PBC	:	Periodic boundary conditions.
PBE	:	Perdew-Burke-Ernzerhof.
PDOS	:	Projected density of states.
PES	:	Potential energy surface.
PGAM	:	Pool genetic algorithm methodology.
QSAR	:	Quantitative structure-activity relationships.
RBHMC	:	Revised BHMC-algorithm.
RHEED	:	Reflection high-energy electron diffraction.
SIC	:	Self-interaction correction.
SIE	:	Self-interaction error.
SQL	:	Structured Query Language.
T	:	Kinetic energy.
TDOS	:	Total density of states.
TMO	:	Transition metal oxide.
TVB	:	Top valence band.
UGA	:	Universal Genetic Algorithm.
VASP	:	Vienna ab initio simulation package.
VB	:	Valence band.

VEA	:	Vertical electron affinity.
VIP	:	Vertical ionization potential.
VMD	:	Visual Molecular Dynamics.
XPS	:	X-ray photo-electron spectroscopy.
XRD	:	X-ray diffraction.

CHAPTER 1: GENERAL INTRODUCTION

1.1 Background of study

Computational investigations of structural, magnetic and other properties of different transition metal oxides (TMOs) become essential tools in present-day material design, which is necessary to fabricate a new TMO material with desirable properties through understanding the structural features in various forms such as nanoparticles, thin films and surfaces systems. Among the TMO materials, cobalt oxides have been the attractive subjects of considerable research efforts in recent years due to their unique properties that can be exploited in many different applications such as heterogeneous catalysts (Ullman et al., 2016), electrochromic devices (Ali et al., 2016), Li-ion batteries (Wang et al., 2002), solar absorbers (Amin-Chalhoub et al., 2016), solid-state sensors (Li et al., 2016), pigments (Wai & Ahmad, 2016), supercapacitors (Iqbal et al., 2016) and superhydrophobic surfaces (Barthwal & Lim, 2015).

Three different types of cobalt oxide exist with stoichiometric forms; namely Co_3O_4, CoO and Co_2O_3 (Abad-Elwahad et al., 2015). The two former types are known as spinel cobalt oxide and rock-salt cobalt oxide, respectively, both showed high thermodynamic stability compared to the latter type (i.e., cobalt sesquioxide Co_2O_3). Of course, the spinel cobalt oxide is found to be the most stable type with the semiconductor characteristic, because its experimental band-gap value is ~1.6 eV (Shinde et al., 2006a). While the next stable cobalt oxide type, namely CoO has band gap of 2.6 eV based on available experimental data (Bredow & Gerson, 2000), which is categorized as a Mott-Hubbard insulator due to the gap produced by the Coulomb interaction among 3d-bands of the cobalt atoms (Parmigiani & Sangaletti, 1999). Here, it's worth mentioning that the overall cobalt oxide is classified as the strongly correlated system, because of the Coulomb electron-electron interaction between the 3d orbitals of Co, where the electrical and magnetic properties are closely linked with the structural geometry of cobalt oxide.

Many experimental studies have been conducted to investigate the neutral and cationic fragmentation patterns of cobalt oxide clusters by utilizing different mass spectrometry techniques. For example, Dibble et al. (2012) utilized the time-of-flight mass spectrometry in the fragmentation process of cobalt oxide clusters. They observed that the intensity peaks of the generated nanocluster sizes have different heights in the mass spectrum, reflecting the high stability of the certain cationic cobalt oxide sizes such as $Co_4O_4^+$ and $Co_6O_6^+$ compared to the rest of the other sizes, which means increasing their opportunity to reach a mass detector, and thus show high abundance peaks. Another study of the fragmentation spectrum for the neutral cobalt oxide nanoclusters showed the same observation (Xie et al., 2010). As a result, it seems obvious that the relative structural stability between cobalt oxide nanoclusters, whether neutral or cationic, is the main reason that explained the mass spectrum data. Therefore, the computational analyses play a critical role to explain the structural stability of different cobalt oxide nanoparticles which lies behind these experimental findings. In addition, the remarkable catalytic activity of cobalt oxide nanoparticles, especially toward water splitting have been demanding more computational works to investigate their structural, electronic and magnetic properties (Risch et al., 2012). A few computational studies have been carried out on this topic in the past using a variety of density functional theory (DFT) codes implemented in several commercial programs such as SIESTA (Soler et al., 2002),Vienna ab initio simulation package (VASP) (Kresse & Furthmüller, 1996c) and Gaussian 09 (Frisch et al., 2009). Despite these works, there is no rigorous methodology used to explore more thoroughly the potential energy surface (PES) of different sizes of cobalt oxide nanoparticles, which is very important for finding the true global and the local energy minimum structures. In fact, most of these studies depend on the structural intuition that can be used for small clusters with a limited number of atoms only. Due to a huge number of possible isomers that can be proposed for large clusters, the structural intuition can not be satisfied for determining the ground state structures and thus is not likely to interpret the experimental results. Therefore, using more accurate methods to explore ground state structures of cobalt oxide nanoparticles are thus mandatory. Furthermore, only a limited number of these studies was addressed the density of state distribution and molecular orbital analysis to better understand the source of magnetic and electronic properties of cobalt oxide nanoparticles.

In the literature, several methods such as metadynamics (Laio et al., 2005), simulated annealing (Kirkpatrick et al., 1983), random sampling (Pickard & Needs, 2011), basin hopping (Wales & Doye, 1997) and genetic algorithm method (Deaven & Ho, 1995) are used to find the ground-state structures of the cluster by systematic search strategy designed based on the chemical composition and other selected criteria. The latter two methods have shown impressive performance in finding not only the ground-state structures of metal and metal oxide clusters but also in exploring their unusual structures (Asgari et al., 2014). For example, Sierka et al. (2007) reported some unexpected structures for small alumina (Al_2O_3) clusters in the gas phase using a genetic algorithm, where the global minimums of neutral $(Al_2O_3)_4$ cluster and cationic $(Al_2O_3)_4^+$ cluster have structural features that are quite different from any known phases of the bulk alumina. Similar predictive power is also shown for the basin hopping algorithm (Drebov & Ahlrichs, 2010). Recently, DFT refinement calculations after algorithm search processing has significantly enhanced the prediction accuracy for finding the ground-state structures of several cluster species (Zhao et al., 2013). Development of both genetic algorithm and basin hopping algorithm in terms of accuracy, flexibility and speed was established in the last decade and still occupies much attention nowadays. For instance, the Birmingham parallel genetic algorithm has been specifically designed to implant the DFT optimization directly inside the body of the algorithm using python code (Davis et al., 2015). Although this new algorithm is highly sophisticated and able to deal efficiently with the cluster systems characterized by complicated PES, it has a limited capability to apply for a broad range of cluster sizes, particularly for large clusters except the availability of a high-performance supercomputer, which requires a greater computational cost for the DFT optimization process of new structures generated by the genetic algorithm, which will be elaborated in detail later. In this study, we design a new basin hopping and genetic algorithm in such a way to add more flexibility to deal with a large scale of systems that have various PES shapes, whilst the balance between the quality of results and the computational cost is carefully preserved. It's worth saying that the Python language and Structured Query Language (SQL) played a major role in written both codes, due to a large number of libraries available in Python, which is compatible with SQL databases. These algorithms are used to investigate the ground-state structures of the neutral and cationic $(CoO)_n$ (n = 3 − 10) cluster sizes. In addition, the stability, electronic and magnetic properties and the fragmentation pattern of $(CoO)_n$ nanoclusters are also determined.

Besides nanoclusters, cobalt oxide (CoO_x) film deposited on metal oxide substrates is also known to have many potential applications such as the universal catalyst for photo electrochemical water splitting (Trotochaud et al., 2013), air pollution control (Gluhoi et al., 2004), water pollutants removal (Klabunde & Khaleel, 1998), etc. However, supported CoO layers on metal oxide surfaces has not received much attention compared to metal surfaces. Only a small number of experimental and theoretical papers deal with the formation of CoO layers on metal oxide substrates can be found in the literatures. For example, one recent study (Zayed et al., 2013) examined the growth patterns of CoO thin films on α-Al_2O_3(0001) surface and showed the cubic, zinc-blende, or wurtzite structures as the possible coexistence morphologies of the CoO overlayers on the alumina surface. In all of these structures, the Co magnetic moments had different arrangements at higher surface coverage, indicating that the growth mode was strongly affected the magnetic properties of the CoO films, which was in agreement with the experimental data (Alaria et al., 2008). Noticeably, studying the adsorption behavior of Co atom and CoO molecule on this substrate significantly helped to understand how these growth modes were formed, which was proposed to be the elementary steps to explore the growth of CoO nanosized films.

The key question that arises in our minds, based on the fact that the surface nature of the grown materials is strongly affected by its growth modes and magnetic properties, is how the growth mechanism and various properties of the deposited CoO film are changed on different surfaces. For instance, in the above-mentioned study, the CoO film had been investigated on polar surface, i.e., α-Al_2O_3, where the reduction of surface polarity interpretation was invoked to explain the observed magnetic and structural properties. As a result, it seems very interesting to investigate systematically the growth of CoO on the non-polar surface such as magnesia surface (MgO) and traced the progression of the growth morphology at different surface coverages and seeing how the magnetic and electronic properties are influenced by the non-polar surface compared to polar one. All of these potential subjects as well as the atomistic scale behavior of Co atom and CoO molecule, including adsorption and diffusion process are addressed extensively in this work study.

The spinel cobalt oxide (Co_3O_4) has received the growing interests, due to its numerous applications, especially as the catalyst for several reactions such as the oxygen reduction (Jiao & Frei, 2009), low-temperature CO oxidation (Xie et al., 2009), water splitting (Liang et al., 2011), methanol oxidation (Zafeiratos et al., 2010) and Fischer-Tropsch reaction (Khodakov et al., 1997). Since surfaces play a pivotal role in all these applications, there has been an increasing attention to understand the physical and chemical properties of Co_3O_4 surfaces in order to produce Co_3O_4-based new materials with excellent performance. Because of the paucity of experimental studies, a little information about the atomic-scale characterization of Co_3O_4 surfaces is known. Moreover, a few theoretical studies covering aspects of this subject can be found in the literature. One of the pioneer works was done by Chen and Selloni (2012), who investigated the energetic stability, atomic structures, electronic and magnetic properties of Co_3O_4 (110) surface by employed DFT with the on-site coulomb interaction U term. They proposed two possible non-stoichiometric terminations for Co_3O_4(110) surface; one exposed both Co^{+3} and Co^{+2} ion-types and the other one revealed only Co^{+3} ions. The former showed more chemical stability under a broad scale of oxygen chemical potentials. Most notably, Co^{+3} cations were shown to become magnetic, although their magnetic moments in the bulk are zero, which drove the surface to exhibit different magnetic orderings relative to that in the bulk. A partial metallization had been also observed in both surface terminations caused by the surface electronic states presented in the bulk band gap, in which these states contributed to the stability of both polar terminations via the charge compensation mechanism. They also reported that the modification in the magnetic state of Co^{+3} ions obviously affected the electronic and magnetic properties of Co_3O_4(110) surface.

Another DFT study (Montoya & Haynes, 2011) has been reported that the formation of Co_3O_4(100) surface is thermodynamic preferred compared to the Co_3O_4(110) and Co_3O_4(111) surfaces. In contrast to the experimental result of Co_3O_4 nanorods, where the (110) face of Co_3O_4 was a predominant feature (Xie et al., 2009). However, two non-stoichiometric terminations of Co_3O_4(100) surface were suggested in this study; (*i*) terminated by Co^{+2} on the upper layer and (*ii*) terminated by Co^{+3} ions and lattice oxygen ions. The favorable termination depended on the oxygen chemical potentials, where the former termination was the preferred one under the oxygen-poor conditions, while the latter was more stable under the oxygen-rich conditions. In addition, the stoichiometric termination models of Co_3O_4(100) surface had been proposed by Zasada et al. (2011), and found to be the most stable terminations. As we will discuss further in the coming sections.

Our study of this particular material does not only cover all possibilities of Co_3O_4(100) surface terminations, including the stoichiometric and non-stoichiometric models under different oxygen conditions, but also answer these important questions of ’how the physical and chemical properties of Co_3O_4(100) surface, which is much closer to the bulk structure?’ and ’does the magnetic state of Co^{+3} surface ions change and affect the electronic and magnetic characteristic of Co_3O_4(100) surface compared with Co_3O_4(110) one?’.

1.2 Objective of research

This research study is one of the endeavors that seek to answer this intriguing question ’what is the chemistry behind the unique activities of cobalt oxides and their potential in many applications’. Many efforts were done to answer this big question in the past years and continuously increased over time. The aim of the current study is to throw some light on the answer of the above question through achieving these following objectives:

(1) To identify the ground-state structures of CoO nanoclusters by using more sophisticated methods than that used previously, including genetic algorithm and basin-hopping Monte Carlo algorithm, which are designed well to explore the potential energy surface of different CoO cluster sizes effectively.

(2) To determine the chemical and physical characteristic such as structural, magnetic and electronic properties and the dissociation pattern of ground-state structures of CoO nanoclusters by DFT calculations in an attempt to provide a much clearer picture of these material properties than earlier, and

trying to understand the relationship between these properties, taking as an example the well-known connection between the electronic and structural properties.

(3) To describe the growth morphology and magnetic properties of the deposited CoO on MgO(100) surface, in which the adsorption and diffusion of Co atom and CoO molecule are fully implemented as the initial steps to realize the growth mechanism of CoO material on this non-polar surface. Implementing the electronic density states and Bader charge analysis to examine the influence of non-polar substrate on the grown CoO material.

(4) To estimate the surface properties involving the surface energy, magnetic and electronic properties of different termination possibilities of spinel cobalt oxide, $Co_3O_4(100)$ surface, and employing charge analysis to evaluate the polarity of some surface terminations.

1.3 Outline of research

Chapter two in this thesis represents the literature review section and involves the brief description of the cobalt oxide system. This is followed by several subsections describing the methodologies used to deal with the research subjects here, such as the genetic algorithm, basin-hopping algorithm, and DFT+U calculations. The background and the progression in these methodologies are also implemented. We then briefly introduce the programs employed in our works to design, analysis and simulate the modeling data of cobalt oxide systems.

In chapter three, we will discuss a new design code of genetic algorithm, including a full description of algorithm mechanism and its characteristic features. The ground-state structures of neutral $(CoO)_n$ $(n = 3 - 7)$ clusters using this genetic algorithm with DFT calculations are also identified, as well as the structural transformation trend from two-dimensional growth to three-dimensional growth of the global ground-state structures of CoO nanoclusters in neutral and cationic states.

In chapter four, using another methodology and so-called (modified basin-hopping Monte Carlo algorithm) to explore further the PES of cobalt oxide clusters is clearly described. The stability comparison between the resulting ground-state structures is carried out and determined by several ways, such as binding energy, second total energy difference, chemical hardness, chemical potential and the highest occupied/lowest unoccupied molecular orbital (HOMO-LUMO) energy gap. The density of state distribution and molecular orbital analysis are also implemented to understand the source of the magnetic property and the stability nature of global ground-state structures as well as the fragmentation pattern analysis of neutral and cationic $(CoO)_n$ ($n = 3 - 10$) clusters.

In chapter five, the growth morphology and magnetic properties of the deposited CoO on the MgO(100) surface at different surface coverages are systematically. The atomic-scale behaviors of Co atom and CoO molecule on the magnesia surface, including the adsorption and diffusion processes, are also discussed as the elementary steps to understand the growth mechanism of CoO film on the MgO(100) surface.

In chapter six, we will describe the possible surface terminations of the $Co_3O_4(100)$ surface, including the stoichiometric and non-stoichiometric surface models. Several aspects for each of these models, such as the surface energy, structural surface relaxation, surface magnetization, electronic structure and the polarity compensation, are also estimated in this chapter. We also compare between these surface models to figure out the most stable termination surface of the $Co_3O_4(100)$ surface as well as their differences from each other.

Chapter seven contains the conclusions which are extracted from the prior works in the aforementioned chapters, where the main findings and implications of this thesis are highlighted as well as some possible directions of future research works.

CHAPTER 2: LITERATURE REVIEW

2.1 Cobalt oxides

2.1.1 Co_3O_4

Cubic normal spinel structure (Figure 2.1) with a lattice constant (a= 8.082 Å (Liu & Prewitt, 1990)) shows higher thermodynamic stability than other cobalt oxides. It consists of three ion types; Co^{+2}, Co^{+3} and O^{-2} in the ratio of 1: 2: 4, where the tetrahedral Co^{+2} ions and the octahedral Co^{+3} ions are magnetic and nonmagnetic, respectively. Crystal field theory can explain the magnetism of both ions via the splitting of the d-orbitals into two groups; t2g and eg orbitals (Figure 2.2) at room temperature, Co_3O_4 is a semiconductor material with a band gap (1.6 eV) separated by t_{2g} states of the tetrahedral Co^{+2} ions and the octahedral Co^{+3} ions (Kim & Park, 2003).

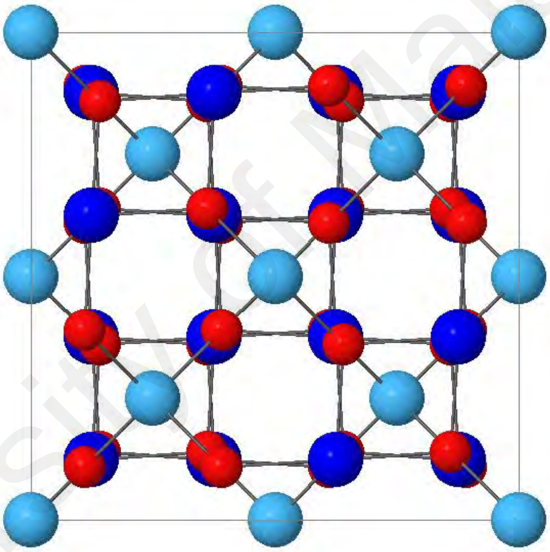

Figure 2.1: The Co_3O_4 unit cell with the normal-spinel structure, which consists of 16 Co^{+3} ions, blue; 8 Co^{+2} ions, cyan; and 32 O^{-2} ions, red.

2.1.2 CoO

Cobalt monoxide has a rock-salt structure with a lattice parameter of 4.263 Å (Sasaki et al., 1979). The structure is simpler than that of above-described Co_3O_4, where the cubic structure of CoO Contains only two sublattice ions: Co^{+2} ions, and O^{-2} ions. These sublattices aligned diagonally in the bulk structure, making each ion surrounded by other

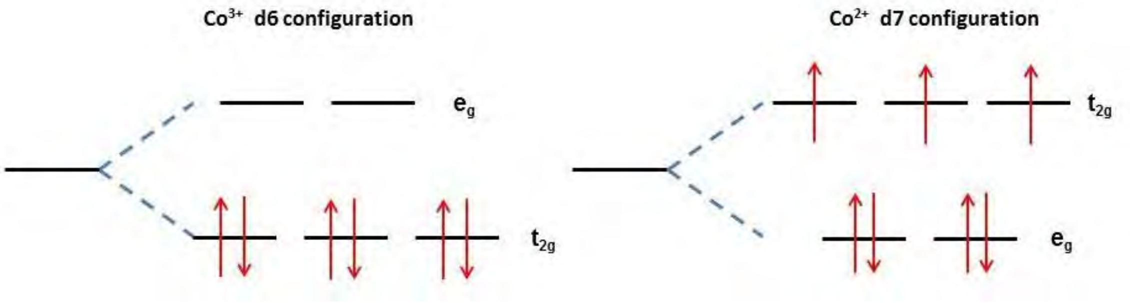

Figure 2.2: The crystal-field splitting of the octahedral Co^{+3} ion and the tetrahedral Co^{+2} ion on the left and right sides, respectively.

six ions (Figure 2.3). The t_{2g} and e_g orbitals becomes manifest due to the splitting of the five degenerate d-orbitals of Co^{+2} ions under the octahedral crystal field. Besides the possibility of high-spin state (quartet multiplicity) generated by the distribution of d^7 electrons in Co^{+2} ions, the low-spin state with doublet multiplicity is also possible (Figure 2.4). Owing to the antiparallel couplings between 3d-Co^{+2} orbitals, the CoO bulk is strongly antiferromagnetic (Boussendel et al., 2010). Additionally, the inherent relation of the magnetic properties of CoO materials with their structural forms such as nanoparticles, thin films and surfaces yields a variety of magnetic behaviours. For example, small CoO nanoparticles (< 16 nm) reveal ferromagnetic behavior at low

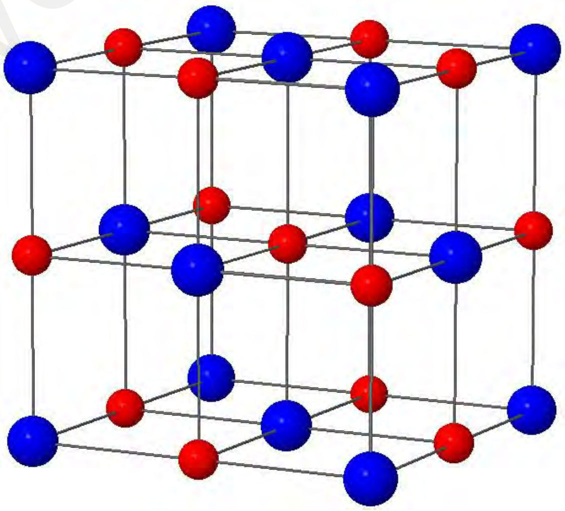

Figure 2.3: The CoO unit cell, which contains two sublattice ions: Co^{+2}, blue; O^{-2}, red. Each ion surrounded by 6 nearest different kind of ions, where the distance between the nearest neighbor kind of ions is $(1/2)\alpha_0 = 2.132$ Å**.**

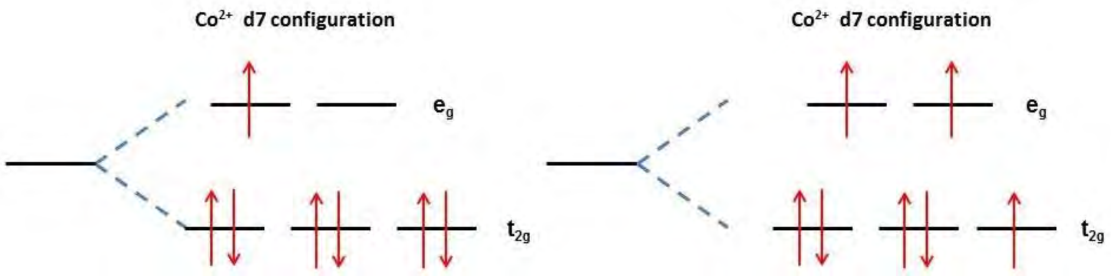

Figure 2.4: The crystal-field splitting of the octahedral Co^{+2} ion in the low-spin (on the left) and in the high-spin (on the right).

temperatures (Ghosh et al., 2005), while larger sizes below Neel temperature (T_N< 350 K) show the characteristic of antiferromagnetism (Zhang et al., 2003).

2.1.3 Co_2O_3

Cobalt Sesquioxide, Co_2O_3, is a thermodynamically less stable cobalt oxide with a corundum structure (hexagonal, Ni_2O_3-like structure), shown in Figure 2.5. The high-pressure phase of Co_2O_3 associated with low-spin Co^{+3} has (a=4.882Å, c=13.88Å) lattice parameters, whereas the low-pressure phase with high-spin Co^{+3} shows (a=4.882Å, c=13.88Å) lattice parameters (Chenavas et al., 1971). In the literature, few details exist regarding the electronic and magnetic properties of Co_2O_3, due to the difficulty of its synthesis; especially, with low thermal stability (Prabhakaran, et al., 2009). The ab initio study reported that this difficulty is caused by the competition with hydroxides and stable cobalt oxides, or to kinetic motives (Catti & Sandrone, 1997).

2.2 Statistical mechanical methods

The nanoparticles or clusters, consisting of a few to thousands of atoms or molecules, demand structural analysis to understand their shape-, size-, and composition-dependent properties and the relationship between these properties. Only the experiments in conjunction with theoretical investigations can provide a complete picture of the cluster geometry and its associated properties. Since cluster sizes have different structural

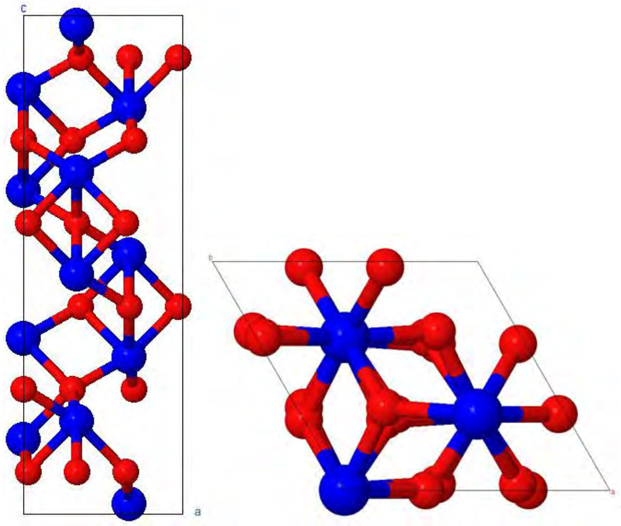

Figure 2.5: Side (left) and top (right) views of the unit cell of Co_2O_3 with a hexagonal structure, which consists of 12 Co^{+3} ions, blue; and 18 O^{-2} ions, red.

possibilities, many theoretical efforts have been devoted to predict the ground-state structures, in particular, the global minimum structure. (Belyaev et al., 2016; Lu et al., 2016; Ishimoto & Koyama, 2016). However, the accuracy of this prediction relies on exploring the PES of N-atom cluster efficiently. DFT calculations or ab initio electronic structure calculations provide accurate PES of small clusters, but they are computationally expensive. For instance, the number of local minima for Lennard-Jones (LJ) clusters increases exponentially with cluster size, as has been previously suggested (Hoare, 1979; Tsai & Jordan, 1993) and this behavior is confirmed by counting the number of transition states of PES (Doye & Wales, 2002; Wales & Doye, 2003). Therefore, the above-mentioned methods are impractical to deal with larger clusters except for clusters with very small sizes. As a result, statistical mechanical methods have received much attention in order to explore the PES of larger clusters such as GA (Deaven & Ho, 1995), BH (Wales & Doye, 1997), simulated annealing (Kirkpatrick et al., 1983), Tsallis statistics (Andricioaei & Straub, 1997), and etc. Among these methods, both GA and BH algorithms have a remarkable ability to find the ground-state structures of different cluster types with a reasonable cost.

2.2.1 Genetic algorithm (GA)

The GA adopts the principles of natural evolution in its searching technique. Similar to the evolutionary processes, GA includes mating (gene crossover), natural selection, and mutation to explore different regions of system space. As an evolutionary algorithm, it also involves differential evolution, evolution strategies, and genetic programming (Back, 1996).

In principle, we can use GA to solve multi-objective problems that contain variables (genes) able to encode together to make a string (chromosome). Each chromosome acts as a possible solution to the problem. To simulate the biological concepts, alleles represent the values of individual variables. The relationship between these concepts is shown in Figure 2.6. The population is a set of individuals, and evolves over a certain number of successive generations. Further details of GA and its specific implementations are provided in the original texts (Mitchell, 1998; Goldberg, 1989; Holland, 1992). In the following paragraphs, we will describe briefly the GA operators, the application of GA in chemistry, the history of using GA in cluster optimization and the Birmingham cluster genetic algorithm program as a well-known GA application as well as the developments in the GA approach.

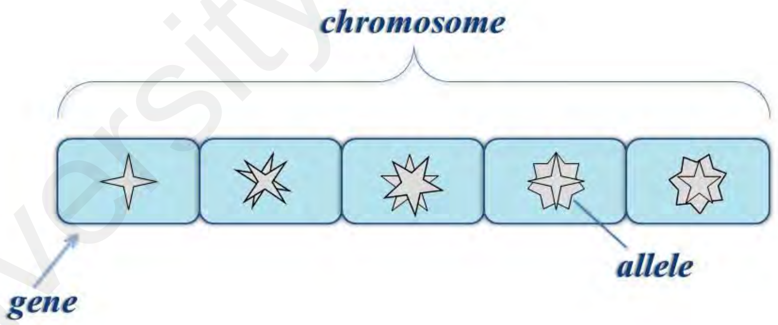

Figure 2.6: Schematic illustration represents the individual of a generic algorithm (GA) optimization technique. The string of variables or "chromosome" represents the individual, which contains variables of the optimization problem or "genes" symbolized by blue rectangles. The "alleles" describe the values of these variables.

The beginning group of individuals, which are able to evolve during the GA processes, is called the initial population. We usually generate these individuals randomly, but it is sometimes useful to build them based on a priori knowledge of their structure to reduce computational cost.

One of the important concepts in GA is known as fitness, where the evaluation of the trial solution (chromosomes) is carried out with respect to the fitness-function being optimized. Thus, in a maximisation problem, the high value or in a minimisation problem, the low value of the function corresponds to high fitness. In the case that the lower and upper boundaries of the function are known, the absolute fitness can be applied to compare fitness values from generation to generation. Otherwise, in each generation the best and worst members of the current population are used to scale the fitness values of all individuals. The latter, called dynamic fitness scaling, is used in most GA applications. For the reasons of determining the probability of an individual to participate in crossover and selecting the best individuals (candidates) which will survive into the next generation, using the fitness concept in GA is important.

Selection points are used for choosing the individual members of the population to enter into the crossover operation. Many of the selection methods found in the literature; however, the “tournament” and “roulette wheel” selections are most commonly used. In the tournament selection, a number of individual members are chosen randomly to form a “tournament” pool, where the two members with the highest fitness in this tournament pool are selected to be the parents for the next crossover step. The roulette wheel method picks one individual member randomly, and selects it for crossover operation when its fitness (f_i) is more than the random generated number between 0 to 1 (i.e. if $f_i > RND[0, 1]$), otherwise the method chooses and examines another member. Figure 2.7 shows how this method can be envisaged as a roulette wheel. The "genetic" information of

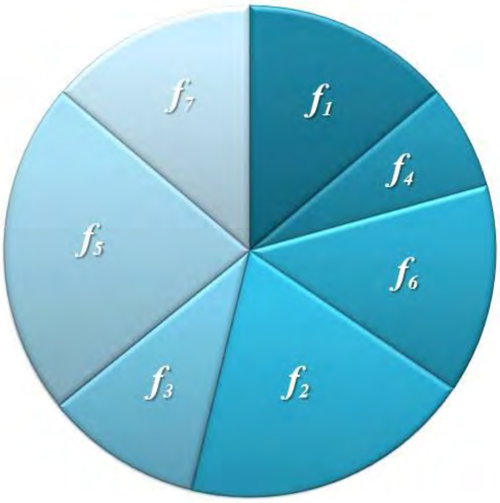

Figure 2.7: The roulette wheel scheme. A slot width on the roulette wheel represents the probability of an individual (i) for the crossover process, which is dependent on the value of its fitness f_i.

a couple of individual (parents) (sometimes more than two individuals) combines to produce “offspring” through the crossover operation. Figure 2.8 depicts two crossover operators that are commonly used in GA applications. In the one-point crossover (see Figure 2.8), two parent chromosomes are cut at the same point, in which the first part of one chromosome unites with the second part of another chromosome and vice versa, thus, two new offspring are generated. In two-point crossover (see Figure 2.8), the cut is made from two points for two parents, and the offsprings are produced by replacing the central sequences of both parents with each other. Although the crossover step provides a new offspring by mixing the genetic information of the parents, no new genetic data is inserted. This leads to lack of genetic diversity of the population "stagnation," where a nonoptimal solution is obtained due to the population converging on the same solution. The “mutation” operator helps to avoid this stagnation by increasing the genetic diversity of the population by introducing a new genetic data. Figure 2.9 illustrates how this might be achieved by randomly changing of one or more genes chosen from an individual. In dynamic mutation, the value of the mutated gene slightly differs from its

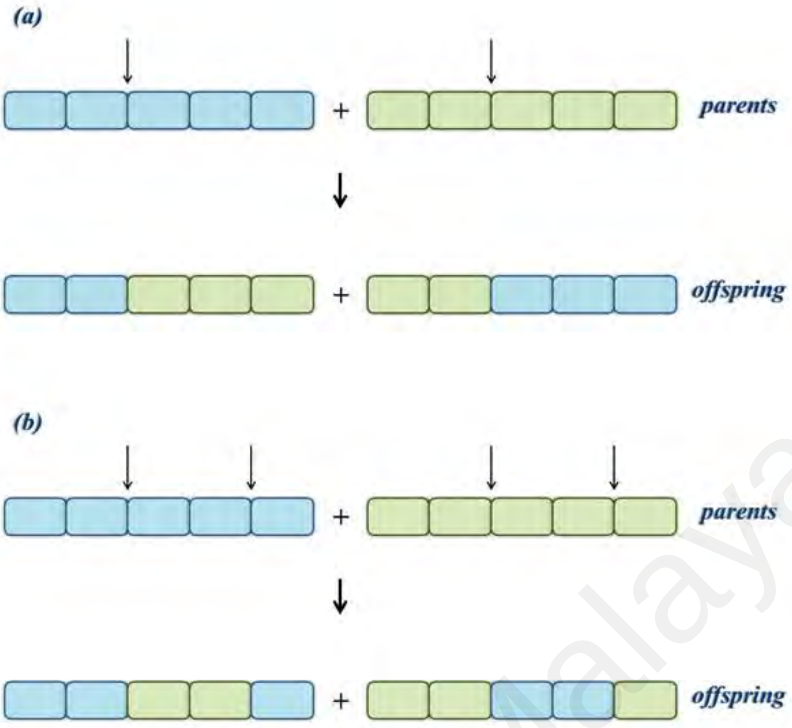

Figure 2.8: The crossover operation scheme in a generic algorithm (GA) optimization technique. (a) One-point crossover: the offsprings are formed after cutting two-parent chromosomes at the same point by combining complementary genetic-parts from the parents. (b) Two-point crossover: similar to the one-point crossover, but the parents are cut from two points instead of one.

original value randomly, while in static mutation this value is changed by a completely random value. The concept of "Natural" selection in biological evolution, which impresses upon "The survival of the fittest," is adopted in the GA idea. The individuals' mutants, parents or offsprings are selected to proceed into the next generation based on their fitness, where their fitness represents their quality relative to the quantity being optimized. Many changes of the selection step can be utilized; however, as an example all mutants are accepted, no parents are accepted, or only the best parents survive (this is also known as "elitist" strategy in order to avoid the best population member becomes worse through generational succession).

The idea of GA is to exchange the genetic information between individuals to develop better and new solutions for the optimization problem. This approach strongly depends on the parallelism to explore the different regions of the problem space simultaneously

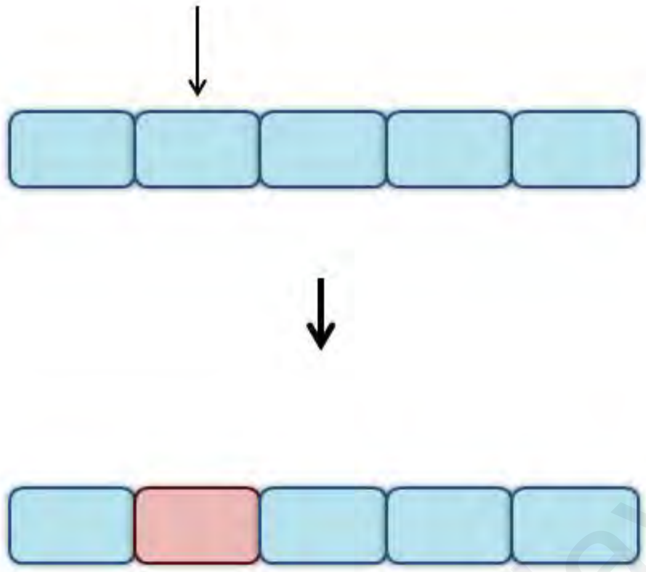

Figure 2.9: The mutation operation scheme in a generic algorithm (GA) optimization technique. In this example, the value of only one gene (variable) has changed, and it is represented here by changing its color from light blue to pink.

and the effectiveness of the crossover operation to spread the genetic information over the population. The recognition by schemata makes the GA searching approach more intelligent to determine the region of space that includes the better solutions. For example, every one of the three individual chromosomes (shown in Figure 2.10) has six genes, in which some of the genes share the same variables' values (alleles) to all chromosomes. For each chromosome, genes 3 and 6 possess circle and square alleles respectively, indicating that these allies represent near optimal or optimal values of those genes (variables). Thus, the good schemata helps the GA to generate individuals with high fitness and confines the region of possible solutions that reduces the computational cost with increasing efficiency. For three decades, GA has received growing attention to deal with the diversity of global optimization problems in physics (Alander & Alander, 1994), chemistry (Paszkowicz, 2009), biology (Esfahanian et al., 2016), etc (Cui & Cai, 2011). In chemistry and biochemistry, for example, GA applications include folding simulations (Unger & Moult,

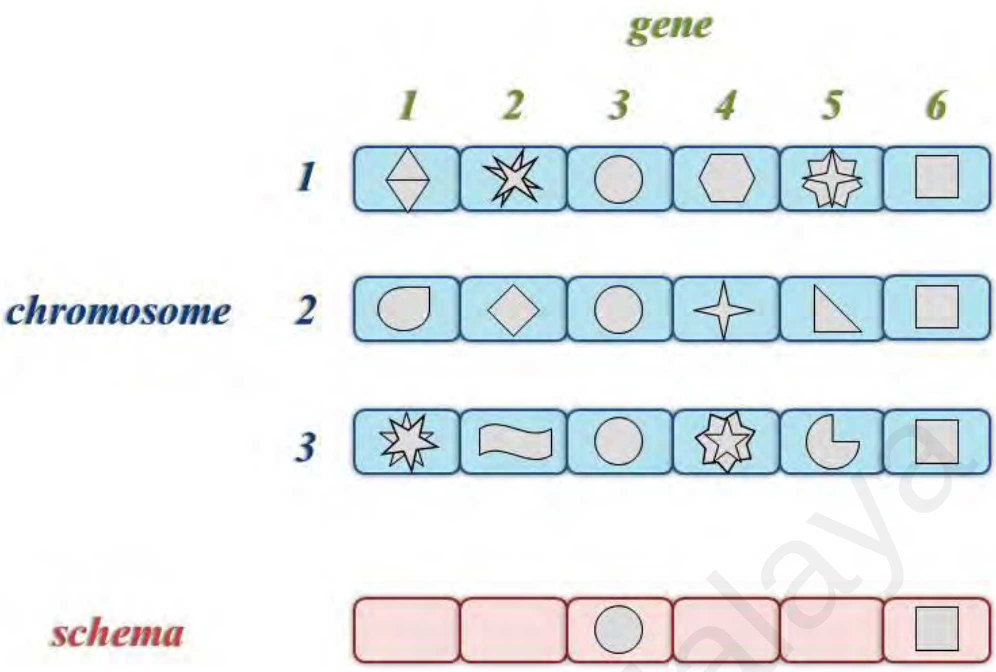

Figure 2.10: Illustration of the schemata concept in a generic algorithm (GA) optimization technique. The three individuals (strings) show the same values (alleles with blue symbols) in the 3 and 6 genes (variables), where these genes make a common schema for the new individuals (shown in red).

1993) and structure prediction of proteins (Bošković & Brest, 2016), selection of DNA and RNA aptamers (Savory et al., 2010), designing combinatorial library mixtures (Brown & Martin, 1997), flexible ligand-receptor docking of drug molecules (Magalhães et al., 2004), quantitative structure-activity relationship quantitative structure-activity relationships (QSAR) (Raj & Muthukumar, 2016), structures predication from NMR spectroscopy of molecule (Filgueiras et al., 2016) and from the X-ray diffraction data of single crystals (Woodley & Catlow, 2008), thin file (Pancotti et al., 2016) and powder (Watts et al., 2016); and optimization and control of chemical reaction systems (Elliott et al., 2004).

In the early of 1990s, GA has been used to investigate the structure of small silicon clusters by Hartke (1993) and different molecular clusters by Xiao and Williams (1993) for the first time. Subsequently, the structures of water and mercury clusters were also studied using GA (Hartke, 1996; Hartke, 2003). After Zeiri (1995) had firstly developed GA applications by using real Cartesian coordinates for the atomic positions (genes) to remove coding and decoding binary genes, Deaven and Ho (1995) introduced the next development by implementing the energy minimization by optimization of generated cluster. The latter significantly facilitates the global minimum searching by reducing the problem space, due to transferring the PES into stepped surface as in the following subsection, namely, the basin hopping algorithm. In the work of Deaven and Ho (1995), another development for GA applications have been added via the introduction of a three-dimensional crossover operator, the so-called cut and splice operator. Many studies have employed this operator, due to its ability to generate offspring with good schemata that belongs to minimum energy regions of the parent clusters. This, in turn, gives the crossover operation more physical meaning. Besides the success of Deaven and Ho (1995) to optimize carbon clusters by their GA application, they found new ground-state structures of Lennard-Jones clusters with different sizes to be more stable than the previously reported structures (Daven et al., 1995).

The Birmingham cluster genetic algorithm (BCGA), which was designed by Johnston (2003), has been considered as an effective GA application for finding the global minimum structures of different clusters (Sharmila & Blessy, 2017; Logsdail, et al., 2012). Of course, many others GA application have also introduced before the BCGA. These GA applications included new genetic operators and different ways to handle population, crossover, mutation, etc. However, here we will describe briefly the BCGA as an example of a reliable GA application and as a target for further development.

Figure 2.11 shows the flow chart of the cluster optimization using the BCGA, including the following operations:

1- Creation of the initial population: For a cluster size of N atoms, a number of initial clusters (chromosomes) are created using the Zeiri approach (Zeiri, 1995), in which the

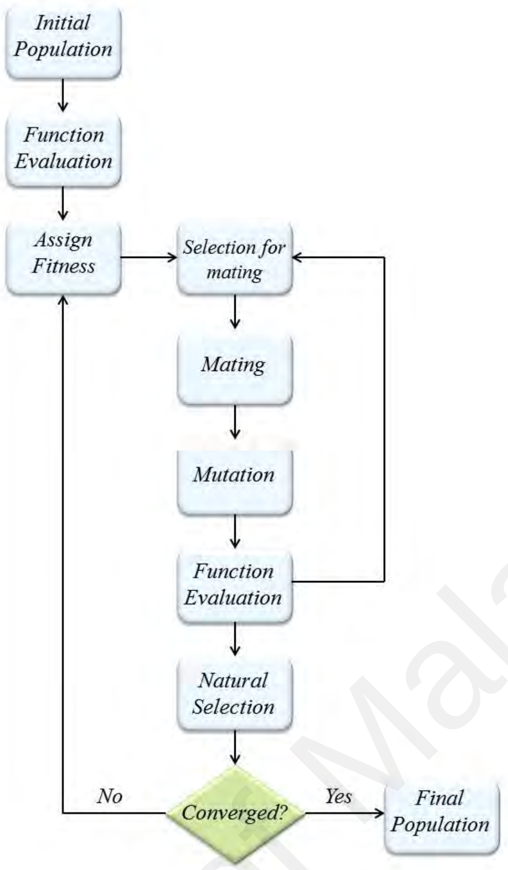

Figure 2.11: Schematic chart used by the BCGA program.

real values of Cartesian coordinates X, Y and Z are chosen randomly for each cluster atom; however, some restrictions are added to avoid atomic radii overlap. This set of clusters, i.e., the initial population is then relaxed to the nearest-neighboring minima using numerical optimization, particularly, a limited-memory quasi-Newton method such as Limited-memory Broyden-Fletcher-Goldfarb-Shanno (L-BFGS).

2- Fitness: For dynamic scaling of every cluster inside the BCGA, the following fitness calculation was used:

$$\rho_i = \frac{v_i - v_{min}}{v_{min} - v_{max}} \tag{2.1}$$

Where ρ_i is the normalized energy value of the cluster, and ν_i is the potential energy of the current cluster, while ν_{max} and ν_{min} are the highest and lowest-energy clusters in the present population, respectively. The highest fitness corresponds to the most negative potential energy (ν_{min}), whereas the least negative potential energy (ν_{max}) refers to the lowest fitness. Based on the above equation, the highest and lowest fitness clusters possess ρ values equal or close to 1 and 0, respectively.

The BCGA implements three fitness functions that were commonly used in the GA applications:

A. Linear:

$$f_i = 1 - 0.7\rho_i \tag{2.2}$$

B. Exponential:

$$f_i = \exp(-\alpha\rho_i) \tag{2.3}$$

where α is set to 3.

C. Hyperbolic tangent:

$$f_i = 1/2[1 - tanh(2\rho_i - 1\,)] \tag{2.4}$$

The degree of efficiently determining the right fitness depends on the choice of these fitness types, are giving the relative weight for good, mediocre and bad clusters effectively plays a pivotal role in the BCGA body.

3- Crossover for selecting parents: The tournament and roulette wheel selections are used to choose the parents for the crossover process. In both, the lowest energy clusters with high fitness are most likely to be select and pass a part of their structural morphology to the next generation. Then, the selected parents are subjected to the crossover operation by using various cut and splice crossover methods. The BCGA implemented cut and splice methods by applying a random rotation about two perpendicular axes for the chosen parent. Subsequently, the parent clusters are cut off horizontally parallel to the xy plane from one or two points, and the complementary fragments of the parent clusters are spliced together thereafter, as seen in Figure 2.12. Several options of the cut methods can be chosen, such as cutting the plane from a random point, across the center point of the cluster, or based on the weight of the cluster fitness by taking more atoms from the cluster with high fitness. Crossover process is halted after a preset number of generation (N_{pop}), where the number of offspring is chosen to be 80% of the population size. As depicted above, each offspring cluster is subjected to energy minimization via relaxation to the nearest local minimum. Obviously, the structural relaxation significantly influence the offspring structures by changing their atomic rearrangements, especially, in the spliced region between the two fragments.

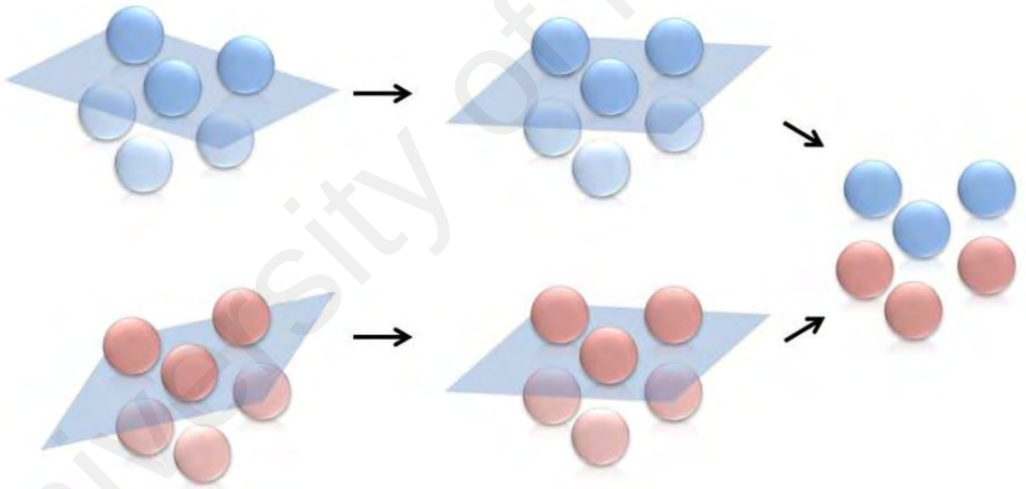

Figure 2.12: The scheme of the single cut and splice crossover operation introduced by Deaven–Ho and used within the BCGA framework.

4- Mutation: The mutation changes the atomic positions for all or some atoms in the cluster. However, a mutation operator is used to avoid the problem of stagnation and to keep the structural diversity of the population, whereby each cluster (individual) has a predetermined probability (P_{mut}) to take place through the mutation operation.

As in the crossover, many mutation operators are involved in the BCGA body. They adopt variations of the structural perturbation of the cluster as follows:

A- Twisting: In this mutation operator, the perturbation of the atomic positions occurred by a random rotation of the upper half of the cluster about the z axis on the fixed lower half.

B- Atom displacement: By using this operator, new values are randomly assigned to the atomic positions of some atoms.

C- Atom permutation: Rather than changing the atomic positions by applying this operator, exchanging the types of one or more atom is employed instead.

D- Cluster replacement: The entire cluster is eliminated and replaced by a new cluster that is generated in the same way as in the initial population.

The structural relaxation to the nearest energy minimum is performed for each mutated cluster by using L-BFGS optimizer.

5- Diversity testing: For conserving the population diversity, the energetic criterion is optionally appended to the BCGA code. Due to this, the high probability of clusters with close energy values can all belong to the same structure. Clusters that have energy difference less than a value of δE (commonly 10^{-6}) are all removed from the current populations, except the one that has the lowest energy value.

6- Selection of the next generation: The highest fitness (lowest energy) clusters selected from old population, new generated clusters and the mutated clusters are formed together in the next generation (new population). Indeed, this selection made the BCGA elitist by ensuring that the evolution from one generation to the next one mostly contains the best members. Once the clusters of the next generation has been collected, most of the above-described operations are repeated again, including fitness, crossover, mutation and diversity testing.

To summarize, Figure 2.13 shows the relation schema between the main operations of general GA. However, many attempts have been recently carried out to enhance the GA results in several ways. For instance, the refinement process is subsequently performed on the GA ground-state structures by sophisticated DFT-based programs that are commonly used. Consequently, this should improve structurally and energetically the quality of the resultant structures of GA (Zhang & Tian, 2008; Huang et al., 2015). Some of the developed GA code has adopted directly the DFT calculations (the so-called hybrid genetic algorithm). It is like a regular GA, except that the robust structure optimizer is employed before passing the fitness evaluation (Hamad et al., 2005; Chen & Dixon, 2013). Another essential development related to applying the pool-based GA approach (see Figure 2.14) instead of the above-mentioned approach (i.e., the generation-based approach) (Bandow & Hartke, 2006). In this approach, the population with *N* individuals serves as a pool of possible parents, in which the fitness, crossover, mutation, and diversity check operations remain unchanged. By rendering the new generated structures with lower energy (high fitness) to replace the highest energy structures in the pool (lowest fitness); the quality of the pool's members improves based on predetermined energetic criteria. Recently, The BCGA has been successfully designed to work within the framework of pool methodology (Shayeghi et al., 2015), as shown in Figure 2.15. Furthermore, the pool-BCGA application has adopted the parallel methodologies that utilize the capability of high computational resource. Noticeably, this new application, the so-called the Birmingham parallel genetic algorithm (BPGA), not only reduces the computational cost, but also elevates the efficiency of the original BCGA code to find the global minimum structures via applying higher optimization level, which is possible with the parallel methodologies of high-performance computation (Davis et al., 2015). It is worth mentioning that the implementation of the parallel methodology inside the pool approach is easier than the

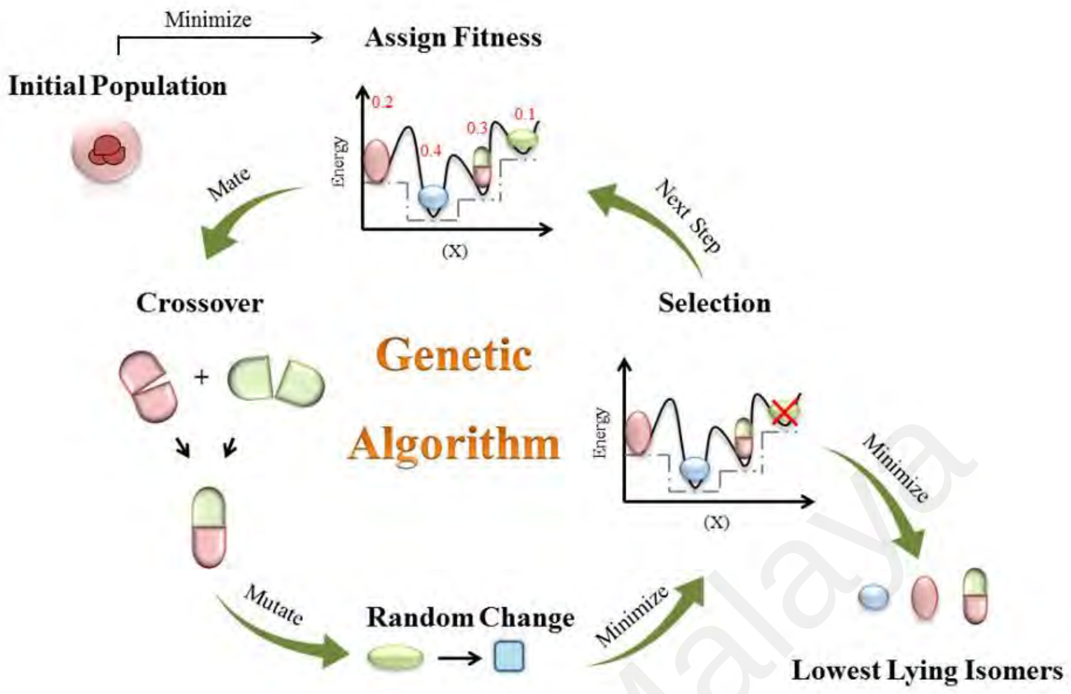

Figure 2.13: General scheme of the BCGA program. The PES as a function of the generalized coordinates (X) is represented by the solid black line, whereas the possible cluster structures are simply illustrated as ellipses and circles. The PES are transformed into a set of basins (dashed black line) which occur owing to the local minimization included in the GA. The initial population of GA consists of the randomly generated structures. The fitness value is determined for each structure after the optimization process, where some of these structures are chosen for the subsequent mating and mutation operations, and the generated offspring is conducted again to the energetic optimization. The next generation includes the highest fitness clusters of the previous ones. These mentioned processes are repeated until the GA convergence criteria is achieved, leading to a set of candidates with low-energy structures.

generation approach, due to its ability to work directly without waiting until all individuals in the generation approach to be fully optimized (Heiles & Johnston, 2013).

2.2.2 Basin-hopping algorithm (BH)

Basin-hopping algorithm (BH) represents an efficient framework of global-optimization, where the primary target of this algorithm is to identify the global minimum structure, i.e., the most stable structure of certain cluster types (Olson et al., 2012). BH method is defined as the simulated annealing approach applied on local minima, and is akin to Monte Carlo-based methods with minimization (D. J. Wales &

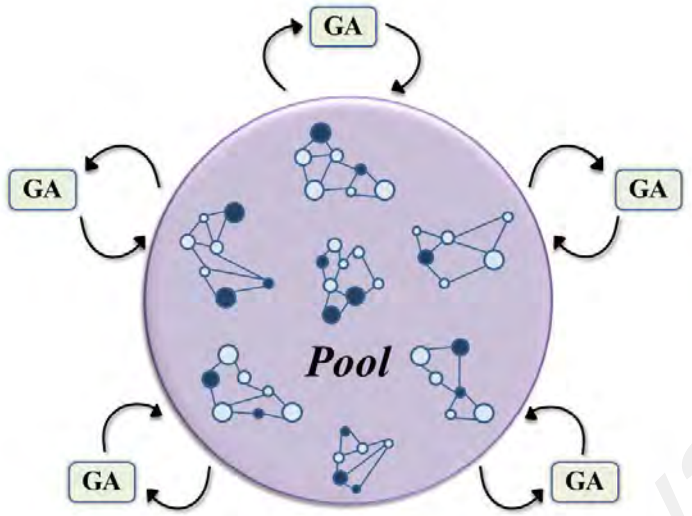

Figure 2.14: Scheme of the pool concept (presenting structural information), where the genetic operators are applied to the N individuals of a global database. The pool size is kept constant during the GA processing.

Doys 1997a; Day et al.,2000). In Monte Carlo methods, the coordination of one or more atoms of clusters are changed by using a perturbation operator, and then, the energy of newly generated structure is evaluated. The new structure is always accepted to replace the old one if its energy is lower, while in the opposite case, in which the new structure has a higher energy than the old one, the probability of acceptance follows the Metropolis criterion. However, this probabilistic criterion determines whether the new geometry can be considered in the Monte Carlo trajectory or a perturbation operator needs to be applied again on the same previous structure to generate another geometry. The acceptance probability depends on the energetic difference between the new and old structures, which can be high in the case of a slight energy difference.

Additional to the step of forming a new structure by applying a perturbation operator, which is also called the trial move, subsequent structural relaxation also takes place as a milestone for the BH method. As a result, the regular PES is effectively transformed to the energy landscape consisting of interpenetrating staircases or a set of basins that represent the lower energy minimum, as shown in Figure 2.16. This transformation is expressed as

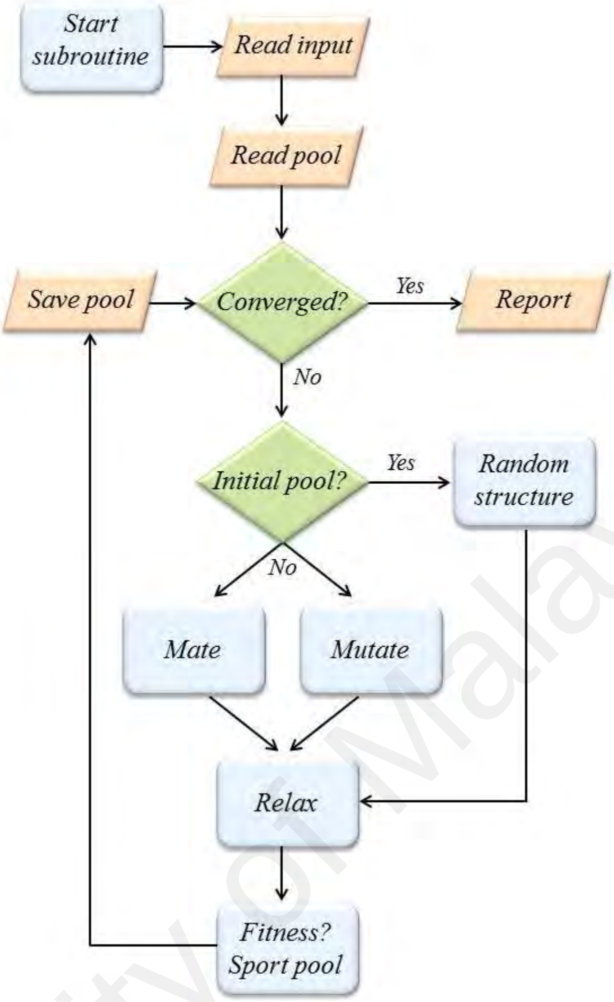

Figure 2.15: Schematic representation of the flowchart of the pool-BCGA application.

follows

$$\tilde{E}_{total}(\{R\}) = min[E_{total}(\{R\})] \tag{2.5}$$

where the minimization process through local structural relaxation is denoted by the symbol (min).

BH methods such as the Basin-Hopping Monte Carlo (BHMC) algorithm, which, as mentioned above, combines the Monte Carlo method and local optimization procedures, are categorized as hypersurface transformation methods aimed to simplifying the shape of PES so that the detection of the global minimum structure is made easier. In contrast to

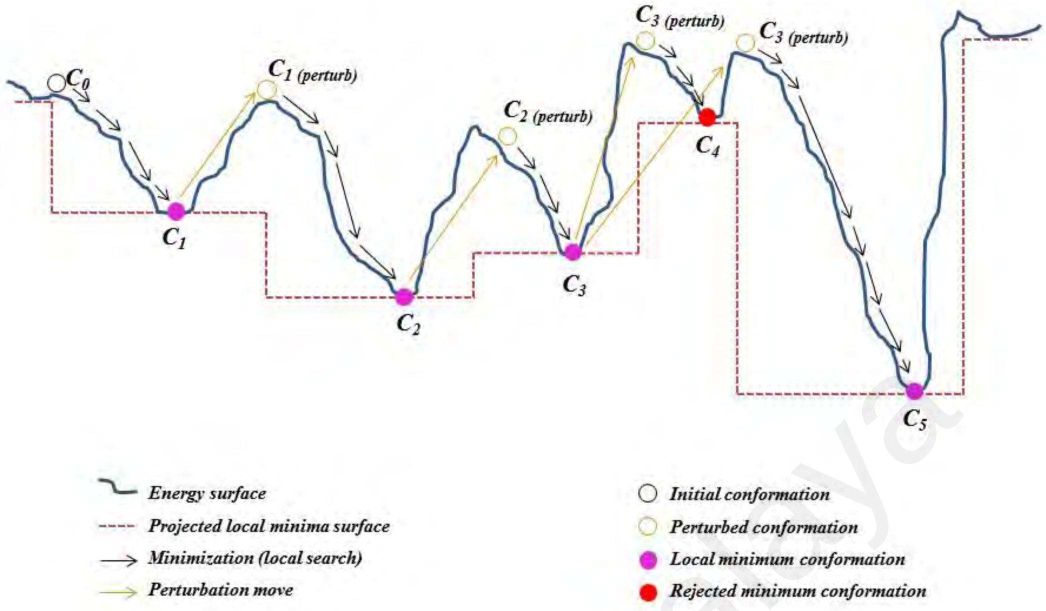

Figure 2.16: Schematic representation of the Basin-hopping (BH) framework, where the PES converts into the staircase form. Two different-colored arrows are used here to represent the local optimization and perturbation operations. At C_4, for example, the minimum doesn't satisfy the Metropolis criterion; therefore, it is rejected, allowing a new perturbation move (trial move).

other hypersurface transformation methods, such as the distance scaling method (Pillardy & Piela, 1997), where there is no guarantee that smooth transformation can occur which does not affect the global minimum or remove the relevant ground-state structures, BHMC algorithm leaves the local minimum regions unchanged but washes out the transition states within the PES. The BHMC trial operator allows exploring different regions of PES even with constant temperature, hence overcoming the inherent complexity within in simulated annealing approach. In a simple BHMC scheme, the temperatures is kept fixed in the Metropolis criterion, and thus the transformation of PES produces a canonical ensemble of local minima (Doye, 2006).

Classical trial operators (perturbation operators) used in BHMC algorithm are the atomic displacement operators. For example, the operator of local atomic displacement randomly changes a set of atomic coordinates around their original positions, which can be expressed as

$$r_i' = r_i + \Delta r_i \tag{2.6}$$

Δr_i carries the direction and magnitude of the atomic displacement, while both of r_i' and r_i represent the new and old atomic positions of atom *i*, respectively.

Li and Scheraga introduced the BHMC algorithm for the first time under the abbreviation (MCM), namely Monte Carlo with Minimization, to solve the multiple-minima problem in protein folding (Li & Scheraga, 1987). This method was generalized by Wales and Doye to be applicable to many systems, involving a wide range of LJ clusters (Wales & Doye, 1997) and Sutton-Chen clusters (Doye & Wales, 1998).

Many modifications have been proposed to enhance the efficiency of the BH algorithms. For example, the monotonic sequence basin-hopping algorithm (MSBH) was suggested by Leary (2000), in which only downhill moves to the minimum of PES funnels were allowed, and restart procedure was used to escape from PES funnels. With this method, Leary (2000) successfully found the global minimum structure of the LJ cluster with size = 98 atoms. By applying the similar restart procedure with the BHMC algorithm as in conventional GMIN package (Wales & Bogdan, 2013), Wales and Head-Gordon (2012) successfully evolved the ability to optimize the coarse-grained models of small proteins. Additionally, the global optimization combined the BH method with parallel tempering, which was also implemented in GMIN package (Wales & Bogdan, 2013), and has been successfully used identified the global minimum energy structures of small oligomers and peptide monomers. For difficult LJ clusters, Wales and Head-Gordon (2012) suggested that the transformation by utilizing two-phase search process coupled with reducing the number of stationary points within the framework of BH algorithm increases the success rate to detect the most stable structures. The combination between the multicanonical MC method and BHMC was proposed by Zhan et al. (2004) as the global optimization method for complex systems, such as LJ clusters with more than 150 atoms. Wales and Head-Gordon (2012) made the investigation of complex LJ clusters easier by providing a simple jump approach to escape from deep local minima into other PES regions. The chance of finding the global minimum structures of LJ clusters rose by employing a symmetric approach within the GA and BHMC algorithms (Oakley et al., 2013).

Although many studies have been performed to improve the BHMC algorithm in determining the global energy minimum structures of a variety of clusters of technological interest, very few develop the BHMC algorithm to work within the DFT framework by an efficient way. Due to the high computational cost of DFT calculations, a powerful BHMC approach aims to reduce its total number of optimization steps performed by using DFT-based method. Therefore, it is interesting to design a methodology which is able to deal with several materials and particle sizes, by employing different trial operators (perturbation operators) as a distinctive feature in exploring a variety of PES surface efficiently with minimal optimization cost. Gehrke and Reuter (2009) employed the single-particle and collective moves in BHMC algorithm to investigate the ground-state isomers of small copper and silicon clusters within the DFT framework. A modified BHMC algorithm proposed by Kim et al. (2008) was found to be 3.8 times more efficient than the standard BHMC to determine the global minimum structure of pure Ag nanocluster with 55 atoms. More recently, Rondina and Da Silva (2013) has introduced a new revised BHMC-algorithm (RBHMC) for unbiased global optimization of several cluster systems, including LJ and Sutton-Chen clusters. In RBHMC algorithm, the main improvement in the MC sampling is characterized by applying a collection of local and non-local trial operators, which can fully explore the PES of the different clusters, such as geometric center displacement, Cartesian displacement, geometric exchange, angular, twist operators, etc. However, more investigation is necessary to improve and examine the ability of the revised or modified BHMC algorithms for the global optimization of different nanoparticle systems.

2.3 Density functional theory (DFT)

DFT method is one of the main tools for studying the ground state properties of several materials. Instead of the wave function used in standard quantum theory, DFT uses the electron density as the basic variable to describe the electronic structure of system. It was first described by Hohenberg and Kohn (1964) as well as Kohn and Sham (1965). Later, a great amount of effort has been made to improve the adoption of this method to be exploited in many computational applications. The usage of DFT-based methods grew exponentially in the last three decades, and many of the prevailing applications of DFT are available nowadays, due to the excellent balance between feasibility and accuracy as well as availability of its use in a wide variety of systems. Currently, DFT method can treat a system containing 1000 atoms within a reasonable time. Furthermore, it is well known that some of a partial electron correlation makes DFT more accurate. Although coupled cluster and post-Hartree-Fock methods (MP2) are used to generate high-quality results, DFT calculations show a comparable or sometimes better performance than these methods in many situations (Oliphant & Bartlett, 1994; Bauschlicher, 1995). In addition, merging DFT with empirical methods as in the empirical DFT functionals reduces the restriction found in the true semi-empirical methods, where the most systems are able to calculate by the empirical DFT methods, in the opposite of the pure semi-empirical methods (Xu et al., 2015).

DFT is the most successful and promising method not only to describe the electronic structure of several systems, but also to calculate a large range of properties: geometries, energies, electric, magnetic, vibrational frequencies, reaction pathways, etc. It commonly uses in computational chemistry, computational physics and condensed-matter physics fields. Not surprisingly, due to a greater contribution of DFT methods in the different scientific societies, particularly in physics and chemistry, Walter Kohn was awarded a half of the 1998 Nobel Prize in Chemistry. The following subsections highlight the most important step forward in the development history of DFT method.

2.3.1 The Schrödinger equation

For the purpose of predicting the geometric and electronic structure of a solid material, calculation of quantum-mechanical total energy of the studied system and the successive minimization of that energy with respect to the nuclear and electronic coordinates is required.

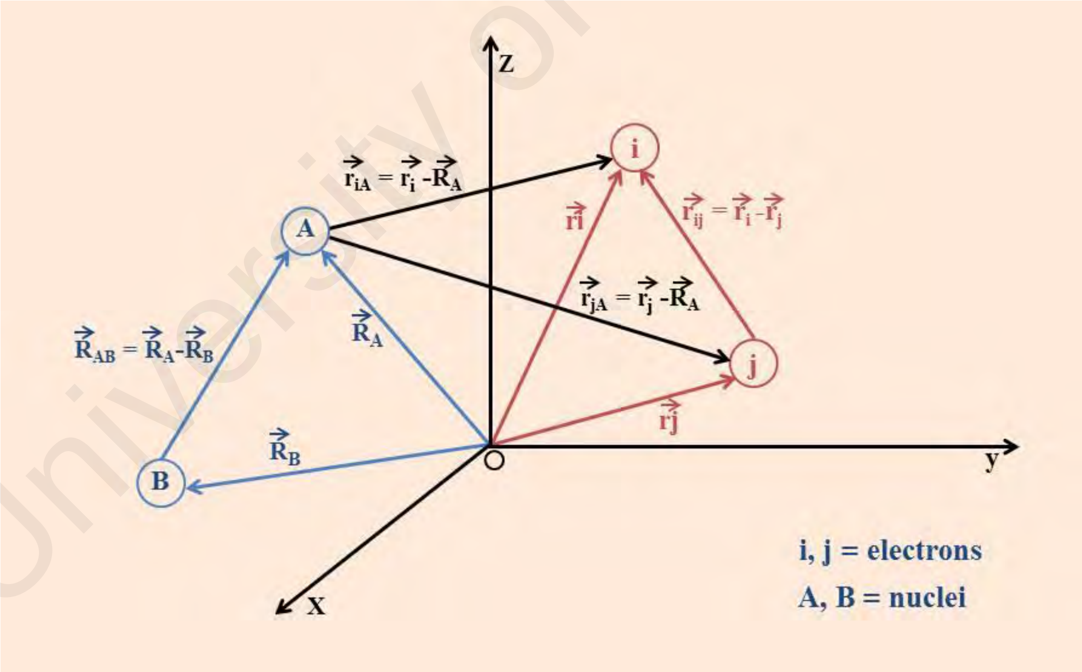

Figure 2.17: Schematic representation of the coordinate system.

The non-relativistic theory is a sufficient approximation to deal with a system containing small atoms, while relativistic effects should be taken into account when treating heavy atoms. In the former case, quantum-mechanical calculations mainly aim to solve the non-relativistic, time-independent Schrödinger equation

$$\hat{\mathrm{H}}\psi = E\psi \tag{2.7}$$

where $\hat{H}$ represents the Hamiltonian operator described by the particle coordinates of $\hat{\mathrm{H}}$ the system, ψ is the wave function, and E is the ground-state energy of the system. The Hamiltonian operator of a system involving a number of particles represented by position vectors: M nuclei, $\vec{R}_A$; and N electrons, $\vec{r}_i$ (see Figure 2.17) with the Coulomb interactions between these particles is defined by:

$$\hat{\mathrm{H}} = \hat{T}_A + \hat{T}_i + V_{A-i} + V_{A-A} + V_{i-i} \tag{2.8}$$

or can be also given in atomic unit, where $m_e = \hbar = e^2/4\pi\epsilon_0 = 1$ and the energy is expressed by Hatree, as follows:

$$\hat{\mathrm{H}} = -\sum_{A=1}^{M}\frac{1}{2M_A}\nabla_A^2 - \sum_{i=1}^{N}\frac{1}{2}\nabla_i^2 - \sum_{i=1}^{N}\sum_{A=1}^{M}\frac{Z_A}{|\vec{r}_{iA}|} + \sum_{i=1}^{N}\sum_{j>i}^{N}\frac{1}{|\vec{r}_{ij}|} + \sum_{A=1}^{M}\sum_{B>A}^{M}\frac{Z_A Z_B}{|\vec{R}_{AB}|} \tag{2.9}$$

The first two terms, i.e., $\hat{T}_A$ and $\hat{T}_i$ operators correspond to the kinetic energy of nuclei and electrons, respectively. The Coulomb components form the potential energy part, including the Coulomb interactions between nuclei and electrons represented by the third term (V_{A-i}), and Coulomb repulsions between the same particle type: the nucleus-nucleus repulsion, fourth term (V_{A-A}); and the electron-electron repulsion, fifth term (V_{i-i}).

Solving the Schrödinger equation (equation 2.7) provides the total ground-state energy. Unfortunately, solving for the exact solution of the Schrödinger equation for the many-body problem is currently impossible, except for the small, simple systems not exceed the dihydrogen cation (H_2^+), due to the complexity of electron-electron repulsions. Several approximations have been made to deal with the many-body problem of the complex systems, as discussed below.

2.3.2 The Born-Oppenheimer approximation

The Born-Oppenheimer approximation (BOA) is the first and common approximation express the Hamiltonian operator (equation 2.8). It has been used successfully to approximate the many-body problem of a complex system due to a large mass difference between the nucleus and the electron ($M_A/m_e \geq 10^4$), M_A as can be seen in equation 2.9. This in turn causes a difference in time scale between the electronic and nucleic (ionic) processes. For instance, the frequencies of electromagnetic radiation generated by the transitions between electronic states in atoms are 1-10 million times more than that of the ionic vibrations in solids and molecules.

Based on the above fact, the BOA assumes that electrons response immediately to changes in the nuclear positions, namely the electrons move in the electrostatic field produced by fixed nuclei. Therefore, the BOA ignores the nuclear kinetic energy and considers the nucleus-nucleus repulsion contribution for a particular set of coordinates as a constant. It then introduces a new expression for the Hamilton operator, including the kinetic energy and potential energy terms of electrons only, as represented in the following equation:

$$\hat{H} = \hat{T}_i + V_{A-i} + V_{i-i} \tag{2.10}$$

Now, the time-independent Schrödinger equation can be written in terms of electronic wave function, as follows:

$$\hat{H}_i \psi_i(r, R) = E_i \psi_i(r, R) \tag{2.11}$$

or in more detail for the subsystem of electrons:

$$(T_i + V_{A-i}(\{\vec{R}_A\}) + V_{i-i})\psi(\vec{r_1}, \dots \vec{r_N}) = E(\{\vec{R}_A\})\psi(\vec{r_1}, \dots \vec{r_N}) \tag{2.12}$$

The electronic wave function $\psi_i(r, R)$ (equation 2.11) describes the electronic motions with regard to the coordinates of electrons as the dynamic variables, and the ionic coordinates ($\vec{R}_A$) are taken only as the external parameter. The Coulomb-potential and kinetic energies form the electronic total energy operator, E_i in equation 2.11. By adding constant for the nucleus-nucleus repulsion term (V_{A-A}), the final total energy can be calculated from the following equation:

$$E_{total} = T_i + V_{A-i} + V_{i-i} + V_{A-A} \tag{2.13}$$

Rather than dealing with the complexity of Schrödinger equation, the classical Newton equation of motion may be used instead by virtue of the enormous mass of the nucleus that leads to the quantum effects to be neglected. However, several approximations have been developed to solve the resulting many-body equation after employing the assumption of BOA.

2.3.3 The Hohenberg-Kohn theorem

The HK theorem replaces the wave function that found in Hartree–Fock based methods by the N-particle density.

Stated briefly as follows:

Theorem 1 - Existence theorem

The total energy of a many electron system is a unique functional of the electron density $\rho(\vec{r})$ under an external potential $V_{ext}(\vec{r})$

$$E|\rho(\vec{r})| = F|\rho(\vec{r})| + \int d^3\vec{r}|\rho(\vec{r})|V_{ext}(\vec{r}) \tag{2.14}$$

where the integration term represents the interactions between the electron system with an external potential, while the first term (i.e, $F|\rho(\vec{r})|$) is an unkown and described by the universal Hohenberg-Kohn functional that includes both of the electronic kinetic energy and the electron-electron potential energy and expressed as

$$F|\rho(\vec{r})| = T|\rho(\vec{r})| + V_{i-i}|\rho(\vec{r})| \tag{2.15}$$

Theorem 2 - Variational principle

For a many electron system under an external potential, the ground-state energy $(E_0|\rho(\vec{r})|)$ can be obtained by the minimization of the energetic functional of the electron density $(E|\rho(\vec{r})|)$

$$E_0|\rho(\vec{r})| = minE|\rho(\vec{r})| \Leftrightarrow \left.\frac{\partial E|\rho(\vec{r})|}{\partial \rho(\vec{r})}\right|_{\rho(\vec{r}) = \rho_0(\vec{r})} = 0 \tag{2.16}$$

The detailed proofs for the above theorems are beyond the objectives of this thesis, but they are easy to find in many literature sources, such as (Hohenberg & Kohn, 1964; Levine, 1999). Although this theorem is powerful, it is impractical. This is because the exact evaluation for the $F|\rho(\vec{r})|$ is an unknown, which is required to solve the many-electron Schrödinger equation. A good evaluation for the $F|\rho(\vec{r})|$ that can be dealt in a practical manner produces a good representative of the $E|\rho(\vec{r})|$ functional, leading to yield a good approximation result to the ground-state energy as well as the electronic density after energy minimization. About one year after the DFT key was given by Hohenberg and Kohn (1964), Kohn and Sham (1965) introduced a practical method to perform the DFT calculations and to reflect their characteristics.

2.3.4 Kohn-Sham Theory

The Kohn-Sham method converts the true many-electron system into a particular system to obtain the ground-state, assuming that the same density of the interacting particles can be generated by a postulated system, namely Kohn-Sham system consisting of non-interacting particles, e.g., electrons (Enciu et al., 2014). In Kohn-Sham theory, the electron density $\rho(\vec{r})$ is parametrized in terms of one-electron orbitals $\phi_i(\vec{r})$, where the summation is over all occupied state as seen in the following equation:

$$\rho(\vec{r}) = \sum_i \phi_i^*(\vec{r})\phi_i(\vec{r}) \qquad (2.17)$$

Kohn and Sham (1965) proposed three terms that can replace the $F|\rho(\vec{r})|$ term used in the Hohenberg-Kohn theorem (equation 2.14); therefore, the total energy functional can be written as

$$E|\rho(\vec{r})| = \overbrace{T|\rho(\vec{r})| + \frac{1}{2} \iint \frac{\rho(\vec{r}) - \rho(\vec{r}')}{|\vec{r} - \vec{r}'|} d\vec{r}d\vec{r}' + E_{xc}|\rho(\vec{r})|}^{F|\rho(\vec{r})|} + \int|\rho(\vec{r})|V_{ext}(\vec{r}) \qquad (2.18)$$

In a simple manner, it also can be expressed as

$$E[\rho] = T[\rho] + E_H[\rho] + E_{xc}[\rho] + E_{ext}[\rho] \qquad (2.19)$$

where the $T[\rho]$ describes the kinetic energy of non-interacting electrons, which is approximated in terms of single-particle orbitals $\phi_i(\vec{r})$, as follow:

$$T[\rho] = \sum_i \int \phi_i^*(\vec{r})\left(-\frac{1}{2}\vec{\nabla}^2\right)\phi_i(\vec{r})d^3\vec{r} \qquad (2.20)$$

and the $E_H[\rho]$ represents the electron-electron Coulomb potential, which is also equal to the classical electrostatic energy generated by the distribution of charge density $\rho(\vec{r})$, expressed as,

$$E_H[\rho] = \iint \frac{\rho(\vec{r}) - \rho(\vec{r}')}{|\vec{r} - \vec{r}'|} d\vec{r}d\vec{r}' \qquad (2.21)$$

while the $E_{ext}[\rho]$ is the interaction of the electron charge density with an external filed, as follows:

$$E_{ext}[\rho] = \int V_{ext}|\rho(\vec{r})|d\vec{r} \tag{2.22}$$

Finally, the other contributions have the potential to affect the total energy and the so-called non-trivial exchange-correlation energy are represented by $E_{xc}[\rho]$.

However, the total energy functional $E[\rho]$ changes relative to the variation quantity of the one-electron orbitals $\phi_i(\vec{r})$, leading to the one-electron Kohn-Sham equation:

$$\left(-\frac{1}{2}\vec{\nabla}^2 + \int \frac{\rho(\vec{r}')}{|\vec{r}-\vec{r}'|}d^3\vec{r} + V_{ext}\vec{r} + \frac{\partial E_{xc}|\rho(\vec{r})|}{\partial \rho(\vec{r})}\right)\phi_i(\vec{r}) = \epsilon_i \phi_i(\vec{r}) \tag{2.23}$$

The effective one-electron potential $V_{eff}(\vec{r})$ is given by

$$V_{eff}(\vec{r}) = V_{ext}(\vec{r}) + \int \frac{\rho(\vec{r}')}{|\vec{r}-\vec{r}'|}d^3\vec{r} + V_{xc}|\rho(\vec{r})| \tag{2.24}$$

with $V_{xc}|\rho(\vec{r})|$ describes the exchange-correlation potential, defined by

$$V_{xc}|\rho|(\vec{r})| = \frac{\partial E_{xc}|\rho(\vec{r})|}{\partial \rho(\vec{r})} \tag{2.25}$$

To keep the single-electron Kohn Sham orthogonal, the Lagrange parameter (ϵ_i) is employed as follow:

$$\int \phi_i^*(\vec{r})\epsilon_i \phi_i(\vec{r}) = 0 \tag{2.26}$$

Practically, the DFT-Kohn Sham calculations aim to minimize a system containing N single-electron potential (equation 2.24), whereby both the ground-state energy and electron density can be gained. However, iterative calculation is needed to treat the electron density $\rho(\vec{r})$ implied in the definition of $V_{eff}(\vec{r})$. Up to this stage, the DFT-Kohn

Sham calculations exactly match the non-relativistic-BOA. In case that the approximations are necessary, the $E_{xc}[\rho]$ remains in order to evaluate the exchange-correlation functional.

2.3.5 Exchange correlation functionals

Within non-relativistic quantum mechanics, the Kohn Sham equation 2.23 is exact and not exposed to a further approximation. However, the Kohn Sham equation depends on the non-interacting system (a fictitious system); therefore, both kinetic energy (T) and the electron-electron repulsion energy (E_H) in equation 2.19 are not representing the true kinetic energy (T') and the true electron-electron potential (E'_H), respectively. Based on this fact, the exchange-correlation energy aims to reduce the gap between the non-interacting system and the real one, and can be written as:

$$E_{xc}[\rho] = T' - T + E'_H - E_H \tag{2.27}$$

Physically, the E_{xc} includes two components: exchange energy, and correlation energy as follows:

1. Exchange energy (E_x):

Owing to the Pauli exclusion principle, the wavefunction is antisymmetric with respect to the coordinate exchange of any two particles. The antisymmetrization of the wave function, which is also known as the exchange energy, generates the electrostatic energy difference that is expressed directly on the basis of occupied Kohn-Sham orbitals,

$$E_x = -\frac{1}{2}\sum_{ij}\iint \frac{\phi_i^*(\vec{r})\phi_i(\vec{r}')\phi_j^*(\vec{r})\phi_j(\vec{r})}{|\vec{r}-\vec{r}'|}\, d\vec{r}d\vec{r}' \tag{2.28}$$

For solids, the computational cost of the E_x calculation is very expensive, and thus it needs the appropriate approximations to be practical. In addition, the efficient approximations used to evaluate the exchange energy generally causes the effects of the self-interaction error (SIE), a deficiency in DFT- Kohn Sham approaches. This arises due to the incomplete cancellation of electron self-interaction in the approximation approaches. SIE is considered as a reason of the DFT-Kohn Sham failure in several calculations, such as transition states of the reactions and charge transfer processes (Vydrov, 2007).

2. Correlation energy (E_c):

This is the correlation energy with regards to the nature of electrons that are correlated, i.e., not independent, which is defined as the difference between the energy of Hartree-Fock limit and the exact non-relativistic energy. Therefore, the correlation energy physically affects the kinetic and potential components, where the kinetic energy decrease, while the potential energy increases.

As mentioned above, the correlation energy calculation is carried out based on the expression (2.28); on the contrary, no general equation is used to obtain the electron correlation energy. However, the way to calculate the correlation energy exactly is by solving the impossible N-electron Schrödinger equation 2.9; and hence, it is practically approximated in all calculations. Often, the correlation and exchange energies are joined together as

$$E_{xc} = E_x + E_c \tag{2.29}$$

Since the true expression for the E_{xc} calculation is unknown, many approximation functionals have been introduced to estimate this term within the framework of DFT-Kohn Sham approach. The most popular examples of these formalisms based on DFT functional development involve the local density approximation, generalized gradient approximation and hybrid functionals, these are briefly discussed in the following subsections.

2.3.5.1 Local (spin) density approximation (L(S)DA)

The local-density approximation (LDA) is the simplest approximation to estimate the E_{xc} in a practical system, which locally treats the electron density as a homogeneous electron gas (HEG); accordingly, the charge density at the studied point represents the evaluation of the E_{xc}. Kohn and Sham (1965) introduced the LDA formula for the first time, which is applicable for practical systems, preserved their densities from the rapid changes. The E_{xc} for a density $\rho(\vec{r})$ within this approximation can be expressed as

$$E_{xc}^{LDA}|\rho(\vec{r})| = \int \rho(\vec{r})\epsilon_{xc}|\rho(\vec{r})|d\vec{r} \qquad (2.30)$$

where $\epsilon_{xc}|\rho(\vec{r})|$ is the exchange-correlation energy per electron of an electron gas with homogeneous density $\rho(\vec{r})$. The exchange energy is simply written based on the well-known analytical formula of HEG as follows:

$$E_{x}^{LDA}|\rho(\vec{r})| = -\frac{3}{4}\left(\frac{3}{\pi}\right)^{1/3} \int \rho^{4/3}(\vec{r})d\vec{r} \qquad (2.31)$$

The numerical evaluation of the correlation energy of HEG density by using quantum Monte Carlo calculations has been performed (Ceperley & Alder, 1980), due to the fact that the exact solution of the correlation energy is mostly unknown. Then, the resulting data have been utilized to parameterize the interpolated form of Ec^{LDA} in different ways, including the parameterizations implemented widely in the DFT codes based on the works of Vosko et al. (1980), Perdew and Zunger (1981), and Perdew and Wang (1992). By generalizing the LDA to deal with electron spin systems, the local spin-density approximation (LSDA) is produced and expressed as $E_{xc}^{LSDA}|\rho \upharpoonleft, \rho \downharpoonleft|$.

In practical applications, L(S)DA shows a remarkable performance with many systems, particularly, when the electron density varies very slowly. For example, it successfully described the elastic and structural geometries of both bulk materials and surfaces (Jones & Gunnarsson, 1989). This success of L(S)DA can be attributed to the compatibility between exchange and correlation energies (Burke et al., 1998). Despite the great advantages of LDA, the bonding properties of both solids and molecules are not predicted accurately using LDA functionals. An illustration of the deficiency of this approximation is that the L(S)DA generally gives the cohesive energies a large overestimation of approximately 20–30% associated with bond lengths which are too short (Harl et al., 2010; Sun et al., 2011). As a result, more robust approximation-functionals are required to yield an accurate prediction of solid and material properties.

2.3.5.2 Generalized gradient approximation (GGA)

The density gradient is introduced as an improvement over L(S)DA to enhance the ability to deal with the non-locality behaviour in realistic systems by providing additional ingredient to the energy functional, i.e., the density gradient $\nabla\rho(\vec{r})$. A set of the resulting functionals grouped together are called the generalized gradient approximation (GGA), which is commonly expressed as

$$E_{xc}^{GGA}|\rho(\vec{r})| = \int \rho(\vec{r})\epsilon_{xc}^{hom}F_{xc}|\rho(\vec{r}), \nabla\rho(\vec{r})|d\vec{r} \qquad (2.32)$$

where F_{xc} represents the enhancement factor (dimensionless) correspond to the gradient dependency, and ϵ_{xc}^{hom} is the exchange-correlation energy density taken from the LDA functionals. It is worth mentioning that the GGA functionals only partially solve the non-locality behaviour; therefore, it is considered as semi-local functionals.

In contrast to the F_{xc}^{LDA}, many forms of F_{xc}^{GGA} can be chosen to deal with various physical constraints. Since satisfying all constraints simultaneously is impossible, usually the selected form depends on the nature of the studied system. This produces many of the

GGA implementations according to the chosen F_{xc}^{LDA}, which are efficiently used in several calculations such as Hammer-Hansen-Nørskov (RPBE) (Hammer et al., 1999), Perdew-Wang (PW86) (Perdew, 1986), Perdew-Wang (PW91) (Perdew & Wang, 1992), etc. One of the most widely used GGAs within the condense matter field is the Perdew-Burke-Ernzerhof (PBE) (Perdew et al., 1996). It can be viewed as an expanded, improved version of the PW91 with a smoothed form of the enhancement factor. In general, the F_{xc} of the PBE implementation divides into the exchange and correlation energy terms only, without including any empirical parameters similar to PW91. Its exchange term, i.e., F_x can be evaluated based on the following expression:

$$F_x(s) = 1 + k - \frac{k}{1 + \mu s^2/k} \tag{2.33}$$

where μ and κ are constants, and s represents the reduced density gradient (dimensionless), $|\nabla\rho|/2(3\pi^2\rho)^{4/3}$. The correlation energy term of PBE, contrary to its exchange term, is more complex, due to the fact that it includes the treatments of spin polarization and the scaling relations.

In general, the GGA functionals are better than LDA in predicting molecular and cluster structures. For solids, they do not show a clear improvement compared to LDA. For example, although the PBE accurately predicts the lattice parameters that agree with the experiments, it fails to truly evaluate some of the bulk characteristics such as the bulk moduli, which, in contrast to LDA which gives an underestimation of bonding properties of solids (Harl et al., 2010; Sun et al., 2011). In addition, both of LDA and GGA generally give band gaps smaller than the measured values for all transition-metal oxides (Hu & Metiu, 2011). DFT+U and hybrid approximations have been proposed to handle these problem cases. These are discussed below.

2.3.5.3 The DFT+U approximation

In GGA and L(S)DA, the orbital-independent potentials cannot properly describe the strongly correlated systems that involve a partially filled d or f orbitals in their transition metal or rare-earth metal atoms. For instance, instead of the Mott insulators of the TMOs with well localized d electrons as found in the experiments, L(S)DA shows delocalized d electrons corresponding to the metal characteristics. The orbital-dependent potentials must be used to correctly describe the d and f electronic behaviour of strongly correlated systems. Among several approaches available to deal with these special systems such the Hartree-Fock (HF) method (Massidda et al., 1993), self-interaction correction (SIC) method (Svane & Gunnarsson, 1990), and GW approximation (Hedin, 1965), the DFT+U methods (e.g., L(S)DA+U) are extremely widely used nowadays. Within the L(S)DA+U, two sets of electrons are distinguished: the first includes the s and p electrons, which are delocalized and can well be understood by LDA or GGA functionals; the second contains the d and f localized electrons, on which an orbital-dependent correction ($\frac{1}{2}U\sum i \neq j\ n_i n_j$) is applied to estimate the Coulomb interaction between d-d and f-f orbitals with n_i occupancy. In L(S)DA+U method, the total energy is written as:

$$E_{tot}^{LDA+U}|\rho_\sigma(\vec{r}\,),\{n_\sigma\}| = E^{LSDA}|\rho_\sigma(\vec{r}\,)| + E^U|\{n_\sigma\}| - E_{dc}|\{n_\sigma\}| \qquad (2.34)$$

where σ is the spin index, n_σ and ρ_σ are the density matrix of d or f electrons, and electron density for spin-σ electrons, respectively. The total energy in L(S)DA+U contains three energy terms as can be noticed in equation 2.9:

- The first term ($E^{LSDA}|\rho_\sigma(\vec{r})|$) is the standard L(S)DA energy functional.
- The second term ($E^{U}|\{n_\sigma\}|$) represents the energy of electron-electron Coulomb interaction and given by (Anisimov et al., 1997):

$$E^U|\{n_\sigma\}| = \frac{1}{2}\sum_{\{m\},\sigma}\{\langle m,m''|V_i|\,m',m'''\rangle n_{mm',\sigma}n_{m''m''',-\sigma} - (\langle m,m''|V_i|\,m',m'''\rangle - \langle m,m'',|V_i|\,m''',m'\rangle)\} \tag{2.35}$$

  where V_i donates the screened Coulomb repulsion between the d or f electrons, the m is the magnetic quantum number.

- The last term ($E_{dc}\ |\{n_\sigma\}|$) aims to remove the energetic contributions of d or f electrons from the LDA energy, can be evaluates as follows:

$$E_{dc}|\{n_\sigma\}| = \tfrac{1}{2}U\,N(N-1) - \tfrac{1}{2}J|N_\uparrow(N_\uparrow - 1) + N_\downarrow(N_\downarrow - 1)| \tag{2.36}$$

  where $N = N_\uparrow + N_\downarrow$. J and U are the exchange and screened Coulomb parameters, respectively.

For simpler approximations, according to the specific conditions such as ignoring the non-sphericity and exchange energy, these are discussed in detail by Anisimov et al. (1997).

Although many approaches are used to select the U value in DFT + U methods, there is no generally accepted approach to decide a suitable value of U that significantly affects the energetic and structural properties of the system under consideration (Hu & Metiu, 2011). This is because the resulting data strongly depends on the types of the localized orbitals and the interaction parameters that chosen for the calculations. Besides the recently proposed linear response approach by (Cococcioni & De Gironcoli, 2005), choosing the U value to fit the experimental data of the studied system is considered as the commonly used approach. This leads to varying the assigned U value based on the quantity fitted. For example, different U values have been employed to study titanium oxides in a broad range from 2.5 to 10 eV. In these studies, the determined U values are fitted into the band gap (Deskins & Dupuis, 2007), X-ray photoelectron (XPS) spectrum (Nolan et al., 2008), the oxidation reaction energy (Hu & Metiu, 2011), etc. (Calzado et al., 2008; Mattioli et al., 2008).

To improve the quality of DFT calculations, the Hybrid functionals have become one of the significant improvements beyond the ordinary LDA-DFT and GGA-DFT limitations, where some of the Hartree-Fock exchange is included so that it partially cancels the electron self-interaction errors present in the strongly correlated systems; therefore, providing highly accurate results. Unfortunately, maintaining the accuracy by using the Hybrid functionals is at the expense of efficiency, which requires high computational power (Hu & Metiu, 2011).

2.3.5.4 Hybridized functionals

L(S)DA and GGA (PBE) together form the cornerstone of the nonempirical building approach. Very efficient methods can be accomplished by employing more non-locality functionals into the exchange-correlation energy (E_{xc}), that reduces the self-interaction errors present in semi-local functionals. The hybrid functionals principally consists of conventional GGAs and a fraction of the exact exchange energy (EXX) as previously mentioned. These functionals are firstly proposed by Becke (1993). However, a general form of hybrid GGAs is given by (Becke, 1996):

$$E_{xc}^{hybrid} = \alpha E_x^{EXX} + (1 + \alpha)E_x^{GGA} + E_c^{GGA} \tag{2.37}$$

where E_x^{EXX} reflects the exact exchange energy mentioned in equation 2.28, and the α coefficient represents the mixing ratio of the exact exchange energy, which can be determined semi-empirically or by alternative routes.

In quantum chemistry, the Hybrid functionals, e.g., B3LYP (Becke, 1993) have occupied a unique position, due to their excellent performance in predicting structural and energetic properties, such as bond lengths, vibrational frequencies and atomization energies for many clusters and molecules compared to semi-local functionals, i.e., GGA and L(S)DA. However, enhancing the ability of Hybrid functionals to treat extended systems such as thin films and surfaces are computationally challenging. In this direction, many efforts have been addressed. For example, Heyd et al. (2003) and Schimka et al. (2011) separately introduced screened hybrid functionals HSE06 and HSEsol, respectively, in which exchange interaction term is divided into the long-range (LR) and short-range (SR), leading hybrid functionals to be available in the field of solid-state (Marsman et al., 2008). The exchange energy for this hybrid functional can be written as:

$$E_{xc}^{HSE} = \alpha E_x^{EXX,SR}(\omega) + (1 + \alpha) E_x^{\omega PBE,SR}(\omega) + E_x^{\omega PBE,LR}(\omega) + E_c^{PBE} \quad (2.38)$$

where $E_x^{EXX,SR}$ represents the short-range exact exchange, and both $E_x^{\omega PBE,SR}$ and $E_x^{\omega PBE,LR}$ reflect the short-range and long-range PBE exchange, respectively. The E_c^{PBE} provides the PBE correlation. ω denotes the range-separation parameter, which determines the extension of short-range interactions. Finally, the derived value of α is found equal to 0.25 based on the perturbation theory (Perdew et al., 1996). Some improvements have been performed more than the regular hybrid functionals by appending the range-separation concept to deal with exact exchange, making these modern hybrids computationally less expensive to a variety of large systems, such as semiconductors, metallic, and insulating solids, and thus providing a better result than standard GGAs and LDA with regards to structure and electronic properties (Henderson et al., 2011). In solids, several drawbacks of hybrid functionals remain when used with metallic systems, which have small band gaps, where it does not sufficiently treat this type of system, particularly the transition metal, (Paier et al., 2007). This may be attributed in some degree to the absence of the long-range correlation of the exchange-correlation energy in the hybrid functionals.

2.3.6 The Bloch theorem

For the DFT calculations of solid materials, which can be envisaged as an infinite system, the periodic boundary conditions (PBC) are introduced by assuming the existence of homogeneous structural images for the studied system in all directions. Under the translational symmetry rules, the supercell can be obtained from a set of atomic coordinates that their spatial pattern periodically repeats.

The eigenvalues of a periodic solid on the basis of Bloch theorem (Bloch, 1929) is given by:

$$\psi_{n\vec{k}}(\vec{r}) = e^{n\vec{k}.\vec{r}} u_{n\vec{k}}(\vec{r}) \tag{2.39}$$

where the band index is represented by n, wavevector of the reciprocal lattice bounded to the first Brillouin zone is symbolized by $\vec{k}$, while the translational invariant, $u_{n\vec{k}}(\vec{r})$, is defined as

$$u_{n\vec{k}}(\vec{r} + \vec{R}_e) = u_{n\vec{k}}(\vec{r}) \tag{2.40}$$

where $\vec{R}_e$ is a crystal lattice vector. The Bloch functions is known as the eigenstates of the equation 2.39 under the translation using a lattice vector $\vec{R}_e$ (equation 2.40).

Accordingly, the Bloch functions transform in the standard way as follows:

$$T_{vecR_e}\psi_{n\vec{k}}(\vec{r}\,) = \psi_{n\vec{k}}(\vec{r} + \vec{R}_e\,) = e^{i\vec{k}R_e}\psi_{n\vec{k}}(\vec{r}\,) \qquad (2.41)$$

In the periodic $\vec{k}$-space, the Bloch functions ($\psi_{n\vec{k}}(\vec{r}\,)$) and their eigenvalues can be written as

$$\psi_{n,\vec{k}+\vec{K}}(\vec{r}\,) = \psi_{n\vec{k}}(\vec{r}\,)E_{n,\vec{k}+\vec{K}}(\vec{r}\,) = E_{n\vec{k}}(\vec{r}\,) \qquad (2.42)$$

where an arbitrary reciprocal-lattice vector is symbolized by $\vec{K}$·

These Bloch functions and their eigenvalues can only be considered in the first Brillouin-zone of the reciprocal lattice. It derives the Schrödinger equation to yield a new equation for the periodic function ($\psi_{n\vec{k}}(\vec{r}\,)$). However, the Hermitian eigenvalue equation can be obtained by applying the periodic boundary conditions over the Wigner-Seitz cell of direct space. Furthermore, increasing the energy values generates an infinite number of solutions for a fixed $\vec{k}$.

2.3.6.1 Planewaves and pseudopotentials

The one-electron orbitals density defined in equation 2.23 can be expanded based on the above-described Bloch functions (equation 2.42) to cover any convenient basis set, and thus the plane-wave basis set in the practical way is given by:

$$\psi^{n}_{\vec{k}}(\vec{r}\,) = \sum_{\vec{k}} C^{n,\vec{k}}_{\vec{\mathbf{k}}}\, e^{i(\vec{K}+\vec{\mathbf{k}}).\vec{r}} \qquad (2.43)$$

with a number of characteristics as follows:

- A planewave basis set does not include any preconceptions affecting the problem form; therefore, it is unbiased.
- In the periodic system, the planewave acts as a rational choice to describe the electron orbitals according to Bloch theorem.
- The Fast Fourier Transforms (FFT) can be directly utilized in exchange between the real space and planewave representations, which significantly reduces the computational cost.

The region close to the nucleus needs an enormous number of basis functions to describe accurately its atomic wavefunctions, which is considered, in turn, as the main drawback of a planewave basis set. This difficulty can be overcome by using pseudopotentials, which principally reflects the potential of the atomic cores. This approximation arises by assuming that only the valence electrons have a significant effect on the chemical and physical properties of a system under the consideration. In addition, the potential of the core electrons and the nucleus, namely the pseudopotential is subject to the following conditions:

- The effect of pseudopotential has not spread beyond the r_c boundary, i.e., outside the core region; therefore, the valence wavefunction stay unchanged.
- Within the core, the pseudo wavefunction correctly matches at the boundary.
- The pseudo wavefunction must be continuous, and has a continuous first derivative at the boundary:

$$\phi^{PS}(r)\bigg|_{r=r_c} = \phi^{AE}(r)\bigg|_{r=r_c} \Leftrightarrow \frac{\partial\phi^{PS}}{\partial r}(r)\bigg|_{r=r_c} = \frac{\partial\phi^{AE}}{\partial r}(r)\bigg|_{r=r_c} \quad (2.44)$$

where the PS index denotes the pseudo energy, while the AE index represents the all-electron energy.

- There is no node in the pseudo wavefunction within the core region.

For pseudopotentials, to be applicable all the above-described criteria must be fulfilled. Of course, more criteria are required to construct various types of pseudopotentials, such as norm-conserving pseudopotentials (NCPP) (Hamann et al., 1979), ultra-soft (also known as Vanderbilt-type) pseudopotentials (USPP) (Vanderbilt, 1990), etc.

The projector-augmented wave method (PAW) (Kresse & Joubert, 1999) has become one of the most important developments of the pseudopotential technique, which is firstly established by Blöchl (1994). The idea of the PAW method depends on the transformation from pseudo (PS) to all-electron (AE) wavefunction. The all-electron wavefunction ψ contains three components, given by:

$$\psi = \tilde{\psi} + \sum_{i}^{N} C_i \phi_i - \sum_{i}^{N} C_i \tilde{\phi}_i \tag{2.45}$$

To distinguish between the pseudo (PS) quantities and the all-electron (AE) quantities, a ψ is functionalized, where $\tilde{\psi}$ represents the pseudo wavefunction, and both ϕ_i and $\tilde{\phi}_i$ denote the all-electron partial waves and the pseudo partial waves, respectively.

The plane waves, which represent the PS wave function, describe very well the wave function in regions further away from the nuclei. Unfortunately, it does not represent sufficiently the AE wave function near the nucleus. In order to correct this, the AE partial waves ϕ_i are introduced in the PAW method, which are constructed from the isolated atoms as the radial part solutions of their Schrödinger equations. It seems reasonable that these AE partial waves match the PS wavefunction outside the core region, but they behave differently inside this region. In addition, the AE partial waves aim physically to correct the nodal structure of the wavefunction close to the nucleus.

Since the AE partial waves have already covered the region near the atomic nuclei, it seems reasonable to cancel the contribution coming from this region again by subtracting the PS partial waves $\tilde{\phi}_i$ part, which described the wavefunction located in this region. The $\tilde{\phi}_i$ are derived from the isolated atoms as the radial solutions of their Schrödinger equations as in the AE partial waves.

2.3.7 Analysis of the electronic properties

Computational materials science offers a powerful means for studying different physical and chemical properties. For example, density of states (DOS) and charge density difference (CDD) calculations give valuable data about the electronic, magnetic and other properties of different substances. These calculations are discussed below.

In the next subsections, only a few of them are discussed, and in particular the DOS and CDD.

2.3.7.1 Density of states (DOS)

The density of states (DOS) is defined as the number of quantum states per unit of energy (E) or per volume (Ω) (Martin, 2004):

$$n(E) = \frac{1}{N_k}\sum_{i}\sum_{\vec{k}} \delta\left(\epsilon_{i,\vec{k}} - E \right) = \frac{\Omega_{cell}}{(2\pi^2)} \int_{BZ} \delta\left(\epsilon_{i,\vec{k}} - E \right) d\vec{k}. \tag{2.46}$$

In the independent-particle state model, $n(E)$ donates the number of electrons (or phonon) per unit energy, and the $\epsilon_{i,\vec{k}}$ represents the number of independent-particle states (typically, electron).

In principle, the integration of equation 2.46 over the entire Brillouin zone (BZ) is not an easy task. This Brillouin-zone integration can be treated with several methodologies.

Some of them are commonly used, such as the linear tetrahedron method (LTM) by Jepson and Anderson (1971), the Gaussian broadening method (GBM) introduced by Methfessel and Paxton (1989), and modified tetrahedron method (MTM) presented by Blöchl et al. (1994).

As indicated above in the equation 2.46, the total density of states can be viewed as a projection over k-points for the electronic band structure. In the real space, the DOS can be analyzed by introducing the local density of states (LDOS), which defined by the following equation:

$$n(\vec{r}, E) = \sum_{i} \sum_{\vec{k}} |\psi_{i\vec{k}}(\vec{r})|^{2} \delta(\epsilon_{i,\vec{k}} - E) \tag{2.47}$$

The projected density of states (PDOS) plays a vital role to understand the interactions between atomic orbitals and is defined as follows:

$$n(\alpha, E) = \sum_{i} \sum_{\vec{k}} |\psi_{\alpha\vec{k}}(\vec{r})\psi_{i\vec{k}}(\vec{r})|^{2} \delta(\epsilon_{i,\vec{k}} - E) \tag{2.48}$$

The PDOS acts principally as a projection of the density of states over the atomic orbitals, as seen in equation 2.48, where the $\psi_{\alpha\vec{k}}$ represents the orthonormal states of $\psi_{i\vec{k}}$.

In plotting the calculated DOS spectrum, more attention is paid to the position of the zero point energy known as the Fermi energy (EF), which refers to the highest occupied electronic states in the studied system at absolute-zero temperature. However, the Fermi energy is theoretically predicted to be related to the highest occupied molecular orbital (HOMO).

In periodic systems, the Fermi energy level is usually shifted to the zero of a continuous DOS spectrum. For other systems, such as molecules and some types of clusters, the determination of the Fermi energy level is carried out by taking the average value between the high-occupied (HOMO) and lowest unoccupied molecular orbital (LUMO), i.e.,

$EF = \frac{1}{2}(E_{HOMO} + E_{LUMO})$. Due to the electronic states of molecules being characterized by discrete energy values, the DOS spectra are shown as the bar diagrams.

2.3.7.2 Charge density difference (CDD)

The charge density can generally be defined as the amount of charge per volume on a discrete grid of points in the real space. In quantum mechanics, it refers to the spatial charge distribution over the unit cell volume of the periodic solid or the volume of the molecule. However, it is strongly related to the position vector $\vec{r}$.

The relationship between the electronic charge density and the wavefunction is described by the following equation:

$$\rho(\vec{r}) = e^2 \sum_{n\vec{k} \in occ} |\psi_{n\vec{k}}(\vec{r})|^2 \tag{2.49}$$

where n is the number of electron bands, e is the charge of electron given in 'coulomb' ($e = 1.6021733x10^{-19}$), the $\psi_{n\vec{k}}(\vec{r})$ is the wavefunction of the electronic bands, and the sum is taken only over the occupied-electronic states.

In solids, tracking the charge-transfer process is important in order to realize the nature of interaction between the components of a system. Therefore, the charge density difference (CDD) is used as a main tool to find the charge transfer path, which can be obtained by the difference between the charge densities of the system and its individual components. For example, in a system consisting of A and B components, the CDD ($\Delta\rho$) is expressed as follows:

$$\Delta\rho = \rho AB - \rho A - \rho B \tag{2.50}$$

where ρAB the charge density of the whole system, while both ρA and ρB are the individual charge density of A and B components, respectively.

For illustration purpose in some cases, e.g., the charge rearrangement during chemical bond formation, CDD can be visualized in various ways, such as a series of isocontours, i.e, 2D contour plots; or a surface model based on discrete isovalue contours, i.e, 3D isosurface plots.

Many the systematic and direct methods have been developed to assign the charge for periodic structures and surfaces. Bader charge analysis is considered as one of the common methods used to describe charges in the periodic systems (Henkelman et al., 2006), because this method offers a computationally lower cost once the quantum chemistry calculation gives the charge densities. More detail describing the concept of Bader charge is discussed in the following subsection.

2.3.7.3 The concept of Bader charge

Bader (1990) introduced a mathematical method to divide an anisotropic space charge distribution into segregated sub-volumes, so that effective analysis of the charge distribution of a system under the consideration can be carried out. It can be applied after obtaining the electronic density distributions by a converged DFT process in a solid. Usually, the separated Bader-volume is corresponding to the region that has an atom in its center, which represents the atomic charge in the model system. Despite serious problems associated with the accuracy of the calculated charge value by using this method (Cassam-Chenaï & Jayatilaka, 2001), it provides a useful tool for the comparison purpose.

Cassam-Chenaï and Jayatilaka (2001) wrote a free software to analyze the Bader charge distribution. In addition, the main software used in this thesis, VASP, generates a "CHGCAR-file" that acts as the input file containing the spatial charge distribution and used to calculate the effective Bader charge accompanying every ion in the studied system.

2.3.8 The Hellmann-Feynman theorem

Hellmann (1937) and Feynman (1939) introduced separately the so called Hellmann-Feynman theorem, which describes the total energy derivative of the electronic ground state of a system and used to compute the forces acting on atoms. In the system's ground state, the expectation value of the Hamiltonian ($\hat{H}$) with respect to an ion position is equal to the force applied on that ion.

By considering ψ as eigenvectors of the Hamiltonian; the energy derivative with respect to an arbitrary parameter λ is expressed by:

$$\frac{\partial E}{\partial \lambda} = \frac{\partial}{\partial \lambda}\langle \psi|H|\psi\rangle = \langle \frac{\partial \psi}{\partial \lambda}|H|\psi\rangle + \langle \psi|H|\frac{\partial \psi}{\partial \lambda}\rangle + \langle \psi\left|\frac{\partial H}{\partial \lambda}\right|\psi\rangle \quad (2.51)$$

For the ground state, the following terms are neglected:

$$\langle \frac{\partial \psi}{\partial \lambda}|H|\psi\rangle\Bigg|_{\psi=\psi 0} + \langle \psi|H|\frac{\partial \psi}{\partial \lambda}\rangle\Bigg|_{\psi=\psi 0} = 0 \quad (2.52)$$

The forces acting on the atoms may be described in a simpler manner as follows:

$$\vec{F} = \frac{\partial E}{\partial \vec{\mathrm{R}}} = \frac{d}{d\vec{R}}\langle \psi|H|\psi\rangle = -\langle \psi\left|\frac{\partial H}{\partial \lambda}\right|\psi\rangle \quad (2.53)$$

Within this approximation, the force is calculated on the basis of the atomic configuration without resolving the electronic states and/or their derivatives. This, in turn, makes the calculation of force simple and efficient.

2.4 Adsorption on solid surfaces

Here, some of the theoretical and experimental knowledge related to the adsorption will be summarized, in order to understand what happens to the gas molecule or cluster when they react on the surface, how to simulate this process, and how the interaction

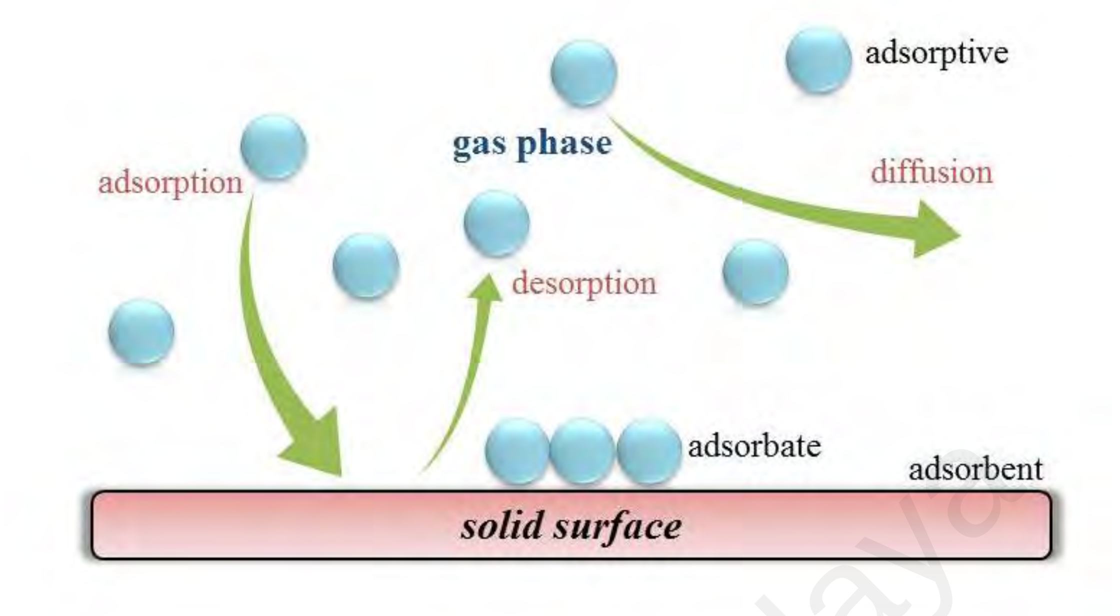

Figure 2.18: The terminology of the adsorption phenomena.

strength of the molecules with the surface helps to predict their growth behavior.

Currently, catalytic reactions produce 90% of chemical products (Senkan, 2001), and some of these materials require that the catalyst surface allow the reactions to take place under mild conditions.

The process of sticking an atom or a molecule in the gas state a solid surface is called adsorption, in which free particles convert from (adsorptive) gas phase onto (adsorbate) on the solid surface (adsorbent). Being the inverse process of the adsorption, desorption is a process of releasing an atom or a molecule from the surface. These concepts and others are illustrated in Figure 2.18. According to the strength of the binding energy and the reaction mechanism, the adsorption phenomena are routinely categorized into two classes:

- The kind of adsorption that does not affect significantly the electronic structure is called physisorption, which is associated with a smaller binding energy.
- The kind of adsorption that strongly perturbs the electronic structure is called chemisorption; it corresponds to the binding energies.

In the case of physisorption, the Van der Waals forces are principally responsible for the adsorbate–substrate interactions, which also imply very weak orbital overlap between the adsorbate and the substrate. In contrast, chemisorption involves genuine adsorbate–substrate interactions that can be attributed to ionic, covalent and metallic bonds. The latter adoption case usually causes substantial changes in the structural, electronic and magnetic properties of the system under consideration.

Three approaches can be used to investigate the adsorption process from different points of view (Desjonqueres & Spanjaard, 2012)

- The thermodynamical or macroscopic approach, which is employed on the system to find the relationship between its thermodynamic properties at equilibrium.
- The microscopic approach, whereby a variety of physical properties can be calculated for the adsorbate-substrate interactions based on the principles of quantum mechanics.
- The statistical mechanical approach, which works as a bridge that connects both previous approaches by linking the quantities of macroscopic approach with that of the microscopic one.

Besides the experimental methods used in the reaction and surface analysis, there is a growing interest in the development of theoretical methods. This provides a broader view of the processes that occur within the different catalytic reactions (Nilsson et al., 2008). However, more approximations are necessary due to the fact that the surface can be considered as an infinitely large system, compared to a single molecule, hence additional effects can be observed as will be discussed below.

The surface coverage of the monomolecular layers (θ) can be defined as follows:

$$\theta = \frac{N}{N_m} \tag{2.54}$$

where the number of the adsorbed molecules on the surface is represented by N, while the number of molecules required to cover fully the surface is represented by N_m. For the gas-surface system, including the adsorptive-substrate interactions, the surface coverage θ is a function of the temperature T and the fractional pressure p, expressed as $\theta = f(p, T)$.

A straightforward measure can easily evaluate the strength of the adsorbate-adsorbent interaction and is known as the adsorption enthalpy (ΔH). On this basis adsorption constitute the equilibrium constants, and the adsorption enthalpy is calculated by the Van't Hoff's equation as follows:

$$\left(\frac{\partial lnK}{\partial \frac{1}{T}}\right) = -\frac{\Delta H}{R} \tag{2.55}$$

where the K and R are the adsorption constant and the universal gas constant (R= 8.314 J mol^{-1} K^{-1}), respectively, and T is the temperature. Some of experimental techniques, such as temperature-programmed reduction and temperature-programmed desorption, are commonly used to estimate both the surface coverage and adsorption enthalpy values.

A set of experimental spectroscopic techniques are routinely used to investigate the structure and the growth morphology of the deposited materials, including electron scattering, X-Ray scattering, ion scattering, scanning probe microscopy and other spectroscopic methods (Nilsson et al., 2008).

Many processes (e.g., adsorption) and other phenomena always occur at the interface between the environment, which includes the surfaces, and a condense phase. Therefore, much interest has been given to the modeling of surfaces and interfaces. Cutting a crystal is the way to generate a surface, which is simulated as an infinite object along the crystalline plane. The crystal cutting creates two semi-infinite crystals, which consist of an infinite number of atoms in the normal direction to the surface, where the translational symmetry (periodicity), which is necessary to apply the Bloch theorem, is lacking. This problem can be dealt with by using a finite slab model as an approximation for the semi-infinite crystal (Causa et al., 1986).

2.4.1 The slab model

The slab model contains a limited number of atomic layers (such as a film that has a finite thickness) parallel to the crystalline plane (hkl) of interest. This slab with limited thickness has two surface planes generated by spontaneous symmetry. However, a slab with a sufficient number of layers, i.e., reasonably thick slab, represents an excellent model for the ideal surface, in which the model adequacy must be tested according to the convergence energy, geometry and electronic properties as a function of the number of atomic layers of the slab. By forcing 3-D periodicity, one uses the 3-D slab model in the actual calculations, shown in Figure 2.19. The three-dimensional (3D) system contains an array of slabs of specific thickness along one direction, isolated by vacuum spaces. This vacuum space should be large enough to avoid undesirable interactions between repeating slab images that usually occur along the z direction, as seen in Figure 2.19.

2.4.1.1 The adsorption energy

A well-designed adsorption model of molecules or atoms on a surface is essential in order to study the ongoing adsorption process (Dovesi et al., 2005). However, in contrast to the type of adsorption process that can be easier to model within the DFT methods, i.e., the chemisorption, the correct model of physisorption may be difficult to obtain due to the weak adsorbate-substrate interactions associated with this process.

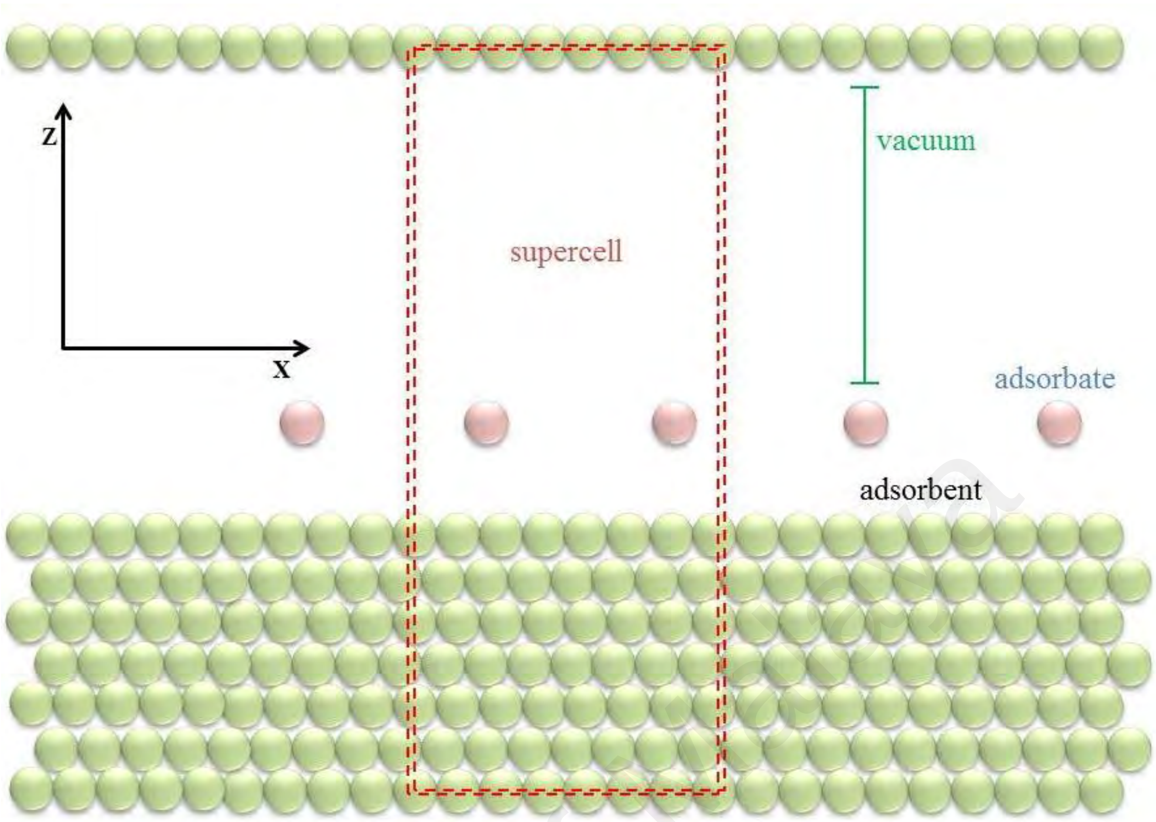

Figure 2.19: Schematic representation of the slab model. The side view of the supercell showing a number of the atomic layers forming the substrate slab. The sufficient vacuum space targets to avoid the interaction between adjacent supercell images.

The adsorption energy (or binding energy), is the principal key to understanding the nature of adsorbate-substrate interactions. It, in fact, describes the tendency of molecules or atoms in an ideal gas state to bind with the surface, and can be defined as,

$$\Delta E = E_{(slab|ads)} - (E_{(slab)} + N.E_{(Mol)}) \tag{2.56}$$

where ΔE is the binding energy, $E_{(slab/ads)}$ is the total energy of the entire system (i.e., the surface in interaction with the N adsorbed molecules per unit cell), and $E_{(Mol)}$ is the energy of one isolated molecule. All of these energies possess negative signs and measure for one unit cell.

Stated briefly by the summation of two contributions is given by:

$$\Delta E = \Delta E_{ads} + \Delta E_L \tag{2.57}$$

The first term, ΔE_{ads}, represents the binding energy of the adsorbed molecule per unit cell per adsorbed molecule, and can be defined as

$$\Delta E_{ads} = E_{(slab|ads)} - (E_{(slab)} + E_{(ads)}) \tag{2.58}$$

where $E_{(slab/ads)}$, as mentioned-above, is the total energy of the periodic array of the molecules adsorbed on the slab, $E_{(slab)}$ is the energy of the pure slab without adsorbed molecules, and $E_{(ads)}$ is the energy of the periodic array of molecules without the slab. The second term in equation 2.57, namely ΔE_L donates the lateral interaction energy between the adsorbate molecules merely without considering the substrate, it is per unit cell. Of course, the ΔE_L can be positive or negative depending on the nature of interaction between the adsorbed molecules; either its repulsive or attractive, respectively. In addition, the distances between the molecules sequentially increase with decreasing the surface coverage, which leads to the value of ΔE_L reduced to near-zero for the lowest coverage, and thus $\Delta E \cong \Delta E_{ads}$.

Investigation of the adsorption process by modeling different surface coverage is very important in order to detect the changes in the structure of the deposited materials and its growth morphology as a function of the surface coverage. This can be performed easily by modifying the size of the unit cell within the supercell approach, in which the density corresponding to the adsorbed molecules can be decreased or increased according to the unit cell size. In the limit of low coverage, the adsorbed molecules are considered as isolated and the lateral interactions are likely to be close to zero.

2.4.1.2 Structures: calculating, modeling, analyzing and viewing programs

It is important, before proceeding to our works in the next subsections, to describe briefly the programs used in calculating, modeling, analyzing and viewing the data gained in this thesis as follows:

- Vienna Ab initio Simulation Package (VASP) is a powerful DFT package developed recently for studying a wide range of materials and their associated properties (Kresse & Hafner, 1993; Kresse & Furthmüller, 1996a; Kresse & Furthmüller, 1996b). It successfully applied to surfaces, interfaces, 3D bulk and cluster systems with periodic boundary condition (Furthmüller et al., 1994) (Kern et al., 1996; Stadler et al., 1998). Most of these applications are based on the ultrasoft pseudopotential and plane wave basis set; however, the newer version includes all-electron pseudopotential option (Sun et al., 2003). In the actual calculations, all-electron Blöchl's projector augmented wave (PAW) approach (Blöchl, 1994; Kresse & Joubert, 1999), which is well known to provide a very accurate result relative to the FLAPW benchmarks, is applied within the GGA of Perdew and Wang parameterization (Perdew & Wang, 1992) to describe the exchange and the correlation terms. Furthermore, the integration is carried out on predefined k points in the Brillouin zone determined on the basis of Monkhorst-Pack scheme (Monkhorst & Pack, 1976).
- Gaussian is the most widely used and most commercialized quantum chemical codes in the field of computational chemistry. The code of Gaussian is programmed by the FORTRAN language, which is built based on the principles of quantum mechanics. It is capable to calculate accurately many properties of the studied system, such as the molecular structure, energy, and vibrational frequencies of a molecular system (Cheng et al., 2011).

- Jmol is an open source, free Java molecular modeling software for a diverse range of chemicals, biomolecules, crystals, and materials (Chen, 2003). It can be run on windows, Linux/Unix, and Mac OS X systems. Jmol has many special features, including animation of vibrations generating from the quantum-mechanical calculations, and calling the crystallographic and the unit cell information. It also supports several graphics file formats, such as VASP (POSCAR), VASP (CONTCAR), Gaussian 09/03/98/93 output, HIN (HyperChem), PDB, SHELX, XYZ, etc. (Willighagen & Howard, 2007).

- VESTA is a 3D viewer program of volumetric data and crystal structures, including the coherent and electron scattering length obtained from neutron and X-ray diffraction, respectively. Additionally, it is used to visualize the calculated volumetric data, such as electrostatic potentials, wavefunctions, and electron densities obtained from electronic state calculations. VESTA is a very useful program in identifying 3D-crystal structures and measuring their different physical quantities (Momma & Izumi, 2011).

- Visual Molecular Dynamics (VMD) is a molecular analysis and visualization software. Although it is specially designed for biological systems, it can be used to visualize a variety of structural formats, including surfaces, interfaces, and clusters. Besides rendering high-quality figures for publication, VMD also analyzes and animates molecular dynamics trajectory data. More details for further features implemented in this program can be seen in the reference (Hsin et al., 2008).

- Origin is a program package for a variety of technical and scientific data analysis and graphics. Origin has a set of distinctive features of plotting and analyzing data. For example, it offers a wide variety of graphing options, extending from simple scatter plots to stacked clustered plots associated with a different assortment of colors and styles. A dizzying array of analysis options is available in this software, including calculus, statistics, and FFT functions. This allows identifying and fitting up to a dozen of peaks or applying different built-in functions from the curve-fit library. Origin represents a good program for technical and scientific graphics, which is more flexible and friendly in used (Deschenes & Bout, 2000; Chen, 2009).

CHAPTER 3: GLOBAL STRUCTURAL OPTIMIZATION AND GROWTH MECHANISM OF COBALT OXIDE NANOCLUSTERS BY GENETIC ALGORITHM WITH SPIN-POLARIZED DFT

3.1 Introduction

Experimental and theoretical studies of cobalt oxide clusters as a heterogeneous catalyst and on its electronic, magnetic, and other properties have received considerable attention recently (Fierro, 2006). Generally, by modifying the shape and size of the cluster one can manipulate directly these properties.

As a catalyst, supported cobalt oxide nanoparticles are used for chemical transformation processes such as in the oxidation of carbon monoxide and nitrogen monoxide, and in the hydrogenation of CO or CO_2 (i.e. in Fischer-Tropsch synthesis; Yung et al., 2007; Y. Xie et al., 2010; Melaet et al., 2014). Increasing the size of cobalt oxide nanoparticles induces the dissociation of CO, thus increasing the efficiency of the Fischer-Tropsch synthesis by reducing the dissociation energies of CO (Lee et al., 2015).

Several spectroscopic techniques such as (IR) vibrational, photodissociation and time-of-flight mass spectroscopy had been conducted to investigate different aspects of neutral and cationic cobalt oxides clusters ($Co_nO_m^{0/+}$) (Dibble et al., 2012; Yin et al., 2009; Dijk et al., 2014). For example, the mass spectrum data of cobalt oxide clusters have shown that the intensity peaks varies with the size of the cluster. The small clusters distinctly reveal higher signal intensity. In particular, the neutral and cationic $Co_4O^{0/+}$ clusters show the highest intensity, which reflects the remarkable structural stability of this small cluster (Dibble et al., 2012; Y. Xie et al., 2010). These dissociation data have also shown that the predominant stoichiometry is when $n = m$, in which the loss of oxygen molecules is the preferred dissociation channel. Therefore, the stoichiometric cobalt oxide clusters ($Co_nO_n^{0/+}$) merit more interest than other aspects.

The key to studying reaction mechanisms and properties of the nanoparticles is through the extensive exploration of the potential energy surface (PES) of their molecular structures. There have been numerous techniques used to investigate the PES namely by statistical mechanics, basin-hopping (BH) and genetic algorithms (GAs), which have been implemented in computer codes such as CBEV/FCEM (Polak & Rubinovich, 2005; Davis et al., 2014), GMIN (Bogdan et al., 2006) and Birmingham cluster genetic algorithm (BCGA) (Johnston, 2003), respectively.

Recently, the electronic structure methods such as Density Functional Theory (DFT) have been used to search the global minimum of PES of neutral cobalt oxide clusters Co_nO_n ($n < 10$) (Uzunova & Mikosch, 2012; Aguilera-del Toro et al., 2014; Ota et al., 2013; Dijk et al., 2014). It was reported that the lowest-energy configurations of Co_nO_n have ring and tower-like structures, differing from the face centered cubic structure of the bulk. Despite recent interests, probing comprehensively the PES using these methods are computationally demanding due to the huge number of different possibility of isomers (Heiles & Schäfer, 2014). Therefore, true understanding and modeling of Co_nO_n clusters are still lacking.

Practically, the most stable structures of the different clusters can be determined using GA approach combined with DFT relaxation (Neogi & Chaudhury, 2015; Lysgaard et al., 2015; Huang et al., 2015). For example, the global minimum geometries of Au-Ag nanoalloys and bismuth-doped tin clusters have been successfully optimized with a coupled method of GA-DFT performed by Johnston et al (Logsdail et al., 2012; Heiles et al., 2012).

3.2 Literature Review

By the means of selected photodissociation of $Co_nO_m^+$ via time of flight mass spectroscopy (Dibble et al., 2012), the $Co_nO_n^+$ clusters were found to be the prominent feature in the mass spectrum. Similar results were also found in the mass spectrum of the neutral Co_nO_m clusters, which reflected the remarkable stability of stoichiometric clusters (Dijk et al., 2014; Yin et al., 2009), as had been mentioned above. This provides a strong reason to investigate thoroughly the structural and other physical and chemical properties of Co_nO_n clusters.

The cationic cobalt oxide cluster had been studied using ion mobility–mass spectrometry analysis combined with DFT study (Ota et al., 2013). The comparison between experimental and theoretical results showed that the $(CoO)_{3-5}^+$ has ring (planar-like) structures, whereas the $(CoO)_{6-7}^+$ exhibit tower (compact-like) structures. Therefore, it can be concluded that the structural transition from two-dimensional (2D) to three-dimensional (3D) structures had occurred at $(CoO)_6^+$. Recently, the tower-like structure had also been suggested for $Co_6O_6^{0/+}$ by Aguilera-del Toro et al. (2014) using DFT calculations. Although both DFT studies showed similar results for some clusters such as the ring-like structures for $Co_4O_4^{0/+}$, they do not agree with the spin state results for certain isomers, and thus exist energy differences. This can be attributed to a limited examination of the possible spin state in the Ota et al. (2013) study, as they did not explore the high-spin states compared to the recent study of Aguilera-del Toro et al. (2014). This disagreement even occurred in studies for the low spin states of certain cluster sizes within the same structural family. For example, Ota et al. (2013) reported a huge energy difference of up to 8.23 eV when changing the spin multiplicity of the $Co_5O_5^+$ monocyclic ring structure from 1 to 3, while Aguilera-del Toro et al. (2014) found it to be slightly less than 0.4 eV. In addition, van Dijk et al. (2014) have recently investigated the structures of cationic cobalt oxide clusters for several sizes of stoichiometry $Co_xO_y^+$ $(x = 3-6, y = 3-8)$ by using IR vibrational spectroscopy combined with the vibrational frequency calculations using density functional theory. They recorded a non-conformity between experiment and calculations, which is likely attributed to limitations in the computational methods used in the modelling of the complex systems with high level of correlations.

Genetic algorithm plays a vital role to find out the global minimum for many different systems, in particular, for finding the ground-state structures of larger clusters in which the intuition may not be sufficient (Santambrogio et al., 2008). Unusual structures can be expected within electronic and structural, hence the use of GA becomes more important in order to explore thoroughly the vast region of the potential energy surface. For instance, genetic algorithm was found to be reliable and efficient for reproducibly, in finding the global minima for MgO clusters (Roberts & Johnston, 2001). Many GA programs can be found in the literature, which outline the developments and reflect the growing interest in the field of the optimization algorithms, particularly in genetic algorithm. Recently, the refinement process has been subsequently performed on the GA ground-state structures by sophisticated DFT-based programs that are commonly used to provide more accurate calculations. Consequently, this should improve structurally and energetically the quality of the resultant structures of GA (Zhang & Tian, 2008; Huang et al., 2015). Some of the developed GA code has directly adopted the DFT calculations and has related to the so-called hybrid genetic algorithm, which uses more accurate DFT calculations in the structural convergence step (Hamad et al., 2005; Chen & Dixon, 2013). The efficiency of this type of GA strongly depends on the balance between the convergence accuracy and speed of the selected DFT method. Most recently, GA have been successfully designed to work within the framework of pool methodology, where the new generated structures with lower energy (high fitness) replace directly the highest energy structures in the pool (lowest fitness), in contrasts to the generation-based methodology. In addition, the quality of the pool's members is enhanced based on the predetermined energetic criteria.

In this work, we report the global and local minimum structures of Co_nO_n (n = 3 − 7) clusters using a new implementation of GA, accompanied by accurate refinement stages. In our GA code (henceforth referred to as Universal Genetic Algorithm (UGA)), multi-convergence relaxation approaches within the framework of pool genetic algorithm methodology (PGAM) have been included. The flexibility to utilize either one or more of these implemented approaches in any order has been carefully considered. We also report for the first time some new structures obtained through the global optimization of Co_5O_5 and Co_6O_6. Other structures were found identical to previous works. The results show a new growth mechanism from the two (planar) to three dimensional (non-planar) shapes via energy-structure relationship profile. In addition, the stability of Co_3O_3 and Co_4O_4 as ring structures show good agreement with the experimental findings.

3.3 Methodology

3.3.1 Universal Genetic Algorithm

The procedure to design UGA is based on the well-known BCGA (Johnston, 2003). The algorithm exploits the flexibility of Python codes and its massively available libraries to deal with several optimization levels. In addition, it makes use of the scaling capability of the PGAM which has been recently implemented in the BPGA (Davis et al., 2015) instead of the generation code methodology (Johnston, 2003). This implementation enables the algorithm to characterize structures of complex and large sized nanoparticles with more efficient scaling (Davis et al., 2015).

A number of Python library routines obtained from the Atomic Simulation Environment (ASE) (Bahn & Jacobsen, 2002), the Grid-based Projector Augmented

Wave (GPAW) (Enkovaara et al., 2010; Mortensen et al., 2005) and the Molecular Orbital PACkage (MOPAC) (Kanters & Donald, 2014) have been gathered to design the UGA. The ASE provides a variety of relaxation methods where a special class of the quasi-Newton methods of limited-memory Broyden-Fletcher-Goldfarb-Shanno (L-BFGS) was implemented for the numerical optimization procedure. The GPAW provides a DFT calculation where the grid-based (GB) code using the projector-augmented wave (PAW) method was implemented for efficient calculations, while orbital-based Linear Combination Atomic Orbital (LCAO) within the GPAW framework was implemented for the fast relaxation process. The MOPAC provides semiempirical program based on the neglect of diatomic differential overlap (NDDO) where the PM7 parameterization method was implemented. All these three relaxation methods can be executed together or as one selective execution process. This option gives flexibility within UGA to incorporate any relaxation algorithms in order to yield more reliable and accurate optimized structures. It is worth mentioning that the compatibility between the object-oriented Python program with the Structured Query Language (SQL) is useful to functionalize the input and output data across all parts of the algorithms.

The rejection of identical structures occurs either in the initial population or between the relaxation process, based on the energetic and structural criteria recently proposed by Vilhelmsen and Hammer (2012). This can be optionally used in the UGA code. Presently, the UGA is designed for structures consisting of two different type of atoms. The atoms are separated in such a away that the distance between atomic radii are kept apart from overlapping each other. Besides, the structural parameters such as bond distance and angle can be varied optionally to generate the initial pool with desired structural configurations. Indeed, this option reduces the computational cost greatly and increases the efficiency of GA in filtering only a few structures for the initial pool. However, this procedure needs to be done properly so that all reliable structures will be taken into account.

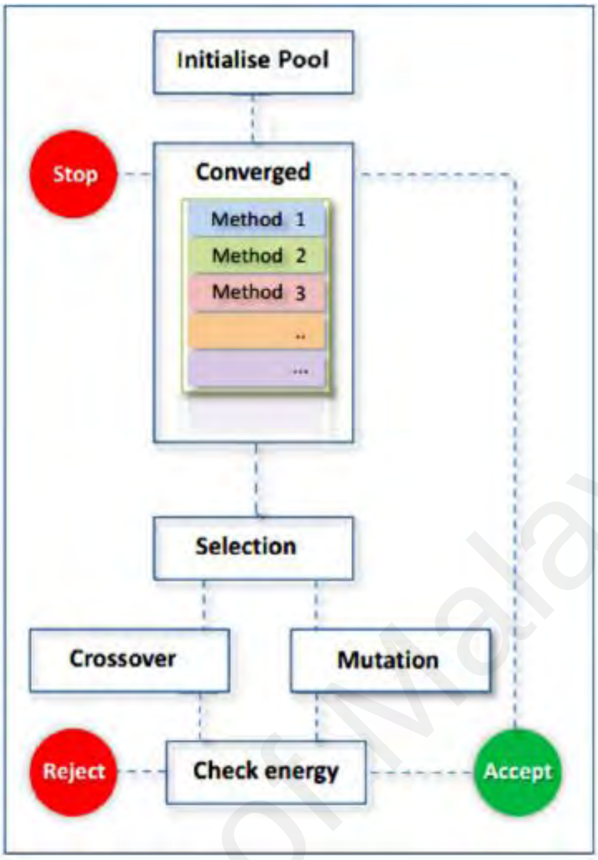

Figure 3.1: The pool scheme used by the Universal Genetic Algorithm program.

All parts of the UGA components involving fitness, crossover and mutation have been constructed according to the BCGA description (Johnston, 2003). UGA code offers the most common fitness functions, including exponential, linear, and hyperbolic tangent based on dynamic fitness scaling by using a normalised value of the energy (ρ). In this work, the hyperbolic tangent, $1/2[1 - tanh(2\rho_i - 1)]$, is used, which provides an explicit relative weighting of good versus mediocre and bad structures. The atomic displacement and the twisting mutations are accessible within the UGA code. The selection of parents is achieved merely by applying the roulette wheel selection. Figure 3.1 shows the general scheme of UGA with multi-optimization methods. In this particular study of cobalt oxide, two cheap and less precise computational methods were utilized in the local minimization of the structural energy i.e the L-BFGS minimizer using the force calculated by LCAO and

PW. For both methods, the non-spin calculations with double-zeta polarized (DZP) basis set were performed after generating the initial pool with 50 molecular structures, which has one or two Co-O bonds for each Co atom. These semi-designed Co_nO_n structures are reasonable starting points, analogous to previous reported structures.

Once the structures in the initial pool have converged and become parents, selection, crossover and mutation processes were carried out for a pair of the parents. 30% of the generated offsprings were randomly mutated by one of the above-mentioned ways. The cut and splice crossover operator of Deaven and Ho was applied (Deaven & Ho, 1995), whereas the cutting plane was performed by the random single cut method (Johnston, 2003). Then, the convergence of the offspring was carried out. In the case where its energy is lower (or higher fitness) than one of the pool structures, the offspring structure will replace the highest energy structure in the pool. The iteration process of the structural energy minimization was halted when the lowest energy structure has converged up to 0.001 eV. Then, by keeping this lowest energy at its converged value, the second iteration was performed until the structural energy difference between the lowest and the highest in the pool became less than 1.5 eV. These two important convergence criteria were considered in order to capture not only the global minimum structures (in the first iteration) but also the nearest local minimum structures with distinct shapes (in the second iteration). In addition, these criteria were allowed to reproduce some structures that have been addressed in previous studies which were used for comparison purpose. It should be mentioned that the above-described genetic algorithm was applied for each cluster size separately.

3.3.2 Refinements

The optimized structures obtained from UGA, including the most stable and other distinct geometries for each cluster size, are subjected to the final refinement optimization by using collinear spin-polarized DFT calculations implemented in the VASP code (Kresse & Furthmüller, 1996a; Kresse & Furthmüller, 1996b; Kresse & Hafner, 1993) with PAW (Kresse & Joubert, 1999; Blöchl, 1994). The energies of these structures were calculated using the generalized gradient approximation (GGA) with the Perdew, Burke, and Ernzerhof (PBE) exchange-correlation functional (Perdew et al., 1996). The core electrons are described by norm-conserving scalar relativistic pseudopotentials (Troullier & Martins, 1991) and the valence electrons included are based on the O $2s^2$ $2p^6$ and Co $3d^8$ $4s^1$ states. A plane-wave cutoff energy of 400 eV and an energy convergence criterion of 1 meV for self-consistency were adopted throughout our calculations. The Gamma point was considered due to the large cubic supercell of $20 \times 20 \times 20$ A^3 which was taken as a container for the individual clusters. The supercell size was large enough to avoid interactions between neighboring cell images. The relaxation of atomic position was stopped when the interatomic forces were less than 1 meV/A. To get the ground-state magnetic moment, all possible spin configurations are checked for each geometrical structure.

3.3.3 Energetics

The binding energies per CoO molecule were calculated using

$$E_b = \frac{1}{n}(E_{Co_nO_n} - n\,E_{CoO}) \qquad (3.1)$$

where n is the number of CoO molecules in the cluster, $E_{Co_nO_n}$ is total energy of the cluster and E_{CoO} is the energy of a CoO molecule.

For finding the relative stability of the cluster, the second-order total energy difference was calculated using

$$\Delta^2 E = 2\, E_{Co_nO_n} - (E_{Co_{n+1}O_{n+1}} + E_{Co_{n-1}O_{n-1}}) \tag{3.2}$$

where $E_{Co_{n+1}O_{n+1}}$ and $E_{Co_{n-1}O_{n-1}}$ are the total energies of the $E_{Co_nO_n}$ neighbors.

3.4 Results and Discussion

Table 4.1 shows the binding energies (E_b), point groups, magnetic moments and spin multiplicities ($2S + 1$) of the global and local minimum structures of Co_nO_n clusters searched by the UGA program and refined with the spin-polarised DFT. The global minima of Co_3O_3 and Co_4O_4 are displayed in Figure 3.2 characterized as triangular and rectangular planar-like structures **I**, respectively, which are in good agreement with recent computational and experimental observations (Uzunova & Mikosch, 2012; Aguilera-del Toro et al., 2014; Ota et al., 2013; Dijk et al., 2014). Structure **I** of the Co_3O_3 cluster is more stable than that of the local minimum structures **II** and **III**. Structures **II** and **III** are a composite of CoO molecules lying horizontally and vertically on the planar ring cobalt oxide dimers as shown in Figure 3.2 that are in line with previous structural predictions (Aguilera-del Toro et al., 2014; Ota et al., 2013; Yin et al., 2009; Dijk et al., 2014).

The most stable structure **I** of the Co_4O_4 cluster has C_{2v} symmetry instead of the suggested D_{4h} symmetry because of the deformation of the initial D_{4h} symmetry by antiferromagnetic (AFM) ordering of the singlet state (Aguilera-del Toro et al., 2014; Ota et al., 2013; Yin et al., 2009). The C_{2v} structure has been observed also for the

Table 3.1: Binding energies (E_b), point groups, magnetic moments and spin multiplicities $(2S + 1)$ for the global and local minimum structures of Co_nO_n clusters.

Cluster	Point group	Eb/eV	(2S + 1)	Magnetic moment/μβ		
				Co_n	O_n	Total
Co_3O_3-I	C_{2v}	-2.861	4	2.10	0.90	3
Co_3O_3-II	C_s	-1.994	2	0.97	0.03	1
Co_3O_3-III	C_s	-2.180	8	5.56	1.44	7
Co_4O_4-I	C_{2v}	-3.295	1	0.00	0.00	0
Co_4O_4-II	C_{3v}	-3.037	7	4.77	1.23	6
Co_4O_4-III	T_d	-2.727	13	9.49	2.51	12
Co_4O_4-IV	C_1	-2.883	9	6.68	1.32	8
Co_4O_4-V	C_s	-2.796	1	0.00	0.00	0
Co_5O_5-I	C_s	-3.320	4	2.64	0.36	3
Co_5O_5-II	C_s	-3.229	2	0.84	0.16	1
Co_5O_5-III	C_{5h}	-3.052	10	7.43	1.57	9
Co_5O_5-IV	C_s	-3.069	12	9.07	1.93	11
Co_6O_6-I	C_1	-3.504	9	6.93	1.07	8
Co_6O_6-II	C_{2h}	-3.285	19	14.45	3.55	18
Co_6O_6-III	C_s	-3.401	1	0.00	0.00	0
Co_6O_6-IV	C_{2v}	-3.395	1	0.00	0.00	0
Co_6O_6-V	C_1	-3.237	1	0.00	0.00	0
Co_6O_6-VI	C_s	-3.184	5	3.26	0.74	4
Co_7O_7-I	C_s	-3.578	12	9.42	1.58	11
Co_7O_7-II	C_1	-3.566	2	0.71	0.29	1
Co_7O_7-III	C_s	-3.361	2	0.70	0.30	1

Co_4O_4 cation recently by an IR vibrational spectroscopic study (Dijk et al., 2014). The stability of structure **I** differs by 0.2 eV in binding energy (refer Table 4.1) compared to the nearest predicted local minimum structure **II**, i.e., bi-capped triangular prism. Figure 3.2 shows this new structure characterized by one of the triangular bases which consists of Co atoms, whereas, the other side consists of O atoms. Both the triangular bases are capped by one atom of O and Co. In addition, the cubic structure **III** was successful searched to lie 0.56 eV higher in energy (refer Table 4.1) than the global minimum structure **I**. The present prediction of structure **III** is in line with previous works (Dijk et al., 2014; Yin et al., 2009; Aguilera-del Toro et al., 2014).

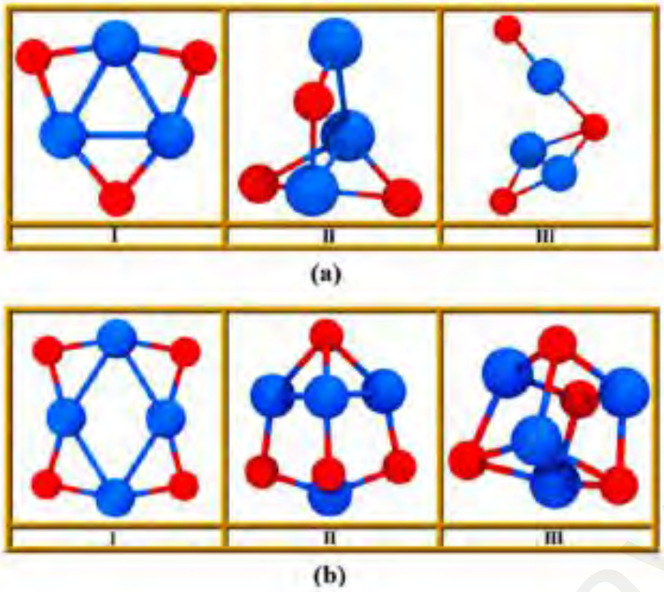

Figure 3.2: Global and local minimum structures for the (a) Co_3O_3 clusters: (I) triangular planar-like structure; (II) and (III) CoO molecules lay horizontally and vertically on the planar of Co_2O_2, respectively. (b) Co_4O_4 clusters: (I) rectangular planar-like structure; (II) bi-capped triangular prism structure; (III) cubic structure. The Co and O atoms are blue and red, respectively.

The stability of planar-like structure **I** especially for the Co_4O_4 cluster explains their abundance in the experimental fragmentation spectra (Dibble et al., 2012; Aguilera-del Toro et al., 2014). As will be seen later, this study found a number of global and local minimum structures of larger clusters such as Co_5O_5 and Co_6O_6 constructed from the structural moieties of these planar-like clusters, in particular Co_4O_4. Thus, this provides another rational explanation of the experimental results.

This study also found a new global minimum for the Co_5O_5 cluster labeled as structure **I** that has two unique lateral perspectives. Figure 3.3 shows the projection of both perspectives, which resembles slightly the structural **I** faces of the Co_4O_4 and Co_3O_3 clusters. Therefore, the structure can be regarded as a CoO molecule bonded with the Co_4O_4 cluster (at the right hand side of structure **I**), or two CoO molecules connected with the Co_3O_3 cluster (at the left hand side of structure **I**). However, experimental cationic Co_5O_5 structure derived from the fragmentation spectra revealed that the global minimum belongs to the ring structure **III** (Ota et al., 2013). Our work shows that a considerable

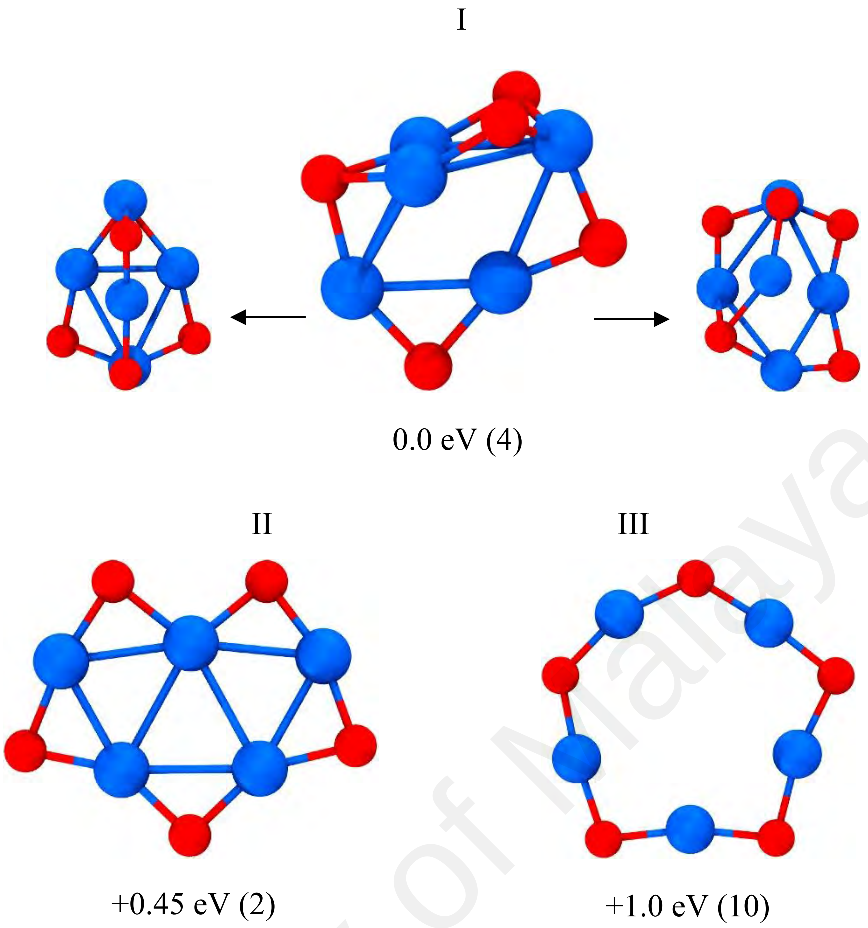

Figure 3.3: Global and local minimum structures for the Co_5O_5 cluster: (I) global minimum structures; (II) planar structure; (III) ring structure. Structures to the left and right hand sides of I represent the Co_3O_3 and Co_4O_4 face views of structure I, respectively. The number below the structures indicate the relative energies and spin multiplicities (in brackets).

total energy difference of 1.33 eV between the new global minimum structure **I** and the ring structure **III** indicates clearly the high stability of the neutral structure **I**. This is supported by the DFT energy difference of 0.93 eV between the Co_5O_5 cationic forms of the structures **I** and **III**. Accordingly, the spin-polarized DFT determined not only the neutral structure **I** as the global minimum but also successfully determined an identical compact structure for its cationic isomer. In fact, the UGA generated many of the planar-like Co_5O_5 structures, which have lower energies than the ring structure **III**. One of the energetic favorable planar-like structures shown in Figure 3.3 is structure **II**. This is in agreement with the structure obtained by a previous DFT calculation (Aguilera-del Toro

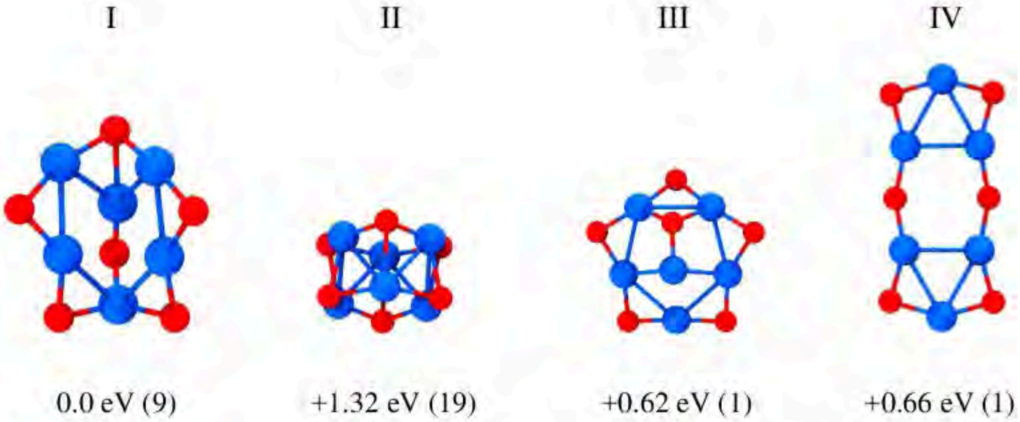

Figure 3.4: Global and local minimum structures for the Co_6O_6 cluster: (I) global minimum structure; (II) tower-like structure; (III) five-ring face structure; (IV) planar structure.

et al., 2014). The tower-like structure **II** displayed in Figure 3.4 has been typically thought as the global minimum structure of the Co_6O_6 cluster (Ota et al., 2013; Aguilera-del Toro et al., 2014). Nevertheless, the result shows a new global minimum structure **I**, which contains a composite of two planar-like faces of Co_4O_4. The two planes share the same Co_2O_2 bridge where the angle between the planes is approximately 60°. It can be considered as an "opened-book" structure (as shown in Figure 3.4) with higher stability than the suggested tower-like structure, which lies 1.32 eV lower in energy. The energetic difference between the global structures and the nearest planar-like structures increase from 0.45 eV to 0.66 eV for the Co_5O_5 and Co_6O_6 clusters, respectively. As a result,

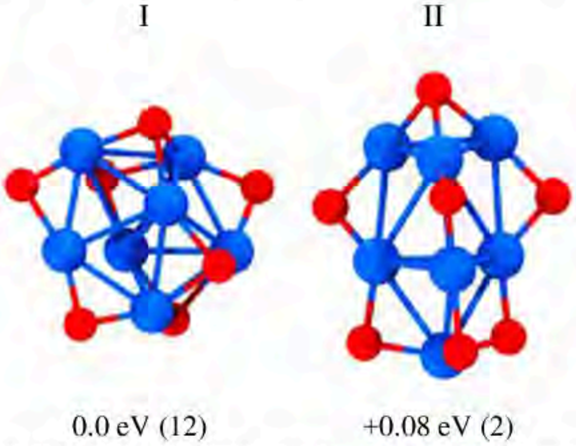

Figure 3.5: Global (left) and competitive low-lying (right) minima structures for the Co_7O_7 cluster.

the planar structures for $n > 6$ become increasingly less stable and difficult to be in the most stable form.

The calculations also generated highly compact structures for the Co_7O_7 cluster as shown in Figure 3.5. The capped octahedron structure **I** represents the global minimum. This is in agreement with the work of Aguilera et al. (Aguilera-del Toro et al., 2014). A competitive low-lying global minimum of structure **II** has three deformed faces of the Co_5O_5 cluster, differing by only 0.08 eV with structure **I**. Structure **II** has low spin multiplicity of 2, whereas, structure **I** has high spin multiplicity of 12 as obtained from the spin polarized DFT optimization.

Previous study reported that the structural transition from planar to compact structure occurs at $Co_6O_6^+$ (Ota et al., 2013). In contrast, the findings of this study reveal that the transition occurs one step earlier, i.e., at $n = 5$ for both the neutral and cationic clusters. Figure 3.6 illustrates the tendency of the planar-like structure to be a global minimum structure decreases from the Co_3O_3 to Co_7O_7 cluster. Moreover, starting from

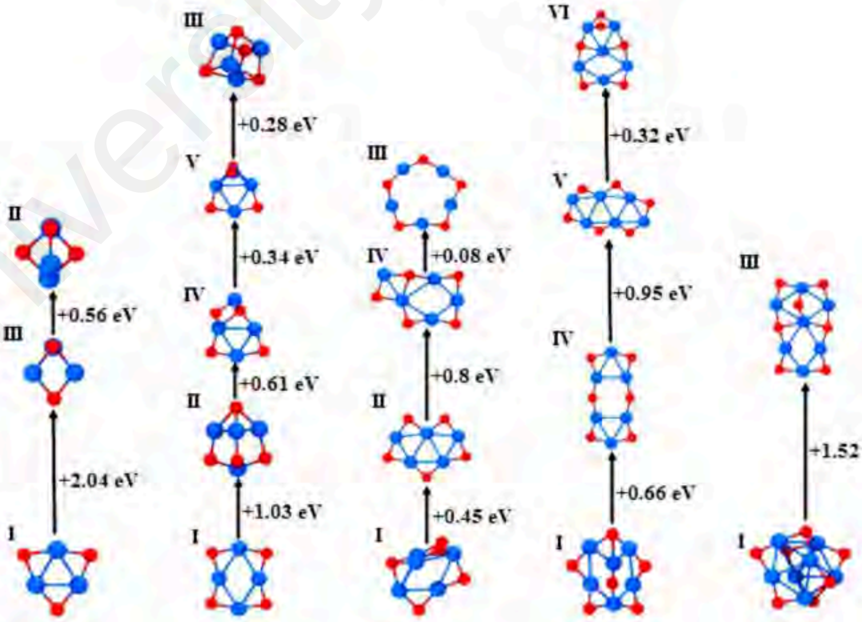

Figure 3.6: Planar-like and compact structures of Co_nO_n ($n = 3 - 7$). The global minimum structures at the bottom and the arrows pointing up the local minimum structures sequentially.

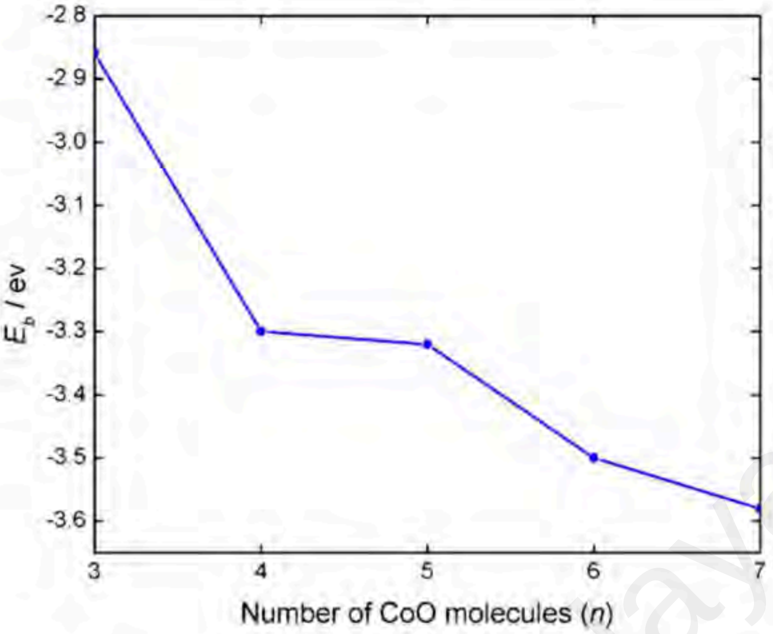

Figure 3.7: Binding energies E_b for the Co_nO_n ($n = 3 - 7$) clusters.

the Co_5O_5 cluster, the tendency towards the global minimum is dominated by compact structures, and gradually rises for larger clusters as found in the Co_6O_6 and Co_7O_7 sizes.

The relative stability of Co_nO_n clusters can be analyzed through the binding energies with higher stability associated with larger negative values. Figure 3.7 demonstrates that the binding energies are more negative with increasing number of CoO molecules. Furthermore, comparable binding energies between the two clusters, Co_4O_4 and Co_5O_5,

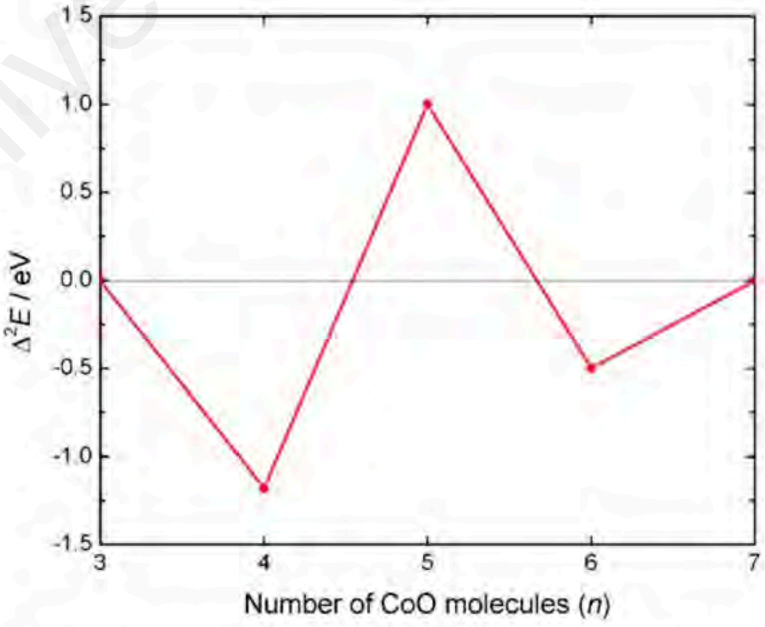

Figure 3.8: Second-order energy differences $\Delta^2 E$ for the Co_nO_n ($n = 3 - 7$) clusters.

reflect the high stability of the Co_4O_4 cluster. Additionally, the second-order total energy difference can be used to measure the stability of the Co_nO_n clusters. Figure 3.8 demonstrates that the clusters with an even number of CoO molecules, particularly, Co_4O_4 and Co_6O_6, are more stable than their odd numbered neighbor, i.e., Co_5O_5 cluster. As expected, the Co_4O_4 cluster shows the highest stability compared to other clusters.

The refinement calculations of the global minimum have also been performed for the cationic $Co_nO_n^+$ ($n = 3 - 7$) clusters by the spin polarized DFT. A limited number of local minima, either in the form of planar-like or compact structures, which must be closest to the global minimum energy were also selected for the refinement calculations. Furthermore, all of these cationic structures were constructed and calculated from the UGA optimized ones. The objective is to determine the energy difference between these two minima of the compact and planar structures ($E_{(compact)} - E_{(planar)}$) that enables one to further analyze the trend of growth mechanism with respect to the cluster size for the neutral Co_nO_n and its cationic counterpart. A large positive value indicates that the cluster tends to be in the planar global minimum and conversely for the negative value.

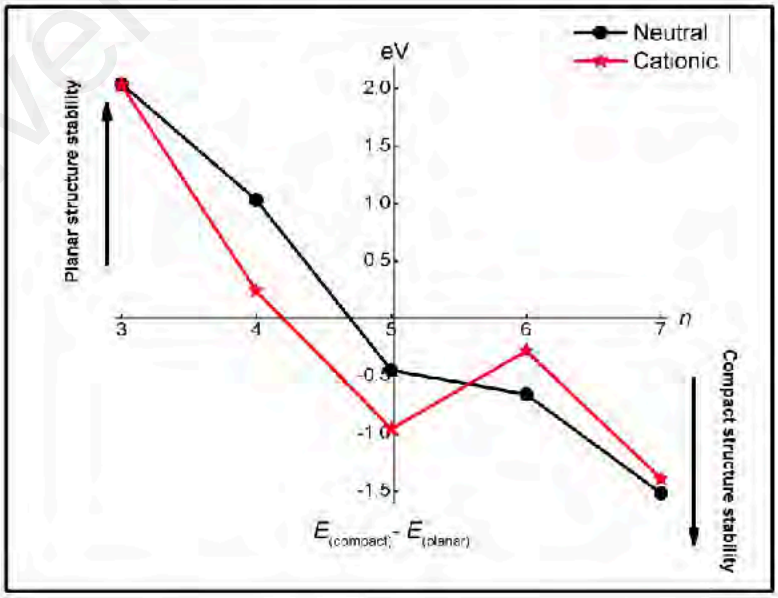

Figure 3.9: Total energy differences between the compact and planar structures of the neutral and cationic Co_nO_n clusters.

For example, Figure 3.9 shows a positive value for the neutral Co_4O_4 corresponding to the $E_{(compact)} - E_{(planar)}$ between structures **II** and **I** (as displayed in Figure 3.6), whereas the negative value for the neutral Co_5O_5 is between structures **I** and **II** (as displayed in Figure 3.6). Most interestingly, Figure 3.9 shows a similar trend between the neutral and cationic forms in the decreasing trend of $E_{(compact)} - E_{(planar)}$ with respect to the cluster size. This similarity supports the previously mentioned prediction on the new global minimum of the neutral Co_5O_5 in the compact form. Detailed comparison of the linearity of the two curves implies that the growth mechanism of the neutral Co_nO_n from planar to compact changes more markedly than the cationic Co_nO_n.

Notably, magnetic effects play a crucial role in the determination of global and local minimum structures of the clusters. For instance, the structures reported in this work have various spin multiplicities as shown in Table 4.1. In addition, a sharp structural transition has been observed in some of these clusters with respect to the changes in the spin multiplicity. Therefore, spin-polarized calculations are necessary to study the structures of Co_nO_n clusters.

3.5 Conclusion

The UGA program has been successfully implemented with multi-convergence methods combined with scaling capability of a pool genetic algorithm methodology. This genetic algorithm with DFT spin-polarized calculations allows the probing of global and local energy minimum structures of Co_nO_n ($n = 3 - 7$) clusters where some of the reported structures were observed for the first time.

The current study predicted global minimum clusters for Co_3O_3 and Co_4O_4 with both having planar-like structures, in agreement with previous results. Their structural faces were imaged in the global and local minimum structures of the larger clusters ($5 \leq n \leq 7$). The stability of the planar-like Co_4O_4 cluster was confirmed via second-order difference

($\Delta^2 E$) and binding energy (E_b) calculations and these accounted for its high yield in the fragmentation spectra of the cobalt oxide nanoparticles.

New global minimum structures for the Co_5O_5 and Co_6O_6 clusters have also been captured. Both of the structures have the Co_4O_4 cluster face, and are significantly more stable than previously proposed structures. The capped octahedron structure of Co_7O_7 was also observed. It was designated as the global minimum and is in line with recent results. The growth mechanism from planar-like to compact structures occurs at the Co_5O_5 cluster. For clusters smaller than this, the planar-like structures are observed to be the dominant global minima.

This work demonstrates that multi-convergence procedures within the genetic algorithm combined with further refinement method can be very useful in global minimization for medium-sized metal clusters, which might be computationally inefficient using first principle density functional theory. Study of a wide range of metal oxide nanoclusters will also be performed to test the capability of this methodology in probing global minimum structures.

CHAPTER 4: STRUCTURAL, ELECTRONIC AND MAGNETIC PROPERTIES OF STOICHIOMETRIC COBALT OXIDE CLUSTERS $(\mathrm{CoO})_N^{Q}$ ($N = 3 - 10$, $Q = 0, +1$): A MODIFIED BASIN-HOPPING MONTE CARLO ALGORITHM WITH DENSITY FUNCTIONAL THEORY

4.1 Introduction

Transition metal oxides (TMOs) are the key components in many applications such as heterogeneous catalysis, microelectronics, photovoltaic cells, magnetism, corrosion protection, coating for thermal applications, and other potential technological applications (Buttrey, 2006; Piccolo & Henry, 2000; Gates et al., 1992; Campbell, 1997; Renaud, 1998). Recently, great interest have been arisen in exploring the physical and chemical properties of TMOs clusters, which are affected by the interplay between the structural and electronic degrees of freedom, making them different from the properties of bulk metals and attractive in many industrial fields (Ozin, 1996).

TMOs such as cobalt(II) oxide (CoO), show a great variety of crystallographic and magnetic structures where the magnetic exchange interaction is strongly dependent on changes in the metal coordination number. The strength of the oxygen-metal bond, which is stronger than the metal-metal bond, making the CoO nanoparticles manifest an easier fabrication process compared to that of the bulk. Small clusters with a few hundred atoms can be produced by laser vaporization techniques. However, it is difficult to characterize low density of particles by means of the usual spectroscopic and crystallographic techniques (Mordi et al., 2009).

Several modeling approaches aim to identify such relevant cluster isomers, including the global and local exploration of the vast configuration space represented by the high-dimensional potential-energy surface (PES). Thus, it is of fundamental interest to identify the global minimum of the cluster structures, which constitute the most stable isomers at T = 0 K. However, energetically higher-lying and also metastable isomers might be observed in experiments due to finite temperature and kinetic effects. Density-functional theory represents a suitable compromise between accuracy and computational demand, and this is the technique employed in the present work to explore the PES.

On the other hand, schemes to explore large configuration space with the local information of a current configuration are necessary to adequately sample the PES and finally identify the local and global minima. Current sampling approaches of global optimization are simulated annealing, basin-hopping and genetic algorithms. Simulated annealing scheme is based upon the Metropolis algorithm (Metropolis et al., 1953), and the basin-hopping method is the simulated annealing method applied to local minima and was invented by Wales and Doye (Wales & Doye, 1997). In this method, Potential Energy Surface (PES) is transformed into a sequence of "interpenetrating staircases" where each plateau corresponds to a local minimum. Contrary to the basin-hopping scheme, the starting point in genetic algorithm is a population of randomly generated cluster structures instead of a single initial configuration. New cluster structures are typically generated by randomly choosing two high-fitness candidates, i.e., the parent structures of the current population, which are then mated to create a child (Deaven & Ho, 1995). Beside using these basic schemes to explore the varieties of PESs, there have been attempts to improve their performance in searching the global minimum structures. In the latter direction, Rondina and Da Silva (2013) have recently suggested a new scheme to improve basin-hopping, where the success of this scheme allows efficient implementation of both local and non-local trial operators within the simplicity of the basin-hopping framework as well as to apply a static and a dynamic approach to deal with the acceptance rate of different trial operators. However, the performance of the various schemes and their modifications can strongly depend upon both the actual system under consideration and upon the huge number of involved technical parameters, e.g. the special type of move performed in the random move scheme.

4.2 Literature Review

Density functional theory (DFT) calculations combined with experiment have been used to determine the geometric structure and the vibrational properties of the low-lying energy isomers of small $(CoO)_n$ clusters (Uzunova et al., 2002; Xie et al., 2010; Harding & Fielicke, 2014). In contrast to the bulk CoO material, which exhibit antiferromagnetic (AFM) behavior, theoretical and experimental results showed ferromagnetic (FM) characteristics for small $(CoO)_n$ clusters (Tamuliene et al., 2009; He et al., 2015; Ghosh et al., 2005; Dutta et al., 2008). Another experimental study using ion mobility–mass spectrometry and supported by DFT calculations suggested that $(CoO)_{3\text{-}5}^+$ exhibit ring-like structures, whereas $(CoO)_{6\text{-}7}^+$ show a compact tower-like structure (Ota et al., 2013). Recently, a pure ab-initio calculation of the neutral Co_2O_2 cluster has shown a planar ring structure only for the high-spin configuration with multiplicity equal to 7 (Uzunova & Mikosch, 2012). In addition, both binding energy and second energy difference calculations of $Co_nO_m^{0/+}$ ($n = 3 - 8, m = 1 - 10$) show that the stability of stoichiometric oxide clusters ($n = m$) tends to be significantly higher than the corresponding non-stoichiometric clusters (Aguilera-del Toro et al., 2014), which is in line with the recent dissociation experiment of cobalt oxide cluster (Dibble et al., 2012). Both computational and experimental investigations revealed that the preferred dissociation channel for $Co_nO_m^+$ clusters to form stoichiometric $Co_nO_n^+$ clusters is the loss of oxygen molecules (Dibble et al., 2012). Therefore, it is reasonable to expect that the dominant fragmentation channel for $Co_nO_n^{0/+}$ clusters is loss of CoO molecules in order to give the smaller stoichiometric cluster of $Co_nO_n^{0/+}$.

Recently, Luo et al. (2014) have computationally demonstrated how the structures of cobalt oxide clusters are changed by adding a ligand, in particular, the transformation from ring into cubic structures for catalytic $(CoO)_4$ cluster when bonded with MeCN.

They have also shown that the bare $(CoO)_4$ cluster has a ring structure, agreeing well with the previous study (Aguilera-del Toro et al., 2014), while the cluster bonded with MeCN ligand favors the cubic structure. This study highlights the importance of exploring the electronic and magnetic properties of $(CoO)_4$ structures in different cases as a promising catalyst. In the same spirit, the $(CoO)_4^{0/+}$ clusters are found to be most abundant in the mass spectrum of $Co_nO_m^{0/+}$, making this cluster size to be considered as a magic number in the fragmentation spectrum, which clearly indicates its high stability (Dibble et al., 2012; Xie et al., 2010). Despite the importance of $(CoO)_4$ in catalytic reactions, very few computational works, to the best of our knowledge, have fully investigated the energetics, and electronic and magnetic properties of $(CoO)_4$.

The study of geometric and electronic structures of M_9O_6 (M= Co, Fe, and Ni) have been carried out by Sun et al. (2000). Three obvious peaks have been found in the total density of state (DOS) diagrams of these three clusters, which are mainly formed by 3d-M, 2p-O, and 2s-O orbitals. The 3d-M orbitals are much higher than 2s-O orbitals, whereas the main interactions between O and M involve the 2p-O and 3d-M orbitals. The 2p-3d hybridization is increased between O and M atoms from Fe to Co to Ni, which in turn affects their stability and magnetic behaviors. For example, the 2p-3d hybridization is very strong in the case of Ni, due to the energy of d level becoming extremely close to the 2p-O orbital, causing the magnetic moments of Ni atoms to drastically reduce close to zero ($0.147\mu_\beta$) compared to Co and Fe atoms. Not only the Co and Fe atoms have considerable magnetic moments, but the O atoms are also ferromagnetically polarized with respect to the direction of the alignment of the adjacent metal atoms.

In this work, we have applied a modified basin-hopping Monte Carlo algorithm with DFT calculations to investigate the structural, electronic and magnetic properties of stoichiometric cobalt oxide clusters CoO_n^q ($n = 3 - 10, q = 0, +1$). The basin-hopping

Monte Carlo algorithm was modified to generate a wide scale atomic displacement far from the previous minimum structure to more effectively determine the global minimum structures. It is designed on the basis of the previous work of Rondina and Da Silva (2013), in which a couple of trial operators are used (one being local and the other non-local), as well as the static approach to treat the acceptance rate. For each CoO cluster size, the most stable structure was identified and compared with previous investigations. The structural stabilities of neutral and cationic CoO clusters are explained by the results of binding energy, second-order total energy difference, chemical hardness, chemical potential and HOMO-LUMO gap. In more detail, we have also investigated the electronic structure, the band structures (including the total density and partial density of states), magnetic properties and spatial symmetry of the most stable clusters, i.e. $CoO_4^{0/+}$.

4.3 Methodology

4.3.1 Modified Basin-Hopping Monte Carlo Algorithm (MBHMC)

Basin-hopping Monte Carlo algorithm (BHMC) is used to explore the optimum structures of a wide variety of clusters. This can be achieved by transforming a PES into the energy landscape consisting of basins representing a set of energy minima (Tsai & Jordan, 1993; Wales & Doye, 1997; Wales & Scheraga, 1999; Doye & Wales, 2002), expressed mathematically as

$$\tilde{E}_{total}(\{R\}) = min[E_{total}(\{R\})]$$

Once the new structures, which may be considered as points on the original PES (denoted by $E_{total}(\{R\})$), are randomly generated by atomic movements and fulfill the Metropolis criterion, the minimization process is carried out to transform the original PES into basins

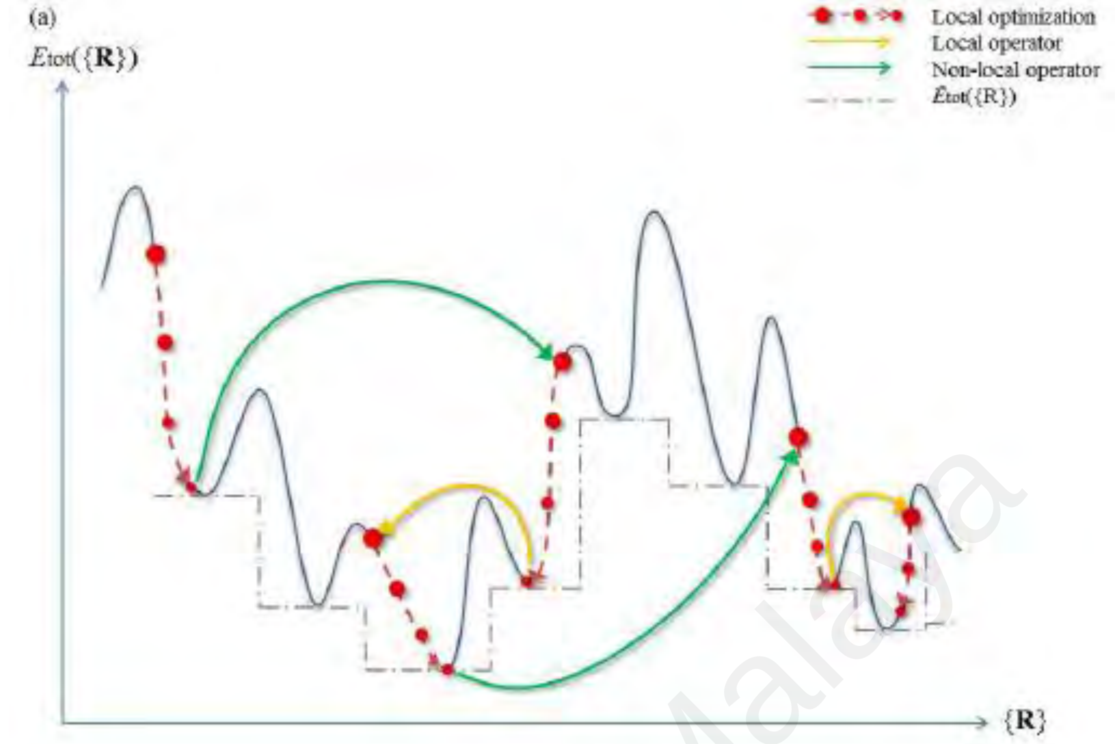

Figure 4.1: The probing of the PES is carried out by using local (solid golden arrows) and non-local (solid green arrows) trial operators together with local optimization (ball-dashed red lines) to transform the PES into basins of energy landscape.

of energy landscape, as shown in Figure 4.1. To achieve this transformation with respect to atomic positions ($\{R\} = r_1, r_2, ..., r_N$), many local optimization algorithms can be used, such as limited-memory Broyden-Fletcher-Goldfarb-Shanno (L-BFGS) (Liu & Nocedal, 1989), conjugate-gradient (Bulger, 2005), steepest-descent (Strodel & Wales, 2008), etc.

A revised or Modified Basin-Hopping Monte Carlo (MBHMC) algorithm has been recently proposed to improve the ability of BHMC to explore in a fast and effective manner the various PES regions (Rossi & Ferrando, 2009; Rondina & Da Silva, 2013). The main difference between these techniques is related to the diversity of structures generated by the trial operators. For example, most of the standard BHMC technique employs a simple trial operator to generate different configurations not far from the previous minimum structures, while the MBHMC uses several trial operators to produce a wide scale of atomic displacement. Therefore, MBHMC generates new configurations with different range of similarity from the former structures, which enhances the capability of BHMC to find the global and nearest local minimum energy structures (Rondina & Da Silva, 2013). Due to the high computational cost of DFT calculations, an efficient MBHMC approach aims to reduce its total number of optimization steps performed by using DFT-based method. This can be achieved through a set of trial operators able to fully explore the PESs of the studied clusters.

Our design of MBHMC exploits the multi-convergence methods available in python libraries, such as L-BFGS and DFT code based on the projector-augmented wave (PAW) method of orbital based (LCAO) or grid based (GB) on real grid space, which are implemented in the Atomic Simulation Environment (ASE) (Bahn & Jacobsen, 2002) and the Grid-based Projector Augmented Wave (GPAW) (Enkovaara et al., 2010; Mortensen et al., 2005) programs. In this work, the local minimization is carried out using non-spin calculation with zeta-polarized (DZP) basis set. L-BFGS optimizer is applied until all the atomic forces are below 0.05 eV/Å. The Structured Query Language (SQL) have been employed to facilitate the storage and acquisition the energetic and geometric data across the MBHMC parts.

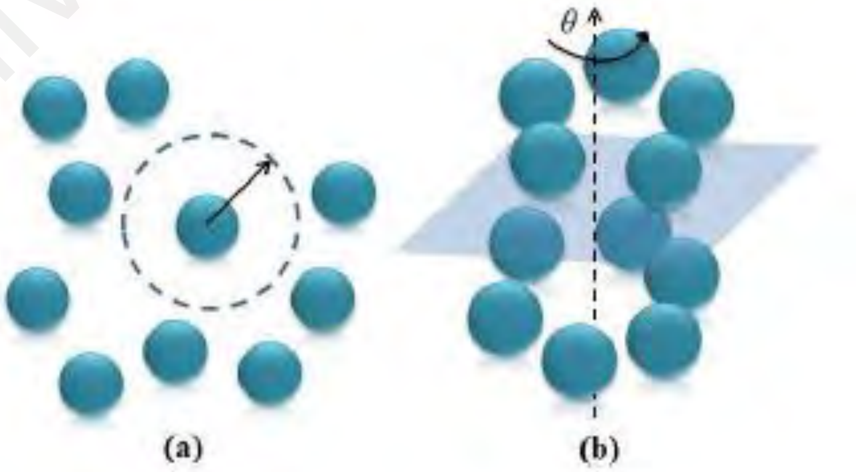

Figure 4.2: Operators used in MBHMC code. (a) Single move operator (local). (b) Twist operator (non-local).

Figure 4.2 shows the single move operator (local) and the twist operator (non-local) as described in references 27 and 20, respectively. Both operators are performed sequentially after DFT optimization of a random initial structure. Combination of these trial operators enable one to probe different regions of the PES. The local operator explores the current vicinity of the PES, while the non-local one discovers a new region of PES. For the single move operator, Δr=1.0, 0.8 and 0.6 Å are defined separately as the maximum radius of the spherical displacement (refer Figure 4.2a). A constant temperature (T = 5000 K) Boltzmann weight ($e^{-\Delta E/KT}$) is applied with the Metropolis criterion. The static scheme, which was recently proposed by Rondina and Silva (Rondina & Da Silva, 2013), is used to avoid the difficulty in energy scaling, due to variation in the structural geometry by using different operators, which in turn caused a controlling problem in the acceptance rate of Metropolis criterion. In this scheme, each of two operators is used sequentially in a way that one of the operators is launched when the other one is halted after a certain number of steps. This allows the acceptance rate of Metropolis criterion to recognize both operators efficiently to yield lower energy structures. For the present work, the local operator stops after 10 steps and waits until 20 steps of the non-local operator are finished before starting again. However, the total number of MBHMC steps varies with the cluster size and is set to 2000 and 3000 for smaller ($3 \leq n < 7$) and larger ($7 < n \leq 10$) clusters, respectively.

4.3.2 Refinements

Spin-polarized DFT calculations are performed for the optimized structures using the VASP code(Kresse & Furthmüller, 1996b; Kresse & Furthmüller, 1996a; Kresse & Hafner, 1993) with the PAW (Kresse & Joubert, 1999; Blöchl, 1994) pseudopotentials for Co ($3d^8 4s^1$) and for O ($2s^2 2p^4$), in which the electronic correlation function is treated using the generalized-gradient approximation of Perdew, Burke, and Ernzerhof (1996).

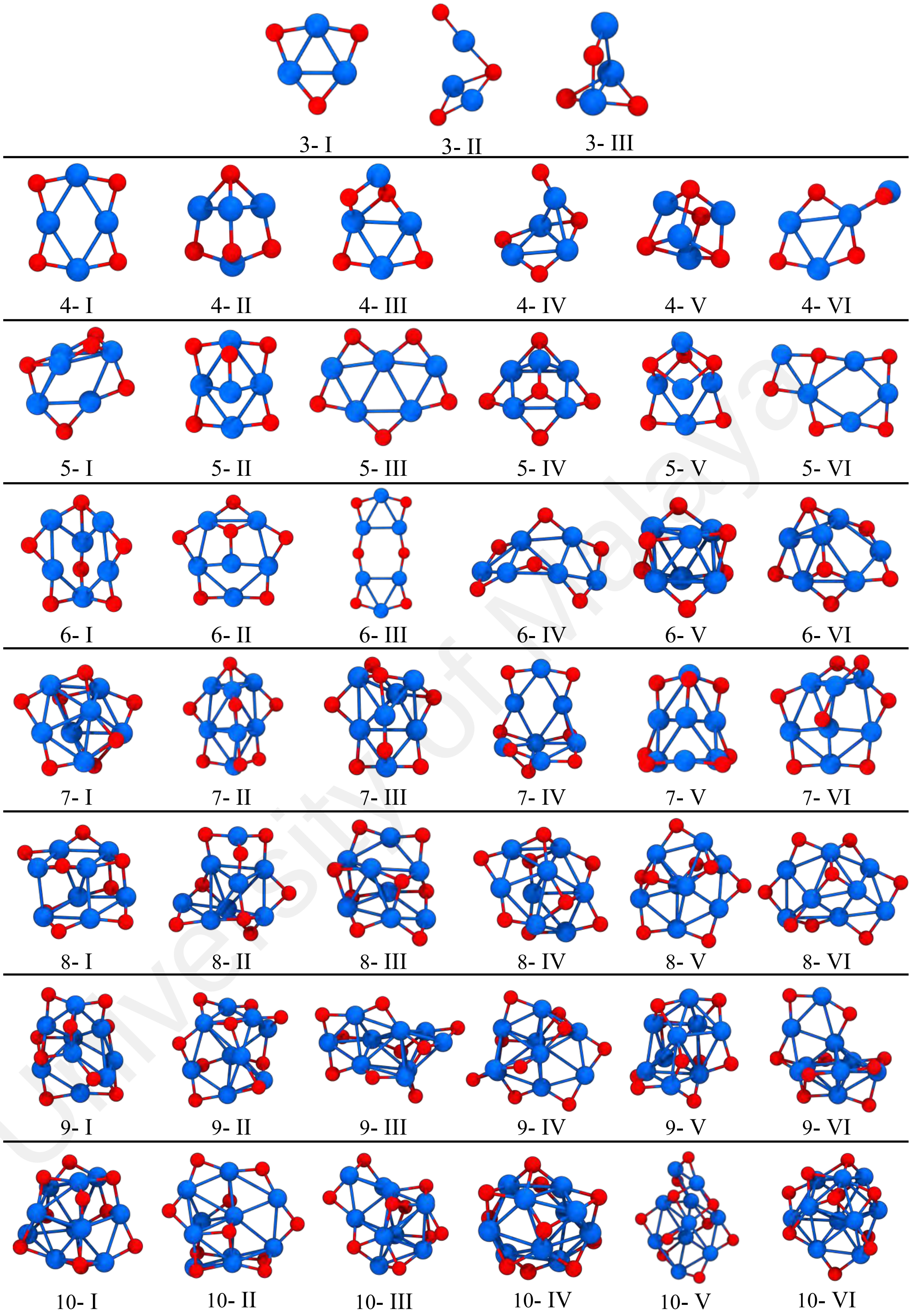

Figure 4.3: Putative global and low-lying minimum energy structures of $(CoO)_n$ (n = 3 − 10) clusters. The red and blue colors represent oxygen and cobalt atoms, respectively.

The wave functions are expanded in a plane-wave basis set with a cutoff of 400 eV.

Calculation on individual cluster is done at the Gamma-point ($k = 0$) in a large cubic cell ($20 \times 20 \times 20$ Å^3), which is large enough to avoid interactions between neighboring cell images. The atomic relaxation is carried out until the interatomic forces are less than 0.001 eV/Å. To study in great detail the nature of molecular orbitals and density of state for two selected clusters, namely $(CoO)_4$ and $(CoO)_4^+$, hybrid DFT-B3LYP calculations are performed with 6-311G++(d,p) basis set using Gaussian 09 program (Frisch et al., 2009).

4.4 Results and Discussion

In this section, we will present in detail the geometrical structures of the $(CoO)_n^{0/+}$ ($n = 3 - 10$) clusters and the electronic and magnetic properties. Figure 4.3 shows the putative global and local minimum energy structures for different cluster sizes (n), designated by I, II, III,... in decreasing binding energies. Some of these structures have been successfully probed by previous theoretical and experimental studies (Yin et al., 2009; Aguilera-del Toro et al., 2014; Dijk et al., 2014).

The binding energies (E_b) and second-order total energy differences ($\Delta^2 E$)) of the $(CoO)_n^{0/+}$ clusters presented in Table.4.1 and Figure 4.5 are calculated per CoO molecule via equations

$$E_b = \frac{1}{n}\,[(n-1)\,E(CoO) + E(CoO)^q - E(CoO)_n^q] \tag{4.1}$$

$$\Delta^2 E = E(CoO)_{n+1}^q + E(CoO)_{n-1}^q - 2\,E(CoO)_n^q \tag{4.2}$$

where n is the number of CoO molecules in the cluster and the total energies of the cluster and its nearest neighbors are determined by $E(CoO)_n^q$, $E(CoO)_{n+1}^q$ and $E(CoO)_{n-1}^q$ respectively.

Table 4.1: Binding energy (E_b/eV), magnetic moment (μ) [Bohr magnetons (μ_β)], adiabatic ionization potential (V IP/eV) and HOMO-LUMO energy gap (ΔE_{H-L} /eV) of the neutral and cationic $(CoO)_n^q$ (n = 3 − 10, q = 0, +1) clusters.

		Neutral/Cation			
Cluster	**Point group**	E_b	μ	*VIP*	ΔE_{H-L}
3-I	C_{2v}	2.86/3.08	3/2	7.13	0.30/0.23
3-II	C_s	2.18/2.41	1/4	7.12	0.08/0.21
3-III	C_s	1.99/2.48	7/8	6.34	0.14/0.19
4-I	C_{2v}/D_{2h}	3.30/3.27	0/1	7.89	0.63/0.42
4-II	C_{3v}	3.04/3.26	6/9	6.92	0.10/0.28
4-III	C_1	2.88/3.06	8/1	7.09	0.37/0.39
4-IV	C_s	2.80/3.00	0/1	6.99	0.26/0.19
4-V	T_d	2.73/3.09	12/13	6.34	0.44/0.08
4-VI	C_s	2.61/3.00	8/7	6.25	0.14/0.11
5-I	C_s	3.32/3.48	3/4	7.01	0.16/0.18
5-II	C_s	3.25/3.44	5/0	6.85	0.03/0.02
5-III	C_s	3.23/3.39	1/2	6.98	0.05/0.20
5-IV	C_s	3.17/3.41	11/2	6.61	0.19/0.20
5-V	C_s	3.08/3.35	15/2	6.42	0.35/0.19
5-VI	C_s	3.07/3.28	11/4	6.77	0.17/0.17
6-I	C_1	3.50/3.65	8/9	6.94	0.32/0.21
6-II	C_s	3.40/3.54	0/1	6.99	0.22/0.15
6-III	C_{2v}/D_{2h}	3.40/3.60	0/1	6.57	0.18/0.10
6-IV	C_2	3.36/3.53	0/1	6.80	0.15/0.10
6-V	C_{2h}	3.35/3.57	2/1	6.44	0.20/0.21
6-VI	C_1	3.34/3.51	14/15	6.78	0.19/0.20
7-I	C_s	3.58/3.77	11/4	6.48	0.28/0.12
7-II	C_1	3.57/3.76	1/4	6.42	0.07/0.11
7-III	C_1	3.55/3.72	7/6	6.58	0.16/0.21
7-IV	C_1	3.53/3.70	17/2	6.57	0.23/0.10
7-V	C_s	3.52/3.66	11/0	6.85	0.24/0.23
7-VI	C_1	3.48/3.59	7/6	7.04	0.21/0.03
8-I	C_2	3.64/3.79	0/1	6.57	0.15/0.14
8-II	C_1	3.62/3.76	8/7	6.66	0.24/0.14
8-III	C_1	3.60/3.76	10/5	6.56	0.26/0.18
8-IV	C_1	3.59/3.74	8/9	6.60	0.16/0.17
8-V	C_1	3.59/3.74	2/3	6.66	0.18/0.12
8-VI	C_1	3.51/3.65	10/7	6.71	0.20/0.03
9-I	C_1	3.69/3.84	13/12	6.44	0.38/0.22
9-II	C_1	3.66/3.80	7/6	6.55	0.14/0.16
9-III	C_1	3.65/3.77	3/14	6.77	0.26/0.10
9-IV	C_1	3.62/3.76	11/0	6.54	0.13/0.12
9-V	C_1	3.61/3.76	15/0	6.48	0.14/0.17
9-VI	C_s	3.58/3.72	13/2	6.53	0.13/0.18
10-I	C_1	3.69/3.85	16/13	6.24	0.18/0.15
10-II	C_1	3.64/3.80	4/3	6.21	0.04/0.13
10-III	C_s	3.63/3.79	4/1	6.18	0.23/0.17
10-IV	C_1	3.61/3.78	4/5	6.11	0.04/0.13
10-V	C_1	3.60/3.75	16/3	6.22	0.04/0.13
10-VI	C_1	3.58/3.73	10/15	6.30	0.01/0.22

4.4.1 Geometrical structures

The binding energies in Table 4.1 show that the putative global minima of the $(CoO)_3^{0/+}$ and $(CoO)_4^{0/+}$ clusters have the planar-like structures 3-I and 4-I (as shown in Figure 4.3), and have successfully reproduced the results obtained previously by DFT calculations (Dijk et al., 2014; Aguilera-del Toro et al., 2014). These planar structures have higher stability than their nearest local minimum structures, namely 3-II and 4-II. Interestingly, the 4-I cation structure has D_{2h} symmetry, which considerably differs from the corresponding neutral one with C_{2v} symmetry. However, this nearly agrees to the D_{4h} symmetry of ring structure that has been proposed recently (Ota et al., 2013; Aguilera-del Toro et al., 2014). It will be discussed later that the global minima 4-I of both $(CoO)_4$ and $(CoO)_4^+$ with C_{2v} and D_{2h} symmetries, respectively, display structural modulation associated with different spin states, which may play a substantial role in determining the energetic stability of these clusters.

The planarity of the global minima structure begins to change at $(CoO)_5^{0/+}$ and for clusters with $n \geq 5$, compact structures become dominantly the global minima. Basically, the compact global minimum structures are composite of the smaller clusters. For instance, 5-I and 6-I structures for both neutral and cationic clusters are characterized by the two-dimensional $(CoO)_4$ plane, i.e., the 5-I structure is a composite of a CoO molecule with the $(CoO)_4$ cluster, whereas the 6-I structure is formed from the two bonded planar-like faces of $(CoO)_4$. It is also important to note that for the global minima clusters with $n \leq 6$, the number of metal-metal bond increases monotonically with n but still clearly countable.

For clusters with $n \geq 7$, the compact global minima are mainly characterized by a relatively large number of metal-metal bonds per n, making these clusters possess less

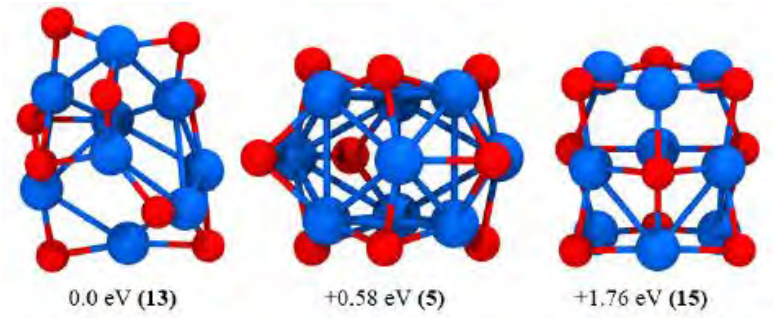

Figure 4.4: Putative global minimum structure (left), cage structure (middle) and tower structure (right) with relative energies and magnetic moments (in brackets).

distinguishable structures. On the other hand, the average of the Co-Co bond length elongate significantly due to increase in the number of bonds between Co and O atoms, in line with a previous report (Tamuliene et al., 2009). However, the putative global minima for $(CoO)_7{}^{0/+}$ is a capped octahedral structure 7-I that displays face deformation of C2v symmetry of both $(CoO)_4$ and $(CoO)_3$ clusters. Meanwhile, the putative global minima structure $(CoO)_8^{0/+}$ is a composite of two planar-like $(CoO)_4$ clusters. These two 4-I planes can be regarded as sub-clusters and can be viewed from the upper and bottom of structure 8-I, which is parallel to each other, The average length of Co-Co bond between the two $(CoO)_4$ sub-clusters is 0.12 Å longer than the Co-Co bond within the $(CoO)_4$.

The tendency to form Co-Co bonds increases as $n \geq 9$. Consequently, a planar-like structure becomes more unfavorable to be formed. The complexity of the structures $(CoO)_9^{0/+}$ and $(CoO)_{10}^{0/+}$ are indicated from the appearance of the lowest symmetry C_1 for most of its energy minimum structures. Our calculations reveal that structure 9-I is more stable than those previously observed structures. For example, the cage and tower structures have been recently suggested by Ge and coworkers (Yin et al., 2009) lying 0.58 and 1.76 eV higher than our predicted putative global minimum energies. Figure 4.4 show the respective new putative global minimum structure for the $(CoO)_9^{0/+}$ clusters compared to the cage and tower structures.

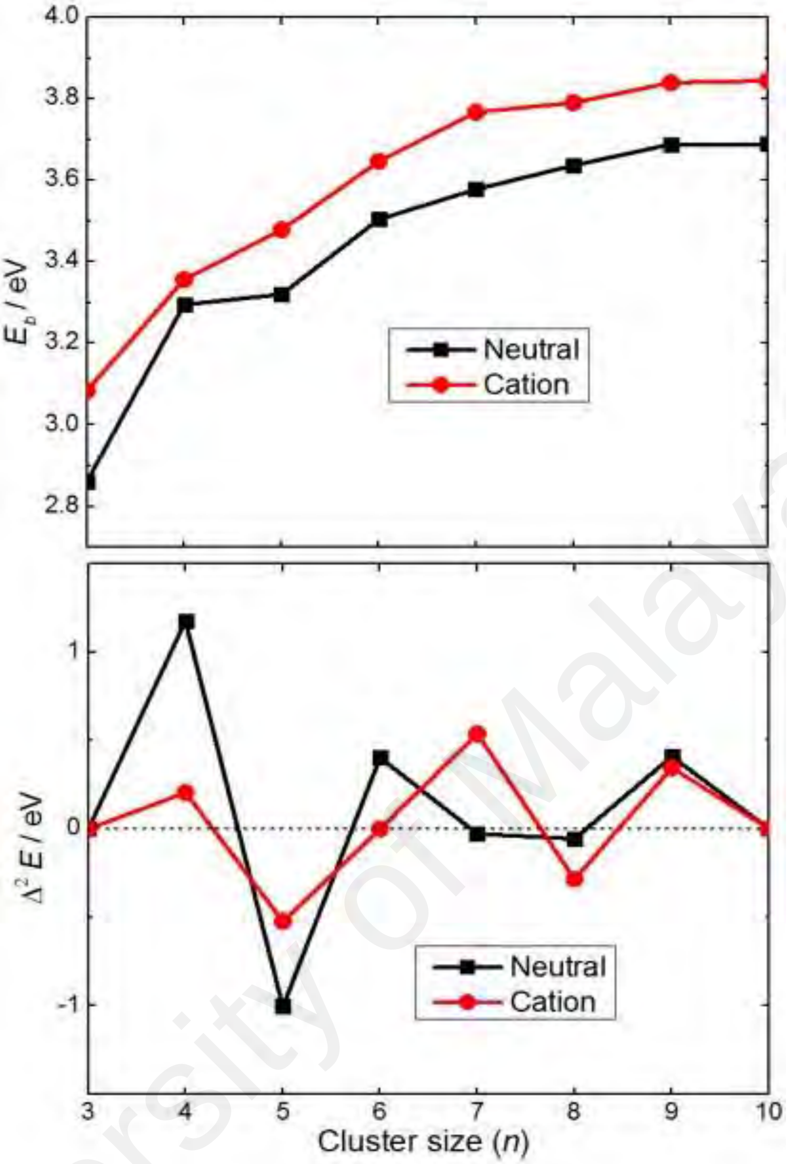

Figure 4.5: Binding energy (upper panel) and second order total energy difference (lower panel) per CoO molecule for $(CoO)_n^q$ ($n = 3 - 10, q = 0, +$) clusters.

4.4.2 Structural stability and electronic properties

The binding energy (E_b) and the second-order total energy difference (ΔE^2) provide information about the stability of clusters and their possibility to reach the mass spectrometer detector. Figure 4.5 shows the binding energies and the second-order total energy differences for the most stable structures *n*-I of neutral and cationic cobalt oxide clusters.

In general, the binding energy increases monotonically with growth of cluster size *n*, as observed for $(FeO)_n$ and $(ZnO)_n$ (Ju et al., 2015; Wang et al., 2007). Noticeably, the binding energies of $(CoO)_n^+$ are larger than those of the corresponding neutral species and this is consistent with recent reported DFT study (Aguilera-del Toro et al., 2014). Furthermore, the comparable binding energy of $(CoO)_4$ with those of $(CoO)_4^+$ and $(CoO)_5$ clusters indicates the high stability of $(CoO)_4$. This can be readily seen from the second-order total energy difference shown at the lower panel of Figure 4.5 where the largest positive value of $(CoO)_4$ indicates its highest stability that is in agreement with mass spectrometry observations (Xie et al., 2010). This figure also displays the stability of $(CoO)_4^+$ agreeing well with previous results (Aguilera-del Toro et al., 2014; Dibble et al., 2012; Ota et al., 2013), whereas the $(CoO)_5^{0/+}$ have the most unstable clusters. These results, particularly, the stability of $(CoO)_4$ cluster are supported by the results of chemical hardness (η) and chemical potential (μ) as shown in Table 4.2. Conventionally, it can be derived from vertical ionization potential (VIP) and vertical electron affinity (VEA) through the finite difference approximations, expressed as, $\eta = (VIP - VEA)/2$ and $\mu = -(VIP + VEA)/2$. High positive value of η and negative value of μ indicate low reactivity of the cluster which indicates the high stability of the cluster. Therefore, the neutral $(CoO)_4$ cluster exhibits largest positive (2.01 eV) and negative (-5.88 eV) values

Table 4.2: Vertical ionization potential (VIP/eV), vertical electronic affinity (VEA/eV), chemical hardness (η/eV) and chemical potential (μ/eV) for the putative global minimum structures of neutral $(CoO)_n$ ($n = 3 - 10$) clusters.

N	VIP	VEA	H	μ
3	7.13	3.27	1.93	-5.20
4	7.89	3.86	2.01	-5.88
5	6.59	3.26	1.66	-4.92
6	7.10	4.06	1.52	-5.58
7	6.93	3.52	1.70	-5.22
8	6.51	4.13	1.19	-5.32
9	6.55	4.17	1.19	-5.36
10	6.25	4.15	1.05	-5.20

for η and μ, respectively, implying the highest stability of $(CoO)_4$ over the rest of the clusters considered in this work.

The HOMO-LUMO energy gaps (ΔE_{H-L}) provide further information on the feasibility of the cluster to participate in chemical reactions. The HOMO-LUMO gaps for the global minimum structures of $(CoO)_n^{0/+}$ ($n = 3-10$) clusters are listed in Table 4.1 and plotted against cluster size n in Figure 4.6. The larger the HOMO-LUMO gap is the more stable is the cluster. Apparently, the HOMO-LUMO gaps of the neutral clusters are larger than those of the corresponding cation, except for $n = 5$. The HOMO-LUMO gaps for the $(CoO)_4^{0/+}$ clusters have maximum values, 0.63 eV and 0.42 eV, respectively, confirming the stability of $(CoO)_4$ over the rest of the clusters. However, the GGA calculations generally underestimates the HOMO-LUMO gap by 40% compared to the true value (Kumar & Kawazoe, 2003) and hence, appropriately used for the comparison purpose only.

Figure 4.7 shows the two highest occupied (HOMO and HOMO-1) and two lowest unoccupied (LUMO and LUMO+1) molecular orbitals of the relatively stable $(CoO)_4$

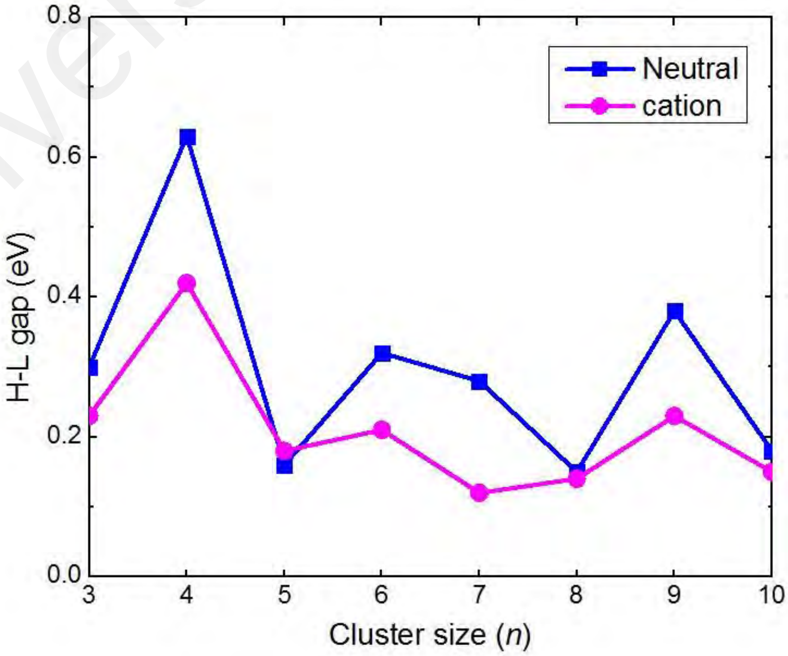

Figure 4.6: HOMO-LUMO energy gap (H-L gap) for putative global minimum structures of $(CoO)_n^q$ ($n = 3-10, q = 0,+$) clusters.

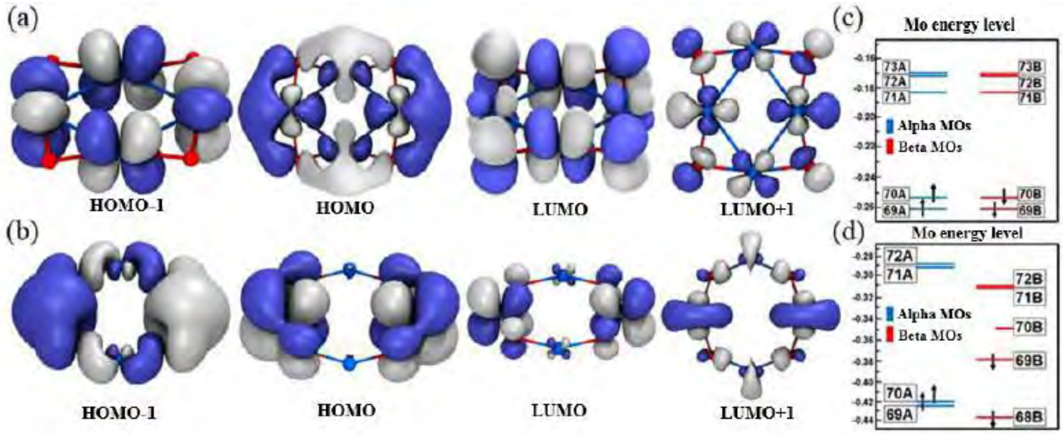

Figure 4.7: Calculated MOs and its energy diagrams of: (a) and (c) neutral $(CoO)_4$ cluster with C_{2v} symmetry; (b) and (d) cationic $(CoO)_4^+$ cluster with D_{2h} symmetry.

and $(CoO)_4^+$ clusters. The right hand side of the orbitals are the energy diagrams for the HOMO and LUMO. As can be seen in Figure 4.7(a), electrons in the HOMO of $(CoO)_4$ cluster are delocalized over the entire ring, arising from the in-plane π interactions between 3*d* orbitals of Co atoms with 2*p* orbitals of adjacent O atoms to form stable build-up electron densities of hybrid *pd*-like orbitals. The HOMO-1 is featured by the localized 3*d* orbitals without any appreciable contribution from 2*p* orbitals of O atoms. On the other hand, the LUMO and LUMO+1 orbitals arise from out-of- and in-plane π^* interactions between Co 3*d* and O 2*p* orbitals to form less stable antibonding orbitals. The same delocalization and localization can also be seen in Figure 4.7(b) for HOMO and LUMO of $(CoO)_4^+$ cluster, respectively, as a result of the interactions between Co 3*d* and O 2*p* orbitals. However, the HOMO of $(CoO)_4^+$ cluster is featured by the build-up of electron densities of π interactions around two opposite Co atoms only, whereby the other two Co 3*d* orbitals have zero overlap with the adjacent O 2*p* orbitals, creating the nodes of electron density in the cluster ring.

Detailed inspection of the energy level shown in Figure 4.7(c) reveals that the delocalization of $(CoO)_4$ is closely related to the spin degeneracy of energy levels. After removing one electron from a $(CoO)_4$ cluster as shown in Figure 4.7(d), α and

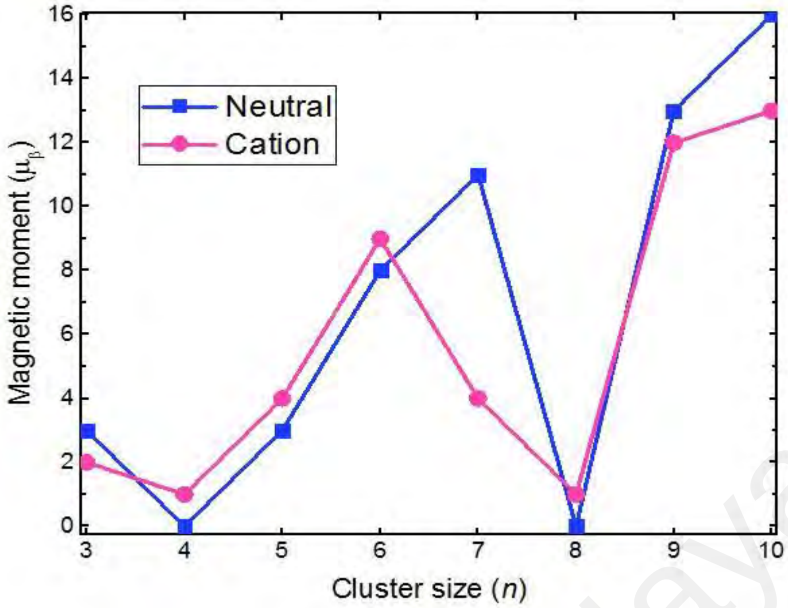

Figure 4.8: Spin magnetic moments for putative global minimum structures of $(CoO)_n^q$ (n = 3 − 10, q = 0, +) clusters.

β states are no longer degenerated, in which the HOMO and LUMO of the $(CoO)_4^+$ are close in energy. Consequently, the average HOMO-LUMO gap of the $(CoO)_4^+$ cluster is reduced compared to the neutral $(CoO)_4$ cluster.

4.4.3 Magnetic property

Clusters containing magnetic Co are ferromagnetic, having large spin magnetic moments because of the parallel spin alignment of unpaired electrons in 3*d* Co orbitals. The presence of non-magnetic oxygen reduces the magnetic moments of the cluster by increasing the number of paired electrons, due to a direct electron exchange between 2*p* O and 3*d* Co orbitals. This can be visualized as in Figure 4.7, where the relevant molecular orbitals are a result of d-p orbital interaction between these atomic orbitals.

The magnetic moments for the putative global minimum structures of $(CoO)_n^{0/+}$ (n = 3 − 10) clusters are presented in Figure 4.8 and for all clusters are listed in Table.4.1. In general, the spin magnetic moments of the putative global minima oscillate between 0 to 16. Except for larger clusters (n=9 and 10), these magnetic moments are all located in low-spin state relative to the maximum magnetic moments possible for each cluster size.

Similar results of oscillation were found for the analogous clusters of $(FeO)_n^{0/+}$ (Wang et al., 2007). As expected, the putative global minima of $(CoO)_4$ and $(CoO)_8$ clusters exhibit a fully antiferromagnetic ordering where the singlet state is the most energetically favored. Their magnetic similarity could be closely attributed to the structural and electronic properties of both clusters. However, by removing one electron, the magnetic moments increase by one unit for their cationic counterparts $(CoO^+)_4$ and $(CoO)_8^+$.

Low-spin configuration is mainly due to antiparallel coupling of spins from *d* orbitals of various Co atoms. On the other hand, the corresponding parallel couplings and the magnetic contribution of the oxygen atoms yield the appearance of high-spin configuration. Accordingly, the local magnetic moment of Co and O atoms are closely related to the magnetic environment of their neighboring atoms and each local magnetic contribution to the overall moment can be quantified. For example, the magnetic moments of $(CoO)_6^+$ and $(CoO)_7$ in Figure 4.8 associated with all O atoms are 12.3% and 10.5% of the total magnetic moments, respectively. This local magnetic moment of O can reach up to 0.65 in high-spin configuration of larger clusters. It will be seen later how different spin configuration of the Co atoms create somewhat different magnetic environment to their nearest O atom. Meanwhile, the local magnetic moments for Co in cluster can generally reduce from 2.66 to 1.52 because of the strong hybridization of the *d* orbitals, which occurs when the Co-Co bond contracts. The value of 2.66 is comparable to that observed in bulk CoO, where the magnetic moment of Co is 2.77 (Archer et al., 2008).

In particular, Figure 4.9 shows bond lengths and local magnetic moments of Co and O atoms in various magnetic spin alignments of the most abundant cluster $(CoO)_4$, where (a) and (b) configurations represent two possible antiferromagnetic spin orderings, while the (c) configuration represents a ferromagnetic spin ordering. Clearly, the Co-Co bond length in (a) is 0.16 Å shorter than in (c), indicating a strong hybridization between

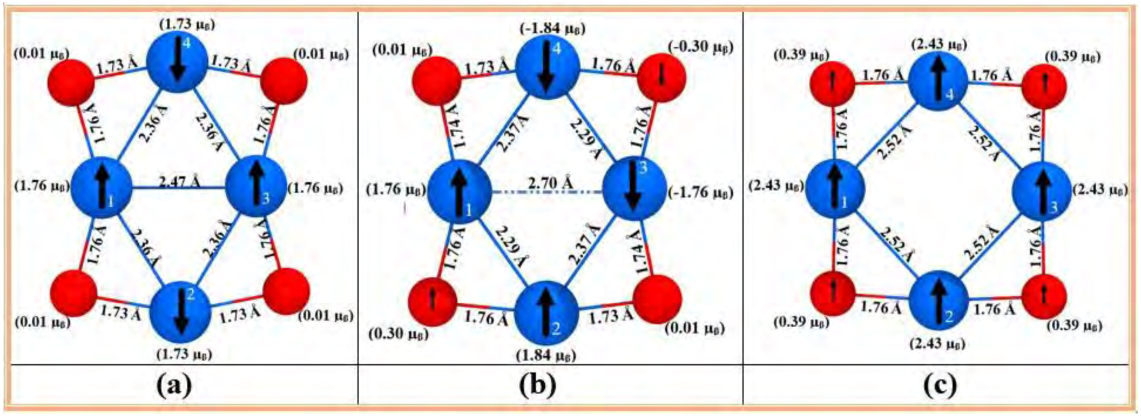

Figure 4.9: The bond lengths and local magnetic moments on Co and O atoms in various magnetic configurations of neutral $(CoO)_4$ cluster. (a) and (b) represent AFM spin ordering in different spin distributions. (c) is a fully ferromagnetic(FM) order. Large and small arrows refer to Co 3*d* and O 2*p* spin-directions respectively.

two Co atoms and this contraction leads to a substantial decrease in the local magnetic moments of Co atoms, i.e., from 2.43 in (c) to 1.76 in (a). Spin alignments of Co atoms in (a) and (b) give rise to a negligible small local magnetic moment of 0.01 for O atoms, whereas alignments in (c) increase the local moments to 0.39. Apparently, O atoms in (c) are ferromagnetically polarized by two nearest neighboring Co atoms (Co-O-Co) with parallel spins. Effect of parallel spin alignment of two neighboring Co atoms can also be observed for two O atoms in (b) with local moments of 0.30. The alignment of electron spin in O depends on the spin direction of adjacent Co atoms, which is a result of the exchange splitting of Co 3*d* states, with the paired low-spin states energetically shifted upward, while the unpaired high-spin states are shifted downward to hybridize strongly with the O 2*p* electrons. Similar energetic splitting and polarization had also been reported for some other clusters (Sun et al., 2000).

Spin alignment in Co atom affects drastically the structural geometry of $(CoO)_4$ cluster. As seen in (a) and (b), the Co_1-Co_3 bond elongates from 2.47 Å to 2.70 Å when the spins align from parallel to anti-parallel. Even though (a) and (b) configurations have the same magnetic moments 0, the Co_1-Co_3 bond length in (a) is almost identical to that of the bulk cobalt, i.e. 2.43 Å (De O'Shea et al., 2010). Therefore, structure (a) can

Table 4.3: The energy (eV) of various magnetic configurations relative to the ground state, taken as zero. The 3d orbitals of two opposite Co pairs are respectively indicated by with and without underlined arrows.

$(CoO)_4$		**$(CoO)_4^+$**	
$\underline{\uparrow}\downarrow\underline{\uparrow}\downarrow$	0.00	$\underline{\uparrow}\downarrow\underline{\uparrow}\downarrow$	0.00
$\underline{\uparrow}\uparrow\underline{\downarrow}\downarrow$	0.33	$\underline{\uparrow}\uparrow\underline{\downarrow}\downarrow$	0.47
$\underline{\uparrow}\uparrow\underline{\downarrow}\uparrow$	0.65	$\underline{\uparrow}\uparrow\underline{\downarrow}\uparrow$	0.20
$\underline{\uparrow}\downarrow\underline{\uparrow}\uparrow$	0.65	$\underline{\uparrow}\downarrow\underline{\uparrow}\uparrow$	0.20
$\underline{\uparrow}\uparrow\underline{\uparrow}\uparrow$	0.84	$\underline{\uparrow}\uparrow\underline{\uparrow}\uparrow$	0.36

be considered as the most stable structure of $(CoO)_4$, stabilized by the ferromagnetic coupling of Co_1-Co_3 bridge. Table 4.3 shows that energetically, the alignment in (b) is 0.33 eV higher than (a). Interestingly, this energy increases monotonically when the electron spins for all Co atoms gradually align in parallel towards a full ferromagnetic ordering. Similar variations of energetic stability of $(CoO)_4^+$ with respect to magnetic ordering can also be noticed, where antiferromagnetic ordering is energetically the most favorable. In fact, the symmetry of $(CoO)_4$ is changed dramatically from C_{2v} to D_{4h} when the spins are aligned from (a) to (c). It can be associated with structural relaxation by breaking the symmetry, and thus to accommodate the magnetic ordering changes, as previously reported by Aguilera et.al (Aguilera-del Toro et al., 2014). According to the Goodenough-Kanamori-Anderson rule, structure (c) with the arrangement of the Co-O-Co angles of 90° is related to the ferromagnetic super-exchange coupling between next-to-nearest Co cations via mediated O atom, which explains the strong relationship in this cluster type between the structure and magnetic properties.

The origin of magnetic properties can be investigated from the band properties of electronic structures. Figure 4.10 shows the total density of states (TDOS) and partial density of states (PDOS) of $(CoO)_4$ for antiferromagnetic and ferromagnetic ordering

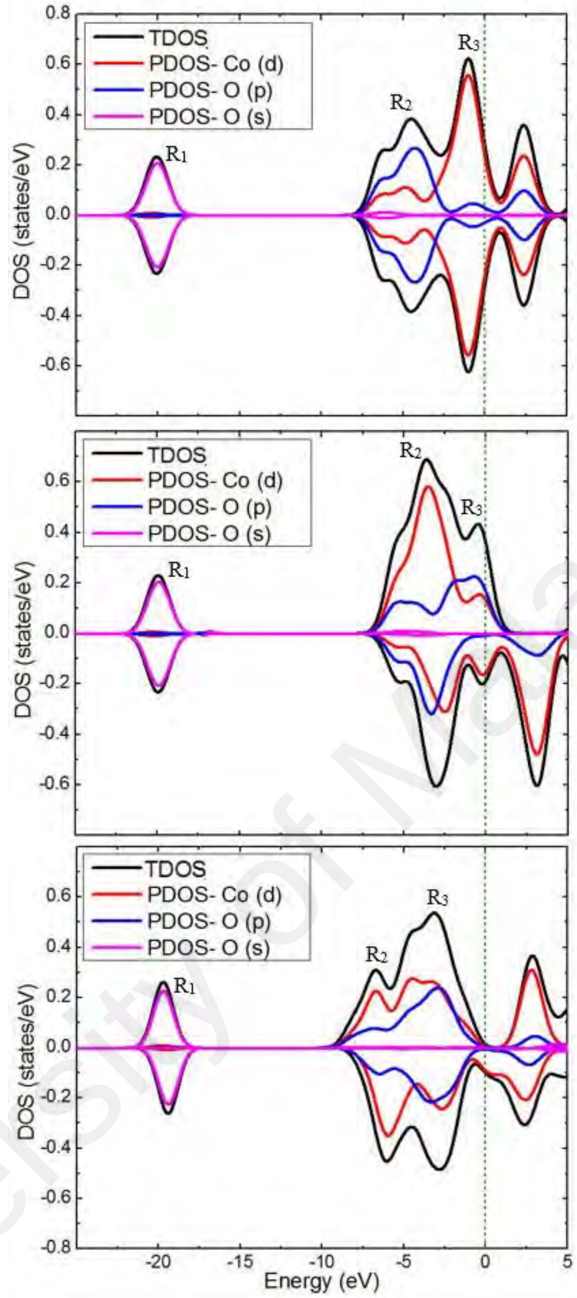

Figure 4.10: Total and partial densities of states of neutral $(CoO)_4$ clusters with C_{2v} symmetry (upper panel) and D_{4h} symmetry (middle panel) represent antiferromagnetic and ferromagnetic ordering structures respectively, and for cationic $(CoO)_4^+$ cluster with D_{2h} symmetry (lower panel).

structures with C_{2v} and D_{4h} symmetries, respectively. The figure also shows the TDOS and PDOS for $(CoO)_4^+$ with D_{2h} symmetry. The Fermi energy level is shifted to zero and marked by a vertical dashed line. Three main band profiles are identified and labeled as R_1, R_2 and R_3 where in all symmetry structures, the first band R_1 is mainly contributed from the O 2*s* orbital.

For the $(CoO)_4$ cluster with C_{2v} symmetry, the largest contribution of the second band R_2 originates from the O 2p orbitals hybridized with the Co 3d orbitals. However, the 3d orbitals dominantly contribute to the R_3 band close to the Fermi level. Accordingly, the evenly populated spin-up and spin-down DOS over the entire cluster ring concentrate on the Co atoms, which leads to an increase in the Co local magnetic moments up to 1.76. The symmetrical spin polarization of the C_{2v} structure makes its total magnetic moment less than the other two symmetry structures, D_{4h} and D_{2h}. Change in symmetry of the $(CoO)_4$ to D_{4h} results in the increase of the R_2 band. This occurs because the Co 3d orbitals are stabilized and fully hybridized with the O 2p. The strong interaction between both spin-up DOS is extended to the R_3 band. On the other hand, the interaction between spin-down DOS becomes weak when approaching the Fermi level. Overall, the asymmetric spin polarization over the entire ring increases the total magnetic moments with the largest value of 2.43 concentrated on the Co atoms.

For the DOS of $(CoO)_4^+$ cluster, R_2 and R_3 bands are shifted away from the Fermi level to lower energy approaching the R_1 band. By comparing DOS to the C_{2v} and D_{4h} structures, the distribution of the spin-up and spin-down DOS can be attributed from the mixture of the two symmetry structures of $(CoO)_4$. Hence, the local magnetic moment of Co atoms of 1.93 is in the range between 1.73 to 2.43.

Figure 4.3 clearly shows that the putative global minimum of $(CoO)_n$ clusters have distinct planar-like (2D) or compact (3D) structures. Hence, investigation of the growth trend from 2D to 3D structures as a function of cluster size needs to be carried out. In doing so, GGA calculations were performed for neutral and cationic isomers of $(CoO)_n$ with $n = 3 - 6$ where relative energies as a function of the spin magnetic moments were obtained. The energies are displayed in Figure 4.11 plotted relative to the most stable energy. For $n = 3$, the neutral and cationic clusters favor to form the most stable

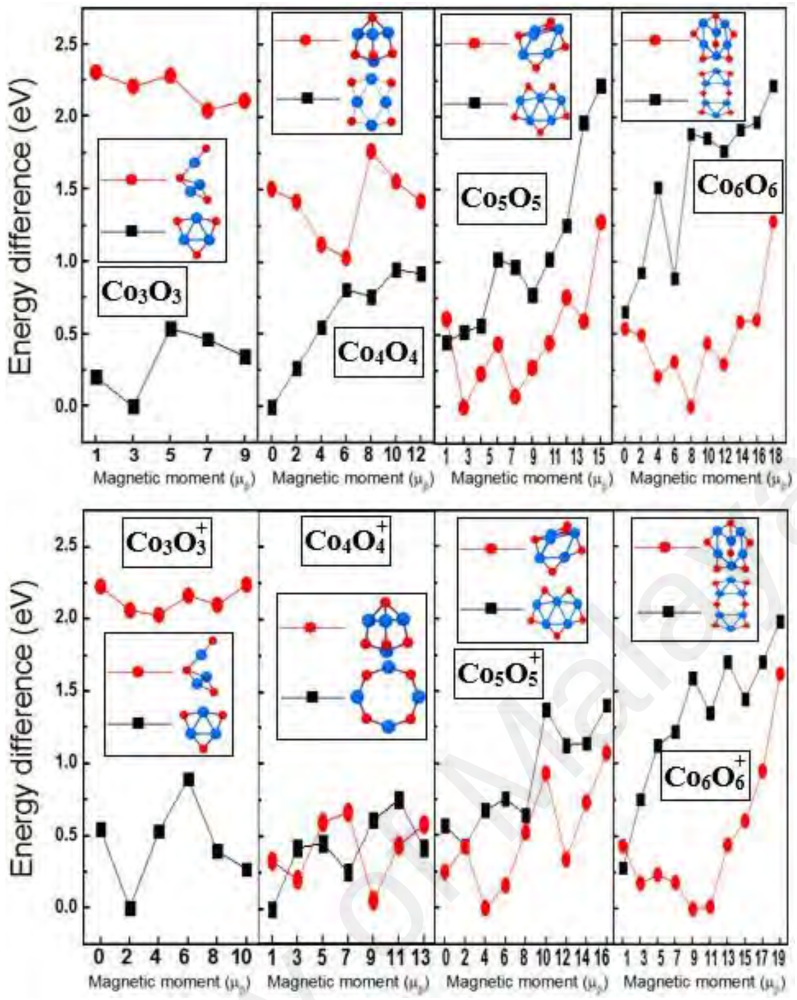

Figure 4.11: The energy differences between 2d and 3d isomers relative to the ground-state energy of the most stable magnetic one for each neutral and cationic $(CoO)_n^q$ ($n = 3 - 10$, q = 0, +) clusters in the upper and lower rows of panels respectively. For example, the upper-left panel shows the energy difference between ring (2d) and compact (3d) isomers relative to the ground-state energy of ring isomers (the most stable one) for neutral $(CoO)_3$ cluster.

structure of planar-like, but this tendency becomes less starting from $n = 4$. In particular, cationic $(CoO)_4^+$ clusters display the structural competition between planar (ring) and compact (bi-capped triangular prism) structures with different spin magnetic moments. However, the stability inclines towards planar structure in most cases of spin states, especially the low-spin one, and the trend reverses completely for $n \geq 5$. In other words, the growth tendency to form 3D structures begins at $n = 5$ for both neutral and cationic clusters, and this tendency gradually increases with cluster size, as seen in Figure 4.11. These results are in contrast to the work of Ota and coworkers (Ota et al., 2013) who found that the structural transition from planar to compact structures begins to emerge at $n = 6$. To evaluate the transition trend, they used different structures with weak stability compared to the structures reported here and examined only a few low-spin states.

4.4.4 Hypothetical dissociation model

The dissociation process of neutral and cationic cobalt oxide clusters using different mass spectroscopy techniques shows the preferentially formation of small clusters, $n = 3$ and $n = 4$ (Xie et al., 2010; Dibble et al., 2012), with a 1:1 stoichiometry of $(CoO)_n$ and $(CoO)_n^+$ clusters. To study the process, the dissociation energies of $(CoO)_n$ and $(CoO)_n^+$ clusters,

$$(CoO)_n^q \rightarrow (CoO)_m^q + (CoO)_{(n-m)} \tag{4.3}$$

as a function of cluster size (n) and its fragment size (m) are calculated, and this is defined as

$$D_n^q = E_m^q + E_{(n-m)} - E_n^q \tag{4.4}$$

where E_n^q is the total energy of parent cluster either neutral or cationic depending on the value of q, and E_m^q and $E_{(n-m(}$ are the total energies of fragments; the first energy term carries the charge of its parent and the second is always neutral.

Figure 4.12 shows the contour plots of the calculated dissociation energy surfaces of $(CoO)_n$ clusters (upper panel) and $(CoO)_n^+$ clusters (lower panel), with the higher energy indicating that the cluster is more stable and difficult to undergo dissociation. Clearly, in the upper panel of Figure 4.12, the highest dissociation energy originates from the dissociation of $(CoO)_4$ as following

$$(CoO)_4 \rightarrow 2(CoO)_2 \tag{4.5}$$

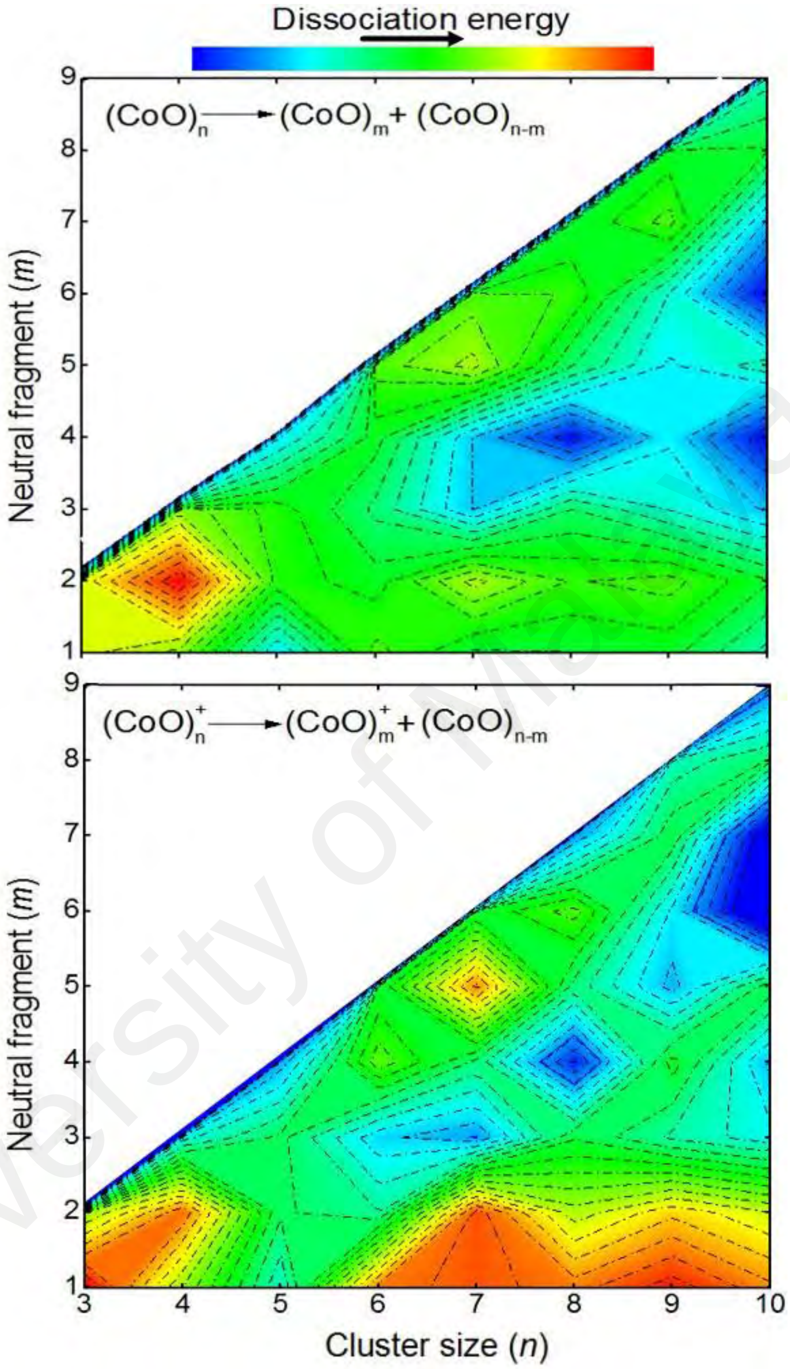

Figure 4.12: Dissociation energies for the neutral (upper panel) and cationic (lower panel) $(CoO)^q_{m/n}$ ($m, n = 3 - 10$, $q = 0, +1$) clusters. The increasing in dissociation energy is indicated by the changing of the color from blue to red.

to yield fragments $(CoO)_2$. This observation confirms that $(CoO)_4$ has the highest stability among all other clusters presently studied and in line with the results displayed in Figure 4.5. As expected for larger cluster sizes, the upper surface of Figure 4.12 shows three minima corresponding to the dissociation channels of $(CoO)_8$ and $(CoO)_{10}$ clusters,

$$(CoO)_8 \rightarrow 2(CoO)_4 \tag{4.6}$$

$$(CoO)_{10} \rightarrow (CoO)_4 + (CoO)_{6.} \tag{4.7}$$

Lowest dissociation energy of these clusters produces high yield of $(CoO)_4$ fragments. These predictions agree very well with abundance of $(CoO)_4$ cluster detected from the time-of-flight mass study, observed by Bernstein and coworkers (Xie et al., 2010). In the vicinity of the minima, $(CoO)_3$ fragments are produced according to the following

$$(CoO)_7 \rightarrow (CoO)_3 + (CoO)_4 \tag{4.8}$$

$$(CoO)_9 \rightarrow (CoO)_3 + (CoO)_6 \tag{4.9}$$

$$(CoO)_{10} \rightarrow (CoO)_3 + (CoO)_7 \tag{4.10}$$

Further dissociation of the $(CoO)_7$ fragments may occur to yield more products of $(CoO)_3$ and $(CoO)_4$ as seen in equations (4.8). Locations of low energy can be seen at the edges of the energy surface, representing the dissociation of

$$(CoO)_5 \rightarrow CoO + (CoO)_4 \tag{4.11}$$

which provides another possible channel in yielding $(CoO)_4$.

Three maximum peaks at the lower surface of Figure 4.12 correspond to the dissociation channels of

$$(CoO)_3^+ \rightarrow (CoO)^+ + (CoO)_2 \tag{4.12}$$

$$(CoO)_7^+ \rightarrow (CoO)^+ + (CoO)_6 \quad (4.13)$$

$$(CoO)_9^+ \rightarrow (CoO)^+ + (CoO)_{8,} \quad (4.14)$$

which indicate the difficulty to remove one $(CoO)^+$ molecule from $(CoO)_3^+$, $(CoO)_7^+$ and $(CoO)_9^+$. This reflects to some degree, the stability of these cationic clusters. However, only the predicted stability of $(CoO)_7^+$ and $(CoO)_9^+$ clusters agree with the second-order energy results presented in Figure 4.5 but not for the $(CoO)_3^+$ cluster. In the vicinity of the maximum, it seems that $(CoO)_4^+$ is stable through dissociation of

$$(CoO)_4^+ \rightarrow (CoO)_2^+ + (CoO)_{2,} \quad (4.15)$$

in agreement well with the second-order energy prediction. Experimental dissociation study of $(CoO)_4^+$ by Dibble et al. (Dibble et al., 2012) revealed that $(CoO)_4^+$ is the major product fragment. However, the current work predicts the favorable dissociation channel due to the loss of one CoO molecule, giving $(CoO)_3^+$,

$$(CoO)_4^+ \rightarrow (CoO)_3^+ + (CoO)_, \quad (4.16)$$

in agreement with other experimental and theoretical works (Freas et al., 1987; Aguilera-del Toro et al., 2014). Very low production of $(CoO)_2^+$ in mass spectrum was confirmed by Dibble et al. (Dibble et al., 2012) and was similarly observed for its neutral counterpart $(CoO)_2$, displayed in the upper panel of Figure 4.12.

In the lower panel of Figure 4.12, two distinct energy minima can be seen from

$$(CoO)_8^+ \rightarrow (CoO)_4^+ + (CoO)_4 \quad (4.17)$$

$$(CoO)_{10}^{+} \rightarrow (CoO)_{6}^{+} + (CoO)_{4} \tag{4.18}$$

Once again, these observations strongly support the abundance of $(CoO)_4$ compared to other clusters and may explain the absence of $(CoO)_{10}^{0/+}$ spectral peaks. In particular, these dissociation channels which lead to the formation of $(CoO)_4^{+}$ and/or $(CoO)_4$ agree well with photodissociation experiments of Duncan et al. (Dibble et al., 2012). Two shallow energy wells can also be seen for the production of $(CoO)_4$, arising from the dissociation of

$$(CoO)_{7}^{+} \rightarrow (CoO)_{3}^{+} + (CoO)_{4} \tag{4.19}$$

$$(CoO)_{9}^{+} \rightarrow (CoO)_{5}^{+} + (CoO)_{4}. \tag{4.20}$$

Equations (4.19) and (4.20) may compensate equations (4.13) and (4.14) to reduce the stability of the $(CoO)_7^{+}$ and $(CoO)_9^{+}$ clusters significantly. This may explain the second-order energy of both clusters lower than that of $(CoO)_4$. Similar to the dissociation of neutral clusters, the trend of producing $(CoO)_3$ fragments occur at the vicinity of the energy minima as following

$$(CoO)_{6}^{+} \rightarrow (CoO)_{3}^{+} + (CoO)_{3} \tag{4.21}$$

$$(CoO)_{10}^{+} \rightarrow (CoO)_{7}^{+} + (CoO)_{3}. \tag{4.22}$$

In addition, two quite important dissociation regions for increasing the production of $(CoO)_4^{+}$ fragments can be seen at the edges of the energy surface, i.e.,

$$(CoO)_{5}^{+} \rightarrow (CoO)_{4}^{+} + (CoO) \tag{4.23}$$

$$(CoO)_{10}^{+} \rightarrow (CoO)_{4}^{+} + (CoO)_{6} \tag{4.24}$$

where dissociation of $(CoO)_5^+$ was experimentally observed by Duncan et al. (Dibble et al., 2012). Another two potential regions leading to the formation of $(CoO)_4$ are

$$(CoO)_8^+ \rightarrow (CoO)_7^+ + (CoO) \tag{4.25}$$

$$(CoO)_{10}^+ \rightarrow (CoO)_9^+ + (CoO), \tag{4.26}$$

which both $(CoO)_7^+$ and $(CoO)_9^+$ fragments may undergo further dissociation as in equations (4.13) and (4.14).

From the dissociation studies of $(CoO)_4$ and $(CoO)_4^+$, both clusters show a remarkable stability compared to other neutral and cationic clusters. Further investigation is required to determine which of the two clusters are likely to be dissociated. Figure 4.13 shows the dissociation energies as a function of cluster size (n), calculated from the dissociation of $(CoO)_n^+$ ($n = 5 - 10$) to form either $(CoO)_4$ or $(CoO)_4^+$ product

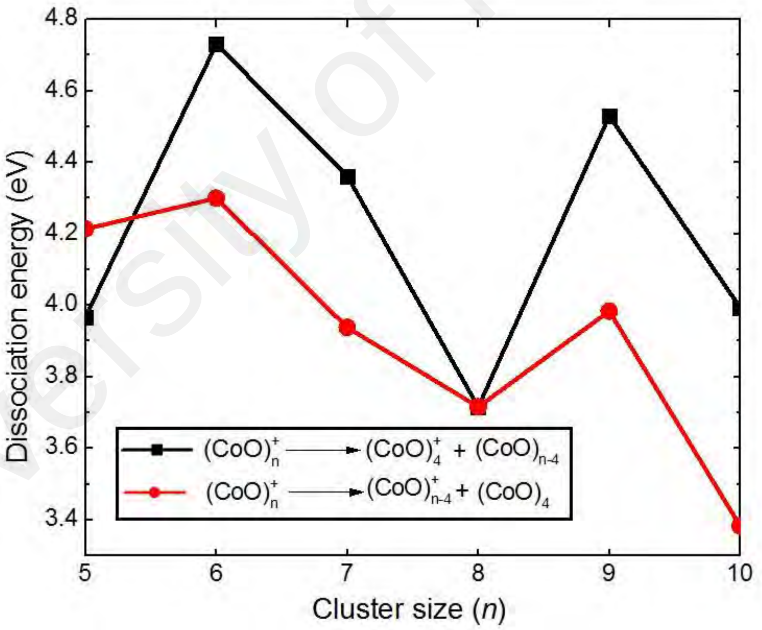

Figure 4.13: Calculated dissociation energies for the cationic $(CoO)_n^+$ clusters leading to the formation of neutral $(CoO)_4$ fragment (red) and cationic $(CoO)_4^+$ fragment (black).

fragment. Except for the dissociation of $(CoO)_5^+$, the dissociation energy for most cluster sizes leading to the formation of $(CoO)_4$ cluster is lower than the formation of $(CoO)_4^+$. This result shows that with a slight change in symmetry i.e. from D_{2h} to C_{2v}, the $(CoO)_4^+$ cluster becomes less stable than $(CoO)_4$ despite the fact that the two clusters have the same number of atoms.

4.5 Conclusion

The structural, electronic and magnetic properties of neutral and cationic cobalt oxide clusters $(CoO)_n^q$ $(n = 3 - 10, q = 0, +1)$ have been studied using the modified basin- hopping Monte Carlo algorithm followed by spin-polarized DFT. From a systematic algorithm minimum search, new global minimum structures of cobalt oxide clusters, such as $(CoO)_9^{0/+}$ are predicted, whereas some structures have been successfully reproduced as predicted by previous experimental and theoretical works (Yin et al., 2009; Aguilera-del Toro et al., 2014; Dijk et al., 2014). It is found that the structural transition from planar-like to compact structure begins at $(CoO)_5^{0/+}$, in contrast to the general notion that the structural changes begins from $(CoO)_6^{0/+}$. Limited DFT calculations performed for $(CoO)_n^q$ with $n = 3 - 6$ as a function of magnetic moment also revealed that the clusters display similar structural transition in most cases of spin states.

Structural analysis of the global minimum clusters revealed that the number of Co-Co bond determines the complexity of structural morphology; however, the number of this metallic bond is limited, and easily countable for clusters with n less than 7 and subsequently increases for larger clusters. It is found to agree experimentally (Xie et al., 2010) that $(CoO)_4$ is the most stable over all other $(CoO)_n^q$ clusters, confirmed by the results of its highest binding energy and second-order total energy difference, and strongly supported by having the highest positive value of chemical hardness, highest negative value of chemical potential and largest HOMO-LUMO gap. Detailed electronic analysis of $(CoO)_4$ cluster reveals that its ring stability is associated with the build-up of π electrons delocalization in HOMO moving circularly around the hybrid *pd*-like orbitals.

It is interesting to observe that the total spin magnetic moments of the global minima of $(CoO)_n^q$ fluctuate between low-spin and high-spin configurations (i.e. between 0 and 16) with $(CoO)_4$ and $(CoO)_8$ spins exhibiting a fully antiferromagnetic ordering, while $(CoO)_{10}$ spins display the highest ferromagnetic ordering. The prominent changes in the local magnetic moment of Co and O atoms can be understood in terms of the magnetic influence from their neighboring atoms. Varying Co-Co bond length in $(CoO)_4$ as one of the selected model clusters revealed that the local magnetic moment of Co atoms decreases proportionally with the bond length as a result of strong hybridization of Co-Co bond. Apparently, the O atom become ferromagnetically polarized by the parallel spins of two nearest neighboring Co atoms (Co-O-Co arrangement) via the exchange splitting of Co 3*d* orbitals with its unpaired high-spin states being shifted downwards to polarize the O 2*p* unpaired spins. This polarization also follows the Goodenough-Kanamori-Anderson rule of ferromagnetic super-exchange coupling between next-to-nearest Co cations via mediated O atom, where the symmetry distortion of $(CoO)_4$ from C_{2v} to D_{4h} probably occurred because of the structural rearrangement of Co-O-Co angles to 90° in order to accommodate the spin magnetic ordering changes.

Furthermore, the total density and partial density of states (TDOS and PDOS) for both C_{2v} and D_{4h} symmetrical structures are determined to investigate the influence of the *p* and *d* valence orbitals on the local magnetic moments. It is found that for the antiferromagnetic C_{2v} structure, the valence band occupies the Fermi energy level and its symmetrical spin polarization is due to the symmetrically populated spin-up and spin-down DOS. In contrary, the valence band of the ferromagnetic D_{4h} structure is shifted away from the Fermi level and its asymmetrical spin polarization is due to the high population of spin-up DOS.

Two potential dissociation energy surfaces of $(CoO)_n^q$ clusters are constructed to study the dissociation pattern and global pathway, connecting the neutral and cationic clusters in one complete graphical picture. The study also confirms the highest stability of $(CoO)_4$ and $(CoO)_4^+$ over other neutral and cationic clusters.

CHAPTER 5: ATOMIC SCALE BEHAVIOUR, GROWTH MORPHOLOGY AND MAGNETIC PROPERTIES OF CoO ON MGO(100) SURFACE: A DENSITY FUNCTIONAL STUDY

5.1 Introduction

The ultra-thin film of transition metal oxides deposited on metals, and polar or non-polar oxide substrates have attracted much attention due to their unique shape, size, and properties that may have great potential application in solar energy materials, chemical sensors, microelectronic device, composite materials and advanced catalysts (Pacchioni & Valeri, 2012; Ramanathan, 2010; Campbell, 1997). Among the 3d-transition metal oxide series, CoO is one of the most promising catalytic systems at ultrathin layer levels. Many reports have shown that CoO/metal-oxides systems are effective catalysts in photoelectro-chemical water splitting (Trotochaud et al., 2013), gas desulfurization (Li et al., 1993), water pollutants elimination (Garbowski et al., 1990), and air pollution control (He & Köhler, 2006).

Since magnetic properties are highly influenced by the atomic arrangement of the growth layer, systematic understanding of the structural-properties relationship of CoO at different atomic levels is imperative. The surface diffusion of the adsorbed Co atom and CoO molecule is a vital step towards understanding the growth mechanisms and the nature of CoO-metal oxide interfaces(Ma et al., 2011; Elkoraychy et al., 2015; Han & Evans, 2015). Although many studies have investigated the adsorption of Co on the MgO(100) surface (Neyman et al., 2004; Fernandez et al., 2007; Rau et al., 2014), few have described the diffusion process, as we will see in the following section.

In comparison with the metal surfaces, cobalt oxides supported on transition-metal oxide surfaces have not received much attention, although their potential catalytic applications are apparent (Trotochaud et al., 2013; Li et al., 1993; Garbowski et al., 1990).

To the best of our knowledge, only a limited number of experimental papers associated with DFT studies can be found in the literature (Alaria et al., 2008; Zayed et al., 2013). This may be attributed to the complexity of these systems and the difficulty in distinguishing a variety of possible structures and magnetic properties. Hence relevant studies addressing this topic will be presented in the next section.

It is worth mentioning that the MgO surface plays an important role on the the crystal growth, dissociation, and chemical reaction process (Takeuchi & Maki, 2007). For example, it is frequently employed for some commercial applications as an alkaline catalyst (Choudhary & Pandit, 1991; Lopez et al., 1991), due to the presence of abundant surface basic sites on MgO that enhance the tendency to transport electronic charge from these basic sites (i.e. O^{-2} anion) to the adsorbed species (Pacchioni, 2013).

CoO has been classified as a strongly correlated Mott-Hubbard insulator with a band gap of 2.8 eV. This is because of the strongly correlated nature of the d-electrons in cobalt. The band gap value of CoO is notably underestimated by pure GGA calculations, due to the inexact cancellation of the Coulomb self-interaction among the d electrons. Although hybrid functionals containing a percentage of exact Hartree–Fock exchange provide a more accurate solution to these problems, they are computationally demanding. Therefore, using the less expensive GGA+U approach that involves a Hubbard term to deal with the strong on-site Coulomb interactions is considered as a good method for the investigation of metal oxide systems especially cobalt oxides (Zayed et al., 2013; Bajdich et al., 2013). In fact, the value of the U parameter is a crucial issue; and it depends on the best reproduction of experimental data such as the cell parameter, band gap and reaction energies. However, the optimal value of U parameter for the same system may be different for various other properties (Castleton et al., 2007).

5.2 Literature Review

Several studies have investigated the adsorption of Co on the MgO(100) surface. For example, Neyman et al. (2004) studied a series of 3d and 4d transition metal atoms on the regular MgO (100) surface by the BP86 and PBEN exchange-correlation functionals. They noticed that the TM atoms adsorbed on O^{-2} site is the most stable site on the relaxed MgO (100) surface. From similar calculated values of the adsorption energies using different exchange-correlation functionals, they also concluded that the metal polarization associated with some orbital mixing represented the nature of the adsorption bonds without noticeable charge transfer between the adsorbate atoms and the MgO substrate. Another comprehensive work carried out by Fernandez et al. (2007), examined the adsorption of the fourth period of Mendeleev's table, M= K to Zn. The calculation of the adsorption energies again showed that the most stable adsorption position is at the top of O of the MgO surface, where both Ni and Ti have the maximum value of adsorption energy. This study also reported that the adsorption of the small metal atoms at the top of Mg site is negligible, but should be taken into account for larger metals (M=K to V). The preferential adsorption of the TM atoms on the top of O site have also been noticed on defected MgO (100) surface (Park et al., 2009), which coincides well with previous DFT work (Fernandez et al., 2007).

A few of these studies concerned the diffusion process of Co atom on MgO surfaces. For instance, Kim and Chung (2006) investigated the atomistic behaviour of the Co atom on the MgO (100) substrate, including the adsorption and diffusion processes. They suggested an unusual diffusion path of the Co atom compared to previous reports for other transition metals adsorbed on the same substrate (Jeon & Yu, 2014; Jeon & Yu, 2013; Park et al., 2009). Some results of this study will be addressed in more depth in the discussion section. On the other hand, Geneste and co-workers have shown that the MgO molecule binds stronger to the magnesia surface (E_{ad} = 2.5 eV) compared to the Mg atom (E_{ad} = 0.5 eV). They have concluded that the surface diffusion of the MgO molecule includes multi-step rotations about the axis perpendicular to the Mg-O bond with barriers of ~ 15 − 20% of the adsorption energy, which could lead to various growth patterns of MgO on MgO(100) substrate based on the deposition techniques used (Geneste et al., 2002).

As we have mentioned before, in the literature there is a limited number of experimental or computational studies that focus on the deposition of CoO on metal oxide surfaces compared to the deposition on metal surfaces. For instance, one recent experimental report investigated the formation of hexagonal cobalt oxide (II) thin film on α-Al_2O_3(0001) surface with or without using ZnO buffer layer. The results showed that the structural and magnetic properties were strongly dependent on the growth mode (Alaria et al., 2008). In the case of CoO growth directly on pure α-Al_2O_3, three-dimensional (3D) growth had been reported whereby, using reflection high-energy electron diffraction (RHEED) method, X-ray diffraction (XRD) showed cubic CoO with (111) orientation, whereas using ZnO buffer layer two-dimensional (2D) growth for CoO thin film with wurtzite structure was revealed. More recently, DFT work had successfully reproduced the experimental data of CoO nanosized layers supported on α-Al_2O_3(0001) surface (Zayed et al., 2013). In the study, the initial steps of CoO monolayer growth, Bader charge analysis, and magnetic arrangements have been examined. The results show three structural morphologies of CoO thin films: zinc-blende, wurtzite and rock-salt structures. The antiferromagnetic solution is found to be more stable in all of these structures with different surface coverage. To the best of our knowledge, no computational study has been reported on the formation of CoO thin film monolayer on MgO(100) substrate. Currently available experimental data reveals the formation of antiferromagnetic CoO films with (100) termination on magnesia surface (Greiner et al., 1966).

In this work, the growth mechanism of cobalt oxide on the surface of MgO(100) has been analyzed using DFT+U calculations. After a detailed description of the computational method and models, we will address the adsorption and diffusion behaviours of Co atom and CoO molecules as initial steps to a better understanding of the CoO film growth. Both charge transfer and density of state distribution have been calculated to clarify the electronic and magnetic properties of CoO/MgO(100) system.

5.3 Methodology

Our periodic density functional (DFT) calculations are performed using the VASP 5.3 code(Kresse & Hafner, 1993; Kresse & Furthmüller, 1996a; Kresse & Furthmüller, 1996b), where the spin-polarized Kohn-Sham equations are solved within the Projector Augmented Wave (PAW) approach (Blöchl, 1994; Kresse & Joubert, 1999). The energy is obtained using the generalized gradient approximation (GGA) as proposed by Perdew-Burke-Ernzerhof (PBE) (Perdew et al., 1996). In these calculations, the Hubbard U term for Co 3d states is added to the plain GGA functional (that is, GGA+U) employing the rotationally invariant approach proposed by Dudarev et al (Dudarev et al., 1998), in which the Coulomb U and exchange J parameters are combined into the one effective parameter U_{eff} = U - J. Indeed, a variety of U_{eff} parameter values have been reported for Co 3d states of CoO material from 4.4 to 7.8 eV (Chen et al., 2011; Anisimov et al., 1991; Pickett et al., 1998). Even U_{eff} = 1 has been applied for CoO/Ir(100) system (Mittendorfer et al., 2012) on the basis of better structural agreement with experimental data. Our recent study on CoO/α-Al_2O_3(0001) system has established a value of U_{eff} =6 after a comparison between the computed and experimental data of CoO was made by changing the U_{eff} value. We found that U_{eff} =6 provides a better value of the band gap (2.83 eV) which comes very close to the empirical value (2.8 eV). The geometrical and magnetic properties of CoO have also been successfully predicted using this U_{eff} value in the non-reducible oxide surface (i.e., α-Al_2O_3) that belongs to the same group of the current surface study (Zayed et al., 2013). The electronic wave functions are expanded in a plane wave basis set with a cutoff of 400 eV. The calculated forces on the ions used the Hellmann-Feynman theorem and included the Harris-Foulkes correction (Harris, 1985). The atomic relaxation is stopped when the interatomic forces are less than 0.001 eV/Å.

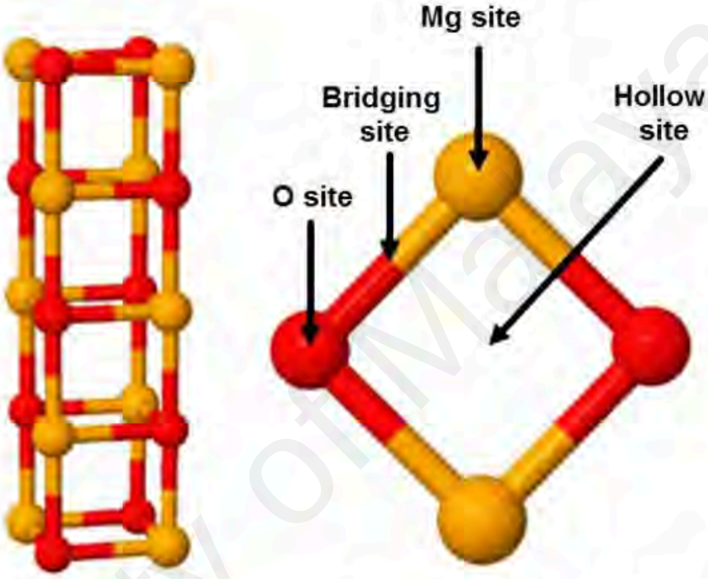

Figure 5.1: Side (left) and top (right) views of the MgO(100) surface showing 1 × 1 cell of the slab model and the probed adsorption sites, respectively. Atom colors: Mg, orange; O, red.

Some previous studies showed that a three- or four-layer slab of MgO is sufficient to model the MgO(100) surface (Geneste et al., 2002; Geneste et al., 2003). Here, the unit cell of the MgO(100) surface is represented by a five-atomic layer slab model which belongs to the face-centered cubic system (see Figure 5.1) . The optimized lattice parameter is a= 4.238 Å and is very close to the experimental value (a= 4.21 Å) (Fuhr & Wiese, 2006). In the z direction, a 22 Å thick vacuum layer above the slab has been included to prevent interactions between the top and bottom slab images of MgO surfaces during the structural optimization process. In all models, the two lower atomic layers of the surface are kept fixed in their bulk position to simulate the presence of the bulk underneath. The surface energy with this choice is reduced by less than 1 mJ/m^2 with respect to the four- atomic layer slab model where the two bottom layers are kept fixed in their bulk positions. These initial calculations are carried out using a 4 × 4 × 1 Monkhorst-Pack k-point mesh.

The adsorption and diffusion of Co atom and CoO molecule are modeled in a 2 × 2 supercell of the above-described magnesia (100) surface in order to avoid lateral interaction between the adsorbates in adjacent cells. Except for the growth of CoO with various surface coverage values, a much larger (4 × 4) supercell model is considered essential to compare the growth pattern of CoO with different magnetic solutions. These calculations are made using the Γ point and a 2 × 2 × 1 Monkhorst-Pack k-point mesh for large and small supercells, respectively. These sets of k-point are chosen to converge the relative energies of different geometries and magnetic solutions to less than 0.01 eV.

For analyzing the charge transfer process in CoO/MgO(100) for different growth patterns with various magnetic arrangements, the Bader charge (Bader, 1985) analysis is employed using the algorithm of Henkelman et al to obtain the expectation values of charge density (Henkelman et al., 2006; Sanville et al., 2007).

5.4 Results and Discussion

It is convenient to define the adsorption energy of the Co atom and CoO molecule before going into detail as follows:

- The adsorption energy of Co atom on the MgO substrate.

$$E_{ad} = E_{Co}^{ads} - E_{slab} - E_{Co}^{free}$$

where E_{Co}^{ads} is the total energy for the surface with the adsorbed Co atom, E_{slab} and E_{Co}^{free} is the total energy of clean substrate and free Co atom, respectively.

- The adsorption energy of CoO molecule with respect to the substrate.

$$E_{ad} = E_{CoO}^{ads} - E_{slab} - E_{CoO}^{free}$$

where E_{CoO}^{ads} is the total energy of one CoO molecule adsorbed on the surface, and E_{CoO}^{free} is the total energy of free CoO molecule.

5.4.1 Adsorption and diffusion of Co atom

Initially, we investigated the adsorption energy of a single Co atom deposited on different possible adsorption sites of the MgO surface; on top of Mg, on top of O, on the FCC hollow site (between two O sites) and on the bridging site (between Mg and O sites), as shown in Figure 5.1. Our results agree well with previous theoretical studies of comparable systems such as the adsorption of Ni, Pd, Ag and Cu atoms on the magnesia surface (Jeon & Yu, 2014; Jeon & Yu, 2013; Park et al., 2009), where the preferred deposition site of the metal atom is on top of the oxygen atom (see Table.5.1).

The (GGA+U) interpolated potential energy surface (PES) for Co adatom on MgO(100) surface is illustrated in Figure 5.2. The minimum PES value is obtained when Co is on top of oxygen sites (two most stable adsorption positions) passes the hollow site, and thus, the calculated diffusion barrier (E_{diff}) is 0.41 eV. In contrast with previous theoretical

Table 5.1: E_{ad} , adsorption energy (eV), $d_{Co-surface}$, distance from the surface plane, ρ_{Co}, Bader charge (e^{-}) and μ_{Co}, magnetic moment (μ_{β}) for Co atom deposition on different site of MgO(100) surface

Site	E_{ad}	$d_{Co\text{-}surface}$	ρ_{Co}	μ_{Co}
On top of O	-1.34	1.95	-0.07	2.5
On top of Mg	-0.79	2.63	-0.04	2.23
Hollow	-0.93	2.23	-0.12	2.21
Bridging*	....	....	....	....

* Above this site, the Co atom transfers to the top of O during the geometry optimization.

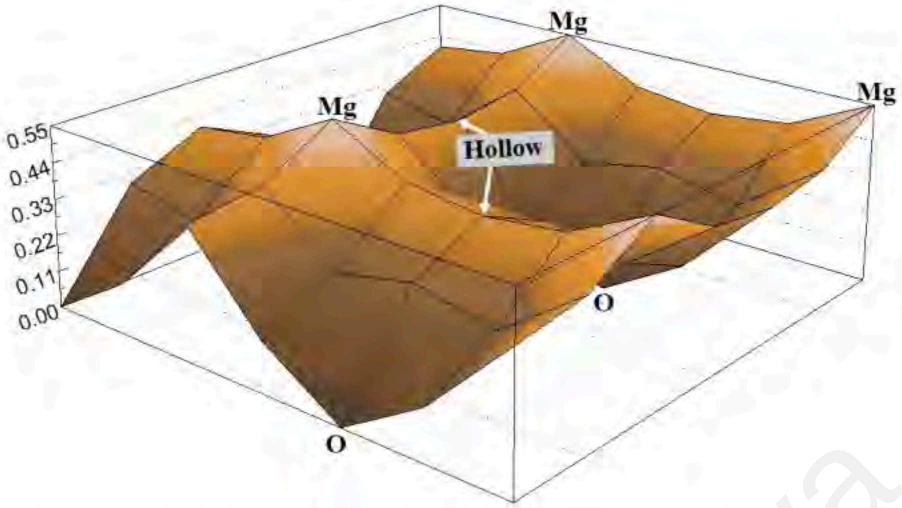

Figure 5.2: GGA+U potential energy surface for a Co adatom on MgO(100). Relative energies are given with respect to the lowest lying state i.e., the Co adatom on top of the O site, and expressed in eV unit.

study by Kim and Chung, where the bridging site showed good stability to adsorb Co atom ($E_{ad} = -0.19$ eV) and had been suggested as the saddle point for the hopping of the Co atom from the O site to the adjacent O sites (Kim & Chung, 2006). In fact, our results demonstrate that the Co atom is not adsorbed on the bridging site of the surface, but is transferred to the top of the O atom after structural optimization (see Table.5.1).

The residence time (τ) of Co adatom on the MgO surface can be found by using an Arrhenius-type equation, expressed as ($\tau = \tau_0 \exp(E_{diff}/KT)$). At room temperature with a typical prefactor $\tau_0 \sim 10^{-13}$ s, the residence time is $\tau \sim 8.3 \times 10^{-7}$ s, i.e., an attempt-to-jump frequency of ~ 1.2 MHz. This residence time value is lower than that reported previously for Cu adatom on the same substrate using LDA method (Musolino et al., 1997), reflecting the higher diffusion ability of cobalt atom on magnesia surface. The data in Table 5.1 also show a small charge transfer from the MgO surface to the Co atom, which is close to zero. This indicates that the interaction between the cobalt atom and the magnesia substrate is not formed via charge transfer from/to the metal to/from the surface. Instead, it is mainly produced by the metal polarization and dispersion effects with slight orbital mixing with the surface atoms, in line with other previous studies (Yudanov et al., 1997; Pacchioni, 2013). Because of weak orbital overlap between Co adatom and MgO(100) surface, it is reasonable to expect that the d electrons of Co stay localized in atomic-like orbitals and thus its magnetic moment remains similar to that of the neutral atom. This observation is in accordance with the recent studies showing large magnetic anisotropy for a single Co atom adsorbed on the MgO(100) surface (Rau et al., 2014; Ou et al., 2015).

Figure 5.3 shows the influence of the strength of on-site Coulomb interaction U on the total energy of Co adsorbed on various sites of the MgO(001) substrate. Since the comparison between the total energies of GGA+U calculations can be only achieved by using the same value of U, structures on different adsorption sites are relaxed for each U value (U= 1-7). Obviously, the different U strengths increase the total energies of Co

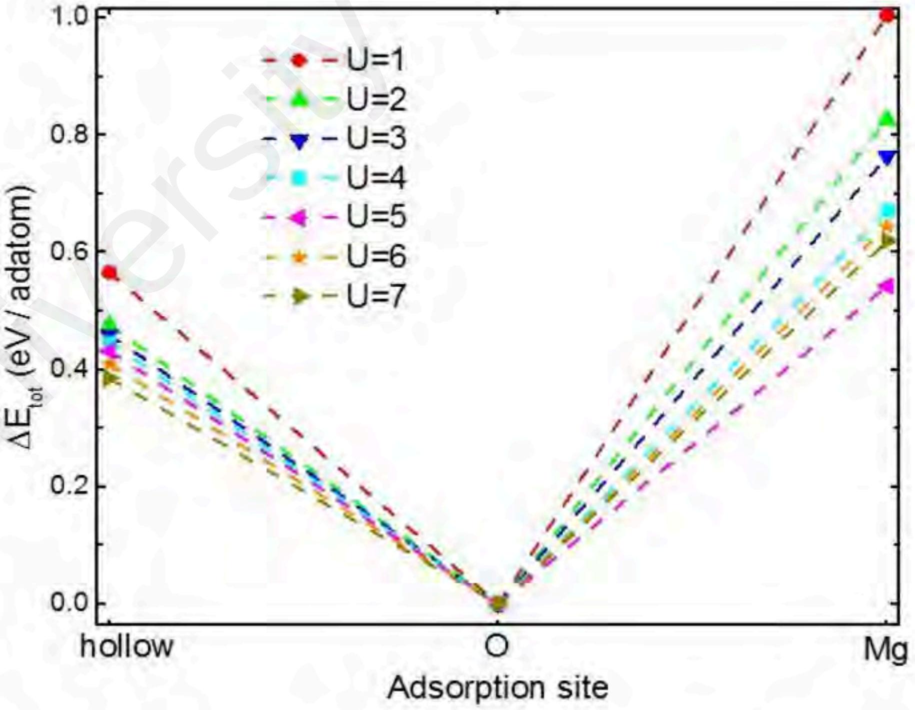

Figure 5.3: Total energy per Co adatom on MgO(100) using GGA+U calculations. Relative energies are given with respect to the Co adatom on top of the O site.

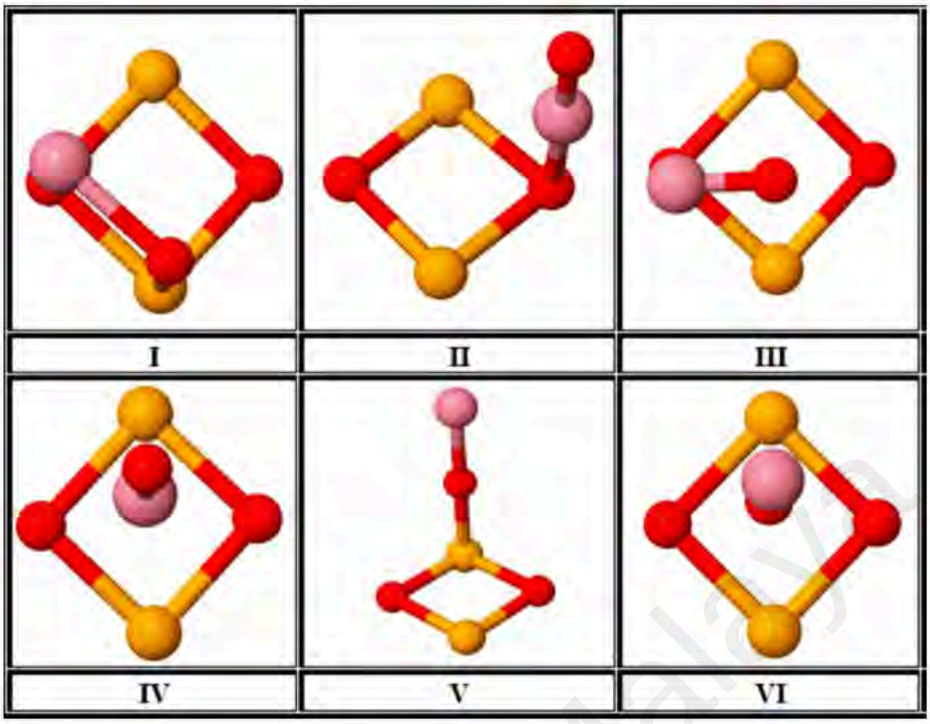

Figure 5.4: Top view of the possible adsorption geometries of CoO molecule on MgO(100). Atom colors: Mg, orange; O, red; Co: pink.

on the different MgO sites in an unequal manner, where the impact of U on O > hollow > > Mg site of the MgO surface and these depend on the degree of interaction with the adsorbed Co atom. Therefore, the total energy of Co adatom on Mg site relative to O site shows considerable variations with U values compared to the corresponding hollow site. However, the Mg site remains less favorable than the hollow or the O site. As a result, the diffusion path keeps constant, while the diffusion barrier slightly varies with U values reported here.

5.4.2 CoO molecule adsorption and diffusion

In the current case, all adsorption geometries of CoO molecule on the MgO(100) surface, shown in the Figure 5.4, are examined. Other possible geometries are simply discarded due to their instability in adsorbing CoO molecule which migrates to form one of the geometries in the Figure 5.4. Our calculations show large negative adsorption energy values (see Table.5.2), indicating that the adsorption process is exothermic. It is

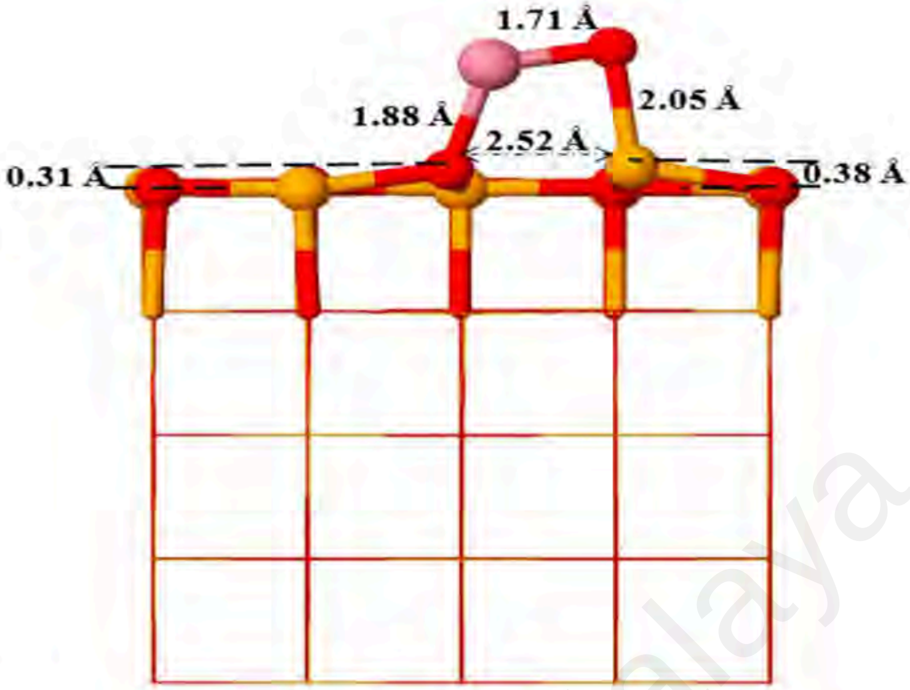

Figure 5.5: Side view of the optimized (I) adsorption geometry of CoO molecule on MgO(100). Atom colors: Mg, orange; O, red; Co: pink.

not surprising, in the most stable adsorption geometries (the upper row of Figure 5.4) to see that the cobalt atom of the CoO molecule is located on top of the oxygen site, in accordance with the data mentioned above, while the oxygen atom of the molecule lies vertically and horizontally with respect to the cobalt.

The maximum adsorption energy occurs when the CoO molecule is held in a position which is isomorphic to that of the MgO substrate (see structure **I**). In this particular case, a strong geometrical distortion is observed (see Figure 5.5), due to the fact that the Co-O bond length in the molecule is significantly shorter by ~ 0.41 Å from the bulk value. This has the effect of pulling apart the surface O and Mg atoms by ~ 0.3 Å thus causing the bond between these adjacent atoms to be broken in order to accommodate the interaction with the CoO molecule (d_{Mg-O} is longer by ~19% than that of the MgO bulk). In addition, the horizontally adsorbed molecule is slightly bent from the Co atom to the surface plane, due to a significant hybridization between 3*d* Co with the surface 2*p* O site orbitals, which is also an explanation for the considerable charge transfer value from the surface

Table 5.2: E_{ad}, adsorption energy (eV), ρ_{Co}, Bader charge (e^{-}) and μ_{Co}, magnetic moment of Co cation (μ_{β}) for different adsorption geometries of CoO molecule on MgO(100) surface

Geometry	E_{ad}	ρ_{CoO}	μ_{Co}
I	-2.66	-0.29	2.61
II	-2.37	-0.16	2.47
III	-2.16	-0.30	2.58
IV	-1.92	-0.21	0.653
V	-1.03	-0.24	2.59
VI	-0.92	-0.28	2.58

to the CoO molecule (see Table.5.2). The magnetic moment of the O atom of the CoO molecule shows a slight polarization (~0.23 μ_{β}), while that of the Co atom is ~2.61 μ_{β} (close to the bulk value ~2.77 μ_{β} (Archer et al., 2008)). Similar findings have been reported for MgO molecule supported on MgO(100) substrate (Geneste et al., 2002).

Figure 5.4 provides an overview of CoO molecule diffusion on the magnesia substrate. It is obvious that two main paths can be suggested to diffuse the CoO molecule from the most stable adsorption site shown in geometry **I**; displacement of the molecule placed vertically on top of the hollow site and the rotation of the CoO molecule about axis on the Co and O atoms. The former makes two saddle-point configurations; geometries **IV** and **VI** which produce relatively large diffusion barriers of 0.74 and 1.75 eV respectively. For the rotational motion, three saddle-point configurations are generated; geometry **III** is produced by 45° horizontal rotation of the molecule around its Co atom, and both geometries **II** and **V** are due to a 90° vertical rotations around its Co and O atoms respectively. From Table.5.2, the calculated diffusion barriers are 0.51, 0.30 and 1.63 eV for these saddle-point configurations respectively.

Apparently, the most favorable diffusion path of the CoO molecule from the above-mentioned paths, is by rotating the molecule vertically 90° degrees around the Co atom placed on the top of the oxygen site of the substrate. On the other hand, pulling the molecule to the hollow site or vertically rotating it around its O atom is energetically unfavorable. Once again, this indicates a strong binding of the Co atom on the O site of the surface. However, the CoO molecule diffuses more freely than the Co atom on the MgO surface, due to its low diffusion barrier, which is smaller by ~26.8% compared to the corresponding Co atom.

5.4.3 CoO growth behavior and magnetic properties

It is well known that MgO is an alkaline substrate where its oxygen anion sites (basic cen- ters) enhance the Co^{+2} cation dispersion, especially with the availability of easy diffusion paths as mentioned previously. Therefore, ensuring the presence of CoO nanoparticles at the initial deposition stage is quite difficult, in accord with experimental data (Zhang et al., 2010). Figure 5.6 shows the energy difference between two- and three-dimensional growth modes of CoO deposit on MgO(100) substrate with various magnetic states as a function of the surface coverage. This figure represents the formation

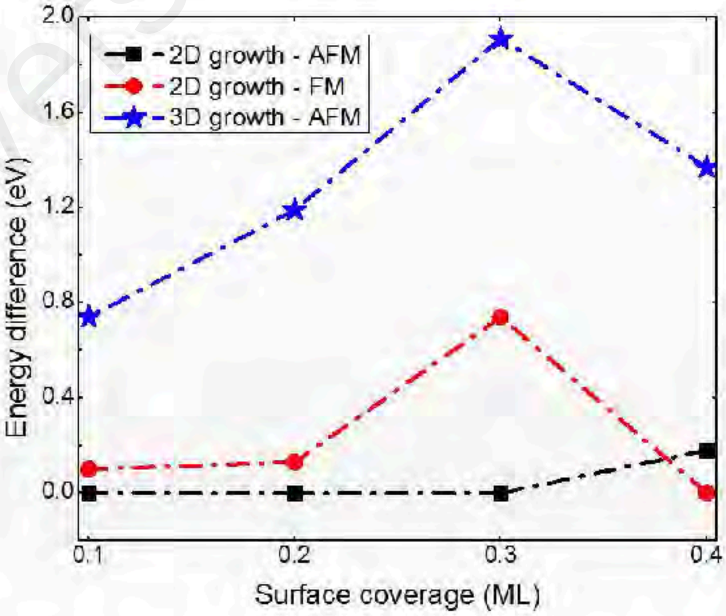

Figure 5.6: Relative energy of CoO growth patterns on MgO(100) at different surface coverage with respect to the magnetic ground state (FM or AFM) of the two-dimensional growth.

of two-dimensional clusters of CoO molecules on MgO(100) which takes place at a surface coverage of less than a half monolayer (< 0.5 ML). This observation seems reasonable by assuming that the weak adsorbate-surface interactions induce nucleation via the Volmer–Weber mechanism (3D cluster growth) while the strong interactions give rise to cluster nucleation by Franck-van der Merwe mechanism (layer-by-layer growth). Accordingly, for the CoO/MgO(100) system, the computed adsorption energy is considerably larger, which reflects that CoO clusters form an intimate contact with MgO substrate, and thus lead to the conclusion that the 2D growth is noticeably preferred compared to the corresponding 3D growth during the deposition process of CoO molecules on MgO. As a general trend, the AFM solution for 2D growth is energetically preferable compared to the FM solution for most coverage reported here, and both are more stable than the 3D growth with AFM solution (as in bulk CoO).

For the purpose of clarifying the growth pattern of CoO/MgO(100) system during the mature growth stage, in particular at the monolayer CoO coverage or a coverage of 8.9 nm^{-2} Co atoms, a gradual shifting from 2D to 3D growth is represented by three configuration models; **I**, **II** and **III** respectively, as shown in Figure 5.7. a. The energetic stability of these configurations follows the order of **I** > **II** > **III** (Figure 5.7. b). Noticeably, the stability is reduced by decreasing the direct interactions between CoO and the substrate. Therefore, the 2D growth of the system is favored by increasing these interactions, but for 3D growth, the opposite is the case. In addition, it is easy to see that the difference of energy between AFM and FM solutions is particularly pronounced (~ 1.2 eV) in the 3D growth of CoO deposit on MgO substrate (configuration **III**), while for configurations **I** and **II**, this energy difference is much lower but still significant (~ 0.2 eV). Two mechanisms that explain the magnetic behaviour of transition metal oxide supported on oxide surfaces are commonly invoked: electronic and geometric. For configuration **I**, as an example,

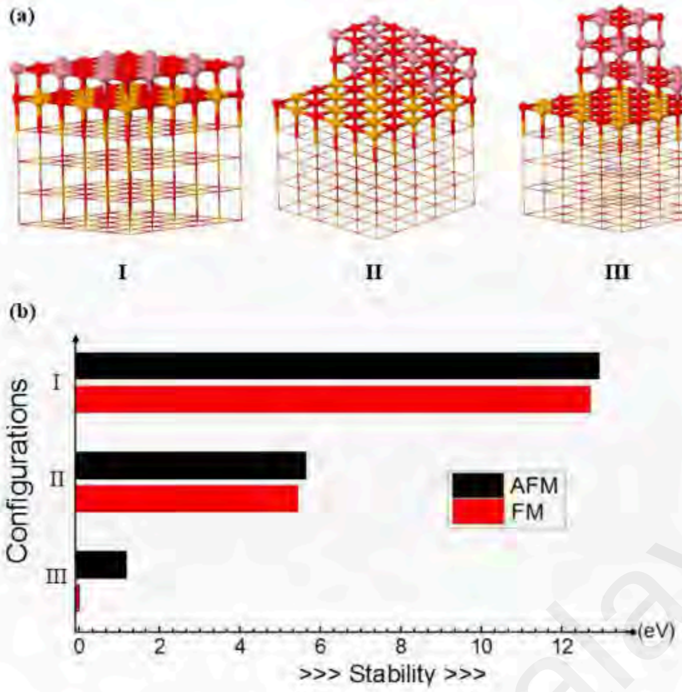

Figure 5.7: (a) Orthogonal views of configuration models of 8.9 nm^{-2} Co atoms coverage (namely, 1 ML) on 4 × 4 cell of the MgO(100) slab in the different growth patterns: I, 2D growth ; II and III, 3D growth (b) Stability of the above configuration models with respect to the FM state of III configuration. Atom colors: Mg, orange; O, red; Co: pink.

both AFM and FM solutions show the same charge transfer value from the substrate to the CoO monolayer (~ 0.12 eV per Co atom), indicating that the AFM order in this model must not be linked to the electronic mechanism via the charge transfer which may facilitate the occurrence of antiparallel magnetic couplings between Co atoms. On the other hand, the structural geometry of CoO monolayer film in configuration **I** has (100) orientation, which is very close to the CoO bulk-like face, where the distance between adjacent Co atoms in the 1 ML film after ionic relaxation is longer by ~ 0.1 Å relative to the calculated bulk value. This permits us to conclude that structure **I** in some degree tends to show the same magnetic behaviour of the bulk CoO which is characterized by a strong AFM coupling between the Co ions. Furthermore, a three-dimensional geometry of the deposited CoO seen in configuration **III** is more intrinsic to the bulk CoO structure, and hence, it shows more antiferromagnetic characteristic as mentioned

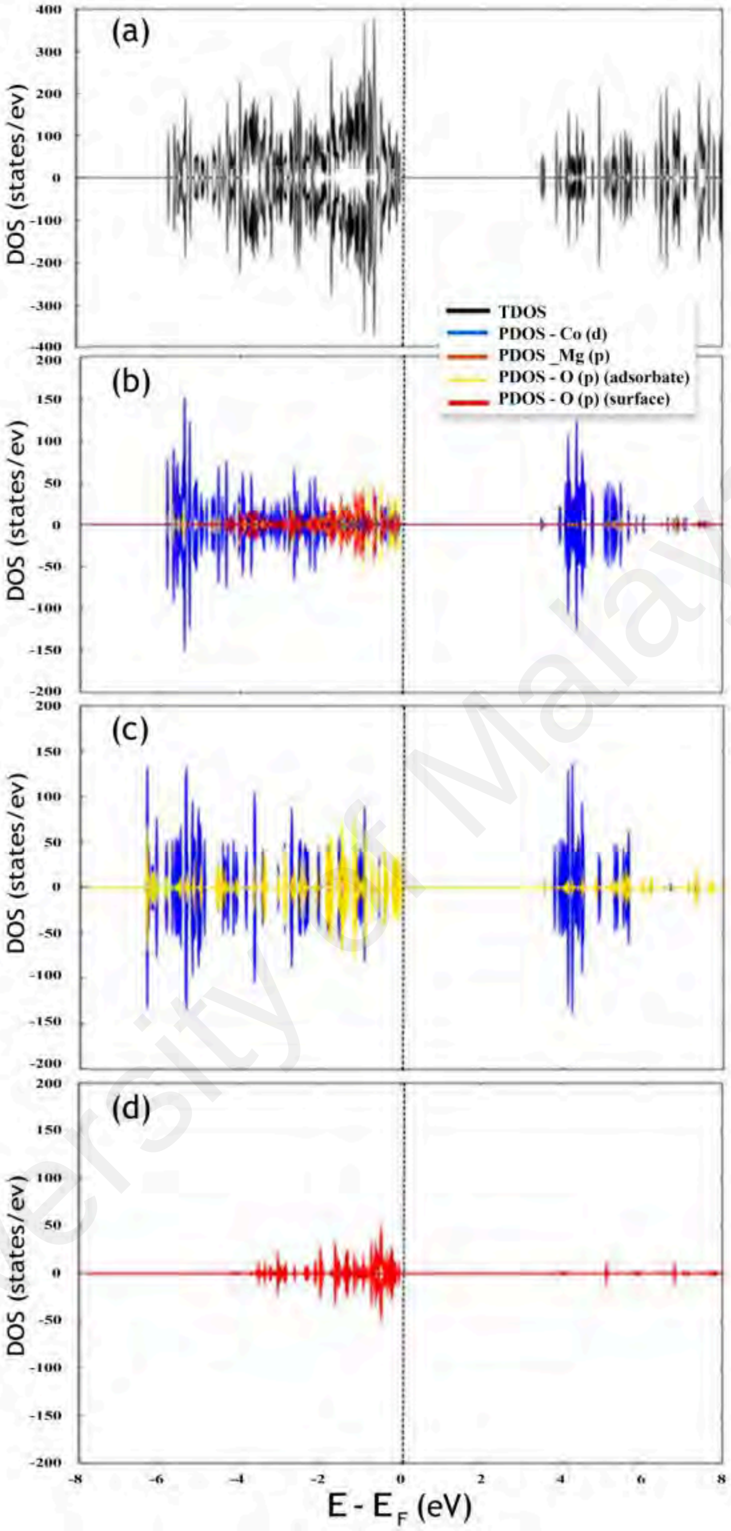

Figure 5.8: Calculated total density of states for a CoO monolayer on MgO(100) (i.e., I configuration model) in (a), and partial density of states for each of these systems: the surface interface for I configuration, the unsupported CoO monolayer and the interface layer of a pure MgO(100) in (b), (c) and (d), respectively.

above. As a result, the interface interaction of the supported CoO on the MgO(100) surface does not change the magnetic coupling of the deposited CoO layer which remains close to that of the bulk CoO, where both show the appearance of AFM state. To confirm this result, further spin-polarized calculations were carried out for the unsupported 1 ML CoO. As expected, the calculated energy difference between FM and AFM solutions has exactly the same value and direction of stability for the supported one, i.e., the AFM solution is more stable by ~ 0.2 eV than the FM one, which means that the magnetism of the supported CoO does not depend on the interaction with the MgO(100) surface. It is worth mentioning that the magnetism of bulk CoO or CoO (100) surface is ascribed to the superexchange interactions occurring between cobalt ions mediated by oxygen, which gives rise to the AFM solution, as previously reported (Staemmler & Fink, 2002).

Figure 5.8 shows the total density of states (TDOS) for a CoO monolayer on the MgO(100) surface, i.e., the above-described configuration **I** model, with AFM solution (see **a**) and the partial density of states (PDOS) for each of the following systems: surface interface (CoO monolayer film + top layer of MgO(100) substrate), the unsupported CoO monolayer and the top layer of a pure MgO(100) surface, as shown in **(b)**, **(c)** and **(d)**, respectively. In **(a)** and **(b)**, both the TDOS of CoO/MgO(100) system and the PDOS of its interface clearly show the symmetrical spin up and spin down states. The latter is quite similar to the combination of PDOS images of its two separate interfaces seen in **(c)** and **(d)**, indicating that the interface interaction of CoO with MgO(100) surface does not significantly change its electronic state distribution. Therefore, this interaction may not influence the magnetic properties of CoO monolayer, in line with the discussion above.

The hybridization between Co 3*d* orbitals of the CoO monolayer and O 2*p* orbitals of the MgO top layer is mainly responsible for the interaction between CoO monolayer and MgO(100) surface. Some depletion of the Co 3*d* state is observed near the Fermi level due to this d-p hybridization (see **(b)**). The O 2*p* and Co 3*d* orbital hybridization is quite obvious from the PDOS distribution. However,there is very little involvement of the Mg 2*p* orbital in the interaction(see **(c)** and **(b)**), implying the non-reactivity of Mg cations of MgO(100) surface which had been reported (Pacchioni & Rösch, 1996; Seminario, 1996).

In comparison with our previous study on the growth morphology of ultra-thin film CoO on α-Al_2O_3(0001) surface, where structural morphologies of the CoO film were different from that of the surface (Zayed et al., 2013), the current results show that the CoO growth exhibits the same crystallographic morphology as the magnesia surface. One known reason for this is because of the small lattice mismatch between CoO film and MgO substrate. Despite the fact that these substrates have a different nature of polarity, in which the α-Al_2O_3(0001) is a polar oxide surface while MgO(100) belongs to a non-polar one, both have produced CoO layer with a relatively stable AFM magnetic state. More investigation is needed to clarify the influence of the substrate morphology and polarity on the magnetic and electronic properties of the deposited CoO material.

5.5 Conclusion

We have used periodic DFT calculations to investigate the growth morphology of CoO deposited on MgO(100) surface. The adsorption and diffusion of Co atom and CoO molecule were calculated using 2x2 and 4x4 supercells. Charge transfer analyses and the density of state calculations of monolayer CoO have been also carried out.

Based on the calculations of adsorption energies of Co on the MgO substrate, it is found that the most preferred binding site for the Co atom is on the O site of the substrate. The interpolated GGA+U potential energy surface of Co binding on the surface indicates that the O site constitutes the minimum, the Mg site is the maximum and the hollow site represents a saddle point for the surface diffusion of Co atom from one oxygen site to the neighboring oxygen sites. Charge transfer analysis indicates that the interaction between Co and the substrate is due to polarization and dispersion forces with a small amount of orbital mixing.

The lowest-energy adsorption structures of CoO on the MgO(100) substrate all have the Co lying on top of the O site. When the CoO molecule lies isomorphically along the MgO substrate (lowest energy structure), there is a strong geometrical distortion where the CoO bond length shortens by 0.41 Å causing the MgO to be about ~19% longer than the bulk. Diffusion of CoO over the magnesia substrate had also been studied. The surface diffusion includes basically the horizontal and vertical rotation steps around its end, where the most favourable diffusion path is the one that involves a 90° rotation about the Co atom. It is also found that CoO moves more freely compared to Co by virtue of the low diffusion barriers.

As far as the growth of CoO layer on the MgO(100) surface is concerned, it is observed that the dominant growth mechanism is 2D compared to 3D growth. This is explained on the basis of a strong adsorbate-surface interaction giving rise to preferential nucleation via layer-by-layer growth. The AFM state is also found to be energetically more favourable compared to the FM state for most of the coverage levels of CoO reported here. Partial density of states and charge transfer characteristics indicate that the interaction between the CoO and MgO(100) surface does not affect the magnetic properties of the former.

CHAPTER 6: ELECTRONIC, MAGNETIC AND STRUCTURAL PROPERTIES OF CO_3O_4(100) SURFACE: A FIRST-PRINCIPLES STUDY

6.1 Introduction

Spinel cobalt oxide (Co_3O_4) plays an essential role in various applications of energy and environment-related areas. For example, the Co_3O_4 is an effective anode material for electrochemical water splitting (Hamdani et al., 2010; Esswein et al., 2009) and a catalyst for many oxidation reactions, including converting chloride to chlorine (Boggio et al., 1985), carbon monoxide to carbon dioxide (Marbán et al., 2008), and ethyl alcohol to acetic acid (Cox & Pletcher, 1990). More recently, supported Co_3O_4 nanoparticles on graphene show promising activities for oxygen reduction, which represents the primary key for renewable-energy technologies such as fuel cells (Liang et al., 2011).

Bulk Co_3O_4 belongs to Fd3m space group and crystallizes in the cubic normal oxide. Its oxygen ions form close-packed face centered cubic (FCC) with cobalt ions of the tetrahedral sites are occupied by Co^{+2} ions, while half of the octahedral sites are occupied by Co^{+3} ions (Zasada et al., 2010). Three most stable (100), (110) and (111) planes exposed by Co_3O_4 are prepared using various methods and their structures are determined by different spectroscopic equipments e.g. X-ray photo-electron spectroscopy (XPS) (Liu et al., 2005; Wang et al., 2009; Klepper et al., 2007; Mane et al., 2002).

A few studies have paid attention to the Co_3O_4 (100) surface (Zasada et al., 2010; Mane et al., 2002). Only two nonstoichiometric models of this surface have been investigated as a function of oxygen potential in these studies. The (1×1) supercell of Co_3O_4 (100) surface is composed of alternate stacking sequence of layers, where one layer involves two cobalt ions (Co^{+2}) with tetrahedral coordination, while the other one contains four cobalt ions with octahedral coordination (Co^{+3}) and eight oxygen ions

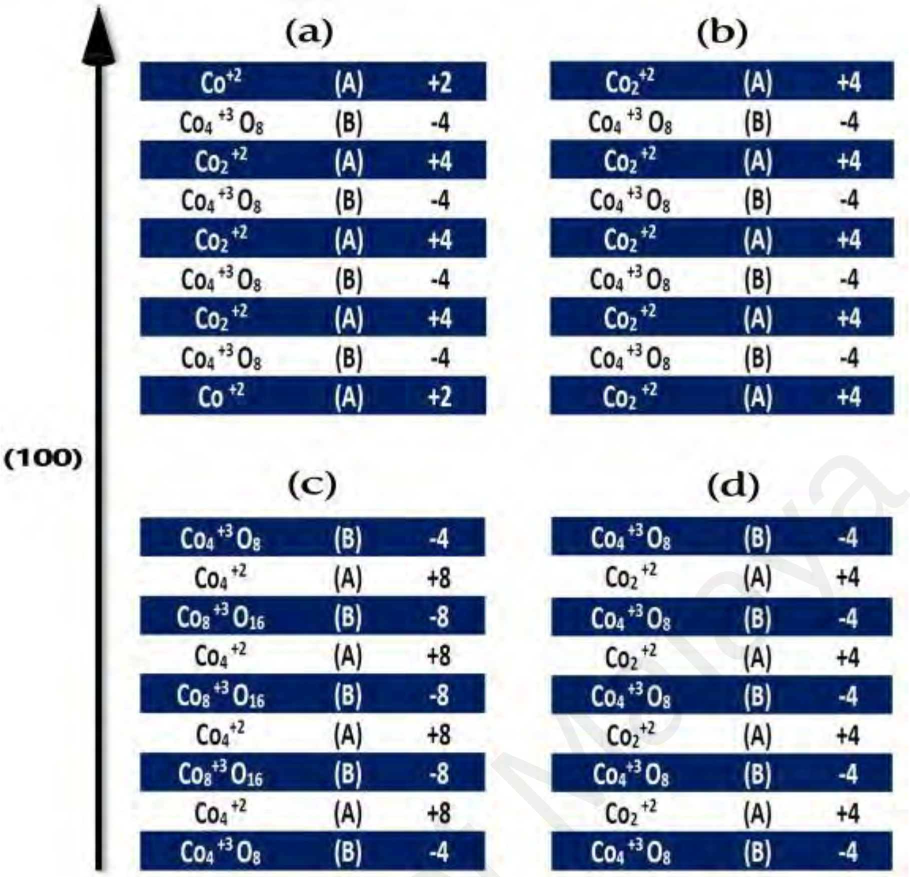

Figure 6.1: Sketch of Co_3O_4 (100) slab models as a stacking of nine charged layers, including the stoichiometric and nonstoichiometric models for both A and B terminations as follows: (a) stoichiometric slab with A-termination (A-stoi), (b) nonstoichiometric slab with A-termination (A-non), (c) stoichiometric slab with B-termination (B-stoi), (d) nonstoichiometric slab with B-termination (B-non).

(O^{-2}). Consequently, two different terminations can be generated, often known as A and B surface terminations. The A termination has both Co^{+3} and Co^{+2} ions, whereas the B termination exposes only Co^{+3} ions. Similar to the ionic nature of bulk Co_3O_4 (Chen et al., 2011), the (100) slab can be viewed as sequential charged layers, depicted in the Figure 6.1. In principle, the stack of charged layers causes increasing polarization with slab thickness, whereas the existence of polarity compensation mechanisms are due to inhibition of “polar catastrophe” (Goniakowski et al., 2007).

Recent studies used DFT calculations within the generalized gradient approximation (GGA) with an on-site Coulomb repulsion U term to study bulk, surfaces and interfaces of Co_3O_4 (Chen et al., 2011; Chen & Selloni, 2012; Vaz et al., 2009; Petitto & Langell, 2004). The GGA+U approach deals effectively with the unwanted de- localization error found in pure GGA calculations, due to the incomplete cancellation of the Coulomb self-interaction of the 3d electrons in the cobalt ions (Cohen et al., 2008). The U_{eff} value of 5.9 eV is proposed by Chen and Selloni (2012), taking the average weight of the calculated U values of different cobalt ions in the bulk based on a linear response approach (Chen et al., 2011). Previous works have determined values of U_{eff} from 2 to 5 eV, which yield qualitatively similar results with regard to the surface electronic structure (Walsh et al., 2007; Zasada et al., 2011). Eventually, the U value of 3.5 eV describes well the experimental data of bulk Co_3O_4, such as the band gap and lattice parameter (Zasada et al., 2011; Montoya & Haynes, 2011); therefore, it is used in this study.

6.2 Literature Review

Despite the growing importance of spinal cobalt oxides in many different areas, the number of computational investigations is very limited in comparison to experimental studies. Some of these efforts are briefly mentioned in this subsection.

High-resolution STEM study combined with periodic GGA and GGA+U density functional (DFT) calculations were used to analyze the shape, structure of the bulk and the surface energies of the (111), (110), and (100) planes present in the Co_3O_4 nanocrystals (Zasada et al., 2011) . The calculated surface energies of the relaxed planes have the following decreasing order: 1.65 J m^{-2} (110) > 1.48 J m^{-2} (111) > 1.38 J m^{-2} (100), which reflect the stability of the (100) plane termination compared to the other lower-index planes, i.e., (111) and (110). This result confirmed previous computational study by Montoya and Haynes (2011), in which different (111) and (110) surface terminations showed less thermodynamic stability compared to the most stable surface (100). In that study, only two nonstoichiometric models of A- and B- terminations for (100) surface were studied as a function of oxygen potential. The (100)-B termination, which only exposed the octahedral Co ion, was thermodynamically preferred under oxygen-rich condition, whereas the (100)-A termination that exposed both octahedral and tetrahedral Co ions was more stable under oxygen-poor condition.

Although the above-mentioned studies demonstrate the relative stability of Co_3O_4 (100) surface, very few studies have been dedicated to detailed structural and magnetic characterization of its possible terminations. However, such kind of studies was previously carried out for the Co_3O_4 (111) and (110) surfaces (Chen & Selloni, 2012; X.-L. Xu et al., 2009). For instance, Chen and Selloni (2012) employ the DFT+U calculations to investigate the energetics, atomic structures, and electronic and magnetic properties of the two possible terminations of the Co_3O_4 (110) surface. The first termination, which exposes the Co^{+3} and Co^{+2} ions, shows stable termination in a broad range of Oxygen chemical potentials. On the other hand, the second termination, which includes only Co^{+3} ions, is preferred under the O-rich condition. Unlike the bulk material, the Co^{+3} ions of the surface layer have nonzero magnetic moments, leading to different magnetic interactions between Co ions. Both terminations show a partial metallic characteristic, due to the existence of surface electronic states in the bottom region of the bulk band gap. These states play a crucial role to stabilize these polarized terminations through the charge compensation mechanism. They found that the polarity was fully compensated when the number of layers reached four.

Six different terminations can be obtained by cutting the spinel cobalt oxide along the (111) plane. Only two of these terminations were selected based on the well-known stability of surfaces with fewer dangling bonds and investigated by using GGA calculation (Xu et al., 2009). Besides that, this study showed that the surface terminated with tetrahedral Co ions is more stable than the surface exposed tetrahedral and octahedral Co ions, and both surfaces showed drastic relaxation for Co^{+2} cations that agrees well with the experimental observations.

In this chapter, we provide a comprehensive theoretical investigation of the energetics, atomic structures, and electronic and magnetic properties of the Co_3O_4 (100) surface using periodic DFT+U calculations. Besides the known nonstoichiometric models of (100) surface, other possible stoichiometric models for each A and B terminations are also examined here.

6.3 Methodology

Periodic density-functional calculations were performed within the projector-augmented wave method (PAW) (Kresse & Joubert, 1999; Blöchl, 1994) as implemented in the VASP 5.3 code (Kresse & Furthmüller, 1996a; Kresse & Furthmüller, 1996b; Kresse & Hafner, 1993). In these calculations, spin polarization was always employed, and the exchange and correlation energies were computed using the generalized gradient approximation GGA in terms of the exchange-correlation functionals proposed by Perdew, Burke, and Ernzerhof (PBE) (Kresse & Furthmüller, 1996b) augmented with the on-site Coulomb repulsion U term in the Co(3d) states. The rotationally invariant approach proposed by Dudarev et al was used to add the Hubbard U term to the GGA functional (Dudarev et al., 1998). The core electrons were replaced with the norm-conserving scalar relativistic pseudopotentials (Troullier & Martins, 1991), while only valance electrons were considered in these calculations, including Co 3d, 4s and O 2s, 2p states. Plane-wave basis sets with cutoffs of 400 eV were applied to expand the electronic states, which gave better convergence for the calculated properties. The forces on the ions, calculated based on the Hellman-Feynman

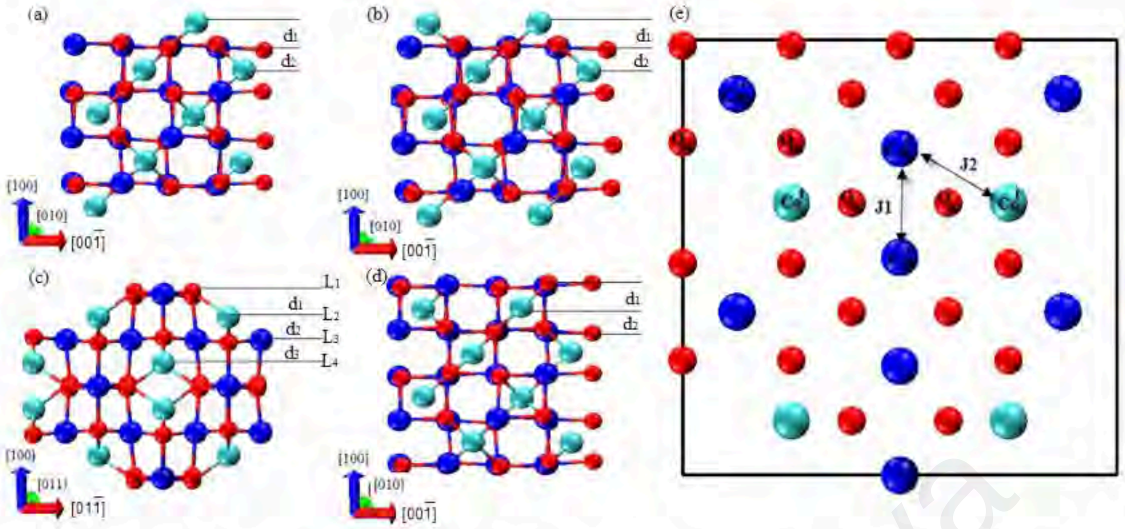

Figure 6.2: Ball and stick models of Co_3O_4 (100): (a) stoichiometric slab with A-termination (A-stoi), (b) nonstoichiometric slab with A-termination (A-non), (c) stoichiometric slab with B-termination (B-stoi), (d) nonstoichiometric slab with B-termination (B-non), (e) top view of the B-stoi models, where the superexchange interactions between surface Co ions are indicated. Distances between the outermost layers (L_1, L_2, L_3 and L_4) are denoted as (d_1, d_2 and d_3). Blue, cyan and red balls indicate Co^O, Co^t and O^{-2} ions, respectively.

theorem and corrected by employing the Harris-Foulkes correction (Harris, 1985). The relaxation of the atomic position was halted when the force on each ion was < 0.01 eV/Å.

Surfaces were modeled by a periodic slab geometry, in which a vacuum width of 27 Å was used to avoid undesirable interactions between consecutive slabs. After optimization, the lattice parameters a = b = 8.15 Å differed by not more than 1% of the experimental values (a = b = 8.08 Å) (Liu & Prewitt, 1990). The symmetric slab of stoichiometric and nonstoichiometric models was used for each A and B termination, which was composed of nine layers to make the total dipole moment zero (Figure 6.2). Slabs with a different number of layers range from seven to eleven layers were also examined, including these exposed A and B terminations on the two opposite sides and have a dipole moment normal to the slab. Overall, we found the surface properties (e.g. the surface electronic structure) can be described well by nine-layers thick slab for both terminations. In these calculations, the square surface cell with 1×1 supercells were employed, and the Brillouin zone integration was performed using (2×2×1) Monkhorst-

Pack *k* points. The energies of surface with nine-layers thick slab using 3×3×1 set of *k* points differed by less than 1 meV from the *k* set used above.

Bader charge analysis (Bader, 1985) was applied to determine the atomic charge using the algorithm proposed by Henkelman and co-workers (Henkelman et al., 2006; Sanville et al., 2007). Some caution must be exercised in interpreting the Bader charge values, since they usually overestimate the dipole moments, and therefore, cannot render precisely the electrostatic properties of a molecule or surface in a solid. Nevertheless, they are still valuable for comparison purposes between different system models, and for giving information about the general trends (Zayed et al., 2013).

6.4 Results & Discussion

6.4.1 Energetic and structures

6.4.1.1 Surface energies

For A-stoi and B-stoi models, the surface energies (γ) are evaluated by;

$$\gamma = \frac{E_{slab} - E_{bulk}}{2A} \tag{6.1}$$

where E_{slab} is the total energy of slab, E_{bulk} is the energy of bulk unit cell comprising the same number of atoms as in slab and *A* is the surface area. Table.6.1 shows the surface energy of both models with different layer numbers. It is obvious that the B-stoi termination reveals low surface energy, which is slightly more stable than the A-stoi. The calculated energy difference does not significantly change with layer thickness, which is in range 16 to 19 meV/$\mathrm{Å}^2$. This could explain the effect of kinetic limitations on the Co_3O_4 thin films grown by pulsed liquid injection MOCVD (Burriel et al., 2005), in which the actual exposed termination depends on the growth conditions during the deposition process.

Table 6.1: Surface energies of Co_3O_4 (100) models with different thickness. The surface energies of nonstoichiometric models, namely A-non and B-non are measured in O-rich limit

	Surface energy (eV/Å^2)			
	A-stoi	A-non	B-stio	B-non
Seven-layer	0.098	0.150	0.079	0.073
Nine-layer	0.097	0.155	0.080	0.070
Eleven-layer	0.097	0.144	0.079	0.080

To study the stability of Co_3O_4 (100) terminations on various experimental conditions, such as oxygen-limiting conditions, it is convenient to consider models with nonstoiciometric slabs, i.e., A-non and B-non models. We measure the surface energy $\gamma(T, p)$ of these slabs as a function of oxygen chemical potential, which defined by the Gibbs free energy $G(T, p, N_{Co}, N_O)$, as follows:

$$\gamma(T,p) = \frac{1}{2A}\left[G^{slab}(T,p,N_{Co},N_O) - N_{Co\mu Co}(T,p) - N_{O\mu O}(T,p)\right] \qquad (6.2)$$

where G^{slab} is the Gibbs free energy of slab, μ_{Co} is the chemical potential of the Co atom, μ_O is the chemical potential of the O atom, A is the surface area of the unit cell, and both N_{Co} and N_O are the numbers of Co and O atoms in the slab, respectively. Under equilibrium condition, $\mu_{Co} = 1/3(\mu_{Co_3O_4} - 4\mu_O)$, where $\mu_{Co_3O_4}$ is the chemical potential of bulk Co_3O_4. Using this relation in Equation (6.2), the following equation for the surface energy can be derived,

$$\gamma(T,p) = \frac{1}{2A}\left[G^{slab}(T,p,N_{Co},N_O) - \frac{1}{3}N_{Co\mu Co_3O_4}(T,p) - \left(\frac{4}{3}N_{Co} - N_O\right)\mu_O(T,p)\right] \qquad (6.3)$$

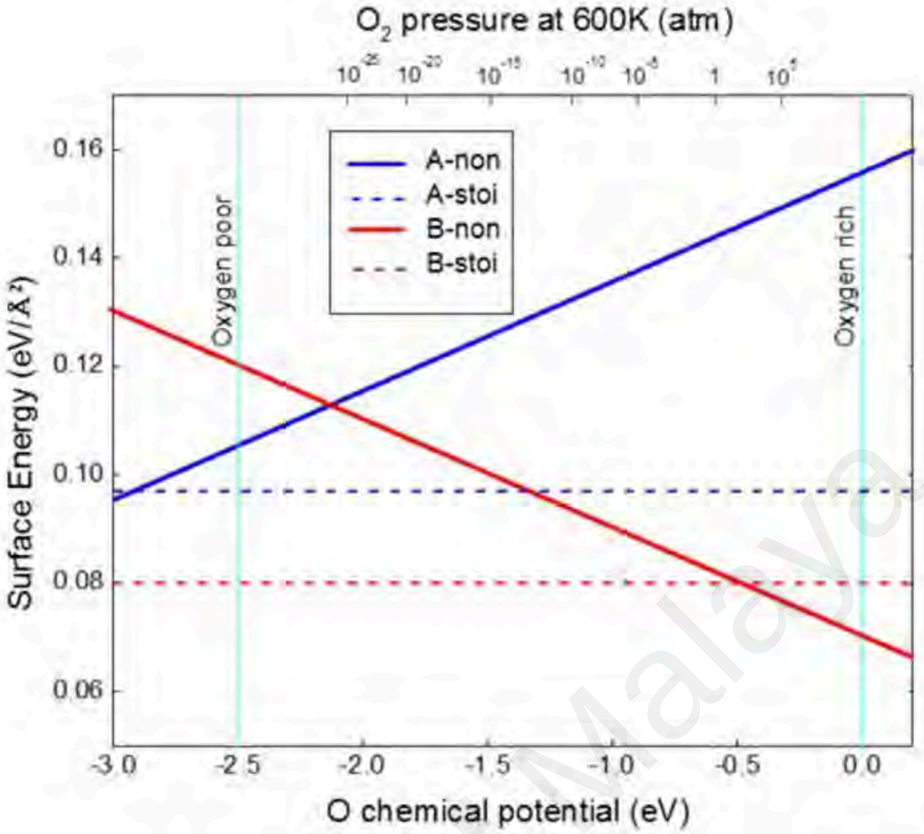

Figure 6.3: Surface energies of the Co_3O_4 (100) models. Vertical lines define the allowed range of the μ'_O . The leftmost line indicates the oxygen-poor limit, while the rightmost line indicates the oxygen-rich limit. Horizontal lines represent the surface energies of both A-stoi and B-stoi models that are μ'_O independent.

In the surface energy diagram (Figure 6.3), $\gamma(T, p)$ is plotted as a function of $\mu'_O = \mu_O (T, p) - \frac{1}{2} E^{tot}_{O_2}$, where $E^{tot}_{O_2}$ is the total energy of the oxygen molecule. The μ'_O range of interest has been determined between the upper and lower boundaries corresponding to the oxygen-rich ($\mu'_O \leq 0$) and oxygen-poor($\mu'_O \geq (\Delta H_f)/4$) conditions, where ΔH_f is the heat of formation of the bulk Co_3O_4. Our calculated μ'_O (0,0) boundaries ($0 \geq \mu'_O \geq -2.50\ eV$) agree well with the previous DFT report (Xu et al., 2009), which estimated these boundaries to be ($0 \geq \mu'_O \geq -2.61\ eV$). The calculated lower limit of μ'_O (0,0) is about 0.2 eV higher than the corresponding experimental value measured under the standard condition, i.e., T= 298.15 K and p= 1 atm (Lide, 2004), and this difference may be due to the ΔH_f value used in Equation (6.3). Calculated surface energies of A-non and B-non slab models at O-rich limit ($\mu'_O \leq 0$) for seven, nine and eleven layers are listed in Table.6.1. Figure 6.3 shows their surface energies in the entire range of μ'_O using nine-layer slabs. For the sake of comparison, this figure also includes the surface energies of the stoichiometric models (i.e., A-stoi and B-stoi), as shown by the horizontal dashed lines. As expected, the B-non model displays high thermodynamic stability under a wide range of possible oxygen chemical potential, while the A-non model becomes energetically preferred at poor oxygen conditions. In general, the stoichiometric models are more stable compared to the nonstoichiometric models in the entire range of μ'_O except near the oxygen-rich limit, where the B-non model shows better stability compared to the B-stio. Clearly, the A-stoi model has a lower surface energy than A-non in the full range of μ'_O.

6.4.1.2 Surface relaxation

For each model, Table 6.2 shows an inward relaxation of the surface layer. This results from the fact that surface ions lose their bulk coordination upon cleaving of the (100) plane, involving Co^{+3}, Co^{+2}, and O^{-2} ions as seen in Figure 6.2. This inward relaxation significantly affects Co^t ions compared to Co^O and O ions, which explains a relatively large contraction associated with A-surface models. Our findings do not point to any lateral displacement of the surface atoms except that in the B-stoi model. This is in contrast to previous theoretical findings for A-non model, which reported the existence of the lateral movement of Co^t ions from the oxygen bridge sites to four-hollow vacant sites on the surface plane.

A common feature of all models is a contraction of Co^t-O bond lengths, of course, due to the low coordination number of Co ions in the surface layer, as shown in Table 6.2. The Co^t-O bond lengths for these models are as follows: A-stoi, 1.80 Å; A-non, 1.85 Å; and B-non, 1.82 Å, where the calculated Co^t-O bond length in the bulk is about 0.15 Å higher than these values. The surface layer of B-stoi model, which has three levels (L_1,

Table 6.2: Atomic displacements from bulklike positions on relaxed Co_3O_4 (100) surfaces. Displacements along [010], [001] and [100] directions are denoted as (Δx, Δy, Δz). The distances between surface layers are represented by (d_1, d_2, d_3) based on the model in the Figure 6.2

		Atomic displacement (Å)			Layer expansion	
		Δx	Δy	Δz	Label	Δ
A-stoi	Co^{t}_{2c}	0.00	0.00	-0.20	d_1	-19.2%
	4 Co^{o}_{5c}	±0.04	±0.04	-0.06	d_2	-10.3%
	6 O_{3c}	±0.03	±0.03	0.00		
	2 O_{4c}	0.00	0.00	0.08		
A-non	2 Co^{t}_{2c}	0.00	0.00	-0.23	d_1	-23.0%
	4 Co^{o}_{5c}	±0.03	±0.03	-0.05	d_2	-10.0%
	4 O_{3c}	±0.04	±0.04	0.07		
	4 O_{4c}	±0.03	±0.03	0.01		
B-stio	4 Co^{o}_{5c}	0.00	0.00	-0.07	d_1	-2.1%
	8 O_{3c}	±0.05	0.00	-0.02	d_2	-3.0%
	4 Co^{t}_{3c}	±0.22	0.00	-0.04	d_3	-4.9%
	4 Co^{o}_{5c}	±0.06	0.00	-0.07		
	4 O_{3c}	0.00	±0.04	0.01		
	8 O_{4c}	±0.04	0.00	0.21		
B-non	4 Co^{o}_{5c}	±0.01	±0.01	-0.09	d_1	-25.9%
	8 O_{3c}	±0.03	±0.03	0.01	d_2	20.1
	2 Co^{t}_{4c}	0.00	0.00	0.21		

L_2 and L_3) as depicted in Figure 6.2, shows different Co^{t}-O bond lengths for different oxygen coordination (henceforth the subscript “nc” denotes the coordination number). For example, about 0.1 Å is the length difference between Co^{t}-O_{4c} bonds of L_3 and Co^{t}-O_{3c} bonds of L_1. In other words, they are shorter by 0.02 Å and 0.11 Å compared to the Co^{t}-O_{4c} bond length in the bulk, respectively. Not surprisingly, the changes in Co^{t}-O bond lengths become more pronounced than for the Co^{o}-O_{3c} bonds, which have values in the range of 1.89 Å- 1.91 Å. However, the change in the lengths of the latter bond reduces the distance between adjacent Co^{o} ions in the surface plane. Further, the Co^{o}_{5c}-O_{4c} bond is comparable in length to that of Co^{o}_{6c}-O_{4c} bond that existed in the bulk.

6.4.2 Surface magnetization

Bulk Co_3O_4, which has the Co^{+2} magnetic ions at tetrahedral sites and the Co^{+3} ions at octahedral sites with zero magnetic moments, is antiferromagnetic (AFM) below T_N ~ 40K (Chen et al., 2011; Xie et al., 2009; Roth, 1964). In agreement with these studies, our spin-polarized calculations confirm the AFM nature of bulk Co3O4 due to the antiparallel alignment between nearest neighbor Co^t ions (i.e., Co^{+2} ions) . In addition, we find the magnetic moment of Co^t ions is $2.65\mu_\beta$ smaller than the experimental value ($3.26\mu_\beta$) (Roth, 1964).

The presence of Co_3O_4 surface breaks the bulk symmetry by reducing the coordination number of the surface ions. Thus, the magnetic behavior of the surface layer may change compared to the bulk. Interestingly, Co^O surface ions show considerable magnetic moments in all Co_3O_4 (100) surfaces, which are distinctly different from the other Co^O ions of the inner layers. The latter ions have the same magnetic moments as the Co^O ions in the bulk (i.e., $0\mu_\beta$). This result is consistent with the early work on Co_3O_4 (110) surface (Chen & Selloni, 2012), in which the Co^{+3} ions of the surface layer had nonzero magnetic moment, shown as underlined arrows in Table 6.3.

As a key to determining the most stable magnetic configuration, we try to analyze the different couplings between the Co magnetic moments. In the surface layer, the presence of the Co^O magnetic ions improves the strength of the superexchange interactions between cobalt ions mediated by oxygen ions. Two types of superexchange interactions are present in all surface models. The first one represents the coupling between two adjacent Co^O ions mediated by an oxygen ion (J1 in Figure 6.2). This superexchange coupling describes the magnetic interactions between Co ions in the same layer, where the Co^O-O-Co^O angle lies in the range 96°-101°. The second type, which represents the normal superexchange

Table 6.3: Surface energies of the Co_3O_4 (100) surface models with various magnetic configurations relative to the lowest energy state, taken as zero. Co^o ions are indicated by underlined arrows, Co^t ions are indicated by arrows without underlines, and bulk-like magnetic configurations represent the Co^o ions with zero magnetic moments.

Surface energy (meV/Å^2)									
A-stoi		A-non		B-stio				B-non	
$\uparrow$ $\underline{\downarrow}\,\underline{\uparrow}\,\underline{\downarrow}\,\underline{\uparrow}$	0.00	$\uparrow\uparrow$ $\underline{\uparrow}\,\underline{\uparrow}\,\underline{\uparrow}\,\underline{\uparrow}$	0.00	$\underline{\downarrow}\,\underline{\uparrow}\,\underline{\downarrow}\,\underline{\uparrow}$ $\uparrow\uparrow\uparrow\uparrow$ $\underline{\uparrow}\,\underline{\uparrow}\,\underline{\uparrow}\,\underline{\uparrow}$	0.00	$\underline{\uparrow}\,\underline{\uparrow}\,\underline{\uparrow}\,\underline{\uparrow}$ $\uparrow\uparrow\uparrow\uparrow$ $\underline{\downarrow}\,\underline{\downarrow}\,\underline{\downarrow}\,\underline{\downarrow}$	13.1	$\underline{\uparrow}\,\underline{\uparrow}\,\underline{\uparrow}\,\underline{\uparrow}$ $\uparrow\uparrow$	0.00
$\downarrow$ $\underline{\uparrow}\,\underline{\uparrow}\,\underline{\uparrow}\,\underline{\uparrow}$	8.5	$\uparrow\uparrow$ $\underline{\downarrow}\,\underline{\uparrow}\,\underline{\downarrow}\,\underline{\uparrow}$	1.0	$\underline{\uparrow}\,\underline{\uparrow}\,\underline{\uparrow}\,\underline{\uparrow}$ $\uparrow\uparrow\uparrow\uparrow$ $\underline{\uparrow}\,\underline{\uparrow}\,\underline{\uparrow}\,\underline{\uparrow}$	2.5	$\underline{\uparrow}\,\underline{\uparrow}\,\underline{\uparrow}\,\underline{\uparrow}$ $\downarrow\downarrow\downarrow\downarrow$ $\underline{\uparrow}\,\underline{\uparrow}\,\underline{\uparrow}\,\underline{\uparrow}$	15.1	$\underline{\downarrow}\,\underline{\uparrow}\,\underline{\downarrow}\,\underline{\uparrow}$ $\uparrow\uparrow$	0.3
$\uparrow$ $\underline{\uparrow}\,\underline{\uparrow}\,\underline{\uparrow}\,\underline{\uparrow}$	14.1	$\downarrow\downarrow$ $\underline{\uparrow}\,\underline{\uparrow}\,\underline{\uparrow}\,\underline{\uparrow}$	5.1	$\underline{\downarrow}\,\underline{\uparrow}\,\underline{\downarrow}\,\underline{\uparrow}$ $\uparrow\uparrow\uparrow\uparrow$ $\underline{\downarrow}\,\underline{\downarrow}\,\underline{\downarrow}\,\underline{\downarrow}$	11.7	$\underline{\uparrow}\,\underline{\uparrow}\,\underline{\uparrow}\,\underline{\uparrow}$ $\downarrow\downarrow\downarrow\downarrow$ $\underline{\downarrow}\,\underline{\downarrow}\,\underline{\downarrow}\,\underline{\downarrow}$	16.6	$\underline{\uparrow}\,\underline{\uparrow}\,\underline{\uparrow}\,\underline{\uparrow}$ $\downarrow\downarrow$	1.1
Bulklike	9.1	Bulklike	35.1	Bulklike	16.7			Bulklike	15.2

interactions occur between two types of cobalt ions located in different surface planes and separated by one oxygen ion (J2 in Figure 6.2). Its Co^o-O-Co^t angle ranges from 115° to 129°, larger than the Co^o-O-Co^o angle of the former type. Finally, we discard the weak superexchange between two Co ions separated by two O ions that existed in bulk-like layers.

The Goodenough–Kanamori-Anderson (GKA) rules imply that the J1 superexchange type with a Co-O-Co angle close to 90° causes the weak ferromagnetic (FM) exchange between these two Co ions. For the J2 superexchange type, where the metal-oxygen-metal angle is close to 120°, they fail to provide a well-defined prediction for the magnetic coupling between metal ions. However, Table 6.3 shows the surface energies of the Co_3O_4 (100) surface models with various magnetic configurations relative to the ground state energy taken as zero.

In general, the surfaces of stoichiometric slabs reveal a strong AFM superexchange interaction, whereas the nonstoichiometric slabs exhibit a weak FM interaction. Apparently, the ground-state magnetic configuration for each of these surfaces depends on the total effect of Co^{o}-O-Co^{o} and Co^{o}-O-Co^{t} superexchange interactions, which in turn relies on the magnitude of the surface relaxation. On the nonstoichiometric models, the large inward relaxation of their surface layers has a strong influence on the surface magnetic configurations. It makes the magnetic Co ions freely interact with each other to accommodate different magnetic configurations, and thus reducing the energy differences between these configurations, as shown in Table 6.3. In contrast, the stoichiometric models have relatively large energy difference between AFM and FM arrangements, this would amounts to 14.1 meV/Å^2 in the A-stio model. Unexpectedly, we find that the Co^{o} ions of the ground-state magnetic configuration of A-stio surface show AFM couplings rather than regular FM based on GKA rules. This refers to the ability of Co^{o}-O-Co^{t} superexchange to change the weak FM behavior of the Co^{o}-O-Co^{o} one.

6.4.3 Surface electronic structures

Recent experimental and theoretical investigations on different Co_3O_4 surfaces reveal the role of surface electronic states in making the bulk band gap shorter (Chen & Selloni, 2012; Sun et al., 2010). This allows a partial metallic characteristic to emerge, which may strongly affect the physical and chemical properties of these surfaces. Therefore, it is of interest to study surface states in the Co_3O_4 (100) surface not only to explore the partial metallization, which may become more common in the transition metal oxides, but also to investigate the electronic interactions between the surface ions. According to our calculations, the inner layers of Co_3O_4 (100) surfaces have similar density of states as in the bulk. For this reason, we only consider the electronic states of surface ions compared

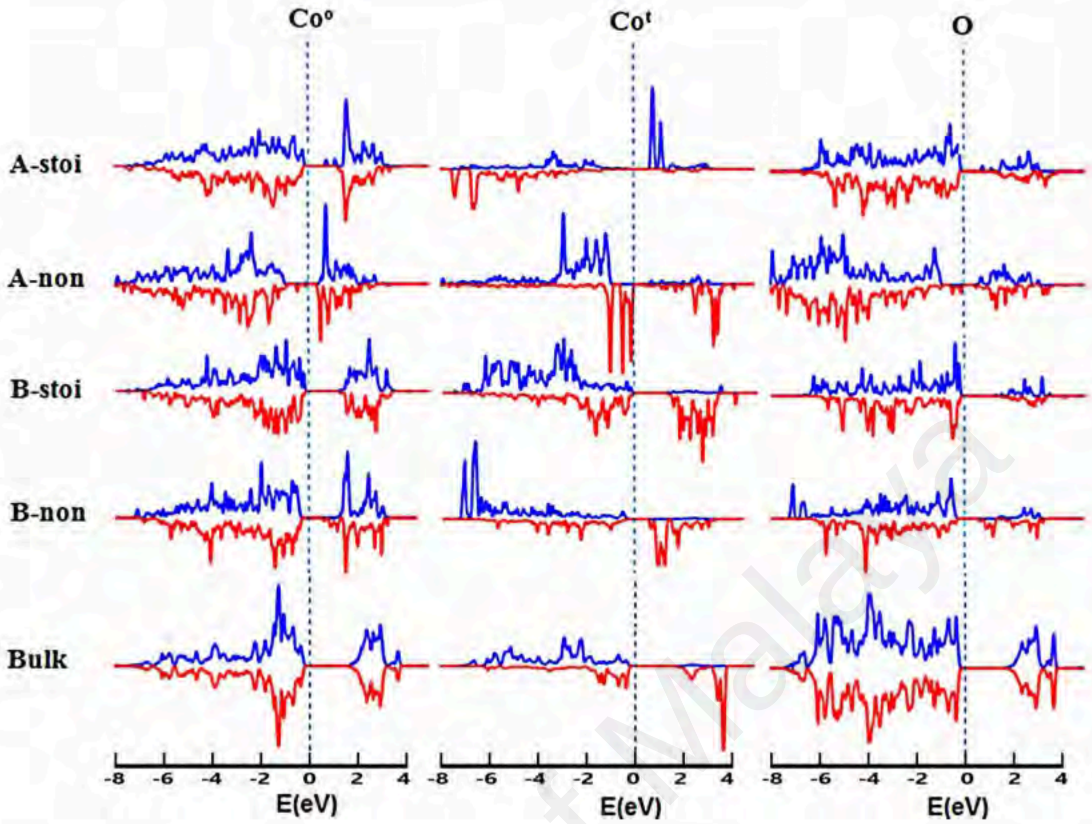

Figure 6.4: Majority (blue profile) and minority (red profile) density of states of octahedral (Co^{o}) and tetrahedral (Co^{t}) cobalt ions of the surface layer for different slab models in comparison with the bulk case.

to that of the bulk.

Figure 6.4 shows the atomic-projected density of states (PDOS) of Co^{o}, Co^{t}, and O ions for each surface terminations. It is easy to see that these ions have different electronic-state distributions compared to that of the bulk. Most importantly, some of these surface states are in the bulk band gap, indicating the presence of metallic character in varying degrees in all these Co_3O_4 (100) surfaces. By gathering the PDOSs of surface ions, the A-non model exhibits the strongest metallic behavior with a narrow band gap compared to the B-stoi model, which has band gap of about 1.15 eV. This result, like several of the earlier ones, highlights the promising role of Co_3O_4 surfaces in the study of surface redox reactions.

The valence band of Co_3O_4 (100) surfaces, which extends from -8 to 0 eV, contains a mixture of 3d-Co and 2p-O states. Noticeably, the presence of these states near the Fermi level shows a strong hybridization between them, which explains the shorter Co-O bonds as mentioned above. On the B-stio termination, the valence band of Co ions near the Fermi level consists of 3d-Co^o spin states associated with a significant contribution of 3d-Co^t states, in particular, that at -4 eV. This is in agreement with the valence-band photoemission study of Co_3O_4 epitaxy on CoO (100) (Langell et al., 1999), where the peak at the top of Co_3O_4 valence band mainly consisted of 3d-Co^o states, overlapping with 2p-O states. Some 3d states of Co^t sublattice, especially those found at -3.8 eV, were also present at the top of the valence band.

On the A-non termination, the electronic states cover most of the bulk band gap region with higher polarity in this surface than others. This comes from the fact that a depolarization field is necessary to stabilize the polarized surfaces by changing their electronic surface states in a way that some states emerge in the bulk band-gap region. This, in turn, allows free charge to flow within the surface layers to neutralize the polarized surfaces.

6.4.4 Charge compensation

Several experimental and theoretical studies have investigated the charge compensation process, whereby the microscopic dipole moments generated by stacking the alternating layers in polar surfaces are vanishing, stabilizing the polar surfaces. The compensated charge (σ_c) is observed to be strongly correlated to the charge density of the bulk termination layer (σ) and the relaxation of the surface layers. This is expressed as;

$$\sigma_c = \sigma\left[\frac{R_1}{R_1 + R_2}\right] \tag{6.4}$$

where R_1 is the mean distance between adjacent anion and cation planes, and $R_1 + R_2$ is the mean distance between the neighboring planes with similar chemical compositions, namely the distance of a layer with its next-neighboring layer (Goniakowski et al., 2007). It reasonable to expect that the topmost layer exhibits a significant compensated charge compared to the inner layer, due to the fact that the topmost layer is subjected to a large relaxation compared to the rest of the surface layers (Chen & Selloni, 2012).

Transition metal oxides (TMO) form bonds with a considerable hybridization between TM and O ions, leading a partially covalent character associated with this type of bond. As a result, the net ionic charges of the TM ions are essentially independent of their oxidation. According to the present calculations of the bulk Co_3O_4, the Co^t ion has a charge of about +1.27 rather than its formal charge of +2, while both of Co^t and O ions possess a charge of about +1.32 and -0.98 instead of +3 and -2, respectively.

The presence of compensated charge for different Co_3O_4 (100) surface terminations can be computationally detected by calculating the total charge for each topmost layer compared to that of the corresponding bulk layer. For comparison between different terminations models with different chemical compositions, the total charge is given per Co ion, where the charge of the determined layer in both surface and bulk is divided by its number of cobalt ions. It was found that the total charge of the topmost layer of the four models are as follows: A-stoi, +1.12; A-non, +0.74; B-stoi, -0.56; -0.56; and B-non, -0.47. In the bulk, the A-termination layer has a charge of about +1.27, while the charge of B-termination layer is about -0.64. Thus, the total charge difference between the topmost layers of the studied surfaces and their corresponding bulk values are 0.15, 0.53, 0.08 and 0.17 for A-stoi, A-non, B-stoi and B-non, respectively. Apparently, the nonstoichiometric Co_3O_4 (100) surfaces have more total charge difference compared to the stoichiometric surfaces in order to compensate the polarity.

These results manifest the well-known inverse relation between the surface energy and the polarity, in which the energetic stability of B-stoi > A-stoi > B-non >>> A-non at high oxygen condition, while the surface polarity has the opposite sequence. In conclusion, the stoichiometric Co_3O_4 (100) surfaces are more stable and have less polar surfaces; therefore, a small compensating charge is needed to stabilize these surfaces. This is in contrary to the nonstoichiometric ones.

6.5 Conclusion

Because of the importance of tricobalt tetraoxide (Co_3O_4) surfaces in many potential applications and the remarkable stability of its (100) plane, we employed DFT+U approach to study the structural, electronic, and magnetic properties of the Co_3O_4 (100) surface. The study takes into accounts all possible surface terminations, including the stoichiometric and nonstoichiometric models for each A and B termination.

The results show an inward atomic relaxation in all surfaces models, where the relaxation of Co^t ions is obviously larger than that of Co^o and O ions. Surface energy calculations reveal the higher stability of stoichiometric models compared to the nonstoichiometric ones. For instance, the B-stoi model is more stable than other models over a wide range of the oxygen chemical potential, but the B-non model becomes more stable under oxygen-rich condition. In contrast to bulk, the Co^{+3} ions are magnetic at the surface, leading to different magnetic behavior. This result agrees well with previous computational findings on the Co_3O_4 (110) surface (Chen & Selloni, 2012) and experiments on Co_3O_4 nanoparticles (Takada et al., 2001; Benitez et al., 2009; Taghizadeh, 2016).

From DOS calculations, we find significant variations in electronic states of Co^o, Co^t and O^{-2} ions compared to that of the bulk. In all models, we noticed the existence of several surface states in the bulk band gap, which induce the appearance of metallic character in different degrees. The A-non model displays the highest metallic nature without a detected band gap, while the B-stoi shows the smallest band gap of 1.15 eV. In addition, these states may play a crucial role in stabilizing these polar terminations by providing a depolarizing field. Finally, the nonstoichiometric Co_3O_4 (100) surfaces (in particular, the A-non model) are more polar than stoichiometric ones, and thus the stability of these previously studied models is relatively small.

CHAPTER 7: CONCLUSIONS AND FUTURE RESEARCH

7.1 Conclusions

In Chapter 3 of this thesis, we reported our investigation of the ground-state structures of Co_nO_n ($n = 3 - 7$) clusters using our newly designed code -The Universal Genetic Algorithm (UGA)-followed by accurate DFT refinement. Our UGA code improved the GA performance by including multi-convergence relaxation approaches within the framework of pool genetic-algorithm methodology, which is advantageous and flexible enough that one can use these implemented approaches in any desired order. For the first time, the results showed new global minimum structures for Co_5O_5 and Co_6O_6 clusters. Other ground-state structures have also been found in different cluster sizes studied in this work. Some of the presented structures are identical to previous literary works. By analyzing the energy-structure relationship of Co_nO_n ($n = 3 - 7$) clusters, we found that the structural transition from 2D to 3D shapes occurred at n=5 cluster size, in contrary to previous studies. The results revealed the remarkable stability of Co_4O_4 cluster with ring-like structures, which is in excellent agreement with experimental and computational findings.

As discussed in Chapter 4, we applied our modified basin-hopping Monte Carlo algorithm (MBMC) accompanied with accurate DFT calculations to study further the structural, electronic and magnetic properties of stoichiometric cobalt oxide clusters CoO_n^q ($n = 3 - 10, q = 0, +1$). The basin-hopping Monte Carlo algorithm was designed based on the previous work of Rondina and Da Silva (2013), in which different operators were used to generate a wide scale of atomic displacement in order to completely explore the potential energy surface. The most stable structures for each CoO cluster size have been investigated and compared with previous studies. The intrinsic stability of $(CoO)_4$ was confirmed by the results of binding energy, second-order total energy difference, chemical hardness, chemical potential and HOMO-LUMO gap. Interestingly, the total spin magnetic moments of the global minimum structures of the cobalt oxide clusters showed that the oscillation mode between low-spin and high-spin configurations for both $(CoO)_8$ and $(CoO)_4$ have fully antiferromagnetic solutions, whereas $(CoO)_{10}$ cluster exhibited the highest spin configuration compared to the smaller clusters. By choosing $(CoO)_4$ as a case study, the result revealed that ferromagnetic spin ordering of nearest neighboring Co atoms affected the magnetic properties of the mediate oxygen atom and was accompanied by the elongation of Co-Co bond due to polarization effects. To accommodate the variance in the spin magnetic ordering associated with changing the $(CoO)_4$ cluster symmetry from C_{2v} to D_{4h}, the magnetic solution differed greatly from antiferromagnetic to ferromagnetic super-exchange coupling according to the Goodenough-Kanamori-Anderson rule. In addition, we found that this change to the ferromagnetic D_{4h} structure is related to the noticeable downshift of the valence band of spin-up electrons to the low-energy region, leading to asymmetric density of states between spin-down and -up electrons over the $(CoO)_4$ structure. In addition, dissociation potential energy surfaces were calculated to show all possible dissociation pathways of neutral and cationic cobalt oxide clusters by the loss of one or more $(CoO)^q$ molecules. Once again, the dissociation pattern of $(CoO)^q$ clusters confirmed that $(CoO)_4$ and $(CoO)_4^+$ are the most stable clusters compared to others.

In chapter 5, besides analyzing the growth mechanism of cobalt oxide (II) on the magnesia surface using DFT+U calculations, we addressed the diffusion and adsorption behaviors of cobalt atom and cobalt oxide (II) molecule on the MgO(100) surface as initial steps to understanding the growth of the CoO film. Not only the charge transfer but also the density of state distribution were calculated to evaluate the magnetic and electronic properties of the CoO/MgO(100) system. Supported by the interpolated map of the potential energy surface of the Co atom adsorbed on the magnesia surface, we indicated that the top of O site represented the most preferred adsorption site, while the Mg site formed a saddle point of the Co atom diffusion between two adjacent O sites on MgO(100) surface, in contrary to previous works. The nature of interaction between Co adatom and the MgO substrate can be mainly explained by the existence of dispersion and polarization forces with a limited orbital mixing. We found that the CoO molecule adsorbed isomorphically along the magnesia surface and was structurally distorted where the CoO bond length became less than its bulk value, causing the underneath MgO to elongate compared to the bulk MgO. In addition, the preferred diffusion channel of CoO on MgO(100) was found to include the vertical and horizontal rotations about its O and Co atoms. We also found that the CoO molecule diffuse more freely than the Co atom above the MgO(100) surface. In addition, the results showed that the CoO layer growth on MgO(100) surfaces formed by the 2D growth mechanism. Furthermore, we found that by using the density of state distribution and charge transfer calculations, the adsorption of CoO layer on the MgO(100) surface did not affect the magnetic characteristic of the CoO layer. Therefore, similar to the bulk, the antiferromagnetic spin ordering was energetically more preferred compared to the ferromagnetic one.

As discussed in Chapter 6, we investigated the energetics, atomic structures, and electronic and magnetic properties of the possible terminations of the Co_3O_4 (100) surface, including the stoichiometric and non-stoichiometric surface models using density functional theory combined with the on-site Coulomb repulsion U term. In all the considered Co_3O_4 (100) models, we found that an inward atomic relaxation occurred at the surface layer. In general, surface energy calculations showed that the stoichiometric models were energetically more stable than non-stoichiometric ones. Both the B-stio and B-non models represented the most stable surfaces over a broad range of oxygen chemical potential and under oxygen-rich condition, respectively. We showed that the Co^{+3} ions, in contrast to bulk, have magnetic spin at the surface, explaining the remarkable magnetic properties of Co_3O_4 (100). This result in is excellent agreement with previous reports, which was more likely responsible for the observed changes in the electronic states of Co^o (Co^{+3}) ions compared to the bulk. Changes in the electronic states were also detected for Co^t (Co^{+3}) and O^{-2} ions. Similar to the previous work on the Co_3O_4 (110) surfaces, we noticed the presence of several electronic states of the surface in the upper half of the bulk band gap. These electronic states made the metallic properties with the different degrees to appear in the studied Co_3O_4 (100) models, which played a crucial role in stabilizing these polar terminations via the charge compensation mechanism.

7.2 Future Research

Our UGA and MBHMC codes have successfully employed to investigate the global and local minimum structures of cobalt oxide (II) clusters. It is a one of our interests to examine the capability of the UGA and MBHMC algorithms to explore the potential energy surfaces of a wide range of metal oxide nanoclusters, which has been less studied. For developmental purposes, improving both codes is also one of our interest and we plan to continue this by adopting the following processes: (a) adopting these algorithms to deal with clusters containing many atom types with different atomic ratios (for example, to the best of our knowledge, there is no study that explore the structure of Co_3O_4 clusters using these efficient algorithms), (b) implementation of interfaces and other electronic structure methods in the relaxation and refinement steps using an efficient parallel algorithm, and (c) developing our codes to explore the ground-state structures of clusters adsorbed on metal and metal oxide surfaces.

We aspire, in view of the scarcity of theoretical investigations, to enhance our knowledge and understanding of cobalt oxide nanofilms supported on different metal oxide surfaces. For example, we had investigated the growth, structure, magnetic, and electronic properties of CoO/MgO (100) surfaces, but our aspiration goes beyond that. We desire not just to study how properties of CoO layers on the MgO surface will be affected by changing the surface orientation such as 111, and 110 surfaces but also to extend this type of study to include a variety of metal oxide surfaces with a different degree of polarity. We look forward to getting a chance to further study the nanofilm properties of the most stable form of cobalt oxides, i.e., Co_3O_4 on different metal and metal oxide substrates in order to unravel the secret behind its multiple catalytic activities.

The above-mentioned interests represent, in general, the first stage of our main goal, which is studying the reactivity of clusters, films, and surfaces of cobalt oxides in many significant reactions of industrial applications. Currently, we hope that this thesis has partially succeeded in proceeding towards this goal and to contribute valuable findings to the literature.

REFERENCES

Abad-Elwahad, S. M., Bukhzam, A. F., & Mekhemer, G. A. (2015). A study of the precursor variation on the surface characterization of supported cobalt oxide catalyst. *American Journal of Materials Science*, *5*(2A), 1–5.

Aguilera-del Toro, R., Aguilera-Granja, F., Vega, A., & Balbás, L. (2014). Structure, fragmentation patterns, and magnetic properties of small cobalt oxide clusters. *Physical Chemistry Chemical Physics*, *16*(39), 21732–21741.

Alander, J. T., & Alander, J. T. (1994). Indexed bibliography of genetic algorithms in chemistry and physics. *Acta Crystallographica Section B: Structural Science*, *732*, 468.

Alaria, J., Cheval, N., Rode, K., Venkatesan, M., & Coey, J. (2008). Structural and magnetic properties of wurtzite CoO thin films. *Journal of Physics D: Applied Physics*, *41*(13), 135004.

Ali, M., Gomaa, A., Fouad, O. A., Makhlouf, S. A., Yusoff, M. M., & Chong, K. F. (2016). Optical and electrochemical properties of Co_3O_4/SiO_2 nanocomposite. *Advanced Materials Research,1133*, 447–451.

Amin-Chalhoub, E., Duguet, T., Samélor, D., Debieu, O., Ungureanu, E., & Vahlas, C. (2016). Chemical vapor deposition of low reflective cobalt (II) oxide films. *Applied Surface Science*, *360*, 540–546.

Andricioaei, I., & Straub, J. E. (1997). On Monte Carlo and molecular dynamics methods inspired by Tsallis statistics: Methodology, optimization, and application to atomic clusters. *The Journal of Chemical Physics 107*(21), 9117–9124.

Anisimov, V. I., Aryasetiawan, F., & Lichtenstein, A. (1997). First-principles calculations of the electronic structure and spectra of strongly correlated systems: the LDA+ U method. *Journal of Physics: Condensed Matter*, *9*(4), 767.

Anisimov, V. I., Zaanen, J., & Andersen, O. K. (1991). Band theory and Mott insulators: Hubbard U instead of stoner I. *Physical Review B*, *44*(3), 943.

Archer, T., Hanafin, R., & Sanvito, S. (2008). Magnetism of CoO polymorphs: density functional theory and Monte Carlo simulations. *Physical Review B*, *78*(1), 014431.

Asgari, M., Behnejad, H., & Fortunelli, A. (2014). Composition-dependent melting behaviour of Na_xK_{55-x} core–shell nanoalloys. *Molecular Physics*, *112*(22), 2933–2944.

Back, T. (1996). *Evolutionary algorithms in theory and practice: Evolution strategies, evolutionary programming, genetic algorithms* (pp. 65-104). New York: Oxford university press.

Bader, R. F. (1985). Atoms in molecules. *Accounts of Chemical Research*, *18*(1), 9–15.

Bader, R. F. (1990). *Atoms in Molecules: A Quantum Theory* (Vol. *22*, p. 130). Oxford: Clarendon Press.

Bahn, S. R., & Jacobsen, K. W. (2002). An object-oriented scripting interface to a legacy electronic structure code. *Computing in Science & Engineering*, *4*(3), 56–66.

Bajdich, M., García-Mota, M., Vojvodic, A., Nørskov, J. K., & Bell, A. T. (2013). Theoretical investigation of the activity of cobalt oxides for the electrochemical oxidation of water. *Journal of the American Chemical Society*, *135*(36), 13521–13530.

Bandow, B., & Hartke, B. (2006). Larger water clusters with edges and corners on their way to ice: Structural trends elucidated with an improved parallel evolutionary algorithm. *The Journal of Physical Chemistry A*, *110*(17), 5809–5822.

Barthwal, S., & Lim, S.-H. (2015). Fabrication of long-term stable superoleophobic surface based on copper oxide/cobalt oxide with micro-nanoscale hierarchical roughness. *Applied Surface Science*, *328*, 296–305.

Bauschlicher, C. W. (1995). A comparison of the accuracy of different functionals. *Chemical Physics Letters*, *246*(1-2), 40–44.

Becke, A. D. (1993). Density-functional thermochemistry. III. The role of exact exchange.*The Journal of Chemical Physics*, *98*(7), 5648–5652.

Becke, A. D. (1996). Density-functional thermochemistry. IV. A new dynamical correlation functional and implications for exact-exchange mixing. *The Journal of Chemical Physics*, *104*(3), 1040-1046.

Belyaev, S. N., Panteleev, S. V., Ignatov, S. K., & Razuvaev, A. G. (2016). Structural, electronic, thermodynamic and spectral properties of Mg_n (n= 2–31) clusters. A DFT study. *Computational and Theoretical Chemistry*, *1079*, 34–46.

Benitez, M. J., Petracic, O., Tüysüz, H., Schüth, F., & Zabel, H. (2009). Decoupling of magnetic core and shell contributions in antiferromagnetic Co_3O_4 nanostructures. *EPL (Europhysics Letters)*, *88*(2), 27004.

Bloch, F. (1929). Über die quantenmechanik der elektronen in kristallgittern. *Zeitschrift Für Physik*, *52*(7-8), 555–600.

Blöchl, P. E. (1994). Projector augmented-wave method. *Physical Review B*, *50*(24), 17953.

Blöchl, P. E., Jepsen, O., & Andersen, O. K. (1994). Improved tetrahedron method for Brillouin-zone integrations. *Physical Review B*, *49*(23), 16223.

Bogdan, T. V., Wales, D. J., & Calvo, F. (2006). Equilibrium thermodynamics from basin-sampling. *The Journal of Chemical Physics*, *124*(4), 044102.

Boggio, R., Carugati, A., Lodi, G., & Trasatti, S. (1985). Mechanistic study of $C1_2$ evolution at Ti-supported Co_3O_4 anodes. *Journal of Applied Electrochemistry*, *15*(3), 335–349.

Bošković, B., & Brest, J. (2016). Genetic algorithm with advanced mechanisms applied to the protein structure prediction in a hydrophobic-polar model and cubic lattice. *Applied Soft Computing*, *45*, 61–70.

Boussendel, A., Baadji, N., Haroun, A., Dreyssé, H., & Alouani, M. (2010). Effect of substrate strain on calculated magnetic properties and magnetic anisotropy energy of CoO. *Physical Review B*, *81*(18), 184432.

Bredow, T., & Gerson, A. R. (2000). Effect of exchange and correlation on bulk properties of MgO, NiO, and CoO. *Physical Review B*, *61*(8), 5194.

Brown, R. D., & Martin, Y. C. (1997). Designing combinatorial library mixtures using a genetic algorithm. *Journal of Medicinal Chemistry*, *40*(15), 2304–2313.

Bulger, D. (2005). Quantum basin hopping with gradient-based local optimisation. Retrieved April 10, 2017 from arXiv:quant-ph/0507193v1.

Burke, K., Perdew, J. P., & Ernzerhof, M. (1998). Why semilocal functionals work: Accuracy of the on-top pair density and importance of system averaging. *The Journal of Chemical Physics*, *109*(10), 3760–3771.

Burriel, M., Garcia, G., Santiso, J., Abrutis, A., Saltyte, Z., & Figueras, A. (2005). Growth kinetics, composition, and morphology of Co_3O_4 thin films prepared by pulsed liquid-injection MOCVD. *Chemical Vapor Deposition*, *11*(2), 106–111.

Buttrey, D. J. (2006). Metal oxides: Chemistry and applications edited by J. L. G. Fierro (National Council for Scientific Research (CSIC), Madrid, Spain). CRC Press/Taylor & Francis Group: Boca Raton, FL. 2006. xxii + 783 pp. $179.95. ISBN 0-8247-2371-6. *Journal of the American Chemical Society*, *128*(34), 11315–11316.

Calzado, C. J., Hernández, N. C., & Sanz, J. F. (2008). Effect of on-site Coulomb repulsion term U on the band-gap states of the reduced rutile (110) TiO_2 surface. *Physical Review B*, *77*(4), 045118.

Campbell, C. T. (1997). Ultrathin metal films and particles on oxide surfaces: structural, electronic and chemisorptive properties. *Surface Science Reports*, *27*(1), 1–111.

Cassam-Chenaï, P., & Jayatilaka, D. (2001). Some fundamental problems with zero flux partitioning of electron densities. *Theoretical Chemistry Accounts*, *105*(3), 213–218.

Castleton, C., Kullgren, J., & Hermansson, K. (2007). Tuning LDA+ U for electron localization and structure at oxygen vacancies in ceria. *The Journal of Chemical Physics*, *127*(24), 244704.

Catti, M., & Sandrone, G. (1997). Ab initio study of corundum-like Me_2O_3 oxides (Me= Ti, V, Cr, Fe, Co, Ni). *Faraday Discussions*, *106*, 189–203.

Causa, M., Dovesi, R., Pisani, C., & Roetti, C. (1986). Ab initio hartree-fock study of the MgO (001) surface. *Surface Science*, *175*(3), 551–560.

Ceperley, D. M., & Alder, B. (1980). Ground state of the electron gas by a stochastic method. *Physical Review Letters*, *45*(7), 566.

Chen, J., & Selloni, A. (2012). Electronic states and magnetic structure at the Co_3O_4 (110) surface: A first-principles study. *Physical Review B*, *85*(8), 085306.

Chen, J., Wu, X., & Selloni, A. (2011). Electronic structure and bonding properties of cobalt oxide in the spinel structure. *Physical Review B*, *83*(24), 245204.

Chen, J. X. (2009).*Guide to graphics software tools* (2 ed., pp. 7-40). London: Springer.

Chen, M., & Dixon, D. A. (2013). Tree growth-hybrid genetic algorithm for predicting the structure of small $(TiO_2)_n$, n= 2–13, nanoclusters. *Journal of Chemical Theory and Computation*, *9*(7), 3189–3200.

Chenavas, J., Joubert, J., & Marezio, M. (1971). Low-spin→ high-spin state transition in high pressure cobalt sesquioxide. *Solid State Communications*, *9*(13), 1057–1060.

Cheng, Y., Zhang, R., Hu, C., Li, S., & Zhang, M. (2011). *Design and implementation of UDLC: Unified job-description language on chemical-grid*. Paper presented at the Electrical and Control Engineering (ICECE), 2011 International Conference on.

Choudhary, V., & Pandit, M. (1991). Surface properties of magnesium oxide obtained from magnesium hydroxide: Influence on preparation and calcination conditions of magnesium hydroxide. *Applied Catalysis*, *71*(2), 265–274.

Cococcioni, M., & De Gironcoli, S. (2005). Linear response approach to the calculation of the effective interaction parameters in the LDA+ U method. *Physical Review B*, *71*(3), 035105.

Cohen, A. J., Mori-Sánchez, P., & Yang, W. (2008). Insights into current limitations of density functional theory. *Science*, *321*(5890), 792–794.

Cox, P., & Pletcher, D. (1990). Electrosynthesis at oxide coated electrodes part 1 the kinetics of ethanol oxidation at spinel electrodes in aqueous base. *Journal of Applied Electrochemistry*, *20*(4), 549–554.

Cui, Z., & Cai, X. (2011). Optimal coverage configuration with social emotional optimisation algorithm in wireless sensor networks. *International Journal of Wireless and Mobile Computing*, *5*(1), 43–47.

Daven, D., Tit, N., Morris, J., & Ho, K. (1996). Structural optimization of Lennard-Jones clusters by a genetic algorithm. *Chemical Physics Letters*, *256*(1), 195–200.

Davis, J. B., Johnston, R. L., Rubinovich, L., & Polak, M. (2014). Comparative modelling of chemical ordering in palladium-iridium nanoalloys. *The Journal of Chemical Physics*, *141*(22), 224307.

Davis, J. B., Shayeghi, A., Horswell, S. L., & Johnston, R. L. (2015). The Birmingham parallel genetic algorithm and its application to the direct DFT global optimisation of Ir_N (N= 10–20) clusters. *Nanoscale*, *7*(33), 14032–14038.

Day, P. N., Pachter, R., Gordon, M. S., & Merrill, G. N. (2000). A study of water clusters using the effective fragment potential and Monte Carlo simulated annealing. *The Journal of Chemical Physics*, *112*(5), 2063–2073.

Deaven, D. M., & Ho, K.-M. (1995). Molecular geometry optimization with a genetic algorithm. *Physical Review Letters*, *75*(2), 288.

De Magalhães, C. S., Barbosa, H. J., & Dardenne, L. E. (2004). Selection-insertion schemes in genetic algorithms for the flexible ligand docking problem. *Genetic and Evolutionary Computation – GECCO 2004 Lecture Notes in Computer Science,* 368-379.

De O'Shea, V. A., Moreira, I. d. P., Roldán, A., Illas, F., et al. (2010). Electronic and magnetic structure of bulk cobalt: The α, β, and ε-phases from density functional theory calculations. *The Journal of Chemical Physics*, *133*(2), 024701.

Deschenes, L. A. (2000). Origin 6.0: Scientific data analysis and graphing software Origin lab corporation (formerly Microcal Software, Inc.). *Journal of the American Chemical Society*, *122*(39), 9567-9568.

Desjonqueres, M., & Spanjaard, D. (1996). *Concepts in surface physics* (2nd ed., pp. 15-34). Berlin: Springer-Verlag Berlin Heidelberg.

Deskins, N. A., & Dupuis, M. (2007). Electron transport via polaron hopping in bulk TiO_2: A density functional theory characterization. *Physical Review B*, *75*(19), 195212.

Dibble, C., Akin, S., Ard, S., Fowler, C., & Duncan, M. (2012). Photodissociation of cobalt and nickel oxide cluster cations. *The Journal of Physical Chemistry A*, *116*(22), 5398–5404.

Dovesi, R., Civalleri, B., Orlando, R., Roetti, C., & Saunders, V. R. (2005). Ab initio quantum simulation in solid state chemistry. *Reviews in Computational Chemistry*, *21*, 1.

Doye, J. P. (2006). Physical perspectives on the global optimization of atomic clusters. *In Global optimization* (pp. 103–139). Springer.

Doye, J. P., & Wales, D. J. (1998). Global minima for transition metal clusters described by Sutton–Chen potentials. *New Journal of Chemistry*, *22*(7), 733–744.

Doye, J. P., & Wales, D. J. (2002). Saddle points and dynamics of Lennard-Jones clusters, solids, and supercooled liquids. *The Journal of Chemical Physics*, *116*(9), 3777–3788.

Drebov, N., & Ahlrichs, R. (2010). Structures of Al_n, its anions and cations up to n= 34: A theoretical investigation. *The Journal of Chemical Physics*, *132*(16), 164703.

Dudarev, S., Botton, G., Savrasov, S., Humphreys, C., & Sutton, A. (1998). Electron-energy-loss spectra and the structural stability of nickel oxide: An LSDA+ U study. *Physical Review B*, *57*(3), 1505.

Dutta, D. P., Sharma, G., Manna, P., Tyagi, A., & Yusuf, S. (2008). Room temperature ferromagnetism in CoO nanoparticles obtained from sonochemically synthesized precursors. *Nanotechnology*, *19*(24), 245609.

Elkoraychy, E., Sbiaai, K., Mazroui, M., Boughaleb, Y., & Ferrando, R. (2015). Numerical study of hetero-adsorption and diffusion on (100) and (110) surfaces of Cu, Ag and Au. *Surface Science*, *635*, 64–69.

Elliott, L., Ingham, D., Kyne, A., Mera, N., Pourkashanian, M., & Wilson, C. (2004). Genetic algorithms for optimisation of chemical kinetics reaction mechanisms. *Progress in Energy and Combustion Science*, *30*(3), 297–328.

Enciu, D., Nemnes, G. A., & Ursu, I. (2014). Spintronic devices based on graphene nanoribbons with transition metal impurities. Towards space applications. *INCAS Bulletin*, *6*(1), 45.

Enkovaara, J., Rostgaard, C., Mortensen, J. J., Chen, J., Dułak, M., Ferrighi, L., . . . Hansen, H. (2010). Electronic structure calculations with GPAW: a real-space implementation of the projector augmented-wave method. *Journal of Physics: Condensed Matter*, *22*(25), 253202.

Esfahanian, M., Rad, A. S., Khoshhal, S., Najafpour, G., & Asghari, B. (2016). Mathematical modeling of continuous ethanol fermentation in a membrane bioreactor by pervaporation compared to conventional system: Genetic algorithm. *Bioresource Technology*, *212*, 62–71.

Esswein, A. J., McMurdo, M. J., Ross, P. N., Bell, A. T., & Tilley, T. D. (2009). Size-dependent activity of Co_3O_4 nanoparticle anodes for alkaline water electrolysis. *The Journal of Physical Chemistry C*, *113*(33), 15068–15072.

Fernandez, S., Markovits, A., Fuster, F., & Minot, C. (2007). First row transition metal atom adsorption on defect-free MgO (100) surface. *The Journal of Physical Chemistry C*, *111*(18), 6781–6788.

Feynman, R. P. (1939). Forces in molecules. *Physical Review*, *56*(4), 340.

Fierro, J. L. (2005). *Metal oxides: Chemistry and applications* (pp.230-321). Boca Raton, FL: Taylor & Francis.

Filgueiras, P. R., Portela, N. A., Silva, S. R., Castro, E. V., Oliveira, L. M., Dias, J. C., . . . Poppi, R. J. (2016). Determination of saturates, aromatics, and polars in crude oil by 13C NMR and support vector regression with variable selection by genetic algorithm. *Energy & Fuels*, *30*(3), 1972–1978.

Freas, R. B., Dunlap, B. I., Waite, B. A., & Campana, J. E. (1987). The role of cluster ion structure in reactivity and collision-induced dissociation: Application to cobalt/oxygen cluster ions in the gas phase. *The Journal of Chemical Physics*, *86*(3), 1276–1288.

Frisch, M. J., Trucks, G. W., Schlegel, H. B., Scuseria, G. E., Robb, M. A., Cheeseman, J. R., . . . Fox, D. J. (2009). *Gaussian09 Revision E.01.* Wallingford, CT.

Fuhr, J., & Wiese, W. (2006). *CRC handbook of chemistry and physic* (88th ed.). Boca Raton: CRC Press

Furthmüller, J., Hafner, J., & Kresse, G. (1994). Structural and electronic properties of clean and hydrogenated diamond (100) Surfaces. *EPL (Europhysics Letters)*, *28*(9), 659.

Garbowski, E., Guenin, M., Marion, M.-C., & Primet, M. (1990). Catalytic properties and surface states of cobalt-containing oxidation catalysts. *Applied catalysis*, *64*, 209–224.

Gates, B. C. (1992). *Catalytic chemistry* (Vol. *458*, pp. 90-121). New York: Wiley.

Gehrke, R., & Reuter, K. (2009). Assessing the efficiency of first-principles basin-hopping sampling. *Physical Review B*, *79*(8), 085412.

Geneste, G., Morillo, J., & Finocchi, F. (2002). Ab initio study of Mg adatom and MgO molecule adsorption and diffusion on the MgO (001) surface. *Applied Surface Science*, *188*(1-2), 122–127.

Geneste, G., Morillo, J., & Finocchi, F. (2003). Ab initio study of MgO stoichiometric clusters on the MgO (001) flat surface. *Surface science*, *532*, 508–513.

Ghosh, M., Sampathkumaran, E., & Rao, C. (2005). Synthesis and magnetic properties of CoO nanoparticles. *Chemistry of Materials*, *17*(9), 2348–2352.

Gluhoi, A. C., Lin, S. D., & Nieuwenhuys, B. E. (2004). The beneficial effect of the addition of base metal oxides to gold catalysts on reactions relevant to air pollution abatement. *Catalysis Today*, *90*(3-4), 175–181.

Goldberg, D. E. (1989). *Genetic algorithms in search, optimization, and machine learning* (pp. 100-142). Boston: Addison-Wesley.

Goniakowski, J., Finocchi, F., & Noguera, C. (2007). Polarity of oxide surfaces and nanostructures. *Reports on Progress in Physics*, *71*(1), 016501.

Goniakowski, J., Noguera, C., & Giordano, L. (2007). Prediction of uncompensated polarity in ultrathin films. *Physical Review Letters*, *98*(20), 205701.

Greiner, J., Berkowitz, A., & Weidenborner, J. (1966). Properties of single-crystal CoO films on MgO. *Journal of Applied Physics*, *37*(5), 2149–2155.

Hamad, S., Catlow, C., Woodley, S., Lago, S., & Mejias, J. (2005). Structure and stability of small TiO_2 nanoparticles. *The Journal of Physical Chemistry B*, *109*(33), 15741–15748.

Hamann, D., Schlüter, M., & Chiang, C. (1979). Norm-conserving pseudopotentials. *Physical Review Letters*, *43*(20), 1494.

Hamdani, M., Singh, R., & Chartier, P. (2010). Co_3O_4 and Co-based spinel oxides bifunctional oxygen electrodes. *International Journal of Electrochemical Science*, *5*(4), 556-577.

Hammer, B., Hansen, L. B., & Nørskov, J. K. (1999). Improved adsorption energetics within density-functional theory using revised Perdew-Burke-Ernzerhof functionals. *Physical Review B*, *59*(11), 7413.

Han, Y., & Evans, J. W. (2015). Adsorption and diffusion of Ru adatoms on Ru (0001)-supported graphene: Large-scale first-principles calculations. *The Journal of Chemical Physics*, *143*(16), 164706.

Harding, D. J., & Fielicke, A. (2014). Platinum group metal clusters: From gas-phase structures and reactivities towards model catalysts. *Chemistry–A European Journal*, *20*(12), 3258–3267.

Harl, J., Schimka, L., & Kresse, G. (2010). Assessing the quality of the random phase approximation for lattice constants and atomization energies of solids. *Physical Review B*, *81*(11), 115126.

Harris, J. (1985). Simplified method for calculating the energy of weakly interacting fragments. *Physical Review B*, *31*(4), 1770.

Hartke, B. (1993). Global geometry optimization of clusters using genetic algorithms. *The Journal of Physical Chemistry*, *97*(39), 9973–9976.

Hartke, B. (1996). Global geometry optimization of clusters guided by N-dependent model potentials. *Chemical Physics Letters*, *258*(1), 144–148.

Hartke, B. (2003). Size-dependent transition from all-surface to interior-molecule structures in pure neutral water clusters. *Physical Chemistry Chemical Physics*, *5*(2), 275–284.

He, C., & Köhler, K. (2006). Selective catalytic reduction of NO by propane over CoO_x/Al_2O_3: an investigation of the surface reactions using in situ infrared spectroscopy. *Physical Chemistry Chemical Physics*, *8*(7), 898–905.

He, X., Song, X., Qiao, W., Li, Z., Zhang, X., Yan, S., . . . Du, Y. (2015). Phase-and size-dependent optical and magnetic properties of CoO nanoparticles. *The Journal of Physical Chemistry C*, *119*(17), 9550–9559.

Hedin, L. (1965). New method for calculating the one-particle Green's function with application to the electron-gas problem. *Physical Review*, *139*(3A), A796.

Heiles, S., & Johnston, R. L. (2013). Global optimization of clusters using electronic structure methods. *International Journal of Quantum Chemistry*, *113*(18), 2091–2109.

Heiles, S., Johnston, R. L., & Schafer, R. (2012). Bismuth-doped tin clusters: experimental and theoretical studies of neutral Zintl analogues. *The Journal of Physical Chemistry A*, *116*(29), 7756–7764.

Heiles, S., Logsdail, A. J., Schäfer, R., & Johnston, R. L. (2012). Dopant-induced 2D–3D transition in small Au-containing clusters: DFT-global optimisation of 8-atom Au–Ag nanoalloys. *Nanoscale*, *4*(4), 1109–1115.

Heiles, S., & Schäfer, R. (2014). *Dielectric Properties of Isolated Clusters Beam Deflection Studies* (pp. 17-59). Dordrecht: Springer Netherlands.

Hellmann, H. (1937). *Einführung in die quantenchemie: Texte imprimé* (p. 285). Leipzig und Wien: F. Deuticke.

Henderson, T. M., Paier, J., & Scuseria, G. E. (2011). Accurate treatment of solids with the HSE screened hybrid. *Physica Status Solidi (b)*, *248*(4), 767–774.

Henkelman, G., Arnaldsson, A., & Jónsson, H. (2006). A fast and robust algorithm for Bader decomposition of charge density. *Computational Materials Science*, *36*(3), 354–360.

Heyd, J., Scuseria, G. E., & Ernzerhof, M. (2003). Hybrid functionals based on a screened Coulomb potential. *The Journal of Chemical Physics*, *118*(18), 8207-8215.

Hoare, M. (1979). Structure and dynamics of simple microclusters. In I. Prigogine & S. A. Rice (Eds.). *Advances in Chemical Physics* (pp. 49–135). New York: Wiley.

Hohenberg, P., & Kohn, W. (1964). Inhomogeneous electron gas. *Physical Review*, *136*(3B), B864.

Holland, J. H. (1992). *Adaptation in natural and artificial systems: An introductory analysis with applications to biology, control, and artificial intelligence* (pp. 89-111). Cambridge, Mass.: MIT Press.

Hsin, J., Arkhipov, A., Yin, Y., Stone, J. E., & Schulten, K. (2008). Using VMD: an introductory tutorial. *Current Protocols in Bioinformatics*, *24*(1), 5.7.1-5.7.48.

Hu, Z., & Metiu, H. (2011). Choice of U for DFT+ U calculations for titanium oxides. *The Journal of Physical Chemistry C*, *115*(13), 5841–5845.

Huang, X., Su, Y., Sai, L., Zhao, J., & Kumar, V. (2015). Low-energy structures of binary Pt–Sn clusters from global search using genetic algorithm and density functional theory. *Journal of Cluster Science*, *26*(2), 389–409.

Iqbal, N., Wang, X., Ge, J., Yu, J., Kim, H. Y., Al-Deyab, S. S., ... & Ding, B. (2016). Cobalt oxide nanoparticles embedded in flexible carbon nanofibers: attractive material for supercapacitor electrodes and CO_2 adsorption. *RSC Advances*, *6*(57), 52171-52179.

Ishimoto, T., & Koyama, M. (2016). Electronic structure and phase stability of PdPt nanoparticles. *The Journal of Physical Chemistry Letters*, *7*(5), 736–740.

Jeon, J., & Yu, B. D. (2013). Surface dynamics of Cu and Ag atoms on hydroxylated MgO (001) surfaces. *Journal of the Korean Physical Society*, *62*(1), 79–85.

Jeon, J., & Yu, B. D. (2014). Atomistic processes of Ni and Pd atoms on MgO (001) surfaces with surface-functional hydroxyl groups: Ab-initio calculations. *Journal of the Korean Physical Society*, *64*(4), 554–560.

Jepson, O., & Anderson, O. (1993). The electronic structure of h.c.p. ytterbium. *Solid State Communications*, *88*(11-12), 871–875.

Jiao, F., & Frei, H. (2009). Nanostructured cobalt oxide clusters in mesoporous silica as efficient oxygen-evolving catalysts. *Angewandte Chemie International Edition*, *48*(10), 1841–1844.

Johnston, R. L. (2003). Evolving better nanoparticles: Genetic algorithms for optimising cluster geometries. *Dalton Transactions,* (22), 4193-4207.

Jones, R. O., & Gunnarsson, O. (1989). The density functional formalism, its applications and prospects. *Reviews of Modern Physics*, *61*(3), 689.

Ju, M., Lv, J., Kuang, X.-Y., Ding, L.-P., Lu, C., Wang, J.-J., . . . Maroulis, G. (2015). Systematic theoretical investigation of geometries, stabilities and magnetic properties of iron oxide clusters $(FeO)_n^{\mu}$ (n= 1–8, μ= 0, ±1): insights and perspectives. *RSC Advances*, *5*(9), 6560–6570.

Kanters, R. P., & Donald, K. J. (2014). Cluster: searching for unique low energy minima of structures using a novel implementation of a genetic algorithm. *Journal of Chemical Theory and Computation*, *10*(12), 5729–5737.

Kern, G., Hafner, J., Furthmüller, J., & Kresse, G. (1996). Surface reconstruction and electronic properties of clean and hydrogenated diamond (111) surfaces. *Surface Science*, *357*, 422–426.

Khodakov, A. Y., Lynch, J., Bazin, D., Rebours, B., Zanier, N., Moisson, B., & Chaumette, P. (1997). Reducibility of cobalt species in silica-supported Fischer–Tropsch catalysts. *Journal of Catalysis*, *168*(1), 16–25.

Kim, C., & Chung, Y.-C. (2006). First-principles study on atomistic behaviors and magnetism of physisorpted Co and Fe atoms on MgO*., IEEE Transactions on Magnetics* , *42*(10), 3174–3176.

Kim, H. G., Choi, S. K., & Lee, H. M. (2008). New algorithm in the basin hopping Monte Carlo to find the global minimum structure of unary and binary metallic nanoclusters. *The Journal of Chemical Physics*, *128*(14), 144702.

Kim, K. J., & Park, Y. R. (2003). Optical investigation of charge-transfer transitions in spinel Co_3O_4. *Solid State Communications*, *127*(1), 25–28.

Kirkpatrick, S., Vecchi, M. P., et al. (1983). Optimization by simmulated annealing. *Science*, *220*(4598), 671–680.

Klabunde, K. J., & Khaleel, A. (1998). *U.S. Patent No. 5,759,939*. Washington, DC: U.S. Patent and Trademark Office.

Klepper, K., Nilsen, O., & Fjellvåg, H. (2007). Growth of thin films of Co_3O_4 by atomic layer deposition. *Thin Solid Films*, *515*(20), 7772–7781.

Kohn, W., & Sham, L. J. (1965). Self-consistent equations including exchange and correlation effects. *Physical Review*, *140*(4A), A1133.

Kresse, G., & Furthmüller, J. (1996a). Efficiency of ab-initio total energy calculations for metals and semiconductors using a plane-wave basis set. *Computational Materials Science*, *6*(1), 15–50.

Kresse, G., & Furthmüller, J. (1996b). Efficient iterative schemes for ab initio total-energy calculations using a plane-wave basis set. *Physical review B*, *54*(16), 11169.

Kresse, G., & Furthmüller, J. (1996c). Software vasp, vienna (1999). *Physical Review B*, *54*(11), 169.

Kresse, G., & Hafner, J. (1993). Ab initio molecular dynamics for liquid metals. *Physical Review B*, *47*(1), 558.

Kresse, G., & Joubert, D. (1999). From ultrasoft pseudopotentials to the projector augmented-wave method. *Physical Review B*, *59*(3), 1758.

Kumar, V., & Kawazoe, Y. (2003). Metal-doped magic clusters of Si, Ge, and Sn: The finding of a magnetic superatom. *Applied physics letters*, *83*(13), 2677–2679.

Laio, A., Rodriguez-Fortea, A., Gervasio, F. L., Ceccarelli, M., & Parrinello, M. (2005). Assessing the accuracy of metadynamics. *The Journal of Physical Chemistry B*, *109*(14), 6714–6721.

Langell, M., Anderson, M., Carson, G., Peng, L., & Smith, S. (1999). Valence-band electronic structure of Co_3O_4 epitaxy on CoO (100). *Physical Review B*, *59*(7), 4791.

Leary, R. H. (2000). Global optimization on funneling landscapes. *Journal of Global Optimization*, *18*(4), 367–383.

Lee, S., Lee, B., Seifert, S., Winans, R. E., & Vajda, S. (2015). Fischer–Tropsch synthesis at a low pressure on subnanometer cobalt oxide clusters: The effect of cluster size and support on activity and selectivity. *The Journal of Physical Chemistry C*, *119*(20), 11210–11216.

Levine, I. (1999). *Quantum chemistry* (5th ed.). Retrieved from 15 April 2017 https://books.google.jo/books?id=WBRXPwAACAAJ.

Li, C., Chen, Y. W., Yang, S. J., & Wu, J. C. (1993). Hydrodesulfurization reactions of atmospheric gas oil over cobalt-molybdenum/alumina-aluminum borate catalysts. *Industrial & Engineering Chemistry Research*, *32*(8), 1573–1578.

Li, Z., Lin, Z., Wang, N., Wang, J., Liu, W., Sun, K., . . . Wang, Z. (2016). High precision NH_3 sensing using network nano-sheet Co_3O_4 arrays based sensor at room temperature. *Sensors and Actuators B: Chemical, 235*, 222-231.

Li, Z., & Scheraga, H. A. (1987). Monte Carlo-minimization approach to the multiple-minima problem in protein folding. *Proceedings of the National Academy of Sciences*, *84*(19), 6611–6615.

Liang, Y., Li, Y., Wang, H., Zhou, J., Wang, J., Regier, T., & Dai, H. (2011). Co_3O_4 nanocrystals on graphene as a synergistic catalyst for oxygen reduction reaction. *Nature Materials*, *10*(10), 780–786.

Lide, D. R. (2003). *CRC handbook of chemistry and physic (84th ed.*, pp. 234-268*)*. Boca Raton: CRC Press.

Liu, D. C., & Nocedal, J. (1989). On the limited memory BFGS method for large scale optimization. *Mathematical Programming*, *45*(1-3), 503–528.

Liu, X., & Prewitt, C. T. (1990). High-temperature X-ray diffraction study of Co_3O_4: Transition from normal to disordered spinel. *Physics and Chemistry of Minerals*, *17*(14), 168–172.

Liu, X., Qiu, G., & Li, X. (2005). Shape-controlled synthesis and properties of uniform spinel cobalt oxide nanocubes. *Nanotechnology*, *16*(12), 3035.

Lopez, T., Garcia-Cruz, I., & Gomez, R. (1991). Synthesis of magnesium oxide by the sol-gel method: effect of the ph on the surface hydroxylation. *Journal of Catalysis*, *127*(1), 75–85.

Lu, Q. L., Luo, Q. Q., Huang, S. G., Li, Y. D., & Wan, J. G. (2016). Analysis of the Structures and Properties of $(GaSb)_n$ (n = 4–9) Clusters through Density Functional Theory. *The Journal of Physical Chemistry A*, *120*(26), 4560-4564.

Luo, S., Dibble, C. J., Duncan, M. A., & Truhlar, D. G. (2014). Ligand-mediated ring→ cube transformation in a catalytic subnanocluster: Co_4O_4 $(MeCN)_n$ with n= 1–6. *The journal of Physical Chemistry Letters*, *5*(15), 2528–2532.

Lysgaard, S., Myrdal, J. S. G., Hansen, H. A., & Vegge, T. (2015). A DFT-based genetic algorithm search for AuCu nanoalloy electrocatalysts for CO_2 reduction. *Physical Chemistry Chemical Physics*, *17*, 28270–28276.

Ma, J., Michaelides, A., Alfe, D., Schimka, L., Kresse, G., & Wang, E. (2011). Adsorption and diffusion of water on graphene from first principles. *Physical Review B*, *84*(3), 033402.

Mane, A. U., Shalini, K., Wohlfart, A., Devi, A., & Shivashankar, S. (2002). Strongly oriented thin films of Co_3O_4 deposited on single-crystal MgO (100) by low-pressure, low-temperature MOCVD. *Journal of Crystal Growth*, *240*(1-2), 157–163.

Marbán, G., López, I., Valdés-Solís, T., & Fuertes, A. B. (2008). Highly active structured catalyst made up of mesoporous Co_3O_4 nanowires supported on a metal wire mesh for the preferential oxidation of CO. *International journal of hydrogen energy*, *33*(22), 6687–6695.

Marsman, M., Paier, J., Stroppa, A., & Kresse, G. (2008). Hybrid functionals applied to extended systems. *Journal of Physics: Condensed Matter*, *20*(6), 064201.

Martin, R. M. (2004). *Electronic structure: basic theory and practical methods* (pp. 189-200). Cambridge: Cambridge university press.

Massidda, S., Posternak, M., & Baldereschi, A. (1993). Hartree-fock LAPW approach to the electronic properties of periodic systems. *Physical Review B*, *48*(8), 5058.

Mattioli, G., Filippone, F., Alippi, P., & Bonapasta, A. A. (2008). Ab initio study of the electronic states induced by oxygen vacancies in rutile and anatase TiO_2. *Physical Review B*, *78*(24), 241201.

Melaet, G., Ralston, W. T., Li, C.-S., Alayoglu, S., An, K., Musselwhite, N., . . . Somorjai, G. A. (2014). Evidence of highly active cobalt oxide catalyst for the Fischer–Tropsch synthesis and CO_2 hydrogenation. *Journal of the American Chemical Society*, *136*(6), 2260–2263.

Methfessel, M., & Paxton, A. (1989). High-precision sampling for Brillouin-zone integration in metals. *Physical Review B*, *40*(6), 3616.

Metropolis, N., Rosenbluth, A. W., Rosenbluth, M. N., Teller, A. H., & Teller, E. (1953). Equation of state calculations by fast computing machines. *The Journal of Chemical Physics*, *21*(6), 1087–1092.

Mitchell, M. (1998). *An introduction to genetic algorithms* (pp. 20-42). Cambridge: MIT press.

Mittendorfer, F., Weinert, M., Podloucky, R., & Redinger, J. (2012). Strain and structure driven complex magnetic ordering of a CoO overlayer on Ir (100). *Physical Review Letters*, *109*(1), 015501.

Momma, K., & Izumi, F. (2011). VESTA 3 for three-dimensional visualization of crystal, volumetric and morphology data. *Journal of Applied Crystallography*, *44*(6), 1272–1276.

Monkhorst, H. J., & Pack, J. D. (1976). Special points for Brillouin-zone integrations. *Physical Review B*, *13*(12), 5188.

Montoya, A., & Haynes, B. S. (2011). Periodic density functional study of Co_3O_4 surfaces. *Chemical Physics Letters*, *502*(1), 63–68.

Mordi, C., Eleruja, M., Taleatu, B., Egharevba, G., Adedeji, A., Akinwunmi, O., . . . Ajayi, E. (2009). Metal organic chemical vapour deposited thin films of cobalt oxide prepared via cobalt acetylacetonate. *Journal of Materials Science & Technology*, *25*(1), 85.

Mortensen, J. J., Hansen, L. B., & Jacobsen, K. W. (2005). Real-space grid implementation of the projector augmented wave method. *Physical Review B*, *71*(3), 035109.

Musolino, V., Selloni, A., & Car, R. (1998). First principles study of adsorbed Cu_n (n=1–4) microclusters on MgO (100): Structural and electronic properties. *The Journal of Chemical Physics, 108*(12), 5044-5054.

Neogi, S. G., & Chaudhury, P. (2015). Structure, electronic properties and vibrational spectra of $(MgF_2)_n$ clusters through a combination of genetic algorithm and DFT- based approach. *Molecular Physics*, *113*(23), 3729–3739.

Neyman, K., Inntam, C., Nasluzov, V., Kosarev, R., & Rösch, N. (2004). Adsorption of d-metal atoms on the regular MgO (001) surface: Density functional study of cluster models embedded in an elastic polarizable environment. *Applied Physics A*, *78*(6), 823–828.

Nilsson, A., Pettersson, L., & Nørskov, J. K. (2008). *Chemical bonding at surfaces and interfaces* (pp. 397-455). Amsterdam: Elsevier.

Nolan, M., Elliott, S. D., Mulley, J. S., Bennett, R. A., Basham, M., & Mulheran, P. (2008). Electronic structure of point defects in controlled self-doping of the TiO_2 (110) surface: Combined photoemission spectroscopy and density functional theory study. *Physical Review B*, *77*(23), 235424.

Oakley, M. T., Johnston, R. L., & Wales, D. J. (2013). Symmetrisation schemes for global optimisation of atomic clusters. *Physical Chemistry Chemical Physics*, *15*(11), 3965–3976.

Oliphant, N., & Bartlett, R. J. (1994). A systematic comparison of molecular properties obtained using Hartree–Fock, a hybrid Hartree–Fock density-functional-theory, and coupled-cluster methods. *The Journal of Chemical Physics*, *100*(9), 6550–6561.

Olson, B., Hashmi, I., Molloy, K., & Shehu, A. (2012). Basin hopping as a general and versatile optimization framework for the characterization of biological macromolecules. *Advances in Artificial Intelligence*, *2012*, 3.

Ota, K., Koyasu, K., Ohshimo, K., & Misaizu, F. (2013). Structures of cobalt oxide cluster cations studied by ion mobility mass spectrometry. *Chemical Physics Letters*, *588*, 63–67.

Ou, X., Wang, H., Fan, F., Li, Z., & Wu, H. (2015). Giant magnetic anisotropy of Co, Ru, and Os adatoms on MgO (001) surface. *Physical Review Letters*, *115*(25), 257201.

Ozin, G. (1996). Synthesis of palladium nanoparticles in water-in-oil microemulsions. *Science*, *271*, 920–941.

Pacchioni, G. (2013). Electronic interactions and charge transfers of metal atoms and clusters on oxide surfaces. *Physical Chemistry Chemical Physics*, *15*(6), 1737–1757.

Pacchioni, G., & Rösch, N. (1996). Supported nickel and copper clusters on MgO (100): A first-principles calculation on the metal/oxide interface. *The Journal of Chemical Physics*, *104*(18), 7329–7337.

Pacchioni, G., & Valeri, S. (2012). *Oxide Ultrathin Films: Science and Technology* (pp. 133-170). Weinheim: Wiley-VCH Verlag.

Paier, J., Marsman, M., & Kresse, G. (2007). Why does the B3LYP hybrid functional fail for metals?. *The Journal of Chemical Physics*, *127*(2), 024103.

Pancotti, A., de Siervo, A., Nascente, P., & Landers, R. (2016). Surface structure characterization of ultra-thin films of Au deposited on Pd (111). *Surface Science*, *648*, 250–255.

Park, J., Park, I., & Yu, B. (2009). Adsorption of transition metal atoms on defective MgO (001) surfaces: Atomic and electronic structures. *Journal of Korean Physical Society*, *54*, 109.

Parmigiani, F., & Sangaletti, L. (1999). Fine structures in the X-ray photoemission spectra of MnO, FeO, CoO, and NiO single crystals. *Journal of Electron Spectroscopy and Related Phenomena*, *98*, 287–302.

Paszkowicz, W. (2009). Genetic algorithms, a nature-inspired tool: Survey of applications in materials science and related fields. *Materials and Manufacturing Processes*, *24*(2), 174–197.

Perdew, J. P. (1986). Density-functional approximation for the correlation energy of the inhomogeneous electron gas. *Physical Review B*, *33*(12), 8822.

Perdew, J. P., Burke, K., & Ernzerhof, M. (1996). Generalized gradient approximation made simple. *Physical Review Letters*, *77*(18), 3865.

Perdew, J. P., Ernzerhof, M., & Burke, K. (1996). Rationale for mixing exact exchange with density functional approximations. *The Journal of Chemical Physics*, *105*(22), 9982–9985.

Perdew, J. P., & Wang, Y. (1992). Accurate and simple analytic representation of the electron-gas correlation energy. *Physical Review B*, *45*(23), 13244.

Perdew, J. P., & Zunger, A. (1981). Self-interaction correction to density-functional approximations for many-electron systems. *Physical Review B*, *23*(10), 5048.

Petitto, S., & Langell, M. (2004). Surface composition and structure of Co_3O_4 (110) and the effect of impurity segregation. *Journal of Vacuum Science & Technology A*, *22*(4), 1690–1696.

Piccolo, L., & Henry, C. R. (2000). Reactivity of metal nanoclusters: nitric oxide adsorption and CO+ NO reaction on Pd/MgO model catalysts. *Applied Surface Science*, *162*, 670–678.

Pickard, C. J., & Needs, R. (2011). Ab initio random structure searching. *Journal of Physics: Condensed Matter*, *23*(5), 053201.

Pickett, W., Erwin, S., & Ethridge, E. (1998). Reformulation of the LDA+ U method for a local-orbital basis. *Physical Review B*, *58*(3), 1201.

Pillardy, J., & Piela, L. (1997). Smoothing techniques of global optimization: Distance scaling method in searches for most stable Lennard–Jones atomic clusters. *Journal of Computational Chemistry*, *18*(16), 2040–2049.

Polak, M., & Rubinovich, L. (2005). Prediction of compositional ordering and separation in alloy nanoclusters. *Surface Science*, *584*(1), 41–48.

Raj, K., & Muthukumar, V. (2016). Quantitative structure-activity relationships analysis of the anticonvulsant activity of erythrinine. *Asian Journal of Pharmaceutical and Clinical Research*, *9*(2), 125–129.

Ramanathan, S. (2010). *Thin film metal-oxides: fundamentals and applications in electronics and energy* (pp. 135-165). New York: Springer.

Rau, I. G., Baumann, S., Rusponi, S., Donati, F., Stepanow, S., Gragnaniello, L., . . . Gangopadhyay, S. (2014). Reaching the magnetic anisotropy limit of a 3d metal atom. *Science*, *344*(6187), 988–992.

Renaud, G. (1998). Oxide surfaces and metal/oxide interfaces studied by grazing incidence X-ray scattering. *Surface Science Reports*, *32*(1), 5–90.

Risch, M., Shevchenko, D., Anderlund, M. F., Styring, S., Heidkamp, J., Lange, K. M., . . . Zaharieva, I. (2012). Atomic structure of cobalt-oxide nanoparticles active in light-driven catalysis of water oxidation. *International Journal of Hydrogen Energy*, *37*(10), 8878–8888.

Roberts, C., & Johnston, R. L. (2001). Investigation of the structures of MgO clusters using a genetic algorithm. *Physical Chemistry Chemical Physics*, *3*(22), 5024–5034.

Rondina, G. G., & Da Silva, J. L. (2013). Revised basin-hopping Monte Carlo algorithm for structure optimization of clusters and nanoparticles. *Journal of Chemical Information and Modeling*, *53*(9), 2282–2298.

Rossi, G., & Ferrando, R. (2009). Searching for low-energy structures of nanoparticles: a comparison of different methods and algorithms. *Journal of Physics: Condensed Matter*, *21*(8), 084208.

Roth, W. (1964). The magnetic structure of Co_3O_4. *Journal of Physics and Chemistry of Solids*, *25*(1), 1–10.

Santambrogio, G., Brümmer, M., Wöste, L., Döbler, J., Sierka, M., Sauer, J., . . . Asmis, K. R. (2008). Gas phase vibrational spectroscopy of mass-selected vanadium oxide anions. *Physical Chemistry Chemical Physics*, *10*(27), 3992–4005.

Sanville, E., Kenny, S. D., Smith, R., & Henkelman, G. (2007). Improved grid-based algorithm for Bader charge allocation. *Journal of computational chemistry*, *28*(5), 899–908.

Sasaki, S., Fujino, K., & Takeuchi, Y. (1979). X-ray determination of electron- density distributions in oxides, MgO, MnO, CoO, and NiO, and atomic scattering factors of their constituent atoms. *Proceedings of the Japan Academy. Series B: Physical and Biological Sciences*, *55*(2), 43–48.

Savory, N., Abe, K., Sode, K., & Ikebukuro, K. (2010). Selection of DNA aptamer against prostate specific antigen using a genetic algorithm and application to sensing. *Biosensors and Bioelectronics*, *26*(4), 1386–1391.

Schimka, L., Harl, J., & Kresse, G. (2011). Improved hybrid functional for solids: The HSEsol functional. *The Journal of Chemical Physics*, *134*(2), 024116.

Seminario, J. M. (1996). *Recent developments and applications of modern density functional theory* (Vol. *4*, pp. 234-576). Amsterdam: Elsevier.

Senkan, S. (2001). Combinatorial heterogeneous catalysis—a new path in an old field. *Angewandte Chemie International Edition*, *40*(2), 312–329.

Sharmila, D. J., & Blessy, J. J. (2017). Molecular dynamics of sialic acid analogues complex with cholera toxin and DFT optimization of ethylene glycol-mediated zinc nanocluster conjugation. *Journal of Biomolecular Structure and Dynamics,35*(1), 182-206.

Shayeghi, A., Götz, D., Davis, J., Schaefer, R., & Johnston, R. (2015). Pool-BCGA: a parallelised generation-free genetic algorithm for the ab initio global optimisation of nanoalloy clusters. *Physical Chemistry Chemical Physics*, *17*(3), 2104–2112.

Shinde, V., Mahadik, S., Gujar, T., & Lokhande, C. (2006). Supercapacitive cobalt oxide (Co_3O_4) thin films by spray pyrolysis. *Applied Surface Science*, *252*(20), 7487–7492.

Sierka, M., Döbler, J., Sauer, J., Santambrogio, G., Brümmer, M., Wöste, L., . . . Asmis, K. (2007). Unexpected structures of aluminum oxide clusters in the gas phase. *Angewandte Chemie International Edition*, *46*(18), 3372–3375.

Soler, J. M., Artacho, E., Gale, J. D., García, A., Junquera, J., Ordejón, P., & Sánchez-Portal, D. (2002). The SIESTA method for ab initio order-N materials simulation. *Journal of Physics: Condensed Matter*, *14*(11), 2745.

Stadler, R., Podloucky, R., Kresse, G., & Hafner, J. (1998). Ab initio studies of the (100), (110), and (111) surfaces of $CoSi_2$. *Physical Review B*, *57*(7), 4088.

Staemmler, V., & Fink, K. (2002). An ab initio cluster study of the magnetic properties of the CoO (001) surface. *Chemical Physics*, *278*(2), 79–87.

Strodel, B., & Wales, D. J. (2008). Free energy surfaces from an extended harmonic superposition approach and kinetics for alanine dipeptide. *Chemical Physics Letters*, *466*(4), 105–115.

Sun, G., Kürti, J., Rajczy, P., Kertesz, M., Hafner, J., & Kresse, G. (2003). Performance of the Vienna ab initio simulation package (VASP) in chemical applications. *Journal of Molecular Structure: THEOCHEM*, *624*(1), 37–45.

Sun, J., Marsman, M., Csonka, G. I., Ruzsinszky, A., Hao, P., Kim, Y.-S., . . . Perdew, J. P. (2011). Self-consistent meta-generalized gradient approximation within the projector-augmented-wave method. *Physical Review B*, *84*(3), 035117.

Sun, Q., Sakurai, M., Wang, Q., Yu, J., Wang, G., Sumiyama, K., & Kawazoe, Y. (2000). Geometry and electronic structures of magic transition-metal oxide clusters M_9O_6 (M= Fe, Co, and Ni). *Physical Review B*, *62*(12), 8500.

Sun, Y., Yang, J.-Y., Xu, R., He, L., Dou, R.-F., & Nie, J.-C. (2010). Evidence for surface states in a single 3 nm diameter Co_3O_4 nanowire. *Applied Physics Letters*, *96*(26), 262106.

Svane, A., & Gunnarsson, O. (1990). Transition-metal oxides in the self-interaction–corrected density-functional formalism. *Physical Review Letters*, *65*(9), 1148.

Taghizadeh, F. (2016). Fabrication and investigation of the magnetic properties of Co and Co_3O_4 nanoparticles. *Optics and Photonics Journal, 6*(08), 62.

Takada, S., Fujii, M., Kohiki, S., Babasaki, T., Deguchi, H., Mitome, M., & Oku, M. (2001). Intraparticle magnetic properties of Co_3O_4 nanocrystals. *Nano Letters*, *1*(7), 379–382.

Takeuchi, M., & Maki, K. (2007). Thin-film deposition of metal oxides by aerosol-assisted chemical vapour deposition: Evaluation of film crystallinity. *Japanese Journal of Applied Physics*, *46*(12R), 7852.

Tamuliene, J., Vaisnoras, R., Badenes, G., & Balevicius, L. (2009). Stability and magnetic properties of Co_2O_m (m= 1,..., 7) clusters. *Lithuanian Journal of Physics and Technical Sciences*, *49*, 137–143.

Trotochaud, L., Mills, T. J., & Boettcher, S. W. (2013). An optocatalytic model for semiconductor–catalyst water-splitting photoelectrodes based on in situ optical measurements on operational catalysts. *The Journal of Physical Chemistry Letters*, *4*(6), 931–935.

Troullier, N., & Martins, J. L. (1991). Efficient pseudopotentials for plane-wave calculations. *Physical Review B*, *43*(3), 1993.

Tsai, C., & Jordan, K. (1993). Use of an eigenmode method to locate the stationary points on the potential energy surfaces of selected argon and water clusters. *The Journal of Physical Chemistry*, *97*(43), 11227–11237.

Ullman, A. M., Brodsky, C. N., Li, N., Zheng, S.-L., & Nocera, D. G. (2016). Probing edge site reactivity of oxidic cobalt water oxidation catalysts. *Journal of the American Chemical Society*, *138*(12), 4229–4236.

Unger, R., & Moult, J. (1993). Genetic algorithms for protein folding simulations. *Journal of Molecular Biology*, *231*(1), 75–81.

Uzunova, E. L., & Mikosch, H. (2012). Electronic structure and reactivity of cobalt oxide dimers and their hexacarbonyl complexes: A density functional study. *The Journal of Physical Chemistry A*, *116*(12), 3295–3303.

Uzunova, E. L., Nikolov, G. S., & Mikosch, H. (2002). Electronic structure and vibrational modes of cobalt oxide clusters CoO_n (n= 1-4) and their monoanions. *The Journal of Physical Chemistry A*, *106*(16), 4104–4114.

Vanderbilt, D. (1990). Soft self-consistent pseudopotentials in a generalized eigenvalue formalism. *Physical Review B*, *41*(11), 7892.

van Dijk, C. N., Roy, D. R., Fielicke, A., Rasing, T., Reber, A. C., Khanna, S. N., & Kirilyuk, A. (2014). Structure investigation of $Co_xO_y^+$(x= 3–6, y= 3–8) clusters by IR vibrational spectroscopy and DFT calculations. *The European Physical Journal D*, *68*(12), 357.

Vaz, C., Prabhakaran, D., Altman, E., & Henrich, V. (2009). Experimental study of the interfacial cobalt oxide in $Co_3O_4/\alpha\text{-}Al_2O_3$ (0001) epitaxial films. *Physical Review B*, *80*(15), 155457.

Vaz, C., Wang, H.-Q., Ahn, C., Henrich, V., Baykara, M., Schwendemann, T., . . . Zhang, L. (2009). Interface and electronic characterization of thin epitaxial Co_3O_4 films. *Surface Science*, *603*(2), 291–297.

Vilhelmsen, L. B., & Hammer, B. (2012). Systematic study of Au_6 to Au_{12} gold clusters on MgO (100) F centers using density-functional theory. *Physical Review Letters*, *108*(12), 126101.

Vosko, S. H., Wilk, L., & Nusair, M. (1980). Accurate spin-dependent electron liquid correlation energies for local spin density calculations: a critical analysis. *Canadian Journal of Physics*, *58*(8), 1200–1211.

Vydrov, O. A. (2007). *Correcting the self-interaction error of approximate density functionals.* (Unpublished doctoral dissertation). Rice University, Texas, United States.

Wai, L. C., & Ahmad, R. (2016). Effect of chromium (II, III) oxide and cobalt oxide on the color and fineness of cement. *Materials Science Forum*, *857*, 373–376.

Wales, D., & Bogdan, T. (2013). *GMIN: A program for finding global minima and calculating thermodynamic properties from basin-sampling*. Retrieved from 20 April 2017 http://www- wales. ch. cam. ac. uk/GMIN.

Wales, D. J., & Doye, J. P. (1997). Global optimization by basin-hopping and the lowest energy structures of Lennard-Jones clusters containing up to 110 atoms. *The Journal of Physical Chemistry A*, *101*(28), 5111–5116.

Wales, D. J., & Doye, J. P. (2003). Stationary points and dynamics in high-dimensional systems. *The Journal of Chemical Physics*, *119*(23), 12409–12416.

Wales, D. J., & Head-Gordon, T. (2012). Evolution of the potential energy landscape with static pulling force for two model proteins. *The Journal of Physical Chemistry B*, *116*(29), 8394–8411.

Wales, D. J., & Scheraga, H. A. (1999). Global optimization of clusters, crystals, and biomolecules. *Science*, *285*(5432), 1368–1372.

Walsh, A., Wei, S.-H., Yan, Y., Al-Jassim, M., Turner, J. A., Woodhouse, M., & Parkinson,B. (2007). Structural, magnetic, and electronic properties of the Co-Fe-Al oxide spinel system: Density-functional theory calculations. *Physical Review B*, *76*(16), 165119.

Wang, B., Nagase, S., Zhao, J., & Wang, G. (2007). Structural growth sequences and electronic properties of zinc oxide clusters $(ZnO)_n$ (n= 2-18). *The Journal of Physical Chemistry C*, *111*(13), 4956–4963.

Wang, G., Chen, Y., Konstantinov, K., Lindsay, M., Liu, H., & Dou, S. (2002). Investigation of cobalt oxides as anode materials for Li-ion batteries. *Journal of Power Sources*, *109*(1), 142–147.

Watts, A. E., Maruyoshi, K., Hughes, C. E., Brown, S. P., & Harris, K. D. (2016). Combining the advantages of powder X-ray diffraction and NMR crystallography in structure determination of the pharmaceutical material cimetidine hydrochloride. *Crystal Growth & Design*, *16*(4), 1798–1804.

Willighagen, E., & Howard, M. (2007). Fast and scriptable molecular graphics in web browsers without Java3D. *Nature Precedings*. Retrieved 20 April 2017 from http://precedings.nature.com/documents/50/version/1.

Woodley, S. M., & Catlow, R. (2008). Crystal structure prediction from first principles. *Nature Materials*, *7*(12), 937–946.

Xiao, Y., & Williams, D. E. (1993). Genetic algorithm: a new approach to the prediction of the structure of molecular clusters. *Chemical Physics Letters*, *215*(1), 17–24.

Xie, X., Li, Y., Liu, Z.-Q., Haruta, M., & Shen, W. (2009). Low-temperature oxidation of CO catalysed by Co_3O_4 nanorods. *Nature*, *458*(7239), 746–749.

Xie, Y., Dong, F., Heinbuch, S., Rocca, J. J., & Bernstein, E. R. (2010). Oxidation reactions on neutral cobalt oxide clusters: experimental and theoretical studies. *Physical Chemistry Chemical Physics*, *12*(4), 947–959.

Xu, X.-L., Chen, Z.-H., Li, Y., Chen, W.-K., & Li, J.-Q. (2009). Bulk and surface properties of spinel Co_3O_4 by density functional calculations. *Surface Science*, *603*(4), 653–658.

Xu, Z., Joshi, Y. V., Raman, S., & Kitchin, J. R. (2015). Accurate electronic and chemical properties of 3d transition metal oxides using a calculated linear response U and a DFT+ U (V) method. *The Journal of Chemical Physics*, *142*(14), 144701.

Yin, S., Xue, W., Ding, X.-L., Wang, W.-G., He, S.-G., & Ge, M.-F. (2009). Formation, distribution, and structures of oxygen-rich iron and cobalt oxide clusters. *International Journal of Mass Spectrometry*, *281*(1), 72–78.

Yudanov, I., Pacchioni, G., Neyman, K., & Rösch, N. (1997). Systematic density functional study of the adsorption of transition metal atoms on the MgO (001) surface. *The Journal of Physical Chemistry B*, *101*(15), 2786–2792.

Yung, M. M., Holmgreen, E. M., & Ozkan, U. S. (2007). Cobalt-based catalysts supported on titania and zirconia for the oxidation of nitric oxide to nitrogen dioxide. *Journal of Catalysis*, *247*(2), 356–367.

Zafeiratos, S., Dintzer, T., Teschner, D., Blume, R., Hävecker, M., Knop-Gericke, A., & Schlögl, R. (2010). Methanol oxidation over model cobalt catalysts: influence of the cobalt oxidation state on the reactivity. *Journal of Catalysis*, *269*(2), 309–317.

Zasada, F., Piskorz, W., Cristol, S., Paul, J.-F., Kotarba, A., & Sojka, Z. (2010). Periodic density functional theory and atomistic thermodynamic studies of cobalt spinel nanocrystals in wet environment: molecular interpretation of water adsorption equilibria. *The Journal of Physical Chemistry C*, *114*(50), 22245–22253.

Zasada, F., Piskorz, W., Stelmachowski, P., Kotarba, A., Paul, J.-F., Płocinski, T., . . . Sojka, Z. (2011). Periodic DFT and HR-STEM studies of surface structure and morphology of cobalt spinel nanocrystals. retrieving 3D shapes from 2D images. *The Journal of Physical Chemistry C*, *115*(14), 6423–6432.

Zayed, A., Marquez, A. M., & Sanz, J. F. (2013). Nanosized CoO films on the α-Al_2O_3 (0001) surface: A density functional study. *The Journal of Physical Chemistry C*, *117*(44), 22714–22722.

Zeiri, Y. (1995). Prediction of the lowest energy structure of clusters using a genetic algorithm. *Physical Review E*, *51*(4), R2769.

Zhan, L., Piwowar, B., Liu, W.-K., Hsu, P., Lai, S., & Chen, J. Z. (2004). Multicanonical basin hopping: A new global optimization method for complex systems. *The Journal of Chemical Physics*, *120*(12), 5536–5542.

Zhang, H., & Tian, D. (2008). Structural evolution of Ag_n^v($v=\pm1,0;n=3-14$) clusters using genetic algorithm and density functional theory method. *Computational Materials Science*, *42*(3), 462–469.

Zhang, L., Xue, D., & Gao, C. (2003). Anomalous magnetic properties of antiferromagnetic CoO nanoparticles. *Journal of Magnetism and Magnetic Materials*, *267*(1), 111–114.

Zhang, W., Tay, H. L., Lim, S. S., Wang, Y., Zhong, Z., & Xu, R. (2010). Supported cobalt oxide on MgO: highly efficient catalysts for degradation of organic dyes in dilute solutions. *Applied Catalysis B: Environmental*, *95*(1), 93–99.

Zhao, X., Nguyen, M. C., Wang, C.-Z., & Ho, K.-M. (2013). Structures and stabilities of alkaline earth metal peroxides XO_2 (x= Ca, Be, Mg) studied by a genetic algorithm. *RSC Advances*, *3*(44), 22135–22139.

LIST OF PUBLICATIONS AND PAPERS PRESENTED

Publications:

1. Hashim, A. H., Zayed, A. O., Zain, S. M., Lee, V. S., & Said, S. M. (2018). Electronic, magnetic and structural properties of Co_3O_4 (100) surface: A DFT+U study. *Applied Surface Science*, *427*, 1090-1095.

2. Zayed, A. O., & Zain, S. M. (2016). Atomic scale behavior, growth morphology and magnetic properties of CoO on MgO(100) surface: a density functional study. *Theoretical Chemistry Accounts*, *135*(8), 193.

3. Zayed, A. O., Daud, M. N., & Zain, S. M. (2017). Global structural optimization and growth mechanism of cobalt oxide nanoclusters by genetic algorithm with spin-polarized DFT. *Journal of Alloys and Compounds*, *695*, 2513-2518.

Conferences:

1. Ala' Omar Zayed and Sharifuddin Md Zain. (2017). *Atomic scale behavior, growth morphology and magnetic properties of CoO on MgO(100) surface: a density functional study*. Presented in International Conference on multidisciplinary Academic (ICMA), Swiss Garden Hotel, Kuala Lumpur, Malaysia (Oral presentation).

2. Ala' Omar Zayed and Sharifuddin Md Zain. (2017). *Atomic scale behavior, growth morphology and magnetic properties of CoO on MgO(100) surface: a density functional study*. Presented in The 9th Conference of the Asian Consortium on Computational Materials Science, Kuala Lumpur, Malaysia (Poster presentation).

Theor Chem Acc (2016) 135:193
DOI 10.1007/s00214-016-1948-z

REGULAR ARTICLE

Atomic scale behavior, growth morphology and magnetic properties of CoO on MgO(100) surface: a density functional study

Ala' Omar Hasan Zayed[1] · Sharifuddin Md Zain[1]

Received: 31 May 2016 / Accepted: 8 July 2016

Abstract In this study, we investigated the adsorption behaviors of the Co atom and CoO molecules on the MgO(100) surface, including the diffusion processes based on density functional theory calculations. The structure and growth morphology of the deposited cobalt oxide at various coverage levels as well as the magnetic properties are also discussed. The CoO molecule is found to bind more strongly to the surface compared to the isolated neutral Co atom, which is physically adsorbed on top of the surface oxygen site. Different to the isolated Co atom, the diffusion path of CoO molecule predominantly involves 90° rotation movements about its ends, while the surface hollow site acts as the saddle point for the hopping of the Co atom between two adjacent oxygen sites. A two-dimensional growth mode is observed to be the dominant layer growth mechanism for CoO on the magnesia surface, where the antiferromagnetic state is energetically more favorable compared to the ferromagnetic state. Based on the charge transfer and the density of state distribution, the interaction with the magnesia substrate does not affect the magnetic properties of the CoO monolayer.

Keywords Adsorption · Diffusion · Growth · DFT · CoO · MgO(100)

1 Introduction

The ultra-thin film of transition metal oxides deposited on metals, polar or nonpolar oxide substrates has attracted much attention due to their unique shape, size, and properties that may have great potential application in solar energy materials, chemical sensors, microelectronic device, composite materials and advanced catalysts [1–3]. Among the 3d-transition metal oxide series, CoO is one of the most promising catalytic systems at ultra-thin layer levels. Many reports have shown that CoO/metal oxide systems are effective catalysts in photoelectrochemical water splitting [4], gas desulfurization [5], water pollutants elimination [6] and air pollution control [7].

Since magnetic properties are highly influenced by the atomic arrangement of the growth layer, systematic understanding of the structural–properties relationship of CoO at different atomic levels is imperative. The surface diffusion of the adsorbed Co atom and CoO molecule is a vital step toward understanding the growth mechanisms and the nature of CoO–metal oxide interfaces [8–10]. Although many studies have investigated the adsorption of Co on the MgO(100) surface [11–13], very few have described the diffusion process. For example, Kim and Chung investigated the atomistic behavior of Co atom on MgO(100) where they studied its adsorption and diffusion processes [14]. They suggested unusual diffusion path of the Co atom compared to previous reports for other transition metals adsorbed on the same substrate [15–17]. Some results of this study are addressed in depth in the discussion section. On the other hand, Geneste and co-workers have shown that the MgO molecule binds stronger to the magnesia surface ($E_{ad} = 2.5$ eV) compared to the Mg atom ($E_{ad} = 0.5$ eV). They have concluded that the surface diffusion of the MgO molecule includes multi-step rotations about the axis perpendicular to the Mg–O bond with barriers ~15–20 % of the adsorption energy, which could lead to the various growth patterns of MgO on MgO(100) substrate based on the deposition techniques used [18].

✉ Ala' Omar Hasan Zayed
haszaid@yahoo.com

[1] Department of Chemistry, University of Malaya, 50603 Kuala Lumpur, Malaysia

Journal of Alloys and Compounds 696 (2017) 2513–2518

Contents lists available at ScienceDirect

Journal of Alloys and Compounds

journal homepage: http://www.elsevier.com/locate/jalcom

Global structural optimization and growth mechanism of cobalt oxide nanoclusters by genetic algorithm with spin-polarized DFT

Ala' Omar Hasan Zayed*, Mohammad Noh Daud**, Sharifuddin Md Zain

Department of Chemistry, University of Malaya, 50603 Kuala Lumpur, Malaysia

A R T I C L E I N F O

Article history:
Received 12 May 2016
Received in revised form
22 October 2016
Accepted 10 November 2016
Available online 14 November 2016

Keywords:
Structural optimization
Growth mechanism
Cobalt oxide
Nanoclusters
Genetic algorithm
DFT

A B S T R A C T

Multi-convergence relaxation procedures within the genetic algorithm method refined by spin-polarized density functional theory were applied to search for the global and local minima of cobalt oxide nanoclusters Co_nO_n ($n = 3–7$). The study found new global minimum structures for the Co_5O_5 and Co_6O_6 clusters, which are more stable than the best previous models. Through comparison with previous theoretical and experimental data, the genetic algorithm accurately predicted the global minima of Co_3O_3, Co_4O_4 and Co_7O_7, and the stability of the planar-like Co_4O_4 from the second-order energy difference calculation. Most interestingly, a new growth mechanism of Co_nO_n from the planar-like to the compact as the global minimum structure was predicted that occurs at the Co_5O_5 cluster.

1. Introduction

Experimental and theoretical studies of cobalt oxide clusters as a heterogeneous catalyst and on its electronic, magnetic, and other properties have received considerable attention recently [1]. Commonly, by modifying the shape and size of the cluster one will be able to manipulate directly these properties.

As a catalyst, the supported cobalt oxide nanoparticles are used for chemical transformation processes such as in the oxidation of carbon monoxide and nitrogen monoxide, and in the hydrogenation of CO or CO_2 (i.e. in Fischer-Tropsch synthesis) [2–4]. Increasing the size of cobalt oxide nanoparticles induces the dissociation of CO, thus increases the efficiency of the Fischer-Tropsch synthesis by reducing the dissociation energies of CO [5].

Several spectroscopic techniques such as IR vibrational, photo-dissociation and time-of-flight mass spectroscopy had been conducted to investigate different aspects of neutral and cationic cobalt oxides clusters ($Co_nO^{0/+}m$) [6–8]. For example, the mass spectrum data of cobalt oxide clusters have shown that the intensity peaks varies with the size of the cluster. The small clusters distinctly reveal higher signal intensity. In particular, the neutral and cationic $Co_4O^{0/+}4$ clusteres show the highest intensity, which reflects the remarkable structural stability of this small cluster [3,6]. These dissociation data have also shown that the predominant stoichiometry is $n = m$, in which the loss of oxygen molecules is the preferred dissociation channel. Therefore, the stoichiometric cobalt oxide clusters ($Co_nO^{0/+}n$) merit more interest than others.

The key to studying reaction mechanisms and properties of the nanoparticles is through the extensive exploration of the potential energy surface (PES) of their molecular structures. There have been numerous techniques used to investigate the PES namely by statistical mechanics, basin-hopping (BH) and genetic algorithms (GA), which have been implemented in computer codes such as CBEV/FCEM [9,10], GMIN [11] and Birmingham cluster genetic algorithm (BCGA) [12], respectively.

Recently, the electronic structure methods such as Density Functional Theory (DFT) have been used to search the global minimum of PES of neutral cobalt oxide clusters Co_nO_n ($n < 10$) [8,13–15]. It was reported that the lowest-energy configurations of Co_nO_n has ring and tower-like structures, differing from the face centered cubic structure of the bulk. Despite recent interests, probing comprehensively the PES using these methods are computationally demanding due to the huge number of different possibility of isomers [16]. Therefore, true understanding and modeling of Co_nO_n clusters are still lacking.

---

* Corresponding author.
** Corresponding author.
E-mail addresses: hazzaid@yahoo.com (A.O.H. Zayed), mnoh@um.edu.my (M.N. Daud).

http://dx.doi.org/10.1016/j.jallcom.2016.11.151

Applied Surface Science 427 (2018) 1090–1095

Contents lists available at ScienceDirect

Applied Surface Science

journal homepage: www.elsevier.com/locate/apsusc

Electronic, magnetic and structural properties of Co_3O_4 (100) surface: a DFT+U study

Ameerul Hazeeq Hashim[a], Ala' Omar Hasan Zayed[a,*], Sharifuddin Md Zain[a,*], Vannajan Sanghiran Lee[a], Suhana Mohd Said[b]

[a] Department of Chemistry, University of Malaya, 50603 Kuala Lumpur, Malaysia
[b] Department of Electrical Engineering, University of Malaya, 50603 Kuala Lumpur, Malaysia

ARTICLE INFO

Article history:
Received 26 July 2017
Received in revised form 26 August 2017
Accepted 11 September 2017
Available online 14 September 2017

Keywords:
Co_3O_4 (100)
DFT
Surface
Stoichiometric
Termination
Electronic properties

ABSTRACT

The three most stable (100), (110), and (111) surfaces exposed by Co_3O_4 are effective catalysts for various oxidation reactions. Among these surfaces, (100) has not yet received ample attention. In this study, we investigated the structural, electronic and magnetic properties of Co_3O_4 (100) surface using density functional theory calculations. By considering both stoichiometric and nonstoichiometric surface structures of the two possible terminations, A and B. Besides the greater stability of the newly proposed stoichiometric models compared to nonstoichiometric models reported in previous studies, the results show that the B termination is energetically preferred over the entire range of oxygen chemical potentials. Unlike the bulk, Co^{3+} octahedral ions become magnetic at the surface, which leads to interesting surface magnetic properties. Density of states (DOS) indicate a small band gap of 1.15 eV for the B-stoichiometric model, due to the presence of surface states in the bulk band gap. More polar surface with a very narrow band gap is found in the A-nonstoichiometric model. These surface states may play an important role in the magnetism and metallicity observed experimentally in several Co_3O_4 systems.

1. Introduction

Spinel cobalt oxide (Co_3O_4) plays an essential role in various applications of energy and environment-related areas. For example, the Co_3O_4 is an effective anode material for electrochemical water splitting [1,2] and a catalyst for many oxidation reactions, including converting chloride to chlorine [3], carbon monoxide to carbon dioxide [4], and ethyl alcohol to acetic acid [5]. More recently, supported Co_3O_4 nanoparticles on graphene show promising activities for oxygen reduction, which represents the primary key for renewable-energy technologies such as fuel cells [6].

Several spectroscopic techniques characterize the Co_3O_4 surfaces, including low Miller index planes [7–9]. Besides experiments, many computational studies had been devoted specifically to the (110) and (111) surfaces [10–12]. For instance, Selloni and Chen employed DFT+U calculations to investigate the energetics, atomic structures, and electronic and magnetic properties of the two possible terminations of the Co_3O_4 (110) surface [10]. Unlike the bulk material, they found that the Co^{3+} ions of the surface layer have nonzero magnetic moments, leading to different magnetic interactions between Co ions. In agreement with experimental data, they also revealed the partial metallic characteristic of both surface terminations because of the existence of surface electronic states in the bottom region of the bulk band gap. Their results not only implied the possible role of this surface in the study of redox reactions, but also quickly evoked the question of whether other Co_3O_4 surfaces reflect similar or different properties.

The (1 × 1) supercell of Co_3O_4 (100) surface is composed of alternate stacking sequence of layers, where one layer involves two cobalt ions (Co^{2+}) with tetrahedral coordination, while the other one contains four cobalt ions with octahedral coordination (Co^{3+}) and eight oxygen ions (O^{2-}). Consequently, two different terminations can be generated, often known as A and B surface terminations. The A termination has both Co^{3+} and Co^{2+} ions, whereas the B termination exposes only Co^{3+} ions. Similar to the ionic nature of bulk Co_3O_4 [13], the (100) slab can be viewed as sequential charged layers, depicted in the Fig. 1. In principle, the stack of charged layers causes increasing polarization with slab thickness, whereas the existence of polarity compensation mechanisms are due to inhibition of "polar catastrophe" [14].

Although the Co_3O_4 (100) surface show high-performance catalytic activity in H_2O dissociation [15], N_2O reduction [16], ammonia oxidation and oxygen evolution reaction [17,18], few

---

* Corresponding authors.
E-mail addresses: baszaid@yahoo.com (A.O.H. Zayed), smzain@um.edu.my (S.M. Zain).

http://dx.doi.org/10.1016/j.apsusc.2017.09.085